2019

THE FABRICATION AND CHARACTERIZATION OF METAL OXIDE NANOPARTICLES EMPLOYED IN ENVIRONMENTAL TOXICITY AND POLYMERIC NANOCOMPOSITE APPLICATIONS

Matthew Logan Hancock

University of Kentucky, matthancock18@gmail.com

Author ORCID Identifier:

https://orcid.org/0000-0001-8492-3512

Digital Object Identifier: https://doi.org/10.13023/etd.2020.007

Right click to open a feedback form in a new tab to let us know how this document benefits you.

Recommended Citation

THE FABRICATION AND CHARACTERIZATION OF METAL OXIDE NANOPARTICLES EMPLOYED IN ENVIRONMENTAL TOXICITY AND POLYMERIC NANOCOMPOSITE APPLICATIONS

———————————————————————

DISSERTATION

———————————————————————

A dissertation submitted in partial fulfillment of the requirements for the degree of
Doctor of Philosophy in Chemical Engineering
in the College of Engineering at the University of Kentucky

By

Matthew Logan Hancock
Lexington, Kentucky
Director: Dr. Eric Grulke, Professor of Chemical and Materials Engineering
Lexington, Kentucky
2019

Copyright © Matthew Logan Hancock 2019
https://orcid.org/0000-0001-8492-3512

ABSTRACT OF DISSERTATION

THE FABRICATION AND CHARACTERIZATION OF METAL OXIDE NANOPARTICLES EMPLOYED
IN ENVIRONMENTAL TOXICITY AND POLYMERIC NANOCOMPOSITE APPLICATIONS

Ceria (cerium oxide) nanomaterials, or nanoceria, have commercial catalysis and energy storage applications. The cerium atoms on the surface of nanoceria can store or release oxygen, cycling between Ce^{3+} and Ce^{4+}, and can therefore act as a therapeutic to relieve oxidative stress within living systems. Nanoceria dissolution is present in acidic environments *in vivo*. In order to accurately define the fate of nanoceria *in vivo*, nanoceria dissolution or stabilization is observed *in vitro* using acidic aqueous environments.

Nanoceria stabilization is a known problem even during its synthesis; in fact, a carboxylic acid, citric acid, is used in many synthesis protocols. Citric acid adsorbs onto nanoceria surfaces, capping particle formation and creating stable dispersions with extended shelf lives. Nanoceria was shown to agglomerate in the presence of some carboxylic acids over a time scale of up to 30 weeks, and degraded in others, at pH 4.5 (representing that of phagolysosomes). Sixteen carboxylic acids were tested: citric, glutaric, tricarballylic, α-hydroxybutyric, β-hydroxybutyric, adipic, malic, acetic, pimelic, succinic, lactic, tartronic, isocitric, tartaric, dihydroxymalonic, and glyceric acid. Each acid was introduced as 0.11 M, into pH 4.5 iso-osmotic solutions. Controls such as ammonium nitrate, sodium nitrate, and water were also tested to assess their effects on nanoceria dissolution and stabilization.

To further test stability, nanoceria suspensions were subject to light and dark milieu, simulating plant environments and biological systems, respectively. Light induced nanoceria agglomeration in some, but not all ligands, and is likely to be a result of UV irradiation. Light initiates free radicals generated from the ceria nanoparticles. Some of the ligands completely dissolved the nanoceria when exposed to light. Citric and malic acids form coordination complexes with cerium on the surface of the ceria nanoparticle that can inhibit agglomeration. This approach identifies key functional groups required to prevent nanoceria agglomeration. The impact of each ligand on nanoceria was analyzed and will ultimately describe the fate of nanoceria *in vivo*.

In addition, simulated biological fluid (SBF) exposure can change nanoceria's surface properties and biological activity. The citrate-coated nanoceria physicochemical properties such as size, morphology, crystallinity, surface elemental composition, and charge were determined before and after exposure to simulated lung, gastric, and intestinal fluids. SBF exposure resulted in either loss or overcoating of nanoceria's surface citrate by some of the SBF components, greater nanoceria agglomeration, and small changes in the zeta potential.

Nanocomposites are comprised of a polymer matrix embedded with nanoparticles. These nanoparticles can alter material and optical properties of the polymer. SR-399 (dipentaerythritol pentaacrylate) is a fast cure, low skin irritant monomer that contains five carbon-carbon double bonds (C=C). It is a hard, flexible polymer, and also resistant to abrasion. It can be used as a sealant, binder, coating, and as a paint additive. In this case, metal oxide nanoparticles were added to the monomer prior to polymerization. Titania nanoparticles are known to absorb UV light due to their photocatalytic nature. Titania nanoparticles were chosen due to their high stability, non-toxicity, and are relatively quick, easy, and inexpensive to manufacture. Channels in thin monomer films were created using a ferrofluid manipulated by magnetic fields.

The mechanical properties of a microfluidic device by rapid photopolymerization is dependent on the crosslinking gradient observed throughout the depth of the film. Quantitative information regarding the degree of polymerization of thin film polymers polymerized by free radical polymerization through the application of UV light is crucial to estimate material properties. In general, less cure leads to more flexibility, and more cure leads to brittleness. The objective was to quantify the degree of polymerization to approximate the C=C concentration and directly relate it to the mechanical properties of the polymer. Polymerization of C=C groups was conducted using a photoinitiator and an UV light source from one surface of a thin film of a multifunctional monomer. The C=C fraction in the film was found to vary with film depth and UV light intensity. The extents of conversion and crosslinking estimates were compared to local mechanical moduli and optical properties. A mathematical model linking the mechanical properties to the degree of polymerization, C=C composition, as a function of film depth and light intensity was then developed. For a given amount of light energy, one can predict the hardness and modulus of elasticity. The correlation between the photopolymerization and the mechanical properties can be used to optimize the mechanical properties of thin films within the manufacturing and energy constraints, and should be scalable to other multifunctional monomer systems.

Matthew Logan Hancock
(Name of Student)

12/13/2019
Date

THE FABRICATION AND CHARACTERIZATION OF METAL OXIDE NANOPARTICLES EMPLOYED
IN ENVIRONMENTAL TOXICITY AND POLYMERIC NANOCOMPOSITE APPLICATIONS

By
Matthew Logan Hancock

Dr. Eric Grulke
Director of Dissertation

Dr. Stephen Rankin
Director of Graduate Studies

12/13/2019
Date

DEDICATION

In memory of Dr. Eric Grulke

ACKNOWLEDGMENTS

I can do all things through Christ who strengthens me. – Philippians 4:13

TABLE OF CONTENTS

LIST OF TABLES

LIST OF FIGURES

OVERVIEW OF DISSERTATION

There is considerable interest in engineered nanoparticle synthesis and development among researchers due to the versatile properties of nanomaterials and their ability to influence chemical and physical phenomena. Generally, nanoparticles can be used in an assortment of applications in medicine, energy, environmental science, material science, and electronics, to name a few. A large selection of nanoparticles is explored throughout this dissertation, including ceria, titania, iron oxide, silica, copper, and silver, each for a specific application as discussed below.

Citric acid coated nanoceria (CeO_2) was synthesized via a hydrothermal method and characterized by a variety of techniques as discussed in Chapter 1. Nanoparticle characterization is essential to help researchers better understand the chemical and material properties that can be used to support future experimentation and applications of the nanomaterial.

Chapter 2 contains the experimental results and their discussion when subjecting the citric acid coated nanoceria to acidic aqueous environments typically found in biological systems and the natural environment. The overall objective is to determine if dissolution occurs and ultimately to give insight into the environmental conditions required for dissolution and stabilization. In addition, the mechanism and rate analysis of dissolution was computed. Furthermore, simulated biological fluids replicating lung, gastric, and intestinal fluids were created and exposed to the nanoceria particles. The results are summarized in Chapter 3.

Chapter 4 presents nanotitania (TiO_2) synthesis methods and characterization results. The nanotitania is intended to be embedded in an acrylate polymeric matrix for the adjustment of optical properties, such as the refractive index. This chapter also contains nanocomposite fabrication procedures that can be used to, although not limited to, manufacture capillary electrophoresis microfluidic chips. The channels created in the monomer films are produced using a ferrofluid manipulated by magnetic fields. The synthesis and characterization of polyacrylic acid coated magnetite (Fe_3O_4) to be used as a ferrofluid is discussed in Chapter 5.

A polymerization model of the multifunctional monomer used to create the microfluidic chips is developed in Chapter 6. Crosslinking gradients as a result of the free radical photopolymerization process are observed experimentally throughout the film depth. The model results are used to estimate material properties, such as Young's modulus and hardness. These results will assist manufacturers in developing a procedure to polymerize and approximate the mechanical properties of a resulting film.

Appendices A, B, and C include the chapter highlights, funding sources, and instrumentation methods/techniques, respectively. Appendix D contains the physicochemical characterization of metal and metal oxide nanomaterials composed of Cu, Ag, CeO_2, and SiO_2. The objective was to determine and characterize the physicochemical nature of the nanoparticle samples and link the data to a US EPA nanomaterial-toxicity database.

THE CHARACTERIZATION OF CITRIC ACID COATED CERIUM OXIDE
NANOPARTICLES PREPARED VIA HYDROTHERMAL SYNTHESIS

1.1 Introduction

1.1.1 Background

Ceria (CeO_2) have been previously utilized as oxidative catalysts [1-3], UV absorbing

materials [4, 5], and for use in purification of motor exhaust gases [6], heat resistant alloy

coatings [7], solid oxide fuel cells [8], sunscreens [9, 10], solid electrolytes [11], diesel fuel

additives [12], semiconductor manufacturing [13], and polishing [14]. There is high

interest in nano-sized materials due to their unique material properties, low manufacturing

cost, decreased toxicity, and greater mobility than the bulk material. Nanoceria particles

can be useful in a variety of material, chemical, and medical applications. Interest has

recently sparked for nanoceria use in biomedical applications [15]. The therapeutic

potential of nanoceria includes treating/addressing cancer [16, 17], radiation-induced

damage [18, 19], cardiac dysfunction [20, 21], neurodegenerative disease [22, 23], retinal

degeneration [24, 25], and wounds [26] to name a few.

In order for nanoceria particles to be effective in biomedical applications, colloidal

stability and small, narrow size distributions are instrumental for positive, meaningful

outcomes [27]. The biodistribution of nanoceria from blood revealed nanoceria

concentration present in the spleen and liver, but little in the brain. The toxicity of nanoceria

is quite low, however large aggregated ceria particles produced granuloma in the lungs and

liver, and fibrosis in the lungs [28-30]. In fact, many negative immune effects are related

to nanoparticle aggregation. The aggregated nanoparticles are generally immunotoxic,

3

while the stable, non-aggregated nanoparticles show no toxicity [31]. Dissolution studies have shown degradation of nanoceria in acidic environments containing carboxylic acids, present in phagolysosomes and in the plant rhizosphere. The dissolution rate was determined to be directly proportional to the particle surface area [32, 33]. Exposure of citrate-coated nanoceria particles to simulated lung, gastric, and intestinal fluids resulted in loss or overcoating of the surface citrate, and in some cases, agglomeration [34]. *In vivo* processing of nanoceria has been found to form cerium phosphate, presumably by a dissolution/re-crystallization process. This transformation includes particle size and valence reduction along with redox activity present in biological and environmental systems that can be related to the free-radical scavenging activity of nanoceria [35-37]. Ceria is a well-known redox catalyst, which provides the basis as a versatile material to be used in a wide variety of applications. The cerium atoms on the surface can store or release oxygen, cycling between Ce^{3+} and Ce^{4+} ions [36, 38-41]. A reduction of particle size is typically accompanied by an increase in Ce^{3+} ions. An increase of Ce^{3+} ions and oxygen vacancies within the crystal structure causes lattice strain which increases the lattice parameter [42].

Nanoceria can be stabilized and particle growth (agglomeration) prevented by coating with citric acid [43-45]. The negative charges present on citric acid's carboxylic acid groups act as a repelling agent between other citrate coated nanoceria particles to create a stable, colloidal sol. Shape analysis determined that nanoceria particle shape was dominated by a truncated octahedral for particles between 3-10 nm [46]. The understanding of nanoparticle behavior in the environment is important due to concerns for their potential

to interact with drinking water systems and reservoirs. The uncertainties come from the lack of understanding of their surface structure and energies [47].

Numerous methods have been used and reported to fabricate nanoceria particles including precipitation [48-50], sol-gel [51-53], spray hydrolysis [54], spray pyrolysis [55], sonochemical [56-58], microemulsion [59], microwave-assisted hydrothermal [60-64], and hydrothermal [43, 65-71]. This chapter is intended to shed some light on the surface properties of citrate-coated nanoceria produced via hydrothermal synthesis. A variety of characterization techniques were implemented to determine size, morphology, surface properties, and citrate complexation on the surface of nanoceria particles.

1.1.2   Cerium Ion Toxicity

Ceria nanoparticles and the cerium ion interact differently within biological systems. The cerium ion is presumed to be more mobile than nanoparticles and also exhibits different cytotoxicity [36]. Stark [72] clearly distinguished molecules, or ions, and nanoparticles as completely separate entities that operate via differing mechanisms in biological milieu. He also notes that the failure to yield reliable experimental results is a direct result of the lack of understanding of the differences between particles and molecules. Therefore, unreacted cerium should be removed from nanoceria directly following the synthesis.

Compared to the cerium ion, nanoceria particles are less toxic, which is part of the concern to remove cerium ion from nanoceria; they might contribute to biological effects

that shouldn't be attributed to nanoceria. In previous studies, a 100 mg cerium ion/kg intravenous (IV) injection was lethal to rats, while only three of eight rats died following an IV injection of 250 mg of 5 nm nanoceria/kg [73]. Pulmonary inflammatory responses to 0.1 mg/kg cerium ion were observed, however there were no changes in responses from 1 mg/kg nanoceria [74]. The LD50 of cerium chloride in mice was approximately 13 mg/kg [75]. In addition, IV injection into dogs of 50 mg/kg cerium chloride resulted in deterioration over 21 days [76]. Cerium ion was injected into rats at concentrations of 9 and 18 mg/kg. As a result, the rat experienced severe hepatotoxicity, including fatty liver and jaundice [77]. In contrast, doses up to 100 mg/kg of 5, 15, 30, and 50 mg/kg of 55 nm ceria in rats were tolerated for 30 days [78]. Once the cerium ion enters into the blood steam, it can cause aggregation of proteins found in plasma [79]. Toxic effects of high dose rare earth elements (REE), that includes cerium, are related to enzyme activity. REEs can enter cells and bind with macromolecules, and therefore inhibit bodily functions [80].

The pharmacokinetics of nanoceria and cerium ion are also quite different. Four hours following IV injection of 5, 15, and 30 nm nanoceria and cerium ion into the blood stream of rats, Dan et al. [73] discovered that the nanoceria was removed from the blood faster than the free ion. Molina et al. [74] compared the lung clearance of 40 nm nanoceria to cerium ions. Both materials showed slow clearance after 28 days: there was 88% of nanoceria and 74% of cerium ion remaining. However, in extrapulmonary organs, only 0.9% of nanoceria and 6.0% of the cerium ion dose were retained. Also, fecal and urinary cerium ion elimination was much higher than nanoceria. Significant amounts of cerium ion were retained in most tissues 28 days post-installation, with most discovered in the bone and liver. This relates well to Yokel et al. [28] where 72% of the total nanoceria dose found

in organs was present in the liver, spleen, and bone marrow after 90 days. In addition, 15 days after an IV injection of cerium chloride, 20, 16, 2, and 2% was in the skeleton, liver, kidneys, and gastrointestinal (GI) tract, whereas 0.7, 0.5, 0.08, 0.08, and 0.05% was in the muscle, spleen, lung, testes, and heart, respectively [81, 82]. However, Takada and Fujita [82] were able to use diethylenetriaminepentaacetic acid (DTPA) to remove cerium ion from contaminated wounds. They successfully showed that significantly less cerium was retained in the liver, bones, kidneys, GI tract, muscle, lungs, spleen, and heart after 15 days. The percent of dose removed though urine was largely increased due to the DTPA.

The potential toxicity is low for inhaled, ingested, or injected nanoceria, however the same is not true for free cerium ions. Longer tissue retention times, coupled with higher toxicity of free cerium ions, supports the need to remove free cerium before injection of nanoceria into the body. Furthermore, the pharmacokinetics of each are not analogous and the separation of cerium ions from nanoceria solutions is critical in order to obtain reliable experimental results.

1.1.3   Cerium Citrate Complexation

How citric acid is bound to the cerium ion has been reported as a variety of possible cerium citrate coordination complexes [83]. Leal [84] suggested the formula $(Cit)_2Ce^{3-}$, however the actual structure, i.e. the exact location of Ce-O bonds, is unknown. Ohyoshi et al. [85] studied, by ion exchange method, complexes resembling $M(H_2Cit)^+$, $M(H_2Cit)_2^-$, MHCit, and $M(HCit)_2^{3-}$, where M represents lanthanides. Again, the structures were not determined, but insight into the number of bonds between cerium and the number of

deprotonated carboxylic acids helps understand the complex formation. Further studies of citrate complexation with lanthanides led to the suggestion of bifurcated and/or chelated bonds between carboxylic acid oxygen groups and the metal ion [86-90]. Baggio and Perec [91] reported a polymeric lanthanum citrate complex consisting of bridged O-C-O groups with a repeat unit of [La(HCit)(H$_2$O)]. This suggests the possibility of multiple citrate molecules bound to one individual Ce ion and the idea of a multilayer coating surrounding a metal oxide core. Getsova et al. [92] indicated HCitH as a common bonding molecule to cerium containing one protonated carboxylic group, and reported that one Ce^{3+} ion can be bonded to ligands participating in other cerium citrate complexes. Zhang et al. [44] proposed possible structures of cerium citrate complexation and suggested the possibility of as many as three citrate molecules bound to one cerium cation. Chen et al. [93] reported formations of dimeric complexes of lanthanide trihydrates with citrate or malate. Models of MHCit and MCit$^-$ are shown in Fig. 5 of Heller et al [94] where 'M' refers to Cm or Eu. The confirmed complexations of MHCit and MCit$^-$ are determined based on the location of the peaks in the IR spectrum. Grulke et al. [32] computed the formation energy of single and bi-ligand complexes in comparison to nanoceria, which revealed in order of stability: bi-ligand complexes > nanoceria > single-ligand complexes. The bidentate chelating configurations were also reported as being favored over bridging and monodentate configurations. Auffan et al. [95] used ATR-FTIR and ^{13}C-NMR to show that citrate formed a chelate with Ce(IV) present on the nanoceria surface through its central carboxyl and its α-hydroxyl groups. Much is still unknown about the complexation of citric acid on the nanoceria surface. However, surface ceria citrate complexation will be addressed throughout this work to help fill in some research gaps.

1.2 Experimental

1.2.1 Materials

The following chemicals, including their sources, purity, and CAS #s, used in the nanoceria synthesis, and adjustment of osmolarity and pH were: cerium(III) chloride heptahydrate, Sigma, 99.9%, 18618-55-8; citric acid monohydrate, Fisher, ACS grade, 5949-29-1; ammonium hydroxide, Sigma, ACS grade (28% NH_3 in H_2O), 1336-21-6; sodium nitrate, VWR, ACS grade, 7631-99-4; sodium hydroxide, VWR, ACS grade, 1310-73-2; and nitric acid, Sigma, ACS grade, 7697-37-2. Lacey carbon, 300 mesh, copper grids (product #01895) from Ted Pella, Inc. were used for electron microscopy. Dialysis tubing from Ward's Science (product #s 470163-404 & 470163-408) with a MWCO of 12-14 kDa was used for dialysis against citric acid and DI water. The citric acid-1,5-$^{13}C_2$ used to produce nanoceria to be analyzed by ^{13}C-NMR was from Sigma, 98%, 302912-06-7.

1.2.2 Methods

Nanoceria was synthesized using a hydrothermal method based on Masui et al. [43]. A cerium chloride heptahydrate and citric acid monohydrate mixture was added to ammonium hydroxide and stirred. The final concentrations were 0.25 M cerium chloride, 0.25 M citric acid, and 1.5 M ammonium hydroxide. The mixture was transferred to an autoclave for 24 hours at 50 °C, and then another 24 hours at 80 °C. The product was then dialyzed against 0.11 M (iso-osmotic) pH 7.4 citric acid for 120 hours, replacing the dialysate every 24 hours, to remove excess cerium salts (Ce ions) and ammonium hydroxide. This was then dialyzed against DI water for an additional 72 hours, replacing

the dialysate every 24 hours, to remove unbounded citric acid from the solution. The dialysate volume was 10x the nanoceria dispersion volume. The resulting mixture was a stable, well-dispersed sol of ceria nanoparticles dispersed in DI water. It was stored under refrigeration protected from light.

The synthesis is summarized in the chemical equation below:
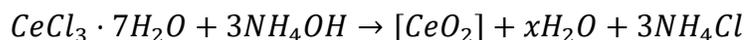
$$CeCl_3 \cdot 7H_2O + 3NH_4OH \rightarrow [CeO_2] + xH_2O + 3NH_4Cl$$

The [CeO$_2$] refers to cerium(IV) oxide, however the valence change between Ce^{3+} and Ce^{4+} accompanied by oxygen vacancies present within the chemical structure create an overall atomic ratio for Ce:O greater than the stoichiometric value of ½. Therefore, an 'x' is listed as the coefficient to H$_2$O in the above formula to account for the remaining oxygen atoms.

1.2.3   Techniques

Transmission Electron Microscopy (TEM)

The nanoceria sol was diluted with DI water to 0.5 mg/mL. The sample was sonicated for 10 minutes in a sonication bath. A lacey carbon, 300 mesh, copper grid was dipped into the solution for approximately 5 seconds and dried overnight at room temperature. Electron microscopy was performed on a Thermo Scientific Talos F200X. The instrument was operated at an accelerating voltage of 200 keV. TEM images were recorded on a Ceta CCD camera and particle size distributions were determined using ImageJ software. The mean

size (μ) and its standard deviation (σ) were computed and the low and high range of measured diameters was reported. Energy-Dispersive X-ray Spectroscopy (EDS) and Electron Energy Loss Spectroscopy (EELS) were also completed on the sample using Thermo Scientific's SuperX G2 and Gatans' Enfinium ER, respectively.

Dynamic Light Scattering (DLS)

Dispersions (0.5 mg/mL) were prepared then sonicated for 10 minutes. Using the Brookhaven 90Plus Particle Size Analyzer, five analysis runs of five minutes each were completed for the pre-dialysis, post-citrate, and post-water dialysis samples, and the average result of each run was analyzed and recorded. All samples were evaluated using the multimodal setting.

X-ray Diffraction (XRD)

Double-sided sticky tape was attached to a glass microscope slide and dried powder was distributed across the tape. Measurements were made using a Siemens D500 X-ray diffractometer with Cu Kα radiation. The analysis was conducted from 25 to 60 degrees 2θ, 0.01 degree step size, and a speed of 1 degree/min. Sharp, distinct peaks in the XRD spectra indicate a crystalline structure.

Thermogravimetric Analysis (TGA)

TGA (PerkinElmer TGA7) was used to determine the organic weight percent of the sample, in this case, the weight percent of citric acid bound to the nanoceria surface. This was repeated five times to get an accurate result of the overall weight percent of citrate. All runs were completed under a nitrogen atmosphere to prevent organic matter oxidation, resulting in pyrolysis of any organic matter on the nanoparticle surface. The sample was heated from 20 to 125 °C at 10 °C/min, held at 125 °C for 30 minutes to release physisorbed water, and then heated to 900 °C at 10 °C/min. The weight loss of the sample beyond 125 °C was determined to be the weight percent of citrate present on the surface. The amount of citrate groups was computed using the results from TGA and the particle size analysis from TEM images.

Fourier Transform Infrared Spectroscopy (FTIR)

A Nicolet 6700 FTIR with a diamond ATR crystal was used to detect organic functional groups on the nanoparticle surface. The lyophilized powder was placed on the crystal and 32 scans were completed, which was then duplicated using a 2nd batch of coated nanoceria. Peaks at 1365 and 1535 cm^{-1} wavelengths are attributed to the carboxylic acid functional groups present in citric acid.

Raman Spectroscopy

Nanoceria particles were placed on a glass microscope slide. The Raman spectra of the samples were analyzed on a Thermo Fisher Scientific DXR Raman microscope equipped with an Olympus brand microscope and a 10x working distance objective. A 780 nm Raman laser with the power set to 10.0 mW was used for sample analysis. The spot size of the laser beam was 3.1 µm. All Raman spectra were collected in a spectral range of 2500–50 cm^{-1}. Each Raman spectrum was an average of five accumulations consisting of 5 seconds each.

UV-Vis Spectroscopy

A BioTek Synergy 2 Plate Reader was used to perform UV spectroscopy. The spectra were collected from a wavelength range of 270 to 410 nm at a step rate of 5 nm. Each spectrum was an average of three total replications at each specified concentration.

Zeta Potential

An Anton Paar Litesizer 500 Particle Analyzer was used to determine the zeta potential of nanoceria dispersions at 0.5 mg/mL. 100 runs were completed in sequence with a 30 second equilibration time at 25 °C. The instrument was equipped with a 40 mW laser emitting at a wavelength of 658 nm. Zeta potential was determined multiple times between

pH 0.5 and 13. Nitric acid and sodium hydroxide were used to adjust the pH. The mean ± S.D. of the results was calculated.

¹³C-NMR

CP/MAS NMR data was collected using a home-built Tecmag Redstone NMR Spectrometer (Houston, TX), Bruker 300 MHz magnet (Billerica, MA), and Chemagnetics (Ft. Collins, CO) NMR probe with 7.5 mm rotors spinning at 4000 Hz. A relaxation delay of 2 seconds was used with 256 acquisition points and 20,480 scans and 1 ms CP contact time. TNMR software (Houston, TX) was used to process the data. 3-methylglutamic acid was used as a reference standard, with the methyl peak referenced to 18.84 ppm.

1.3 Results & Discussion

1.3.1 Particle Size & Morphology

The size and morphology of the synthesized nanoceria were initially characterized by TEM. Fifty particles were measured via ImageJ of Figure 1-1A. The average diameter is 4.24 nm with a standard deviation of 1.18 nm. The largest particle measured was 6.38 nm, while the smallest was 2.07 nm in diameter. The particles appear to be hexagonal in shape as shown in Figure 1-1B.

EDS mapping using the dark field STEM was also completed on the nanoceria product as shown in Figure 1-2. Both cerium and oxygen were found as expected. It is interesting to note that the nanoceria was only found on the edges of the lacey carbon film and protruded into vacuum spaces on the copper grids. This is evident in both Figure 1-1 and Figure 1-2 as well as other TEM and STEM images obtained as part of this study.

EELS can provide information about the surface oxidation state of cerium, i.e., Ce^{3+} or Ce^{4+}. The ionization edges in the high-loss region of the EELS spectrum are affected by the oxidation state of the elements present in the sample. Charge transfer between atoms due to oxidation reduces the screening effect on the ejected electron. The binding energy increases, shifting the ionization edges farther right on the EELS spectrum. The relative intensities of the M5 and M4 peaks are directly related to Ce^{3+} and Ce^{4+} concentrations, respectively. Figure 1-3 shows the M5/M4 peak heights for the nanoceria (a) core and (b) surface. The M5 peak is equivalent in height to M4 in the particle core, representing primarily Ce^{4+}. However, on the surface, the M5 peak is greater than M4, representing primarily Ce^{3+} valence state [96].
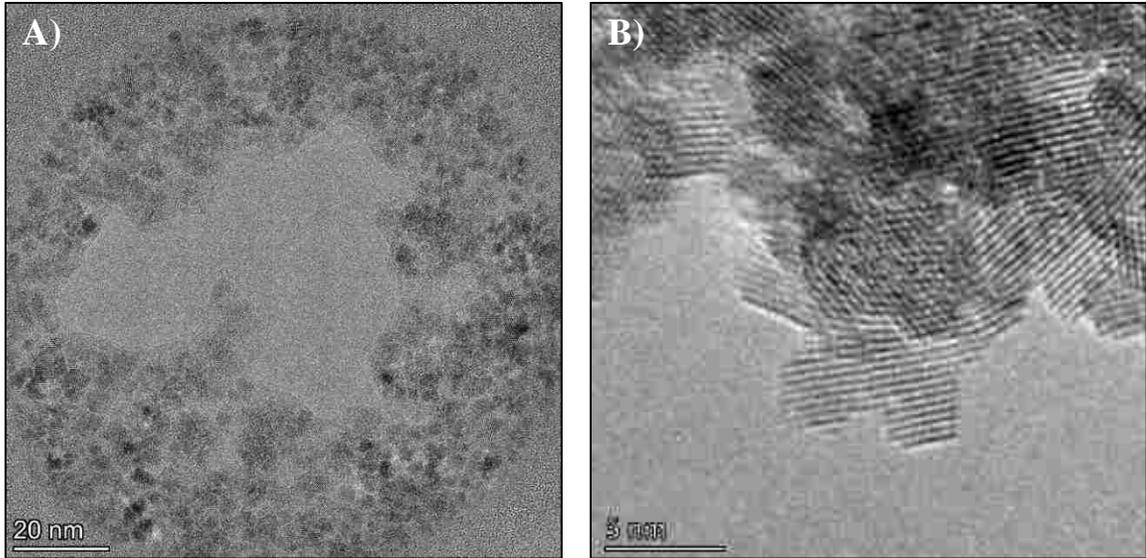
Figure 1-1: (A) Low magnification TEM image of nanoceria agglomerate. Agglomeration appears to be due to drying on the copper grid. (B) High magnification TEM image of individual crystalline nanoceria hexagonal particles.
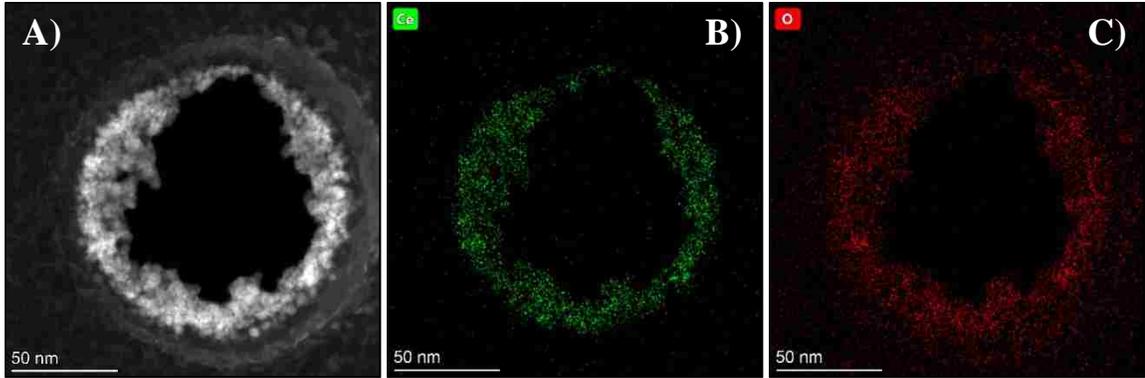
Figure 1-2: (A) Dark field STEM image of nanoceria particles, (B) EDS map of cerium, (C) EDS map of oxygen.
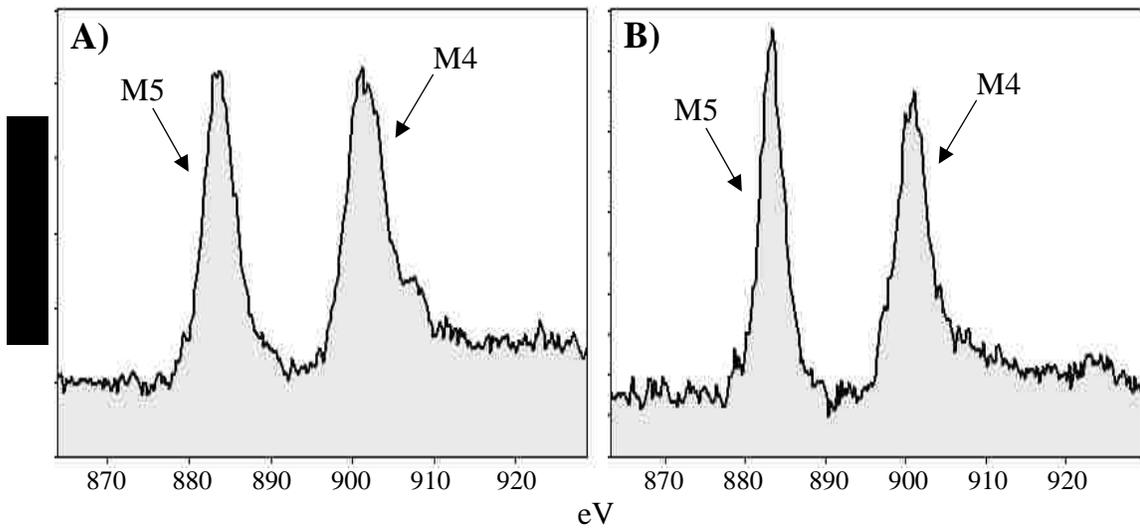
Figure 1-3: EELS analysis of nanoceria particles with labeled M5 and M4 peaks: (A) The M5 peak is equivalent in height to M4 in the particle core; (B) The M5 peak is greater than M4 on the particle edge.
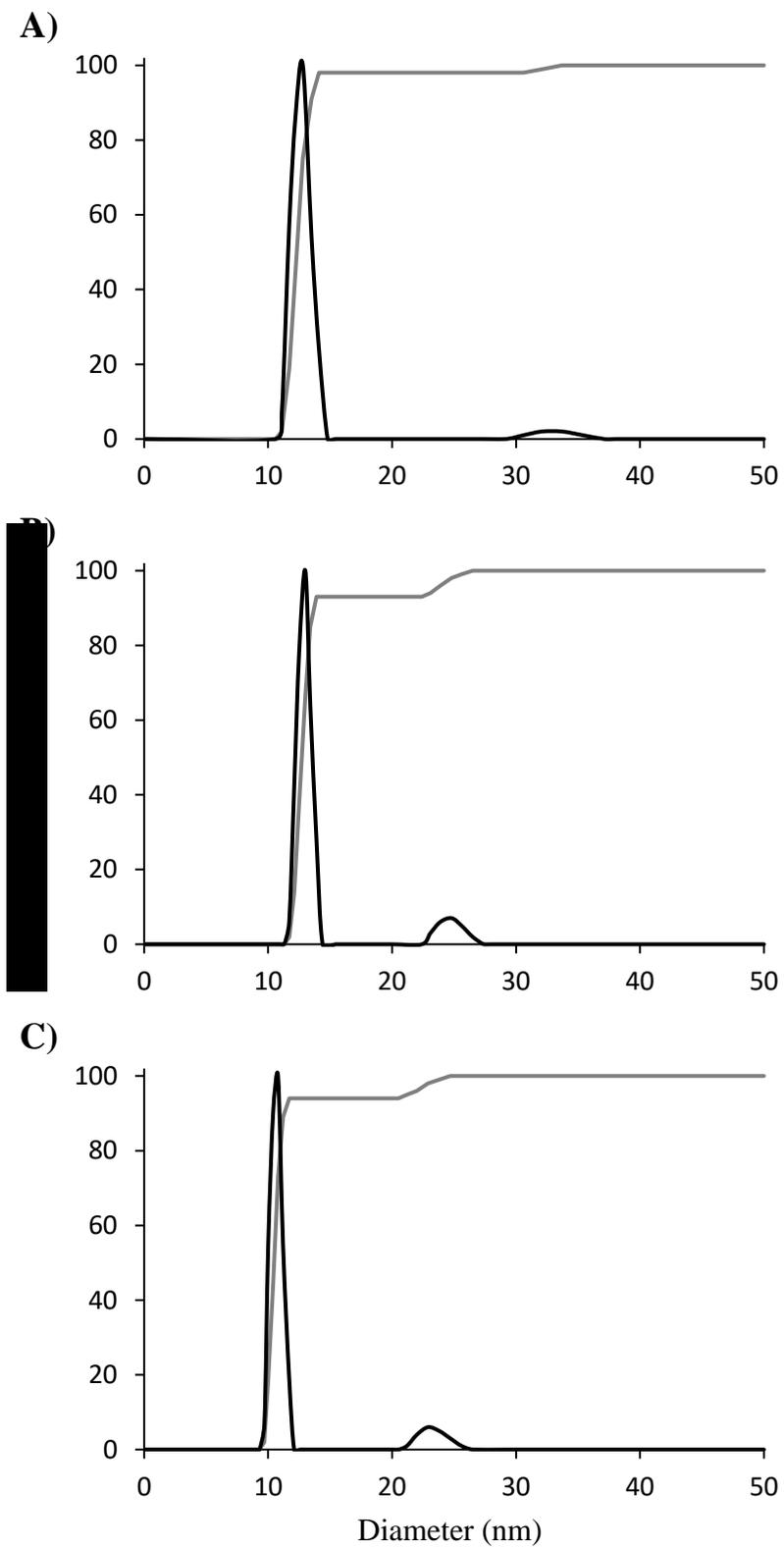
Figure 1-4: DLS of nanoceria – Black: Distribution, Gray: Cumulative: (A) pre-dialysis, (B) post-citrate dialysis, & (C) post-water dialysis.

DLS was completed at all stages of the synthesis: pre-dialysis, post-citrate dialysis, and post-water dialysis (Figure 1-4). All three samples had bimodal distributions. The 1st peak contains more than 90% of the sample by surface area percent. There is a small decrease in size, from approximately 12.8 to 10.8 nm hydrodynamic diameter (1st peak) after both sets of dialysis.

Table 1-1: The number of particles (N_p) in each circular area with diameter, D_g.

D_g (nm)	N_p	log (D_g/D_p)	log (N_p)
10	5	0.377	0.699
15	10	0.553	1.00
20	16	0.678	1.20
25	23	0.775	1.36
30	30	0.854	1.48

D_f	1.64
A	1.23
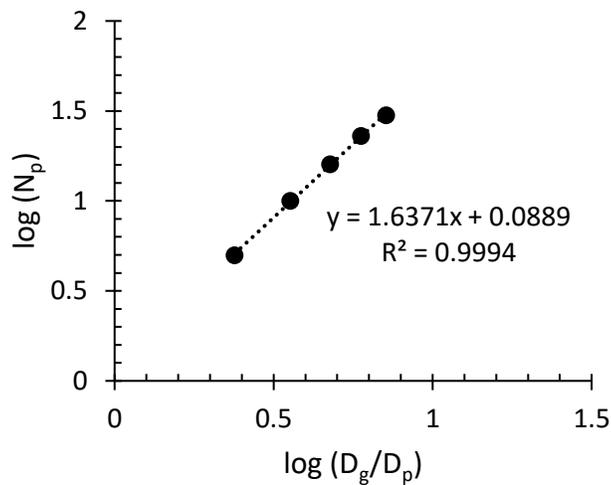
Figure 1-5: Fractal analysis of the nanoceria agglomerates.

$$y = 1.6371x + 0.0889$$
$$R^2 = 0.9994$$

19

The hydrodynamic diameter is not equivalent to the particle diameter as determined by TEM. Thus, it appears that in solution the particles are slightly agglomerated. This is common among a variety of metal oxide nanomaterials. It is possible to estimate the number of particles per agglomerate. The fractal dimension is a variable used to define agglomerate morphology, which can vary depending on particle density within an agglomerate. The fractal dimension is expressed as follows [Equation (1-1)]:

$$N_p = A \left(D_g \middle/ D_p \right)^{D_f}$$

(1-1)

Where N_p is the number of primary particles in the agglomerate, A is a dimensionless prefactor, D_g is the characteristic diameter of the agglomerate, D_p is the primary particle diameter (determined by TEM to be 4.24 nm), and D_f is the fractal dimension [97]. The number of particles were counted in predetermined circles with known diameters. For instance, circular areas were drawn onto the TEM image with diameters of 10, 15, 20, 25, and 30 nm, and individual particles were counted inside each area. These results were linearized and graphed, and a best-fit line fit to the data as shown in Figure 1-5. The slope is equal to the fractal dimension (1.64), and the intercept can be used to determine the prefactor (1.23). Table 1-1 shows the number of particles (N_p) in each circular area with diameter, D_g. Using Equation (1-1), the number of particles present in a 10.8 nm agglomerate is estimated to be on average 5.7.

1.3.2   Crystalline Structure

The XRD pattern of nanoceria matches that of face-centered cubic fluorite, JCPDS card no. 34-0394 [98-101]. The diffraction peaks are labeled and matched to the selected area electron diffraction (SAED) pattern as shown in Figure 1-6. The peaks are broad, representing that of a small crystallite size. The average particle size (D) was estimated using the Debye-Scherrer formula, where k is a constant (0.9), λ is the wavelength of the x-ray (0.154 nm), β is FWHM (full width at half maximum), and θ is the diffraction angle as shown in Equation (1-2).

$$D = \frac{k\lambda}{\beta cos\theta} \qquad\qquad (1\text{-}2)$$

The average particle diameter is 5.15 nm, as shown in Table 1-2. This is within standard error of the size analysis of the TEM images. The interplanar spacing, d_{hkl}, for each crystal plane with Miller indices (*hkl*) was calculated using Bragg's law as shown in Equation (1-3). The lattice parameter, a, was then calculated as follows [Equation (1-4)] and was found to be 0.541 nm:

$$2d_{hkl}sin\theta = \lambda \qquad (1\text{-}3)$$

$$\frac{1}{d_{hkl}^{2}} = \frac{1}{a^2}(h^2 + k^2 + l^2) \qquad (1\text{-}4)$$

Table 1-2: XRD data for the nanoceria particles.

XRD Peaks (2θ)	FWHM (°)	Diameter (nm)	d_{hkl} (Å)	Lattice Parameter (Å)
28.6	1.6	5.12	3.12	5.40
33.1	1.4	5.92	2.70	5.40
47.5	1.8	4.82	1.91	5.41
56.3	1.9	4.74	1.63	5.41

Avg. Diameter	5.15 nm

A)

Intensity (a.u.)

(111)

(200)

(220)

(311)

2θ (degree)

25   30   35   40   45   50   55   60

B)

111
200

220
311
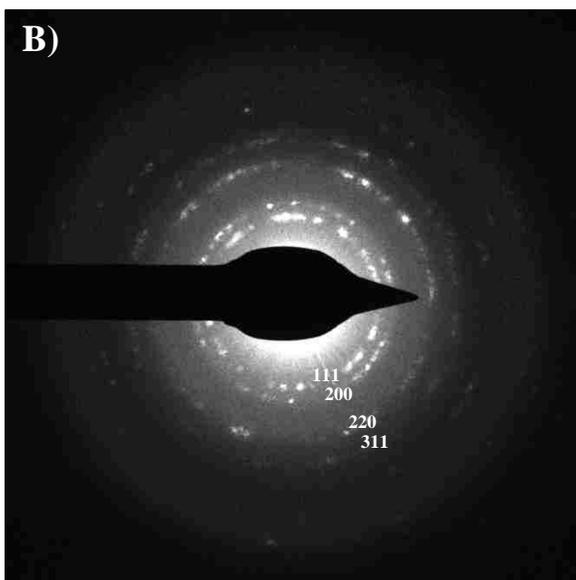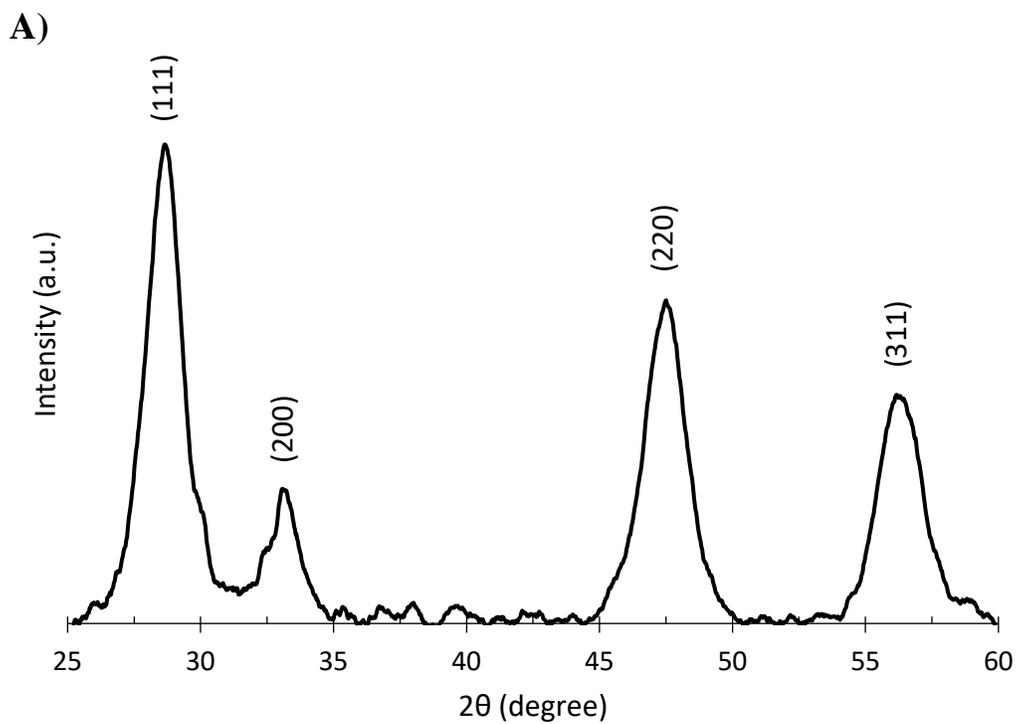
Figure 1-6: The (A) XRD and (B) SAED pattern for the nanoceria particles including crystal planes (JCPDS card no. 34-0394).

1.3.3   Surface Composition

The surface of the nanoceria is coated with citric acid. The citric acid molecules are adsorbed to the ceria particle surface and serve two purposes. First, they prevent further growth of the core ceria particle by restricting cerium ion access. Second, they prevent agglomeration by repelling neighboring particles due to their net negative charge. The result is a stable colloidal sol of citrate-coated nanoceria particles less than 10 nm in diameter.
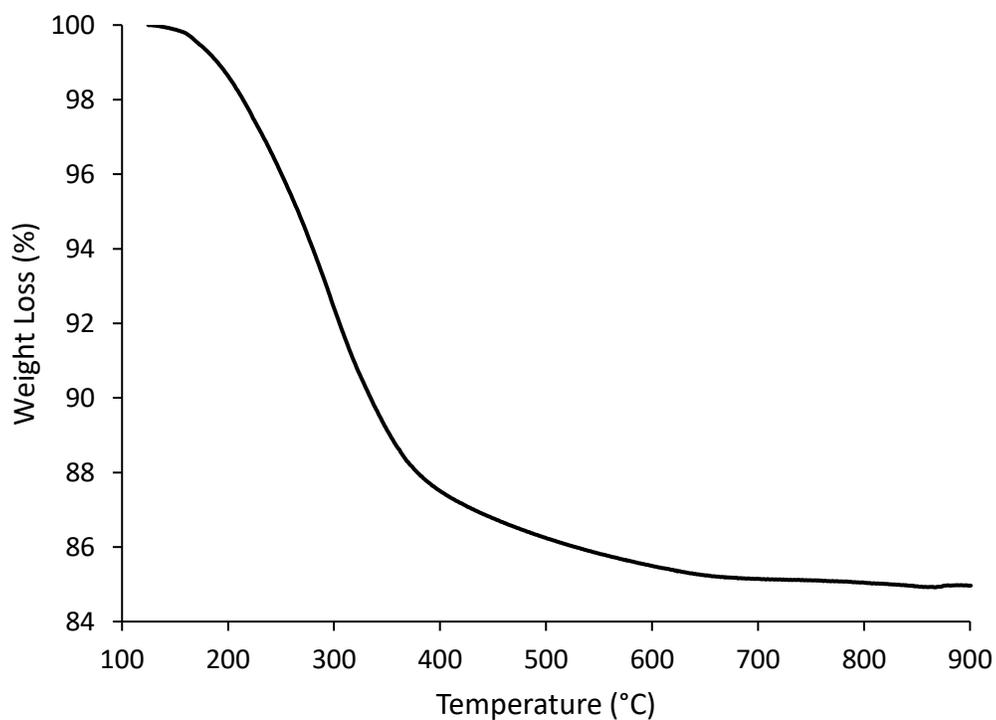
Figure 1-7: TGA weight loss of nanoceria contributing to citric acid.

TGA was completed on the lyophilized particles to determine the percentage of free water and citric acid present on the surface. Approximately 5% by weight is composed of free water present on the surface. This was determined by holding the temperature at 125 °C for 30 minutes. The TGA curve from 125 to 900 °C is shown in Figure 1-7. The weight loss dropped by 15% that can be attributed to citric acid. The weight percent of citric acid can be used to determine the number of citrate molecules per nm^2 on the particle surface [Equation (1-5)]:

$$A = \frac{W \rho r N_A}{3 M_W (1 - W)}$$

(1-5)

Where A is the number of citrate molecules/nm^2, W is the percent weight loss, ρ is the density of the core particle (7.22 g/cm^3), r is the particle radius, N_A is Avogadro's number, and M_W is the molecular weight of citric acid (192.1 Da). Assuming a core diameter of 4.24 nm (as determined by analyzing the TEM images), there are approximately 2.82 citric acid molecules per nm^2, corresponding to 160 citric acid molecules on the surface of each CeO_2 particle. This would result is a coating thickness of approximately 4.44 Å. The average diameter of citric acid molecules is in the range from 0.57 (hydrodynamic) to 0.72 nm (crystalline) [102]. This would mean that the surface is between 70 and 115% covered [103]. Therefore, on average, a citrate monolayer is present on the nanoceria surface.

In addition, the number of cerium ions incorporated on the surface of each particle can be estimated by calculating the number of CeO_2 unit cells present within one particle, using the lattice parameter as determined by XRD, 5.41 Å. Assuming a core diameter of 4.24 nm, there are approximately 1,000 CeO_2 molecules per particle, 390 of which are on the surface. See Figure 1-8 for the graph of the number of surface cerium ions in relation to the particle diameter. Therefore, there are 160 citric acid molecules bound to 390 cerium atoms. This indicates that two cerium atoms are potentially bound to one citric acid molecule.
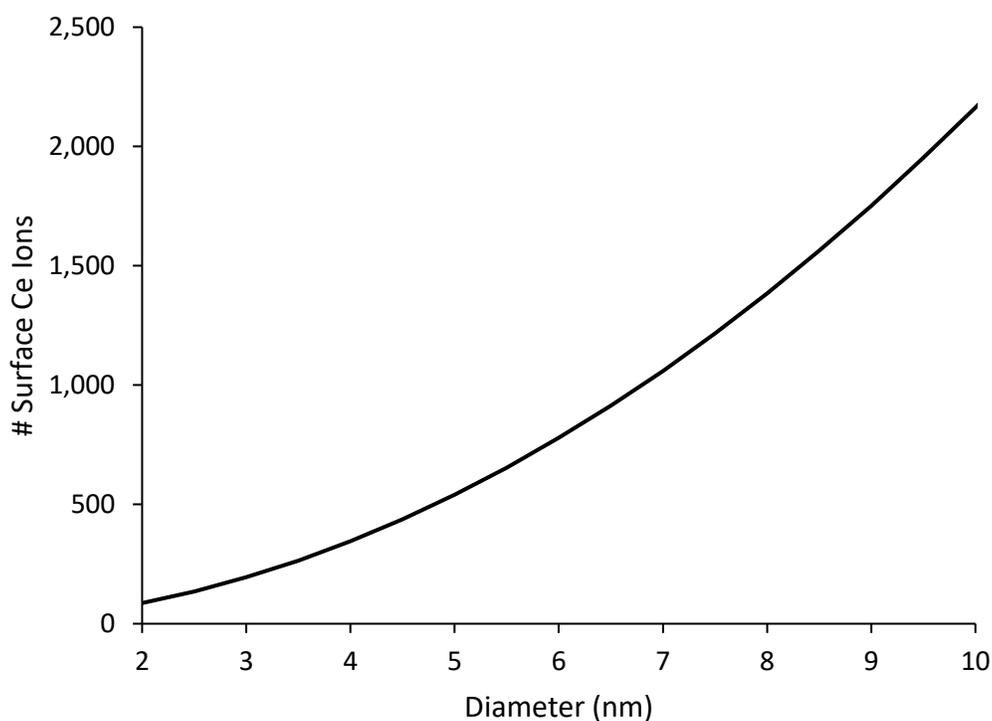
Figure 1-8: The number of surface cerium ions in relation to the particle diameter.

Figure 1-9 shows the FTIR spectrum of the citrate-coated nanoceria. The broad peak around 3200 cm^{-1} resembles the stretching band of a hydroxyl group. The peaks at 1535 and 1365 cm^{-1} are attributed to the antisymmetric and symmetric stretching band of a carboxyl group, respectively, confirming citric acid bonding to the surface of the nanoceria.

The peaks are similar to the peak locations of the dual strong peaks present in Figure 3 of Heller et al. [94] – 1568 and 1390 cm^{-1} vs. 1535 and 1365 cm^{-1}. Keep in mind that the metals used in this study were Cm and Eu. This could mean that the ligand is any of the $HCitH_2^-$, $HCitH^{2-}$, $HCit^{3-}$, or Cit^{4-} species, depending on the pH. The IR spectra trend is that the peak location wavenumber decreases as the ligand becomes more deprotonated, i.e. the pH increases. The pH of the pre-dialysis solution is 9.81, which decreases to 8.52 post-citrate dialysis, and then to 7.67 post-water dialysis. The neutral pH post-dialysis with citric acid and water is expected. According to Heller et al. [94], citrate molecules between a pH of 6 and 12 are $HCit^{3-}$. This species presents a wide variety of possible citrate complexes on the nanoceria surface given the deprotonation of three of the four possible hydroxides (three carboxyls and one hydroxyl).
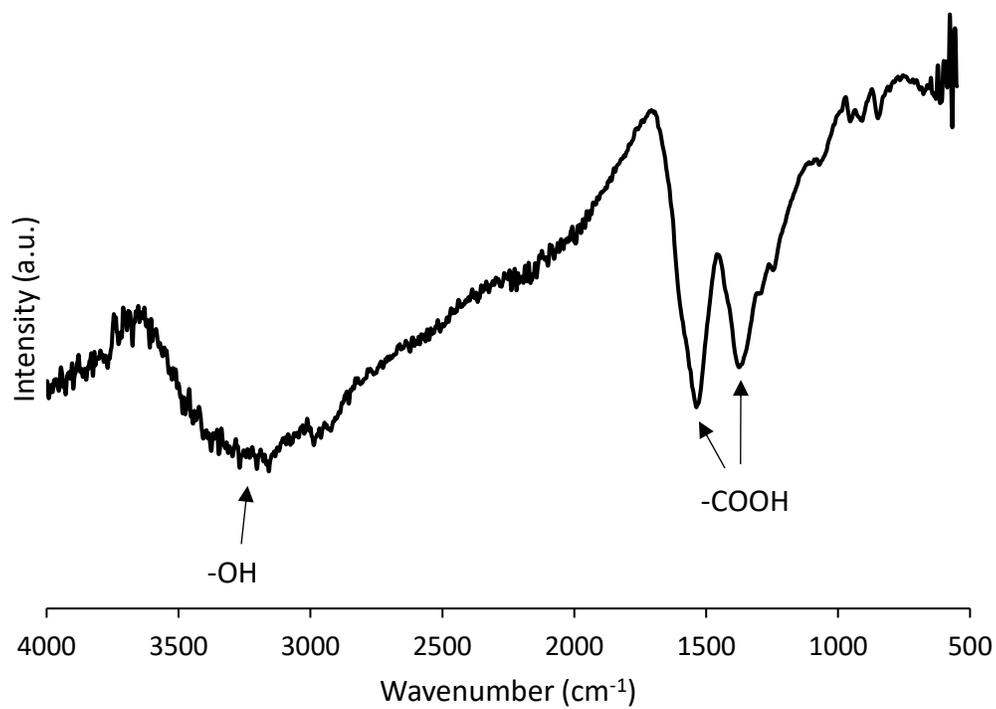
Figure 1-9: FTIR spectrum of citrate-coated nanoceria.

Figure 1-10 shows the citrate-coated nanoceria Raman spectrum. The peak at 465 cm^{-1}, which contains F_{2g} symmetry typical among fluorite structure metal dioxides, is described as a symmetric breathing mode of oxygen atoms surrounding the cerium ions [104]. The small peaks at 940 and 780 cm^{-1} are representative of citric acid on the surface of the nanoceria. Unlike the FTIR peaks, the citric acid peaks are barely noticeable, but are present. The peak around 1400 cm^{-1} is due to the microscope slide holding the sample. Similar to the XRD peaks, the broad peaks are attributed to the small particle size. In addition, other factors such as lattice strain, and consequently, valence, may affect the Raman peak size and shift [60].
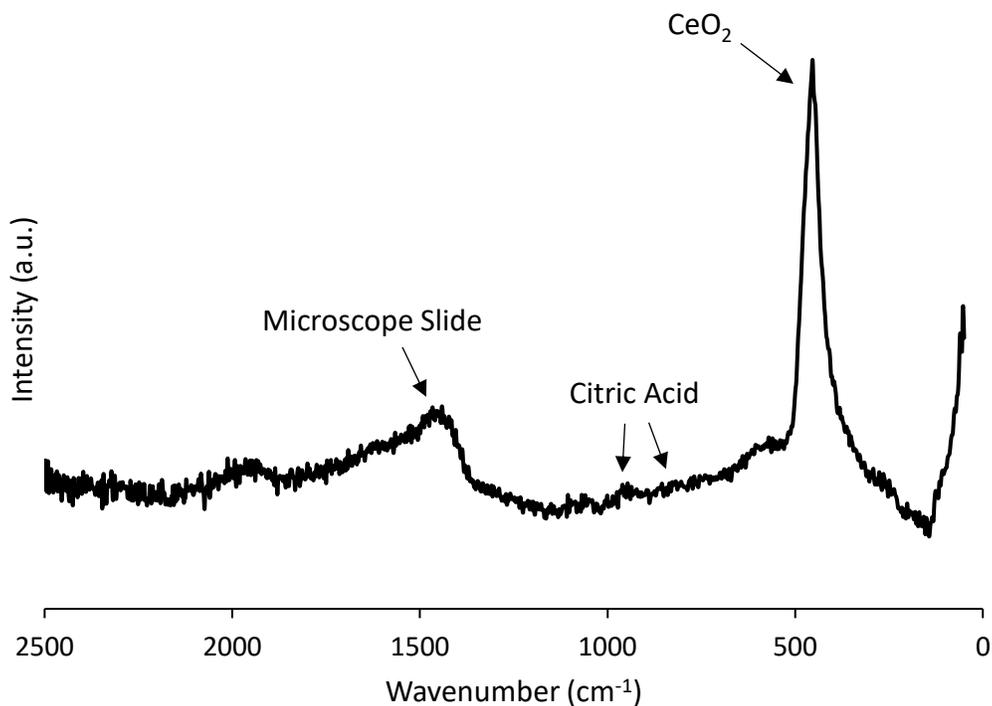
Figure 1-10: Raman spectrum of citrate-coated nanoceria.

The zeta-potential was determined for the citrate-coated nanoceria sol from pH 0.5 to 13 as shown in Figure 1-11. The zeta-potential determines the charge of a particle in suspension. A zeta-potential greater than +30 or less than -30 mV decreases the potential for agglomeration in the medium due to repulsive electrostatic forces [105]. The data was fitted using the Carreau model, which has been previously used to model zeta-potential, ζ, as a function of pH [103], as shown below in Equation (1-6):

$$\frac{\zeta - \zeta_\infty}{\zeta_o - \zeta_\infty} = [1 + (a \cdot 10^{pH})^2]^{(b-1)/2} \tag{1-6}$$

where ζ_∞ is the limiting zeta-potential at high pH, ζ_o is the limiting zeta-potential at low pH, and a and b are constant coefficients. The model predicted the isoelectic point (IEP) at pH 1.41. Agglomeration occurred below pH 2 and above pH 12. A plateau was not observed at a low pH, however the high pH plateau was estimated up to a pH of 12. The ζ_∞ was estimated to be -42.7 mV. The citric acid coating prevents agglomeration and contains negative charges that lower the zeta-potential values.
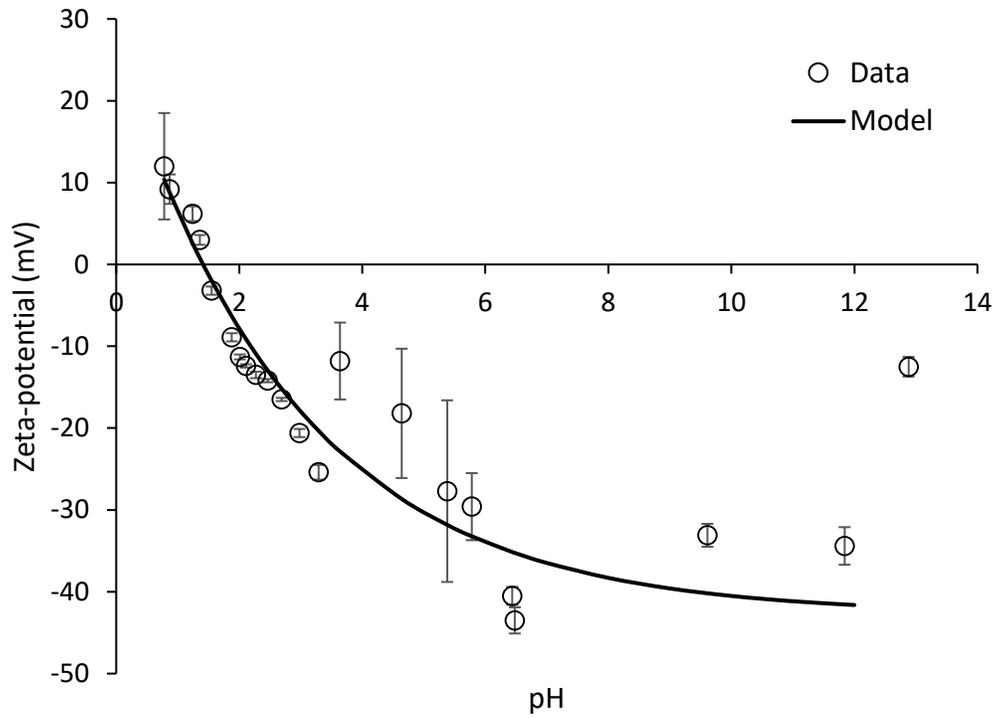
Figure 1-11: Zeta-potential of citrate-coated nanoceria with fitted Carreau model.

Figure 1-12 shows the UV-Vis spectra of citrate-coated nanoceria. Ceria absorbs light from a wavelength of 270 to 370 nm, well within the UV spectrum. Five concentrations are shown, some of the readings were too high for the instrument to read, therefore the graphs were terminated at that point. They were still included to show UV absorption at higher wavelengths for the larger nanoceria concentrations. A decrease in nanoparticle size has been reported to shift the UV adsorption edge to lower wavelengths [71].
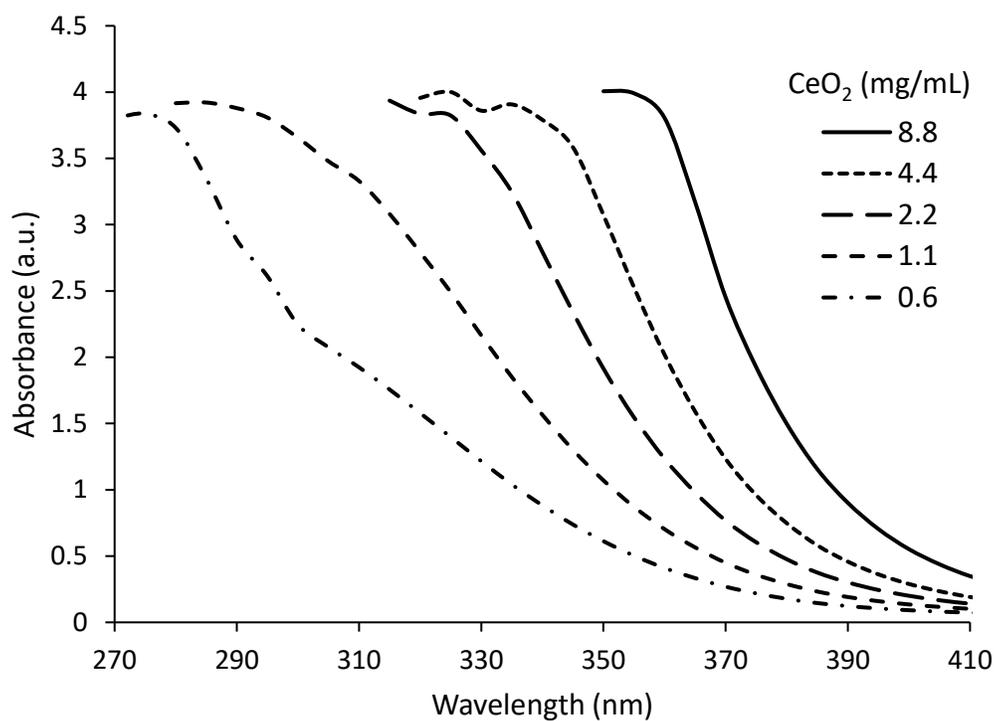
Figure 1-12: UV-Vis spectra of citrate-coated nanoceria.

^{13}C-NMR was completed on the lyophilized particles coated with unlabeled and ^{13}C-labeled citric acid. The labeled citric acid was only partially labeled, the terminal -COOH groups (C2) contained ^{13}C. The results are shown in Figure 1-13 and compared to the citric acid reference. The labeled spectrum indicates that the citrate bonded to the nanoceria particle during synthesis is retained through dialysis due to the C2 peak of the labeled nanoceria. In addition, the peak shifts at 87 and 165 ppm (dashed lines) may be a result of the C3 and either C2 or C1 carbons bonding to the nanoceria surface, respectively. This would suggest that the central carbon bonded to the hydroxyl (C3) group and either the central carboxyl (C1), one of the terminal carboxyls (C2), or perhaps two of the three total carboxyls participate in complexation with the nanoceria surface. The original C3 peak at 78 ppm remains which means that either free citric acid is still present or there is a possible combination of citrate bonding mechanisms. These results are similar to Auffan et al. [95]; they suggest that citrate formed a chelate with cerium through its central carboxyl and its α-hydroxyl groups.

Possible ceria-citrate complexes are shown in Figure 1-14. According to the TGA analysis results, it is likely that two cerium atoms are bound to one citrate molecule, which indicates that at least two oxygen atoms are complexing with ceria, thus rejecting model 1. ^{13}C-NMR results indicate that the central carbon bonded to the hydroxyl (C3) appears to be interacting with ceria. This would immediately reject models 1 and 3, at least as favored complexes. According to the FTIR peak locations and pH measurements, the citrate HCit^{3-} species favors model 5 if all three of the deprotonated oxygens participate in bonding with ceria. However, ^{13}C-NMR shows a large portion of the end carbon atoms bonded to the carboxylic acids (C2) remain unbonded to cerium, which could consist of any combination

of the five models shown or more. One possibility that arises from the ^{13}C-NMR results, and supported by Auffan et al. [95], is that the carboxylic acid functional group (C1) geminal to the central hydroxyl (C3) is favored to complex with ceria. This is shown in model 2 and again in model 5, accompanied by a terminal carboxyl (C2) bond.
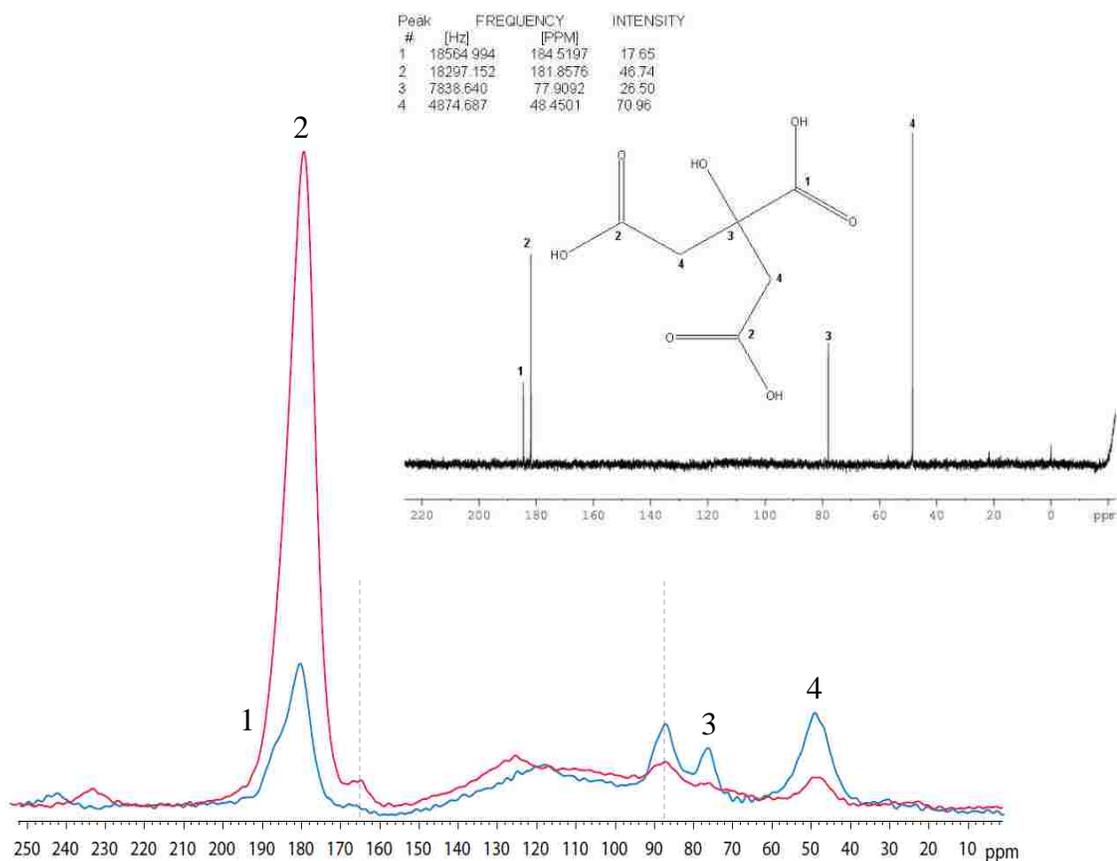
Figure 1-13: ^{13}C-NMR spectra of ^{13}C-labeled (red) and unlabeled (blue), including the citric acid reference (DrugBank ID# DB04272) with numbered carbon atoms. Dashed lines are placed at 87 and 165 ppm.
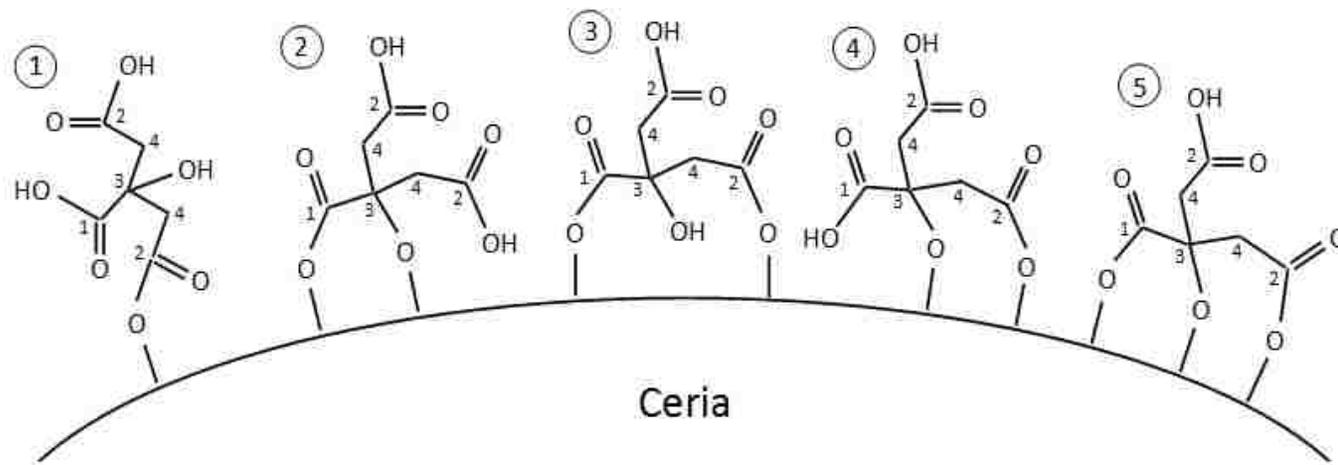
Figure 1-14: Possible bonding structures modeling ceria-citrate complexation.

1.4 Conclusions

Citrate-coated nanoceria particles were produced via hydrothermal synthesis and dialyzed against citric acid and water to remove unreacted cerium ions and salts. Characterization techniques were implemented to determine particle size and morphology, crystalline structure, and surface composition and properties. Particles were analyzed by TEM to be hexagonal in shape and determined to be 4.24 nm in diameter with a standard deviation of 1.18 nm. EELS indicates that the core is primarily Ce^{4+}, while the surface contains primarily Ce^{3+} atoms. The XRD and SAED patterns match the face-centered cubic fluorite crystal structure. The crystallite diameter was calculated to be 5.15 nm using XRD peaks, similar to TEM image analysis. A 15% weight loss due to citric acid was determined by TGA and FTIR, which corresponds to 2.82 citric acid molecules/nm^2. The zeta-potential was largely negative at a neutral pH with an IEP at pH 1.41. ^{13}C-NMR supports that the central carboxyl geminal to the hydroxyl complexes with ceria. In addition, one of the terminal carboxyls may also bond with ceria.

Some content of this chapter has been published in the following reports, as cited herein:

E. A. Grulke, M. J. Beck, R. A. Yokel, J. M. Unrine, U. M. Graham, and M. L. Hancock, "Surface-controlled dissolution rates: a case study of nanoceria in carboxylic acid solutions," *Environmental Science: Nano,* vol. 6, no. 5, pp. 1478-1492, 2019. [32]

R. A. Yokel, M. L. Hancock, E. A. Grulke, J. M. Unrine, A. K. Dozier, and U. M. Graham, "Carboxylic acids accelerate acidic environment-mediated nanoceria dissolution," *Nanotoxicology,* vol. 13, no. 4, pp. 455-475, 2019. [33]

2.1   Introduction

2.1.1   Background

Ceria (cerium oxide) nanomaterials have several applications such as acting as redox catalysts/metal supports [1], sunscreens [10], heat resistant coatings [7], and much more [47]. Biomedical applications of ceria-based compounds as a therapeutic have the potential to inhibit cancerous tumor growth [17], reduce radiation-induced damage [18], and heal wounds [26], etc. [106, 107]. The cerium atoms on the surface can store or release oxygen, cycling between Ce^{3+} and Ce^{4+}, and can therefore relieve and/or create oxidative stress within living systems [40].

██████████   Nanoceria in Plant Systems

Nanoceria acts as a colloid in aqueous environments, including within bodily fluids and in the soil near plant root systems. Carboxylic acids are secreted from plant roots which are known to complex with metals/metal oxides within the rhizosphere [108]. Factors that

affect the stability of colloids include temperature, pH, surface structure, ligands (both organic and inorganic) adsorbed onto the surface, and metal/nonmetal ions and their concentrations in solution surrounding the particles [109]. Ceria has been recently reported to interact with soil and plant roots, where it is known to dissolve and transform in the presence of chelating agents at low pH [110]. In cucumber plants, there was clear evidence of ceria uptake and transport throughout the plant, and a fraction of the ceria formed cerium carboxyl complexes. No phytotoxicity was reported to the plant itself [111]. Nanoceria was partially biotransformed in cucumber plants to cerium phosphate within the roots and cerium carboxylates in the shoots, presumably aided by carboxylic acids excreted by the roots [112]. Ceria transformation within cucumber plants was also found to be affected by phosphate, with a higher percentage of cerium carboxylates in the shoots without the addition of phosphate, than with [113]. Nanoceria can be taken up by food crops, however limited biotransformation was observed in soil cultivated soybeans [114]. Coated and uncoated ceria nanoparticles were found in the roots and shoots of corn plants. The organic matter content of the soil also played a critical role in nanoceria uptake [115]. Cerium was detected in plant tissues, indicating nanoceria translocation within tomato plants [116]. The uptake and toxicity of nanoceria within radish seedlings were significantly reduced upon addition of a citric acid coating to the particle surface [117]. Nanoceria was reported to partially dissolve due to organic acids present within radish root exudates [118]. Agglomeration of nanoceria was reported in algae growth medium beyond 28 hours of exposure [119]. Collin et al. [120] urged future studies to look into environmental exposures and transformations of nanoceria surfaces.

██████ Nanoceria within Biological Systems

Nanoceria has been shown to accumulate and remain within biological systems and organs for several months [121]. Long term persistence of nanoceria in rats was reported for 90 days. A significant amount was present within the liver, spleen, and bone marrow [28]. Nanoceria was present inside the liver and spleen of mice for up to 5 months [22]. Nanoceria was retained in rat retinas after 120 days. There was no toxicity of the nanoceria inside the eye, even after several months of exposure [122]. Yokel et al. [30] discussed the uptake, distribution, and toxicity of nanoceria within biological systems. Cellular uptake studies of nanoceria in adenocarcinoma lung (A549) cells favored the particles with a negative zeta potential. However, positive zeta potential particles were preferred for bovine serum albumin (BSA) adsorption. This suggests that surface interactions play a critical role in biological processes [123]. Nanoceria injection into rats led to persistence in the lung accompanied by granuloma formations after 30 days [124]. Significant amounts of cerium was discovered in the spleen and liver of rats 1, 20, and 720 hours after intravenous nanoceria infusion [78].

2.1.2   Nanoceria Dissolution

Nanoceria was recently shown to degrade within aqueous acidic environments, accelerated by carboxylic acids [33]. The dissolution rate was determined to be relative to the nanoparticle surface area and modeled to obtain dissolution rate coefficients [32]. Citrate-coated nanoceria particles were exposed to simulated lung, gastric, and intestinal fluids. The exposure resulted in loss or overcoating of the surface citrate, and in some cases,

39

agglomeration [34]. Exposure of vitamin C and glutathione led to dissolution-accompanied aggregation of mesoporous silica CeO_2 nanoparticles [125]. The shortening of ceria nanorods from 25 nm to 8 nm after 14 days at 200 °C was reported [126]. Partially degraded nanoceria formed cerium phosphate within rats, presumably by a dissolution/re-crystallization process [35-37]. Nanoceria (33 and 78 nm) was determined to dissolve at pH less than 5 and to a greater extent at pH 1.65. The dissolution rate was proportional to the surface area [127]. Nanoceria dissolution was observed at pH of 5.5 in the presence of citric acid and other reducing agents after 21 days [113]. Citric acid adsorption onto the surface of nanoceria varied due to pH and particle size [128]. Partial dissolution was observed at pH 4, however not in artificial soil solutions at pH 7 or 9 over 28 days [129]. Dissolution of nanoceria in aqueous solution was shown to be pH dependent: dissolution at pH less than 7 [130].

In this report, nanoceria stabilization and dissolution in the presence of carboxylic acids was tested over a time scale of up to 30 weeks. Sixteen carboxylic acids at pH 4.5 were tested: citric, malic, isocitric, glyceric, lactic, tartaric, α-hydroxybutyric, β-hydroxybutyric, succinic, pimelic, glutaric, tricarballylic, adipic, acetic, tartronic, and dihydroxymalonic acid. Controls such as ascorbic acid, ammonium nitrate, sodium nitrate, and water are also tested to assess their effects on nanoceria dissolution and stabilization. Ascorbic acid was used by Muhammad et al. [125], and 20 mM sodium salt used by Dahle et al. [127]. Ammonium nitrate was used in the initial nanoceria synthesis. Further, DI water was used at a pH of 6.5. The goal was to test whether carboxylic acids accelerate or stabilize dissolution in acidic aqueous environments, and to determine the mechanism of dissolution depending on the molecular structure of each ligand relating to agglomeration

or stabilization. In addition, the factor of UV light was included to simulate exposure to sunlight by plants and compared to the same set-up when protected from light.

2.1.3 Light vs. Dark Environments

In order to assess the affect of light, samples were placed under direct sunlight and compared to replicates stored in the dark. This simulates plant environments and biological systems, respectively. Ceria was reported to be used as a possible UV filter in sunscreens [10, 131]. Oxygen defects present in the crystal lattice can presumably be altered by UV irradiation causing an oxidation switch of the cerium atoms between Ce^{3+} and Ce^{4+}. This could explain the observance of a blue shift of the absorption edge in the UV-A region [132]. Studying the effects of UV irradiation on nanoceria would be beneficial for environmental applications. Colloidal nanoceria solutions were found to be non-toxic to fibroblasts, and were capable of preventing damage from UV irradiation [133]. When exposed to artificial sunlight, ceria nanoparticles produced hydroxyl radicals and induced lipid peroxidation of the gills of cardinal tetra, a native species of the Rio Negro region [134]. In addition to ceria, titania and zinc oxide are known to be photoactive. A recent study analyzing the effect of nanoparticle degradation on titania under UV light exposure showed anatase TiO_2 nanoparticles degraded more under the light condition than in the dark at pH 5.5 [135]. Silver-titania hybrid nanoparticles under light and dark conditions displayed differing bactericidal activity. Activity was increased under UV light, presumably due to the generation of reactive oxygen species [136]. The citric acid coating can also be altered by UV irradiation. Photolysis of citric acid under a Hg lamp formed 2-

methyl-2-hydroxysuccinic, 3-hydroxyglutaric, and tricarballylic acids, presumably due to CO_2 and -OH release [137].

The valance state of Ce^{3+} and Ce^{4+} on the surface of nanoceria has been shown to be altered by the addition of H_2O_2. Ceria nanoparticles with a high Ce^{3+}/Ce^{4+} ratio transitions from colorless to yellow upon addition of H_2O_2, due to the oxidation of Ce^{3+} to Ce^{4+}. The solution then transitions back to colorless after approximately 15 days, due to the reduction of Ce^{4+} to Ce^{3+} [39, 41]. This color transition is an important observation since the degradation of nanoceria will likely result in the change in oxidation state of surface cerium ions from Ce^{4+} to Ce^{3+}.

2.2 Experimental

2.2.1 Materials

The following chemicals, including their sources, purity, and CAS #s, used were: citric acid monohydrate, Fisher, ACS grade, 5949-29-1; DL-malic acid, Alfa Aesar, 98%, 6915-15-7; DL-isocitric acid, trisodium salt hydrate, Acros Organics, 95%, 1637-73-6; DL-lactic acid, TCI, >85%, 50-21-5; DL-glyceric acid, TCI, 20% in water (ca. 2 mol/L), 473-81-4; DL-tartaric acid, TCI, >99%, 133-37-9; glutaric acid, Acros Organics, 99% 110-94-1; tricarballylic acid, Alfa Aesar, 98%, 99-14-9; adipic acid, Sigma, 99%, 124-04-9; acetic acid, Sigma, ACS grade, 64-19-7; pimelic acid, Alfa Aesar; >98%, 111-16-0; succinic acid, TCI, >99%, 110-15-6; tartronic acid, Sigma, >97%, 80-69-3; sodium mesoxalate monohydrate, Chemodex, >98%, 31635-99-1; DL-2-hydroxybutyric acid

sodium salt, Alfa Aesar, >97%, 5094-24-6; DL-3-hydroxybutyric acid sodium salt, Chem Impex Int'l Inc., 100.3%, 150-83-4/306-31-0; ascorbic acid, TCI, >99%, 50-81-7; ammonium nitrate, Fisher, ACS grade, 6484-52-2; sodium nitrate, VWR, ACS grade, 7631-99-4; sodium hydroxide, VWR, ACS grade, 1310-73-2; nitric acid, Sigma, ACS grade, 7697-37-2; and sodium azide, Sigma, 99.8%, 26628-22-8. Lacey carbon, 300 mesh, copper grids (product #01895) from Ted Pella, Inc. were used for electron microscopy.

2.2.2   Methods

Hexagonal nanoceria particles (4.24 +/- 1.18 nm) (average +/- SD) were synthesized using a hydrothermal method [43]. The product was dialyzed for 120 hours at ten times the volume, changing the dialysate every 24 hours, against 0.11 M iso-osmotic citric acid adjusted to pH 7.4. The nanoceria sol was then stored in the dark at 4 °C.

Prior to Transmission Electron Microscopy (TEM) imaging, samples were sonicated for 10 minutes in a sonication bath. Lacey carbon, 300 mesh, copper grids were dipped into the solution for approximately 5 seconds and dried overnight at room temperature. A TEM was used to obtain images of particles throughout the experiment duration. The Thermo Scientific Talos F200X instrument equipped with a SuperX G2 EDS detector was operated at an accelerating voltage of 200 keV. The TEM images were recorded on a Ceta CCD camera.

Dynamic Light Scattering (DLS) was performed using the Brookhaven 90Plus Particle Size Analyzer, three analysis runs of five minutes each were completed for each

sample, and the average result of each run was analyzed and recorded. All samples were evaluated using the multimodal setting.

Nanoceria, 1 mg, was dispersed in 2 mL (500 µg/mL total concentration) of 0.11 M iso-osmotic aqueous media at pH 4.5 representative of that of lysosomes [138, 139]. Sodium hydroxide and nitric acid were used to adjust the pH of each solution and sodium nitrate to adjust the osmolarity. A variety of carboxylic acids were tested as shown in Figure 2-1. Ascorbic acid was used by Muhammad et al. [125]. 20 mM sodium salt was used by Dahle et al. [127]. This concentration was replicated in this experiment, corresponding to 20 mM $NaNO_3$ and NH_4NO_3. Ammonium nitrate was used in the initial nanoceria synthesis. Further, DI water was used as a control at pH 6.5. As a bactericide, 0.02% sodium azide was added to each sample. Each sample was repeated in duplicate and one placed next to a window for exposure to natural UV irradiation from the sun, and the other in the dark, or covered by aluminum foil.

Hydrodynamic particle size was repeatedly determined by DLS over 30 weeks (approximately 5,040 hours). Some samples were stopped early due to full dissolution. TEM and particle size/shape analyses were also completed on citric acid and β-hydroxybutyric acid samples under the light and dark condition at 0, 1, 2, 4, and 8 weeks. Furthermore, snapshots were taken at 0, 1, 2, and 4 weeks of the samples exposed to citric acid and water under the light and dark condition for comparison.
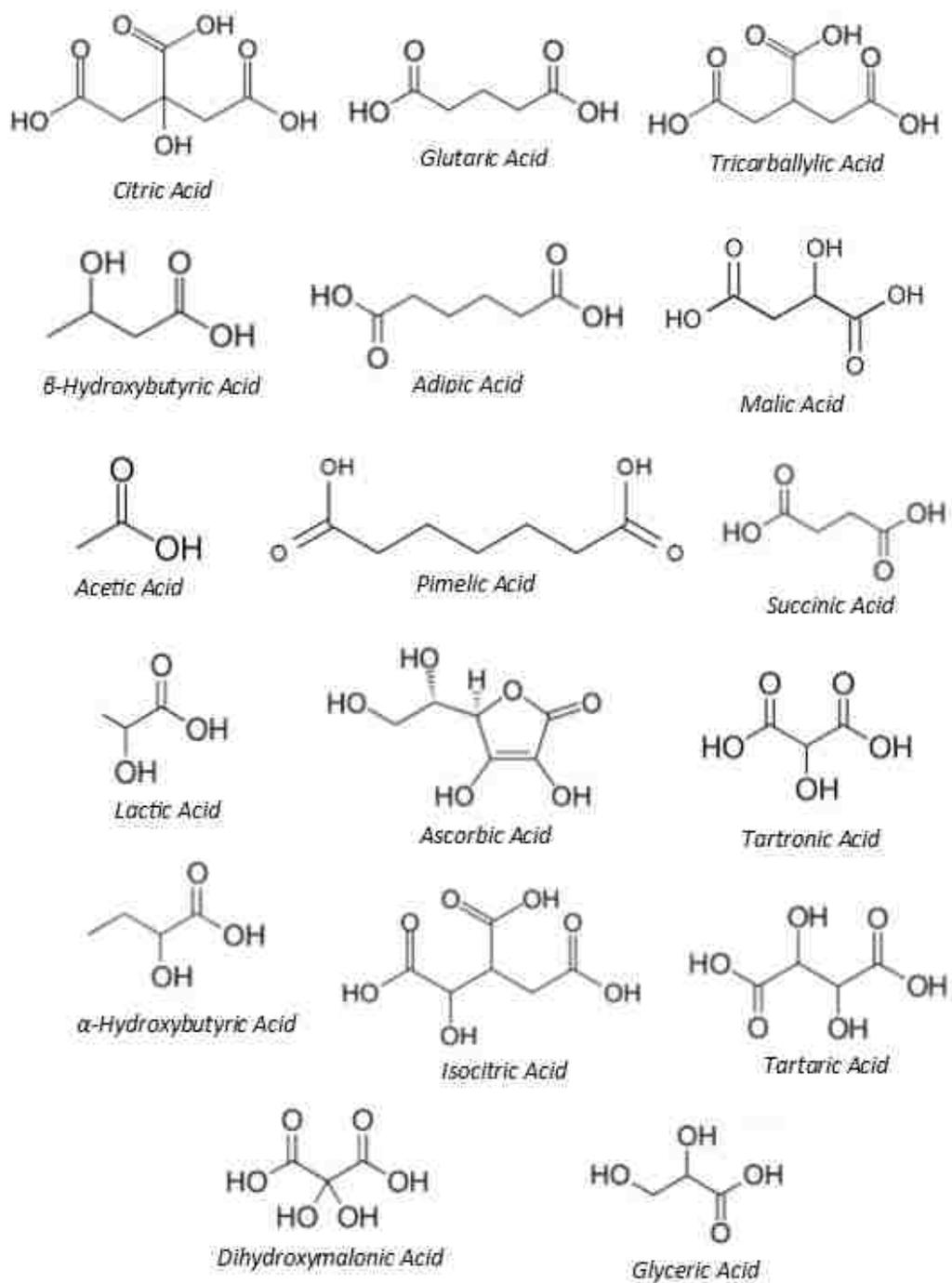
Figure 2-1: The sixteen carboxylic acid molecular structures plus ascorbic acid.

2.3 Results & Discussion

2.3.1 Nanoceria Carboxylic Acid Dispersions

████████ Color Change

In the presence of light, the majority of the nanoceria dispersions change color from light yellow to colorless. Those that were protected from light (covered by the Al foil) did not change color and remained light yellow. The particles exposed to light also degraded at a much greater rate than those that were protected from light, evident from the DLS results.

Nanoceria exposed to citric acid and DI water in the light and dark conditions up to 4 weeks are shown in Figure 2-2. There are two vials shown in each panel. The vial on the left was kept in the dark, covered by Al foil, while the vial on the right was exposed to UV radiation from sunlight. The sample in the citric acid column exposed to light for 4 weeks showed a color change from yellow to clear, possibly indicating a valence state change from Ce^{4+} to Ce^{3+}. The citric acid sample exposed to light appears to be completely colorless after 4 weeks. No color change was present for the sample kept in the dark. A slight color change was noticeable for the control sample in water, however a yellow tint was still present after 4 weeks, for both the dark and light exposed samples.

The color change from yellow to colorless could also be representative of particle dissolution. The particles in citric acid exposed to light were completely dissolved by 4 weeks as indicated by DLS and TEM. In Table 2 of Grulke et al. [32], the changes in the valence state at the edge and core of the nanoparticles were shown over 12 weeks of dissolution. Ce^{3+} concentration increased as particle size decreased in both locations, but

only slightly. Figure 7 of Yokel et al. [33] shows little to no change within 4 weeks, however after 12 weeks, an increase in the M5 peak, corresponding to an increase in the Ce^{3+} valence state, is apparent.

Week	Sample	
	Citric Acid	DI Water
0		
1		
2		
4		
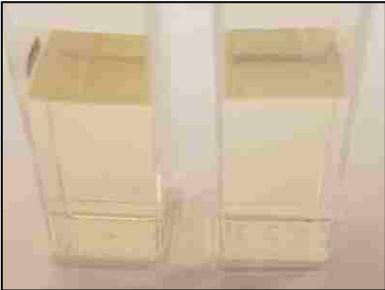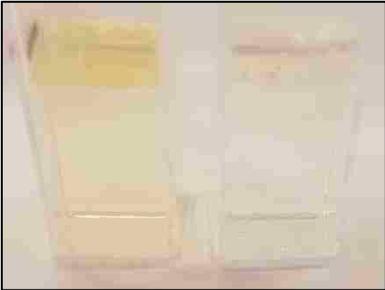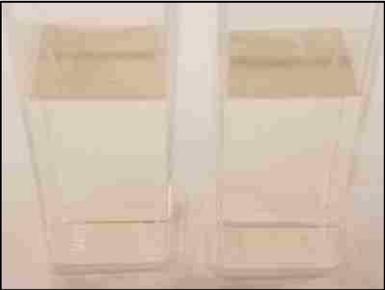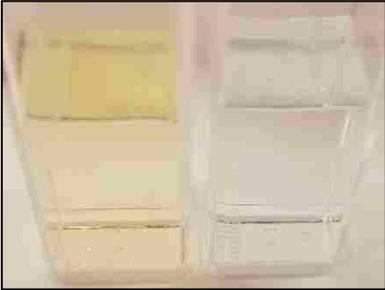
Figure 2-2: Nanoceria particles exposed to citric acid (left column) and water (right column). The vials on the left of each panel were kept in the dark, covered by Al foil, while the vials on the right were exposed to UV radiation from sunlight.

■■■■■ DLS Analysis

There was a total of 40 conditions tested, each conducted in duplicate to confirm experimental accuracy. The 17 acids shown in Figure 2-1 were accompanied by controls: sodium nitrate, ammonium nitrate, and water. Each sample was exposed to either sunlight or protected by Al foil. The DLS results are shown in Figure 2-3. Each sample typically contained a bimodal distribution, represented by the blue and red bars on the 3D graphs. The peak heights of these bars are representative of the percentage of the sample at that size. Some of the samples completely dissolved the nanoceria particles well before the end of the experiment, therefore those graphs were cut off at 1,000 hours.

Although all of the results are shown in Figure 2-3, these graphs can be summarized in five categories. The first contains three samples that completely dissolved the nanoceria particles within 1,000 hours when exposed to sunlight. The second contains one sample that prevented agglomeration over the entire experimental duration, but unable to completely dissolve the nanoceria particles. The third contains four samples that prevented agglomeration for an extended period of time (approximately 1,500-2,000 hours). The fourth contains nine samples that showed initial dissolution, then agglomeration within 300-400 hours, when exposed to sunlight. The fifth contains three samples that agglomerated immediately following exposure to the nanoceria particles, whether exposed to light or not. All categories, expect for group five, prevented agglomeration in the dark for most of the experimental duration. Five samples in group four agglomerated in the dark towards the end of the experiment (approximately 4,000-5,000 hours).

Group one includes the samples exposed to citric, malic, and isocitric acids. For all three samples protected under Al foil, there was an immediate reduction in hydrodynamic particle size, followed by slow dissolution over time. The solution color remained yellow for the experimental duration. For those exposed to sunlight, there was an immediate reduction in hydrodynamic particle size accompanied by a color change from yellow to clear. The nanoceria particles were fully dissolved within 600 hours for citric and malic acid samples, and 800 hours for isocitric acid. This indicates that UV light accelerates nanoceria dissolution, since nanoceria particles are known to be photoactive upon exposure to UV radiation. Furthermore, this result gives some insight into the molecular structure of the ligand needed to stabilize the nanoceria surface and prevent agglomeration. All three contain a carboxylic acid functional group geminal to a hydroxyl. NMR results (Figure 1-13) confirm that this type of structure may be influential in bonding with ceria.

Group two includes one sample: glyceric acid. When covered by Al foil, there was a slight reduction in hydrodynamic particle size over time and the color remained yellow, similar to group one. However, when exposed to light, there was an immediate reduction in hydrodynamic particle size for about 1,000 hours, then a steady increase for the remainder of the time. Also, a color change from yellow to clear, then back to yellow just before the increase in size was observed. All hydrodynamic particle sizes were under 50 nm, therefore no evidence of significant particle agglomeration.

Group three contains lactic and tartaric acids, ammonium nitrate, and water. Again, there was a small reduction in hydrodynamic particle size over time and no noticeable color change, similar to groups one and two when covered by Al foil. The overall decrease in hydrodynamic particle size in lactic acid was the greatest dissolution rate across every

49

sample covered by the foil, as shown in prior publications [32, 33]. When exposed to light, all samples showed a small reduction in hydrodynamic particle size over approximately 1,500-2,000 hours, followed by agglomeration to micron-sized particles. Also, the color changed from yellow to clear, then back to yellow just before agglomeration, similar to group two.

Group four includes nine samples: α-hydroxybutyric, β-hydroxybutyric, succinic, pimelic, glutaric, tricarballylic, adipic, and acetic acids plus sodium nitrate. As was the case for groups one through three for the samples covered by foil, there was a small reduction in hydrodynamic particle size over time with no noticeable change in color. A handful of the samples appeared to agglomerate towards the end of the experiment, between 4,000-5,000 hours. For those exposed to sunlight, there was a slight reduction in size, followed by agglomeration around 300-400 hours. The color remained yellow throughout the experimental duration. The majority of these samples agglomerated at drastically different time points in reference to light vs. dark conditions. This again confirms the statement that UV light accelerates nanoceria dissolution due to the photoactive nature of nanoceria upon exposure to UV radiation.

Group five contains three samples: tartronic, dihydroxymalonic, and ascorbic acids. The nanoceria particles immediately agglomerated when exposed to these acids, in both light and dark environments. This shows that these acids were unable to create a stable environment for the nanoceria particles. The color remained yellow throughout the experimental duration when exposed to tartronic and dihydroxymalonic acids. However, a color changed from yellow to reddish-brown was observed for the nanoceria subjected to ascorbic acid. Ascorbic acid also completely dissolved the nanoceria agglomerates within

50

1,000 hours. Ascorbic acid dissolution-accompanied aggregation of nanoceria was also shown by Muhammad et al. [125].

As mentioned earlier, the carboxylic acid group geminal to a hydroxyl may be essential for nanoceria-ligand complexation. Nine of the carboxylic acids tested contain this structure. Of the nine, three (citric, malic, and isocitric acid) completely dissolved nanoceria when exposed to sunlight and one (glyceric acid) prevented agglomeration throughout the entire experimental duration. Two (lactic and tartaric acid) stabilized nanoceria for an extended time period before agglomeration. One (α-hydroxybutyric acid) prevented agglomeration for a short period of time, while the remaining two (tartronic and dihydroxymalonic acid) agglomerated immediately upon exposure. This result indicates that while the carboxylic acid geminal to a hydroxyl group may be important, other functional groups may also play a role. For instance, citric, malic, and isocitric acid molecules all contain at least one more carboxylic acid group (citric and isocitric acids contain two additional groups). The same is true for tartaric, tartronic, and dihydroxymalonic acids, however the carbon chain is shorter for these molecules and do not contain any -CH_2 groups, which may prevent molecular configurations required for complexation with nanoceria. The remaining three (glyceric, lactic, and α-hydroxybutyric acids) do not contain a second carboxylic acid group. This suggests that a long carbon chain backbone containing a carboxylic acid geminal to a hydroxyl in addition to a second carboxylic acid group may be necessary for complexation with nanoceria.

ID	Condition	
	Light	Dark
Group 1 Citric Acid		
Malic Acid		
Isocitric Acid		
Group 2 Glyceric Acid		

ID	Condition	
	Light	Dark
Group 3		
Lactic Acid		
Tartaric Acid		
NH$_4$NO$_3$		
Water		

ID	Condition	
	Light	Dark
Group 4 α-Hydroxy-butyric Acid		
β-Hydroxy-butyric Acid		
Succinic Acid		
Pimelic Acid		

ID	Condition	
	Light	Dark
Glutaric Acid		
Tricarballylic Acid		
Adipic Acid		
Acetic Acid		

ID	Condition	
	Light	Dark
NaNO$_3$		
Group 5 Tartronic Acid		
Dihydroxy-malonic Acid		
Ascorbic Acid		

Figure 2-3: DLS results for the 40 conditions separated by groups one through five. Each 3D graph contains exposure time, in hours, on the x-axis; hydrodynamic diameter, in nm, on the y-axis; and peak height/size percentage on the z-axis. Most samples had bimodal distributions. The smaller peak is in blue and the larger peak in red. The y-axis shifts between linear and logarithmic coordinates to best show the hydrodynamic particle size before and after agglomeration.

███████   TEM Analysis

TEM analysis was conducted on two samples, citric and β-hydroxybutyric acid, to compare to the DLS results. These two samples were chosen to represent samples in groups one and four. In the presence of sunlight, citric acid prevented agglomeration and completely dissolved the nanoceria particles within 2 weeks. On the other hand, particles exposed to β-hydroxybutyric acid agglomerated within 4 weeks. Shown in Figure 2-4 are TEM images at varying magnification of each sample exposed to sunlight and covered by the Al foil.

The nanoceria particles exposed to both acids in the dark appear to imitate each other quite well, similar to the DLS results. Nanoceria was present in each sample in 15-25 nm agglomerates throughout 8 weeks. Large micron-sized agglomerates were not detected by TEM in the dark condition for either sample.

ID	Week	Magnification		
		150k	500k	1050k
Citric Acid (light)	0			
	1			
	2			
	4			
	8			

ID	Week	Magnification		
		150k	500k	1050k
Citric Acid (dark)	0			
	1			
	2			
	4			
	8			

ID	Week	Magnification		
		58k	150k	500k
β-hydroxybutyric Acid (light)	0			
	1			
	2			
	4			
	8			

ID	Week	Magnification		
		58k	150k	500k
β-hydroxybutyric Acid (dark)	0			
	1			
	2			
	4			
	8			
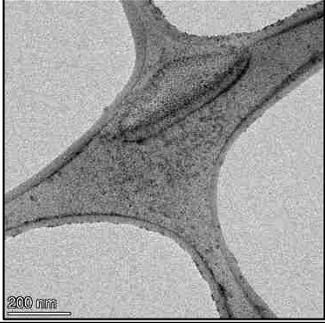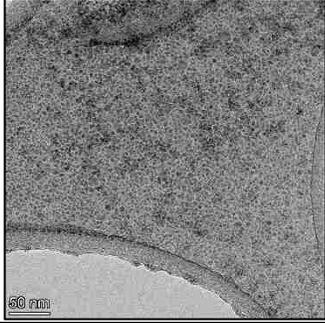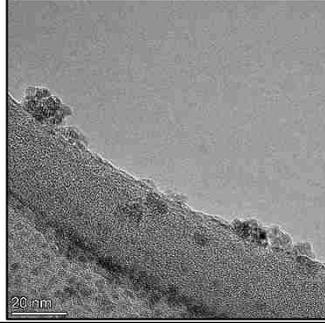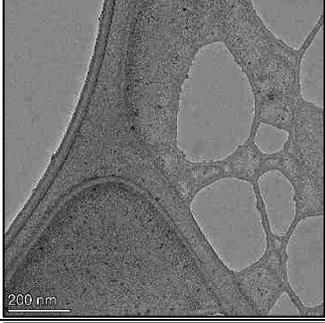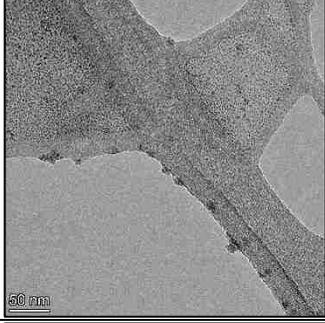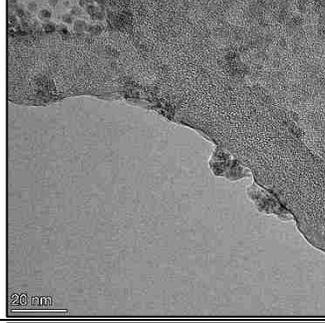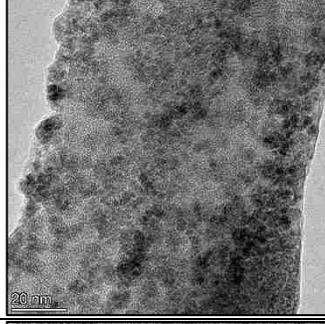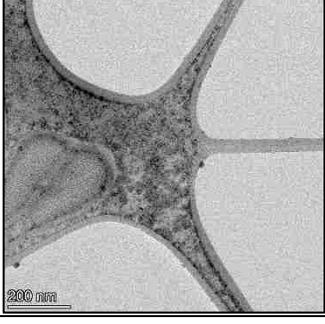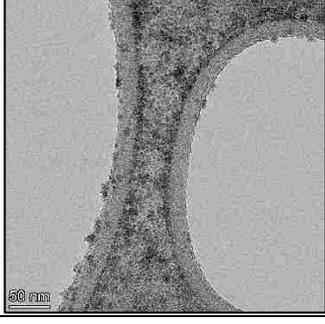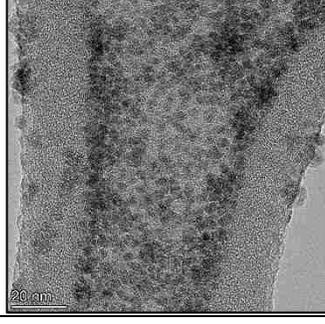
Figure 2-4: TEM images at 150k, 500k, and 1050k magnification for citric acid exposed nanoceria and 58k, 150k, and 500k magnification for β-hydroxybutyric acid exposed nanoceria. Samples were taken at 0, 1, 2, 4, and 8 weeks exposure times. Each sample contains a set of images exposed to sunlight and, consequently, covered by Al foil. The scale bars for each magnification (column) are consistent.

However, the samples exposed to sunlight produced drastically different TEM images, as expected by the DLS results. The number of nanoceria particles exposed to citric acid were significantly reduced between weeks 0 and 1. By week 2, most of the particles completely disappeared with no evidence of cerium determined by EDS. Instead, approximately 5 nm features were observed in weeks 2, 4, and 8. These features were not stable and were altered by the high intensity electron beam, confirming that they are not cerium oxides (Figure 2-5). Allen et al. [140] shows similar results and considers how these fine features may be associated with a complex of cerium and HMT (hexamethylenetetramine). However, as evident by the STEM EDS mapping analysis (Figure 2-6), the features include sodium, likely from the sodium nitrate. From these results, it also appears that the 15-25 nm agglomerates on the edges of the lacey carbon film are nanoceria.
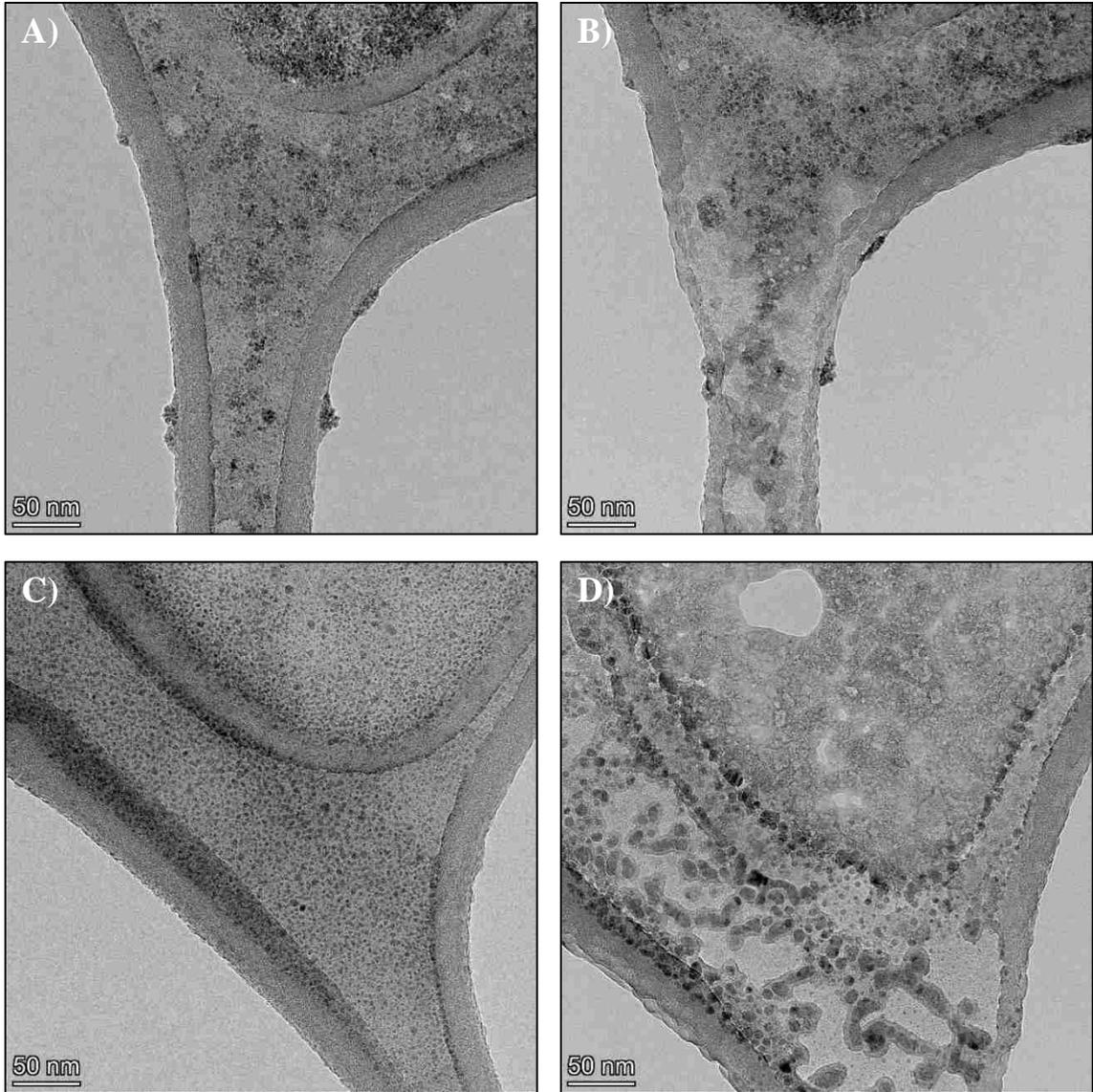
Figure 2-5: TEM images before and after electron beam exposure upon high magnification. Nanoceria particles exposed to (A) citric acid for 2 weeks in the dark pre-high magnification; (B) post-high magnification. Nanoceria particles exposed to (C) citric acid for 8 weeks in the sunlight pre-high magnification; (D) post-high magnification. The features are altered by the high intensity electron beam.
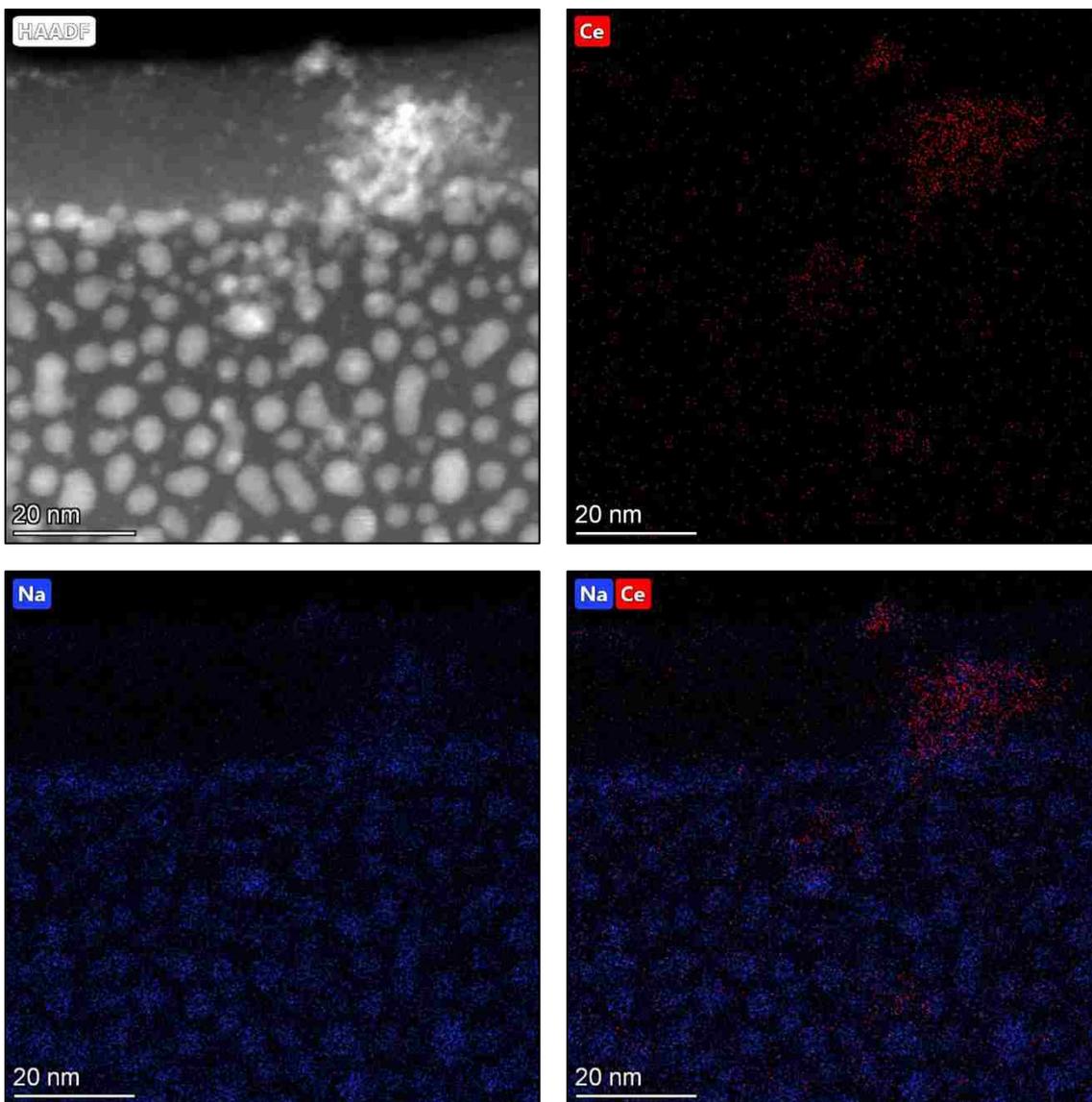
Figure 2-6: STEM HAADF and EDS mapping of β-hydroxybutyric acid-exposed nanoceria in the sunlight for 2 weeks. The features contain sodium, but not cerium. On the other hand, the nanoceria appears to localize on the edges of the lacey carbon film as 15-25 nm agglomerates (upper right of the image).

The β-hydroxybutyric acid condition appeared to reduce the overall number of nanoceria particles from week 0 through week 2, similar to the citric acid condition. However, by week 4, large micron-sized agglomerates were detected, made up of hundreds of nanoceria particles that persisted throughout the experimental duration. An EDS scan of the agglomerate confirms the presence of cerium (Figure 2-7). This confirms the DLS results of this sample at 4 weeks, that ceria agglomerated into micron-sized particles.
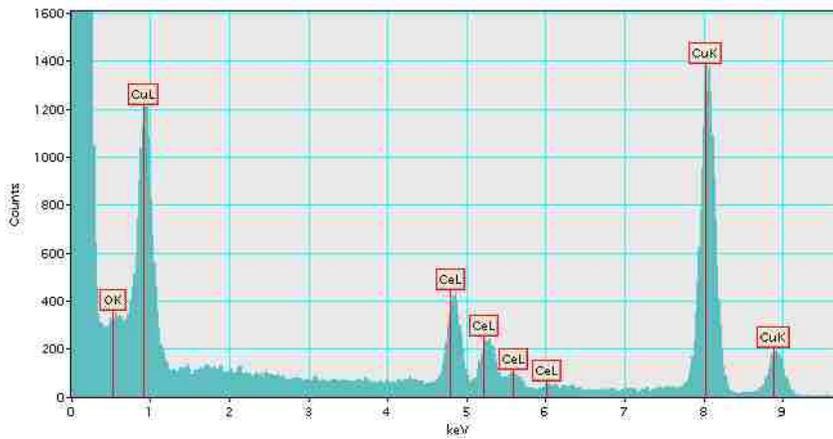
Figure 2-7: EDS map of β-hydroxybutyric acid exposed nanoceria in the sunlight for 4 weeks. The micron-sized agglomerate contains cerium and oxygen confirming agglomeration of hundreds of nanoceria particles. The copper is from the sample grid.

██████ Dissolution Rate Analysis

2.3.1.4.1 Kinetic Rate Modeling

A kinetic model can be used to describe the dissolution rates of ceria when exposed to these ligands and to accurately determine the residence time of an individual particle. Nanoceria dissolution occurs over multiple weeks in aqueous dispersions, with apparent half-lives of dissolution ranging from 800 to 60,000 hours, depending on the local media [33]. The experimental set-up for this study was slightly different: 1 mL of nanoceria at a concentration of approximately 500 µg/mL, was introduced into dialysis cassettes. The dialysis cassettes were immersed in 200 mL (2.5 µg/mL total concentration) bath of 0.11 M isosmotic aqueous media at pH 4.5. The ammonium nitrate was at a concentration of 20 mM and water at a pH of 6.5. All the samples were stored at 37 ºC in the dark. Over time, 1 mL of the solution outside of the cassette was collected and analyzed for cerium content by Inductively Coupled Plasma Mass Spectrometry (ICP-MS). Samples of the nanoceria within the dialysis cassette were also taken at 8, 16, and 24 weeks for mass balance computations.

Early in the previous study, zero-, first-, and second-order kinetic models were applied to dissolution data. All of these models showed generally poor correspondence. There was good correspondence between data and prediction when a model for surface-controlled dissolution of solid particles [141] was applied to the data. This model links the rate of solid dissolution from a spherical particle to its current surface area. It requires knowledge of the particle size and/or size distribution, the number of Ce atoms in a particle of a specific size, and the number of nanoceria particles in the cassette. It was assumed that

66

Ce ion/carboxylic acid ligands do not reform nanoceria and that the chemical potential for dissolution does not change during the experiments. With these assumptions, the dissolution process is dependent only on the number of nanoceria particles in the cassette and their size. The apparent dissolution rate constant is estimated by nonlinear regression to minimize the differences between the measured Ce ion concentrations in the bath and the model predictions. Furthermore, it is assumed that the dissolved Ce salts are sufficiently soluble in the aqueous phase so as to not create a thermodynamic barrier to nanoceria dissolution.

The rate loss of Ce ions from a nanoceria particle is:

$$\frac{dn(t)}{dt} = -kS(t) \tag{2-1}$$

Where n(t) is the number of atoms in a nanoparticle with diameter, d (nm); k is the dissolution rate constant (Ce atoms nm^{-2} h^{-1}), and S(t) is the surface area of the particle (nm^2). The nanoparticle volume(nm^3) is:

$$V(t) = \frac{\pi}{6} d(t)^3 \tag{2-2}$$

The nanoparticle surface area is:

$$S(t) = 4\pi r(t)^2 = \pi d(t)^2 \tag{2-3}$$

The number of Ce atoms per nanoparticle is:

$$n(t) = \frac{\pi}{6}\left(\frac{d(t)}{10^7}\right)^3 \frac{\rho N_A}{M_w} \tag{2-4}$$

Where ρ is the nanoparticle density (7.22 g/cm^3), M_w is the molecular weight of ceria (172.11 g ceria/mol), and N_A is Avogadro's number. Substitute back into Equation (2-1):

$$\frac{dn(t)}{dt} = -kS(t) = -\alpha n(t)^{2/3} \tag{2-5}$$

Where

$$\alpha = k\pi^{1/3}\left(\frac{6M_w 10^{21}}{\rho N_A}\right)^{2/3} \tag{2-6}$$

The factor α has units of (atoms)$^{1/3}$/h. The solution of Equation (2-5) is:

$$n(t) = \left[n(t=0)^{1/3} - \frac{\alpha}{3}t\right]^3 \tag{2-7}$$

This equation gives negative values of n(t) when the particle is fully dissolved. If desired, this can be corrected by applying the Heaviside step function [141]. Equation (2-7) gives the number of Ce atoms remaining in a nanoparticle of size, n, at any time after the start of the experiment. The number of cerium atoms as determined by ICP-MS in the solution surrounding the cassette is used to determine the number of molecules of ceria

remaining in the cassette by a simple mass balance. The initial concentration, or number of

molecules per particle, was estimated using the average particle size of the nanoceria as

determined by TEM. Nanoceria size changes during growth and dissolution were also

imaged via TEM and analyzed using ImageJ and methods for particle size distributions by

TEM [142].

Table 2-1: Dissolution rate coefficients: controls and carboxylic acids [32].

Media	Dissolution Rate Constant (Ce atoms nm^{-2} h^{-1})
Controls:	
Water, pH 6.5	0.00019
Ammonium nitrate, pH 4.5	0.0030
Carboxylic acids, pH 4.5:	
Glutaric acid	0.0045
Tricarballylic acid	0.0046
β-Hydroxybutyric acid	0.0050
Pimelic acid	0.0050
Citric acid	0.0057
Acetic acid	0.0057
Adipic acid	0.0062
Succinic acid	0.0072
Malic acid	0.0075
Lactic acid	0.014

Ceria dissolution occurs in the presence of all ligands. The rate constant for each condition is shown in Table 2-1, averaged over two experimental trials. The water is more than an order of magnitude lower than those of the carboxylic acids. The ammonium system has a rate coefficient about two-thirds of those of the slowest carboxylic acid system. Since ammonia water plus citric acid was used in the synthesis of these nanoceria, it is not surprising that an ammonia solution at pH 4.5 in the absence of citric acid might permit the dissolution of nanoceria particles.

Carboxylic acid solutions accelerated dissolution and the ligand matters. The pKa's of the acids do not correlate with dissolution rate. All of the carboxylic acids caused measurable nanoceria dissolution over this time scale. Dissolution rates are partially controlled by the particle's surface area and occur layer-by-layer, as the particles are not porous. Since carboxylic acids are known to stabilize nanoceria during particle growth, it should not be surprising that they can influence nanoceria dissolution rates. Figure 2-8 shows model predictions of the number of cerium atoms in the nanoceria particles vs. time. Lactic acid had the highest dissolution rate coefficient and, by the end of 21 weeks, nanoceria was essentially depleted from the cassette. This matches well with the data seen in Figure 2-3 for the lactic acid dark condition as the particles decreased in size at a greater rate than any other condition in the dark. However, complete dissolution was not observed in this prior set-up. Two major differences in each experimental set-up were the use of the dialysis cassette and the nanoceria concentration (2.5 µg/mL vs. 500 µg/mL) that could explain why complete dissolution was observed in one condition, but not the other.
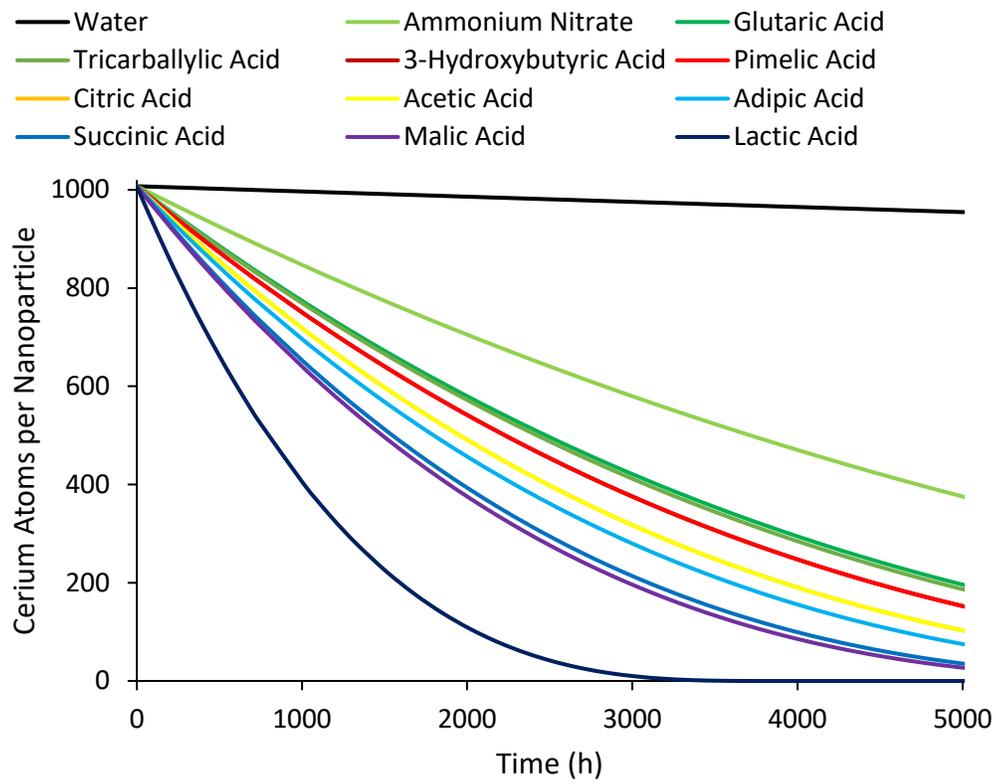
Figure 2-8: Dissolution of nanoceria dispersed in dialysis cassette over time expressed as number of Ce atoms per nanoparticle.

2.3.1.4.2   Statistical Analysis

The starting material and the ceria in the citric acid pH 4.5 dark condition after 7 weeks were dried onto a lacey carbon copper TEM grid to determine a difference in particle size and morphology after bathing for an extended period of time (Figure 2-9). ImageJ was used to measure the diameter of each particle in order to obtain a size distribution of the nanoceria. For the starting material (week 0), approximately 50 particles were measured and the mean diameter is 4.24 nm with a standard deviation of 1.18 nm. The particles appear to be spherical in shape. For the ceria at 7 weeks, approximately 72 particles were measured and the mean diameter is 3.74 nm with a standard deviation of 0.61 nm (Table 2-2). Some particles appear to be spherical in shape, while others are elongated and contain rough edges. EDS confirms the presence of ceria, oxygen, and chlorine in the sample. The chlorine is from the reactant required in synthesis, cerium chloride heptahydrate. The particles at week 0 appear to be larger than those at week 7, which is confirmed by DLS. The contrast in the TEM images (dark regions) was measured and ranged between 12-20 nm which is consistent to the DLS results.

Table 2-2: ImageJ size analysis summary of nanoceria dissolution. Left: Ceria at week 0 (starting material). Right: Ceria at week 7 in citric acid pH 4.5, dark.

	Week 0		Week 7	
	Area (nm^2)	D (nm)	Area (nm^2)	D (nm)
Mean	15.21	4.24	11.27	3.74
SD	7.93	1.18	3.76	0.61
Min	3.38	2.07	5.55	2.66
Max	31.98	6.38	26.52	5.81
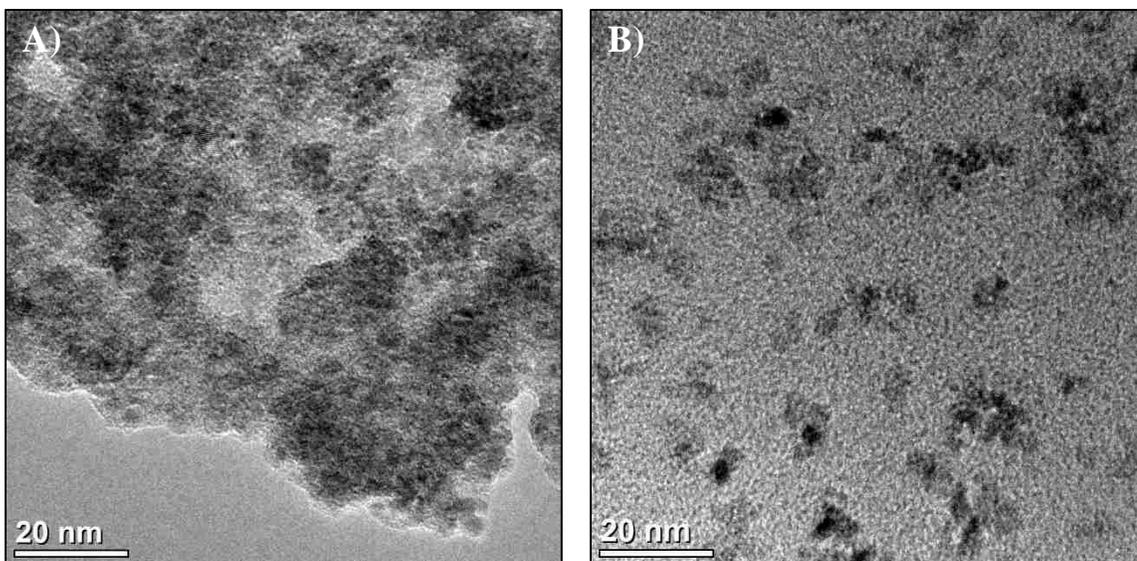
Figure 2-9: TEM images of nanoceria dissolution: (A) Ceria at week 0 (starting material), (B) Ceria at week 7 in citric acid pH 4.5, dark.

Overall, after 7 weeks bathing in citric acid pH 4.5 absent of sunlight, the diameter decreased by 11.8% and the area, approximately 25.9%. Also, the standard deviation of the ceria is much larger at week 0 than that at week 7 (Figure 2-10). The particle size range decreased as well indicating clear dissolution.
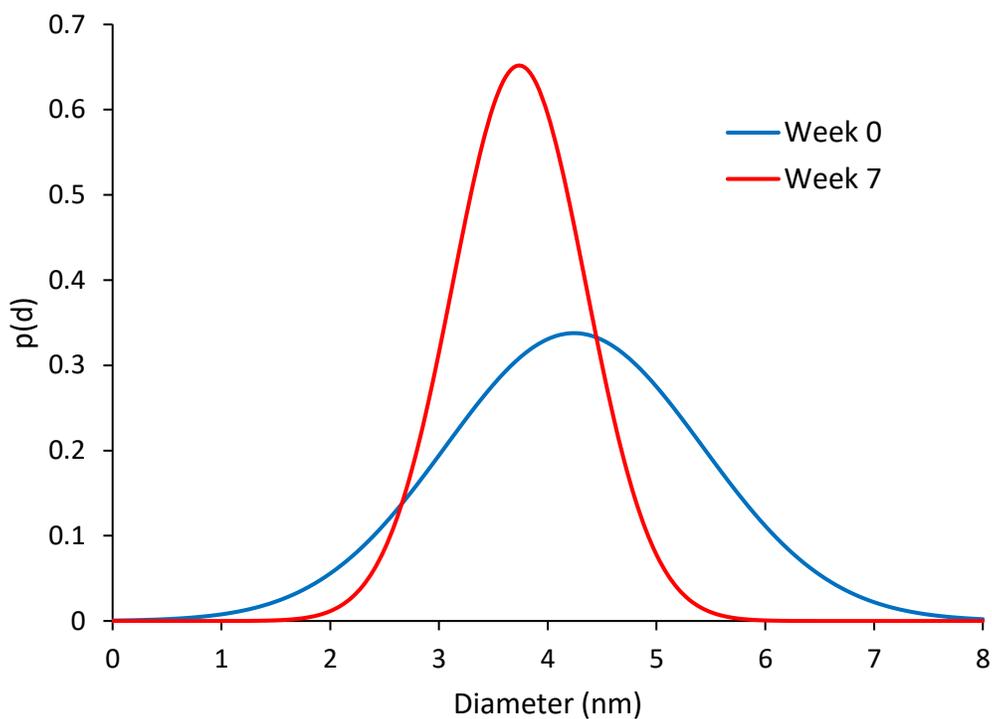
Figure 2-10: The probability density function (PDF) of the nanoceria at week 0 and week 7 in citric acid pH 4.5, dark.

The Feret diameter corresponds to the length between parallel tangent lines of a particle. The minimum diameter is labeled as 'min Feret' and the maximum, 'max Feret.' A contour plot relating these two variables helps visualize the morphology of the particle. Circular particles lie on the diagonal of the graph (min Feret equals max Feret). Any deviation from that point indicates irregularity in the particle morphology. By week 7, there is clear evidence of deviation from circular to an irregular or elliptical shape. Also, particles larger than 6 nm max Feret diameter have completely disappeared by week 7. The aspect ratio is the ratio of the Feret diameters. A circular particle will have an aspect ratio of 1. Figure 2-11 shows the irregularity of the particle shape for the ceria at week 7 and the uniformity of those at week 0. Nearly all particles start with an aspect ratio greater than 0.7 and in 7 weeks, approximately 20% have an aspect ratio below 0.7, suggesting that the particles lose their shape as they dissolve.
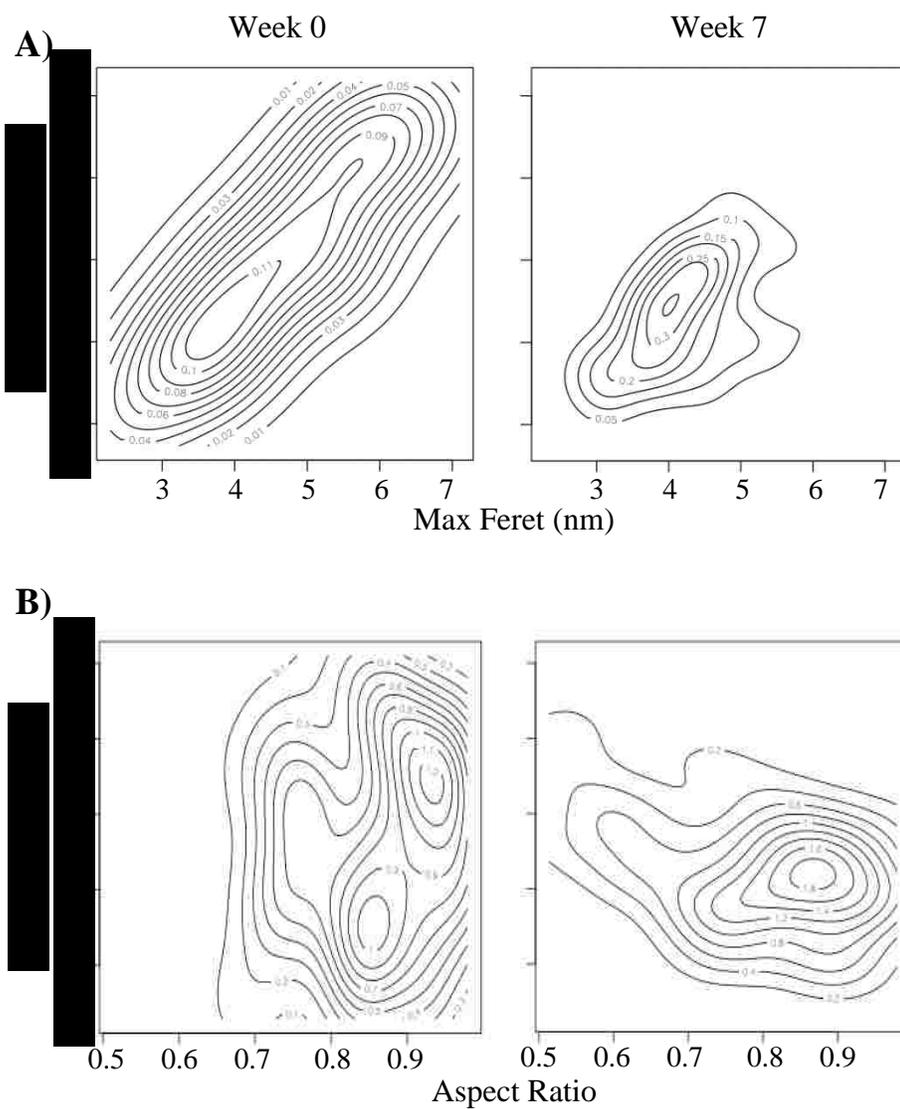
Figure 2-11: Contour plots of (A) minimum Feret vs. maximum Feret diameters and (B) maximum Feret diameter vs. the aspect ratio. Left: Ceria at week 0 (starting material). Right: Ceria at week 7 in citric acid pH 4.5, dark.

Finally, the kinetic rate law used to describe the results from the dialysis cassette experiment can also be used to model the nanoceria particle size distribution as a function of time. The cumulative distribution function (CDF) was used to calculate the diameter at the probabilities (25%, 50%, and 75%) that any given particle is smaller than the expected value. The distribution of the ceria particles at time 0 is large and quickly shrinks as time goes by as shown in Figure 2-12.
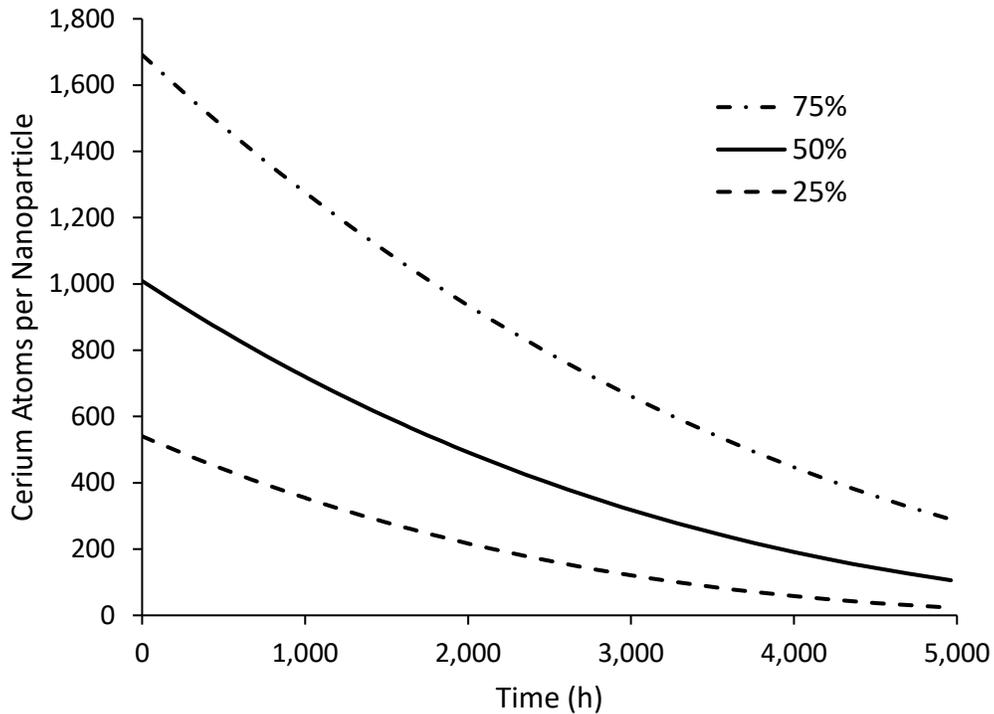
Figure 2-12: The particle size distribution model of the nanoceria dissolution exposed to citric acid pH 4.5, dark as a function of time with CDF probabilities (25, 50, and 75%). The dissolution rate constant was 0.0057 atoms nm^{-2} h^{-1} for this condition.

2.4 Conclusions

Nanoceria coated with citric acid was exposed to a variety of carboxylic acids at pH 4.5 along with a few controls: sodium nitrate, ammonium nitrate, and water in light and dark environments to simulate sunlight exposure to plants and within biological systems, respectively. The hydrodynamic particle size was determined by DLS over 30 weeks. For most of the samples exposed to sunlight, a color change from yellow to colorless was observed indicating a valence state transition from Ce^{4+} to Ce^{3+}. This is common for particles to transition oxidation states from Ce^{4+} to Ce^{3+} as they dissolve.

Of all the carboxylic acids tested, nanoceria exposed to only three (citric, malic, and isocitric acids) fully dissolved in less than 1,000 hours of exposure time when subjected to sunlight. Glyceric acid prevented agglomeration, but nanoparticles were still present after 30 weeks of exposure. The remainder of the samples formed micron-sized particles either immediately or between 300-2,000 hours of exposure. In the dark, particles were still present at the end of 30 weeks for all carboxylic acids and the controls. This indicates that UV light accelerates nanoceria dissolution. The lactic acid condition dissolved the particles at a greater rate than any other condition in the dark. TEM imaging of citric and β-hydroxybutyric acids supported the DLS results. Furthermore, the results gave insight into the molecular configurations of carboxylic acid compounds required for stable complexation with nanoceria. A long carbon chain backbone containing a carboxylic acid geminal to a hydroxyl in addition to a second carboxylic acid group may be necessary for complexation with nanoceria. In addition, a kinetic study applying a surface-controlled dissolution model of solid, spherical particles corresponded well to the data.

3.1   Introduction

Nanoparticles are typically coated to improve stability, preventing agglomeration and reducing its toxicity to biological systems [143]. When exposed to a biological milieu, the coating can be removed or altered by biological fluids, or overcoated creating a corona. Altering the nanoparticle surface can greatly influence its fate *in vivo* [31, 144]. An understanding of nanoceria behavior in simulated biological environments would prove valuable in identifying how cells will respond. The effects of human simulated lung, gastric, and intestinal fluid on nanoceria surface properties will be studied in this chapter. Nanoparticle exposure to simulated lung, gastric, and intestinal fluids have been shown to alter structure and surface morphology [145-147].

Exposure to the simulated biological fluids (SBFs) is expected to alter the surface charge and coating of the citrate-coated nanoceria particles. In order to test this hypothesis, nanoceria was coated with citric acid and extensively characterized prior to and immediately following exposure to the SBFs. The nanoceria was characterized using the methods as described in Appendix C: Transmission Electron Microscopy (TEM), Dynamic Light Scattering (DLS), Zeta Potential, Fourier Transform Infrared Spectroscopy (FTIR), Thermogravimetric Analysis (TGA), and X-ray Diffraction (XRD).

3.2 Experimental

3.2.1 Materials

The following chemicals, including their sources, purity, and CAS #s, used were: acetic acid (glacial), Fisher, ACS grade, 64-19-7; calcium chloride dihydrate, Fisher, USP/FCC/EP, 10035-04-8; cerium(III) nitrate hexahydrate, Fluka Analytical, $\geq$ 99%, 10294-41-4; citric acid monohydrate, Fisher, ACS grade, 5949-29-1; citric acid trisodium salt dihydrate, VWR, ACS grade, 6132-04-3; disodium hydrogen phosphate, Fisher, ACS grade, 7558-79-4; lecithin from egg, MP Biomedicals, $\geq$ 96%, 8002-43-5; hydrochloric acid, Sigma, ACS grade (37%), 7647-01-0; magnesium chloride, Strem Chemicals, 97.5%, 7786-30-3; maleic acid, TCI, 99%, 110-16-7; nitric acid, Sigma, ACS grade, 7697-37-2; pepsin, MP Biomedicals, 9001-75-6; potassium chloride, Sigma, ~99%, 7447-40-7; sodium acetate, Sigma, $\geq$ 99%, 127-09-3; sodium chloride, Sigma, $\geq$ 99%; 7647-14-5; sodium hydrogen carbonate, Sigma, ACS grade, 144-55-8; sodium hydroxide, VWR, ACS grade, 1310-73-2; sodium nitrate, VWR, ACS grade, 7631-99-4; sodium oleate, TCI, >97%, 143-19-1; sodium sulfate, Sigma, $\geq$ 99%, 7757-82-6; and sodium taurocholate hydrate, Alfa Aesar, 97%, 145-42-6. Cow milk (2%) was used. Lacey carbon, 300 mesh, copper grids (product #01895) from Ted Pella, Inc. were used for electron microscopy. Dialysis tubing from Ward's Science (product #s 470163-404 & 470163-408) with a MWCO of 12-14 kDa was used for dialysis against DI water.

3.2.2   Methods

Nanoceria particles were synthesized following the method described in Mai et al. [70]. 35 mL of 6 M sodium hydroxide and 5 mL of 0.05 M cerium nitrate hexahydrate were combined and stirred for 30 minutes at 350 rpm. The contents were then placed into a stainless-steel autoclave. The autoclave was heated in an oven at 180 °C for 24 hours. The autoclave was removed from the oven and cooled to room temperature for an additional 24 hours. The resulting suspension containing cerium oxide and sodium nitrate was removed from the autoclave and centrifuged at 4200 rpm for 15 minutes, washed and repeated three times. The excess supernatant was decanted, and the resulting nanoceria left in the centrifuge tube was vortex mixed with additional deionized water, so that all particles were collected. This suspension was then dialyzed against 500 mL of deionized water for 72 hours at 350 rpm, changed every 24 hours, to remove excess salt and cerium ions. The nanoceria suspension was centrifuged at 4200 rpm for 15 minutes, washed and repeated three times, and then dried overnight at 80 °C.

The synthesis is summarized in the chemical equation below:
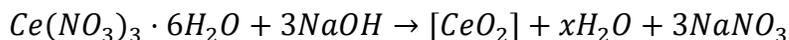
$$Ce(NO_3)_3 \cdot 6H_2O + 3NaOH \rightarrow [CeO_2] + xH_2O + 3NaNO_3$$

The [CeO_2] refers to cerium(IV) oxide, however the valence change between Ce^{3+} and Ce^{4+} accompanied by oxygen vacancies present within the chemical structure create an overall atomic ratio for Ce:O greater than the stoichiometric value of ½. Therefore, an 'x' is listed as the coefficient to H_2O in the above formula to account for the remaining oxygen atoms.

The dried nanoceria particles (approximately 0.3 g) were added to 200 mL of 0.05 M citric acid adjusted to pH 4.5. The suspension was stirred for 24 hours at 350 rpm, then centrifuged at 4200 rpm for 15 minutes, washed and repeated three times with DI water, and dried at 80 °C overnight.

Five SBFs: simulated lung fluid (Gamble's solution, which represents the interstitial fluid deep within the lung, SLF), fasted-state simulated gastric fluid (FaSSGF), fed-state simulated middle gastric fluid (FeSSGF), fasted-state simulated intestinal fluid (FaSSIF), and fed-state simulated middle intestinal fluid (FeSSIF) were prepared as described in Marques et al. [148] with one modification: the glyceryl monocholate was removed from the FeSSIF recipe. This prevented isolation of washed, dried nanoceria following exposure and was therefore excluded from the recipe.

70 mg of citrate-coated nanoceria were added to 15 mL of each SBF. The tubes were placed on an orbital shaker (INNOVA 4000, New Brunswick Scientific) and agitated at 250 rpm and 37 °C. Exposure to the SBFs varied in time: 2 hours for the gastric fluids, 3 hours for the lung fluid, and 6 hours for the intestinal fluids. Each exposure was conducted in triplicate. Following exposure, the suspensions were centrifuged at 3500 rpm for 10 minutes, washed and repeated three times with DI water, and dried at 80 °C overnight.

Each nanoceria sample: uncoated, citrate-coated, SLF exposed, FaSSGF exposed, FeSSGF exposed, FaSSIF exposed, and FeSSIF exposed was characterized and the results compared to determine any change in surface charge and morphology.

3.3   Results & Discussion

3.3.1   Particle Size & Morphology

STEM was used to determine particle size, shape, and elemental composition. STEM images of the uncoated and citrate-coated nanoceria as well as the nanoceria after SBF exposure show it was cubic-shaped (Figure 3-1). The mean, +/- SD, particle size was 21.1 +/- 14.2 nm for the citrate-coated nanoceria. The nanoceria primary particle size and shape were unaffected by the exposure to the SBFs. The hydrodynamic diameter results determined by DLS, as percent surface area, are displayed in Figure 3-2, and summarized in Table 3-1. The hydrodynamic diameter of each of the nanoceria samples was much greater than the primary particle size determined by TEM, suggesting significant particle agglomeration. The hydrodynamic diameter for the citrate-coated nanoceria was ~25% smaller than the uncoated. This can be attributed to the greater repulsion of the negatively charged citrate surface groups between each particle.

Exposure to FaSSIF and SLF slightly increased the hydrodynamic diameter by ~25% and ~35%, respectively. Exposure to FaSSGF increased it by ~80%, while FeSSIF by a significant ~155%. The largest increase resulted from exposure to FeSSGF, ~645%. Small increases from SLF, FaSSIF, and FaSSGF exposure can be due to loss of the citric acid coating. On the other hand, a larger increase, accompanied by greater weight loss from TGA (Section 3.3.2), from FeSSIF and FeSSGF exposure was most likely a result from overcoating by the biological fluid components.

Figure 3-1: STEM images of nanoceria particles before and after SBF exposure and surface cerium, oxygen, and carbon elemental mapping. Each of the images in a row are the same size. A 50 nm scale bar is in the first column of the row.

Diameter (nm)

85
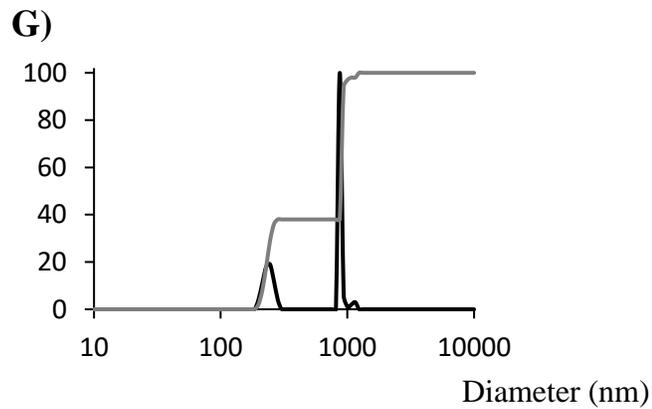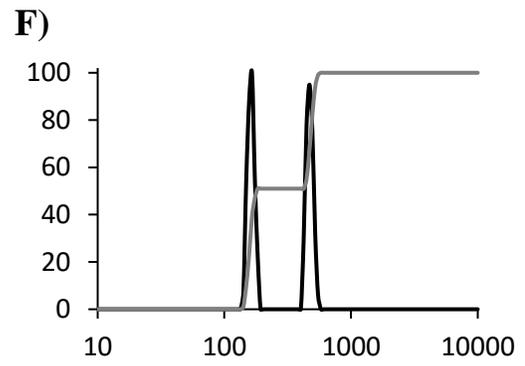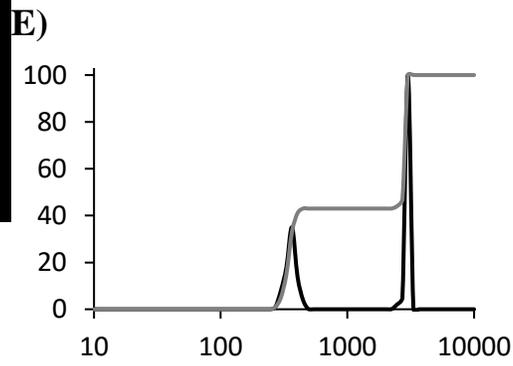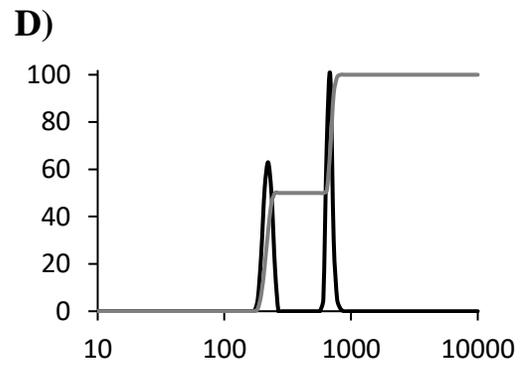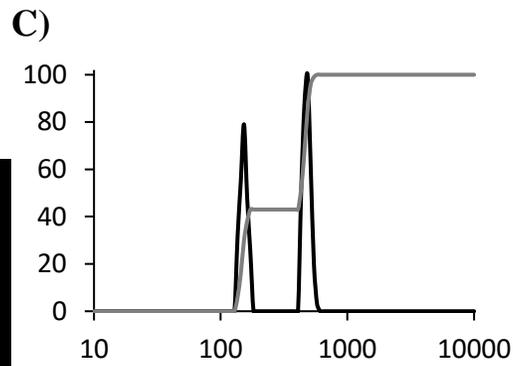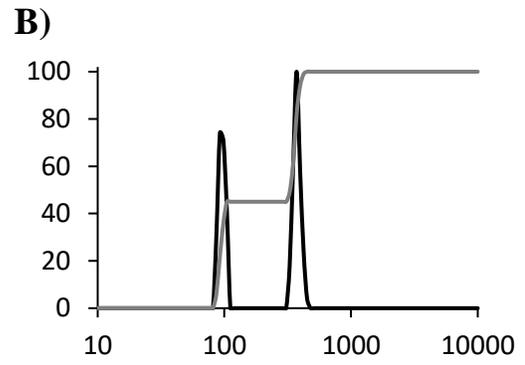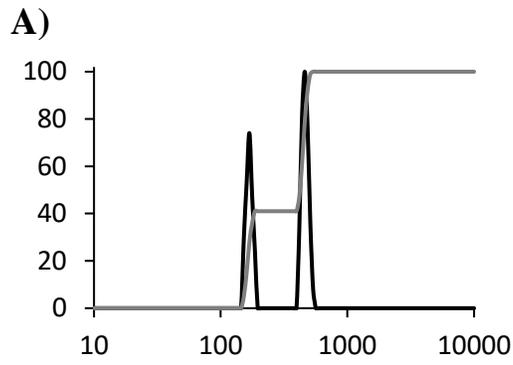
Figure 3-2: Nanoceria hydrodynamic diameter, as percent surface area, before and after SBF exposure determined from DLS – Black: Distribution, Gray: Cumulative: (A) Uncoated, (B) Citrate-coated, (C) SLF exposed, (D) FaSSGF exposed, (E) FeSSGF exposed, (F) FaSSIF exposed, and (G) FeSSIF exposed.

Table 3-1: Nanoceria hydrodynamic particle size determined from DLS.

Nanoceria Sample	Bimodal Size Distribution (% by nm range)
Uncoated	41% 150-180; 59% 415-540
Citrate-coated	45% 85-105; 59% 310-450
SLF exposed	43% 135-170; 57% 430-575
FaSSGF exposed	50% 185-250; 50% 600-775
FeSSGF exposed	43% 270-445; 57% 2450-3000
FaSSIF exposed	51% 135-185; 49% 420-550
FeSSIF exposed	38% 185-285; 62% 870-1150

3.3.2   Surface Composition

The citrate-coated nanoceria had an ~10 mV greater absolute negative surface charge at neutral pH than the uncoated with a lower pH plateau (ζ_∞) of -31.1 mV as seen in Figure 3-3 and Table 3-2 using the Carreau model [Equation (1-6)]. FTIR peak assignments were: -C-H, -CH$_2$, and -CH$_3$ – 1000 to 1500; C-O- – ~1100; -C-H – 1350 to 1480; -COOH – ~1380 and 1540; -N-O – ~1650; C=O – 1670 to 1820; and -OH – between 3000 and 3600 cm^{-1}. Citrate-coated nanoceria contained a -COOH peak (1380 cm^{-1}) in the FTIR spectrum that was not present in the uncoated spectrum (Figure 3-4A). The citrate-coated nanoceria had a 1% greater weight loss than the uncoated during TGA analysis (Figure 3-5), which is significant for larger particles (21.1 nm). This translates to approximately 0.8 citrate molecules per nm^2 on the surface of each particle, or 1,125 citrate molecules per particle, using Equation (1-5). This corresponds to about ½ a monolayer.

Exposure to SLF resulted in loss of the FTIR peak at ~1380 cm^{-1}, and less weight loss during TGA heating than the citrate-coated nanoceria. This was not accompanied by a less negative surface charge as might be anticipated with less citric acid on the surface, suggesting some association of SLF components with the CeO$_2$ surface, potentially acetic acid.

Nanoceria exposure to FaSSGF resulted in the loss of the FTIR peak at ~1380 cm^{-1} that is attributed to citric acid. This was accompanied with by a less positive zeta potential at the FaSSGF pH (1.6), and less weight loss during TGA heating than the citrate-coated nanoceria. The possible loss of citrate from the nanoceria surface may be due to FaSSGF's very low pH (1.6).

Exposure of nanoceria to FeSSGF increased the isoelectric point (IEP) to pH 3.5 from 2.7. This, coupled with the reduction of the 1380 cm^{-1} FTIR peak, and large weight loss increase during heating, may be due to overcoating by FeSSGF components. The additional peaks between 1300 and 1800 cm^{-1} are consistent to milk components (Figure 3-4B), likely from K-casein. EDS elemental scans show FeSSGF-exposed nanoceria had the most carbon on its surface among the SBF-exposed nanoceria. The increases in hydrodynamic diameter and IEP can be attributed to adsorption of milk components on the nanoceria surface.

Exposure to FaSSIF greatly reduced the 1380 cm^{-1} FTIR peak, and less weight loss due to heating than citrate-coated nanoceria. The surface charge at the FeSSIF pH (6.5) was slightly more negative. This suggests removal of the citrate coating, and potential replacement by FaSSIF components, perhaps maleic acid.

Finally, nanoceria exposure to FeSSIF greatly reduced the 1380 cm^{-1} FTIR peak, and the surface charge became slightly less negative at FeSSIF pH (5.8). However, there was a considerable increase in weight loss during TGA heating, indicating an overcoating by FeSSIF components, possibly maleic and/or oleic acid.
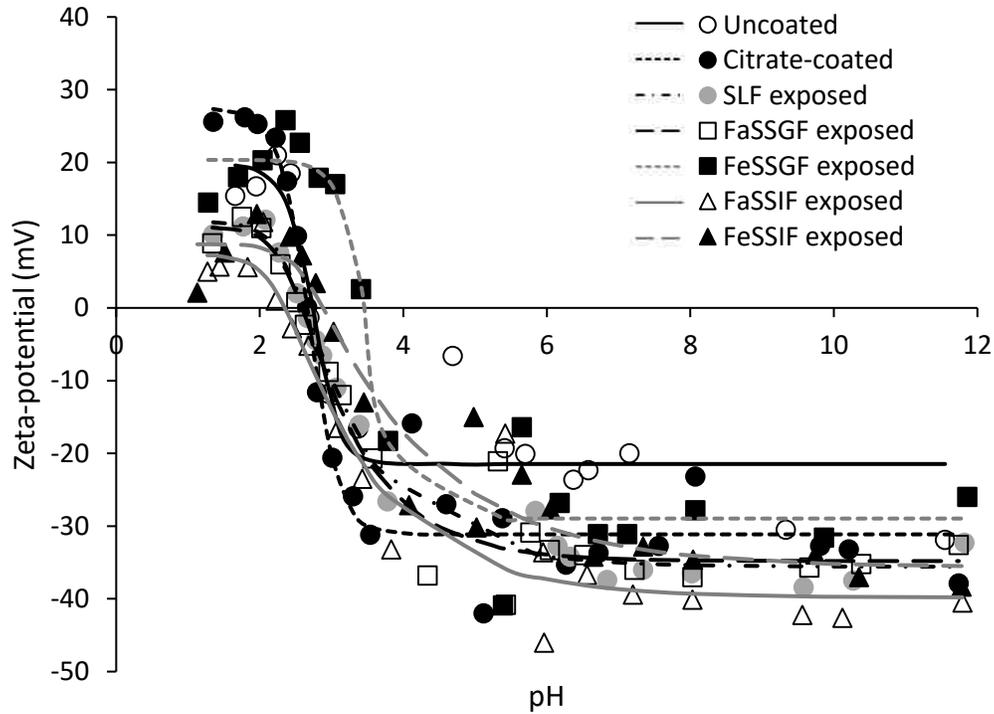
Figure 3-3: Nanoceria surface charge (zeta potential) before and after citrate coating, and after exposure to each SBF.

Table 3-2: Carreau model estimates of the isoelectric point (IEP), and upper (ζ_o) and lower (ζ_∞) pH plateau zeta potentials.

	Uncoated	Citrate-coated	SLF exposed	FaSSGF exposed	FeSSGF exposed	FaSSIF exposed	FeSSIF exposed
IEP (pH)	2.7	2.7	2.6	2.6	3.5	2.4	2.9
ζ_o (mV)	19.8	27.5	11.9	11.1	20.4	7.3	8.8
ζ_∞ (mV)	-21.5	-31.1	-35.6	-34.8	-29.0	-39.8	-35.6
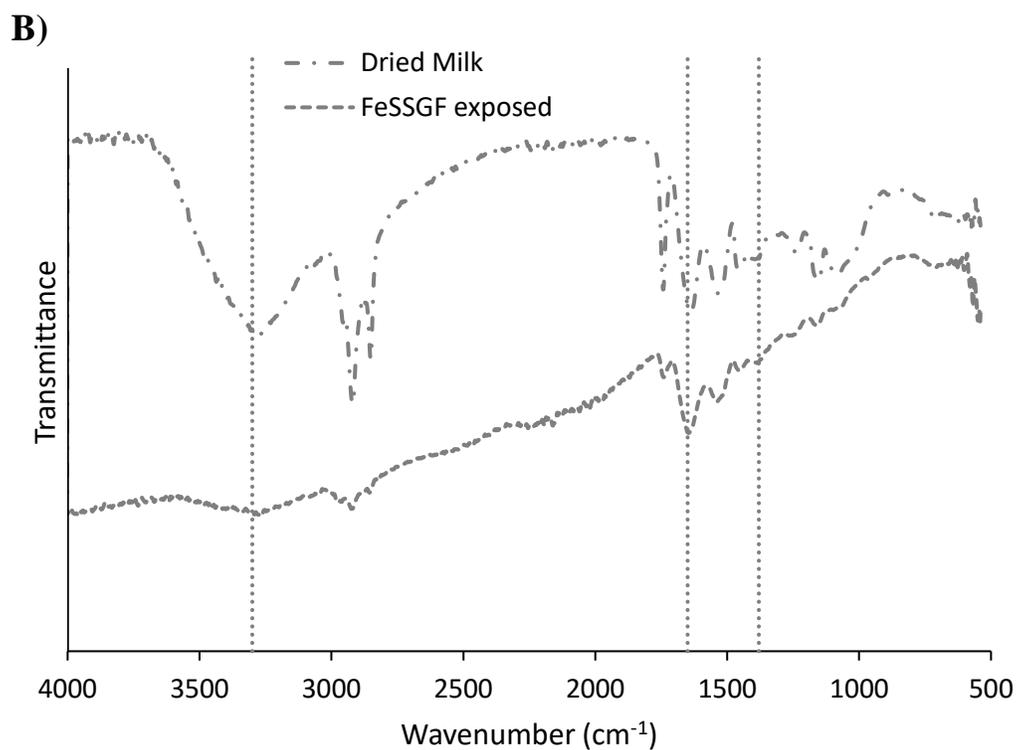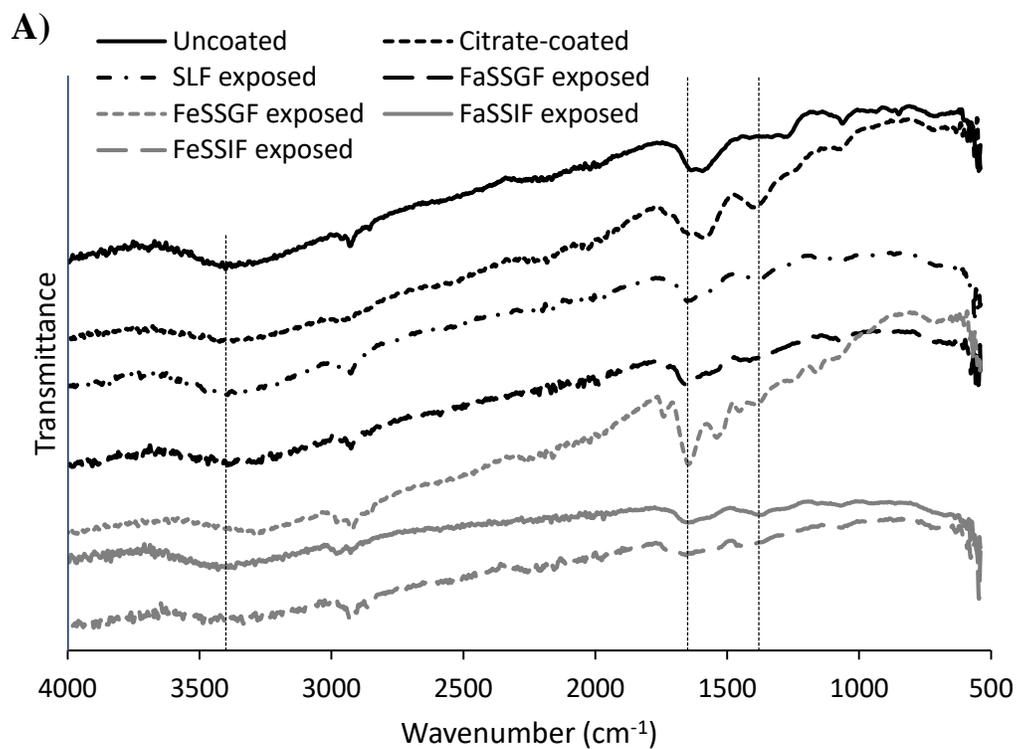
Figure 3-4: FTIR of (A) the nanoceria before and after citrate coating, and after exposure to each SBF; (B) dried milk and nanoceria after FeSSGF exposure. Vertical dashed lines indicate -OH at 3400, N-O at 1650, and -COOH at 1380 cm^{-1}.
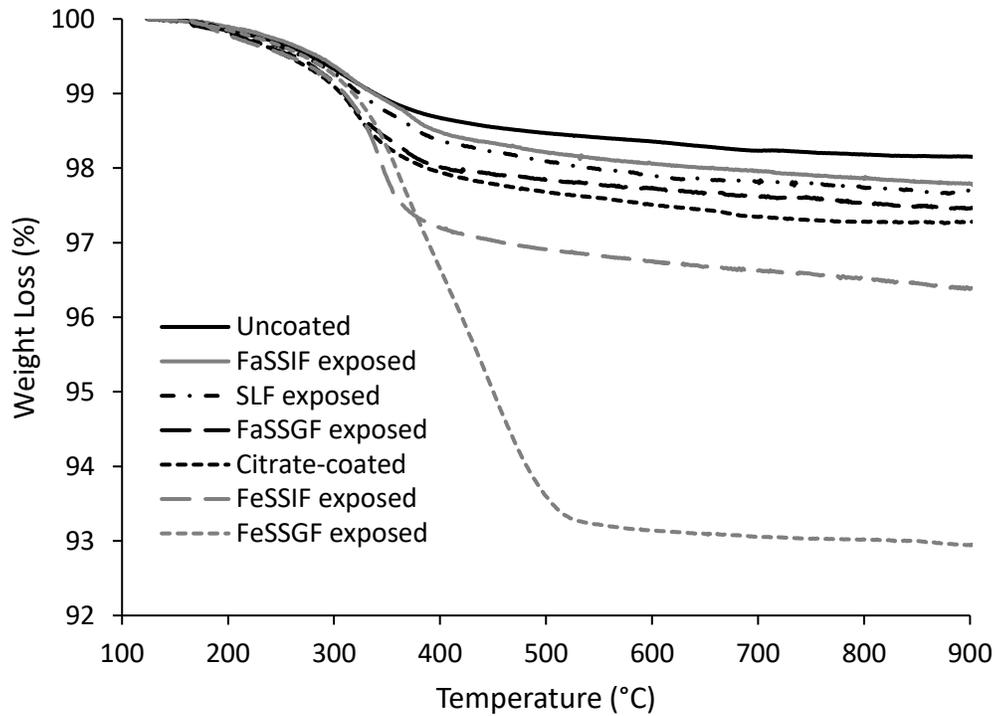
Figure 3-5: TGA analysis of nanoceria before and after citrate coating, and after exposure to each SBF.

3.3.3 Crystalline Structure

XRD analysis, including the labeled crystal planes, of the citrate-coated nanoceria is shown in Figure 3-6. The crystalline structure remained unaffected by the SBF exposure. The XRD pattern matches that of face-centered cubic fluorite, JCPDS card no. 34-0394 [60].
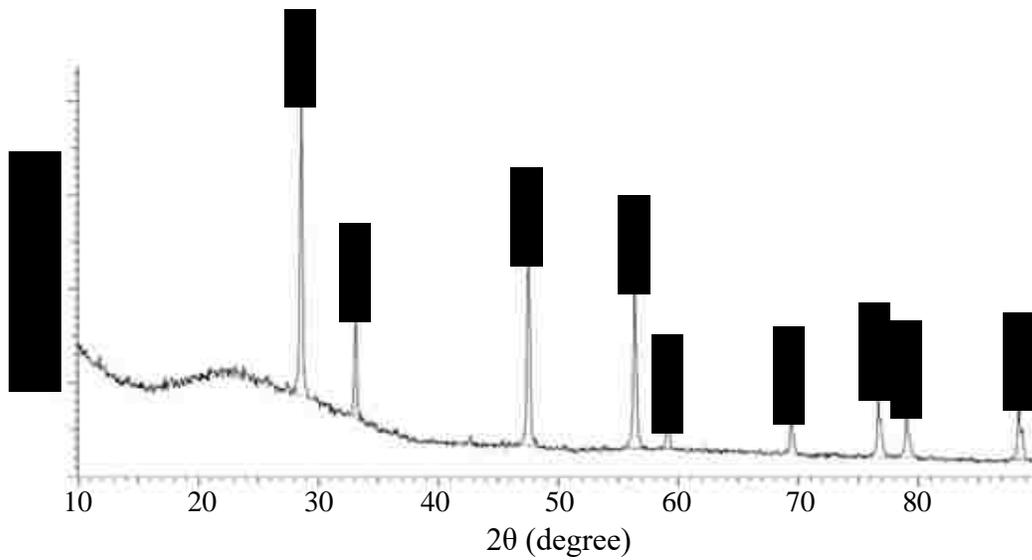
Figure 3-6: XRD of the citrate-coated nanoceria particles including crystal planes (JCPDS card no. 34-0394).

3.4 Conclusions

Crystalline nanoceria particles were produced to have a cubic morphology, approximately 21.1 nm in length. The particles were citric acid coated following the synthesis. The coating increased the surface charge and decreased the hydrodynamic diameter due to the repulsion forces of the negative citrate surface groups. Exposure to SBFs, including simulated lung, gastric, and intestinal fluids, slightly altered the citrate coating. After exposure to FeSSGF, the hydrodynamic diameter and weight loss during heating increased, suggesting overcoating of milk components to the nanoceria surface, and confirmed by additional peaks between 1300 and 1800 cm^{-1} in the FTIR spectrum. Similar, but less profound, changes were seen following FeSSIF exposure, however there were no new peaks in the FTIR spectrum. Exposure to SLF, FaSSGF, and FaSSIF resulted in subtle changes. In addition, the biological response and cell toxicity of the nanoceria exposed to the SBFs were discussed in the publication, and no statistically significant results were obtained [34].

4.1 Introduction

Microfluidic chips are commonly utilized to study the fluid flow through micron sized channels. These chips can be used in a variety of applications in the medical, environmental, and engineering fields. The lab-on-a-chip, derived through the use of microfluidics [149], processes low fluid volumes to determine chemical composition by chromatography, analyze DNA sequences [150], for clinical diagnostics [151], environmental monitoring [152], and fabricate lithographic technology, such as inkjet printing [153]. Each chip is composed of a network of microfluidic channels, sample reservoirs, and micro-sensors [154]. Typically, optical detection techniques are employed to verify performance and quantitative results, creating challenges in chip fabrication [155].

Glass is known as a common material to use for microfluidics. However, plastic reduces production costs and simplifies manufacturing procedures. In addition, there are a wide variety of plastic materials available to be used with a large selection of material properties to choose from, depending on the microfluidic application [156]. Hummingbird Nano (HBN) Inc. has developed a rapid and sustainable method for fabricating capillary electrophoresis microfluidic chips by creating channels in thin monomer films using a ferrofluid manipulated by magnetic fields. The channels are molded in a highly functionalized, viscous monomer, dipentaerythritol pentaacrylate (SR-399). Polymerization through the application of ultraviolet (UV) light will create a solid polymer matrix surrounding the ferrofluid. The ferrofluid is then recovered to be reused, and micron sized channels are successfully embedded within the polymer.

94

Optical sensing devices can be placed directly adjacent to the material at the point of manufacture. To avoid detection losses, the refractive index of the polymer can be matched to that of the fiber optic cable as shown in Figure 4-1. Inorganic nanoparticles with known refractive indices and well-defined size distributions are used to control the refractive index of the nanocomposite chip material. Metal oxide nanoparticles can be synthesized with particle dimensions small enough to efficiently reduce light scattering, maintaining the monomer's transparent properties. Nanocomposite transparency requires that the average diameter of the nanoparticles, d, must be less than $\lambda/4$ [157]. To minimize haze, there must be no agglomeration of nanoparticles in the monomer dispersion.
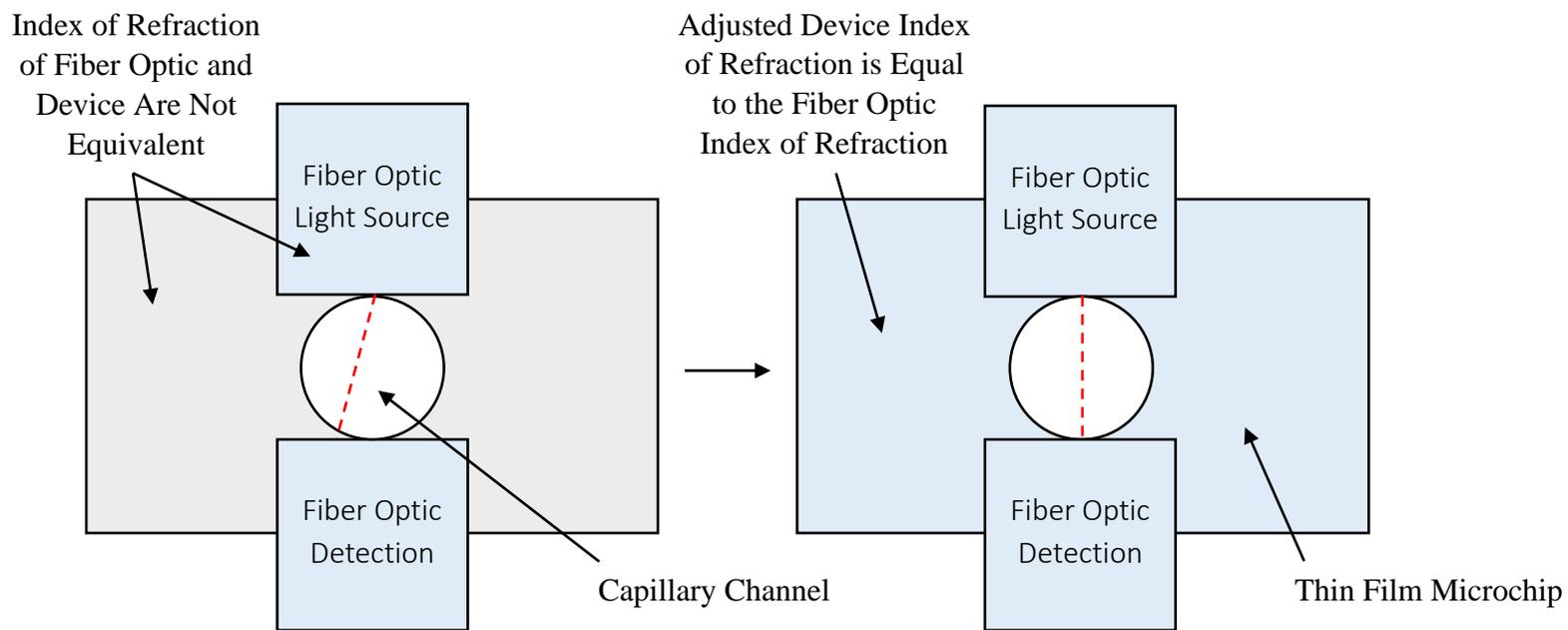
Figure 4-1: Schematic for the refractive index adjustment of the microfluidic chip.

In collaboration with HBN, funded by an NSF SBIR Phase II, a nanocomposite comprised of SR-399 and metal oxide nanoparticles was developed with the appropriate refractive index and material properties suitable for the manufacture of capillary electrophoresis microfluidic chips. The following research elements are critical to supporting nanocomposite chip manufacture:

1. a robust, three-dimensional model of the polymerization of SR-399 with local extent of conversions and crosslinking,

2. synthesis of metal oxide nanoparticles in sustainable, 'green' recipes, and

3. nanoparticle stabilization of the dispersions for reproducible polymerizations.

Table 4-1 summarizes the key research elements for this project.

Table 4-1: Key project research elements.

Manufacturing Material	Research Element	Issues	Actions
Nanocomposite	Photopolymerization model (Chapter 6)	Nanoparticles absorb light; Conversion and crosslinking gradient occurs throughout the film thickness	Prediction and measurement of crosslinking gradient throughout the film thickness
	Nanoparticle Synthesis	Low cost, non-toxic metal oxide nanoparticle (see those listed in Table 4-2)	Solvent choice for nanoparticle synthesis affects the manufacturing process
	Nanoparticle Functionalization	Surface hydroxyl groups can be replaced for dispersion in the monomer	Acrylosilane coupling agents to link to monomer functional groups
	Nanocomposite Fabrication	Nanoparticles must yield a stable monomer dispersion	Size, surface properties, and solvent choice affects the dispersion
Ferrofluid	Ferrofluid Characterization (Chapter 5)	Particle distribution and surface surfactant composition of magnetic nanoparticles dispersed in an aqueous medium	Ferrofluid supplied must be used continuously for channel molds
	Ferrofluid Recovery	Ferrofluid to be recycled and reused	Ferrofluid can be recovered through the use of its magnetic properties

Figure 4-2 shows a typical synthesis workflow for this design. Initially, the nanoparticles will be synthesized with well-defined particle size and shape distributions, and then functionalized to reduce agglomeration in the monomer dispersion. Next, SR-399 will be added to the resulting dispersion and the solvents removed and recycled. The monomer dispersion needs to have a shelf-life of approximately six months. The channels will be molded into the monomer mixture by the ferrofluid and then polymerized. The ferrofluid should be immiscible in the monomer dispersion and ultimately, recovered and reused.
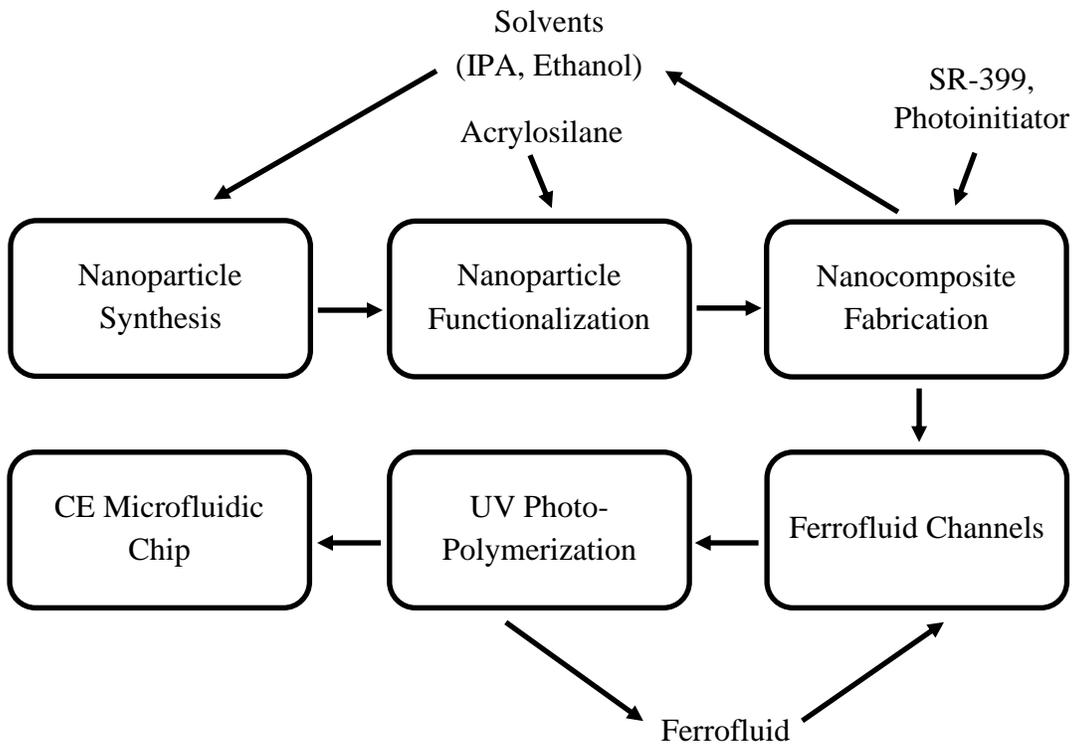
Figure 4-2: Process flow diagram of microfluidic chip manufacture.

Research results are expected to lead to an innovative, low cost, high quality manufacturing system for capillary electrophoresis chips. These chips can operate effectively with low sample consumption, low energy input, and provide quick and easy sample analyses through embedded optical detectors. SR-399's non-toxicity and fast cure response to UV light makes it a preferred molding material. Nanoparticles can be prepared through sustainable recipes, the ferrofluid and organic solvents can be recycled, and the entire process is scalable. Once manufactured, these chips can be used in a variety of applications in the medical, environmental, and engineering fields.

Inorganic nanoparticles with known refractive indices and well-defined size distributions are used to control the refractive index of the nanocomposite chip material (Table 4-2). Furthermore, the addition of hard, crystalline nanoparticles to the polymer matrix allows for precise control of material properties such as electrical conductivity, magnetism, tensile strength, and hardness to be used for specific applications. Metal oxides, such as titania (TiO_2), ceria (CeO_2), silica (SiO_2), alumina (Al_2O_3), zinc oxide (ZnO), etc. can be synthesized with particle dimensions small enough to efficiently reduce light scattering, maintaining the monomer's transparent properties.

Table 4-2: Refractive index of various metal oxides [158].

Material	Refractive Index
Al_2O_3	1.62 @ 600 nm
SiO_2	1.46 @ 600 nm
TiO_2	2.2-2.7 @ 550 nm
ITO	2.05 @ 550 nm
ZrO_2	2.1 @ 550 nm
ZnO	-
CeO_2	2.2 @ 550 nm
Ta_2O_5	2.16 @ 550 nm

Titania was chosen because of its material properties. Titania is highly stable, non-toxic, and is relatively quick, easy, and inexpensive to manufacture. In addition, the refractive index of titania is approximately 2.0 (amorphous), 2.45 (anatase), and 2.70 (rutile) [159-161]. The refractive index of SR-399 is 1.49, and thus by using titania will provide a wide range to work with. However, due to the large difference between the refractive index, light scattering, known as haze, can be an issue moving forward with titania and will need to be addressed in future experiments.

Titania can be crystalline or amorphous. It has been previously studied as an antimicrobial agent [162-164], a photocatalyst to split water (amorphous is cheaper, but less efficient than crystalline titania) [165], a low temperature oxygen and gas sensor [166, 167], and for use in solar cells [168] and producing high refractive index titania thin films/nanocomposites [161, 169].

4.2 Crystalline Titania Nanoparticle Synthesis

4.2.1 Experimental

██████ Materials

The following chemicals, including their sources, purity, and CAS #s, used in the crystalline nanotitania synthesis were: titanium(IV) isopropoxide (TTIP), Alfa Aesar, >97%, 546-68-9; acetic acid, Sigma, ACS grade, 64-19-7; and nitric acid, Sigma, ACS grade, 7697-37-2. Lacey carbon, 300 mesh, copper grids (product #01895) from Ted Pella, Inc. were used for electron microscopy.

██████ Methods

Crystalline titania nanoparticles were fabricated following the procedure as listed in Mandzy et al. [170] from titanium tetraisopropoxide (TTIP) using water as the main component. 25 mol of water, 0.42 mol of acetic acid, and 0.003 mol of nitric acid were mixed under constant stirring at 350 rpm. 0.13 mol of TTIP was added and stirring was continued for 1 hour. The resulting mixture was transferred to a pressure vessel and heat-treated at 130 ℃ for 90 minutes. The synthesis is summarized in the chemical equation below:

$$Ti(OCH(CH_3)_2)_4 + 2H_2O \rightarrow TiO_2 + 4(CH_3)_2CHOH$$
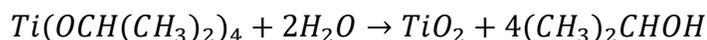
The nanoparticles will be used to adjust the refractive index of the microfluidic chip so that optical detection is not obscured. Stoichiometrically, the ratio of water to TTIP,

known as the hydrolysis ratio, is 2; while in this recipe, the ratio is nearly 200. Low hydrolysis ratios have been reported to result in partial hydrolysis and organic groups are retained in the precipitate. Higher hydrolysis ratios are necessary for complete hydrolysis and the precipitation of crystalline titania [171-173]. The particles were prepared in an aqueous dispersion in order to functionalize the surface with hydroxyl (-OH) groups.

4.2.2   Results & Discussion

███████   Particle Size & Morphology

The particle size of the resulting nanoparticles was determined from Dynamic Light Scattering (DLS) (Figure 4-3) and the Transmission Electron Microscope (TEM) (Figure 4-4). The surface area distribution as indicated by DLS shows approximately 10 nm particles, with some particles as large as 65 nm in diameter. The intensity distribution, however, shows particles as large as 400 nm. The intensity distribution is based on light scattering. Larger particles scatter more light than smaller particles. A small fraction of large particles results in significant scattering which will skew the size distribution. Although the concentration of these agglomerates may be small, they are still present in the dispersion.

The TEM results in crystallites averaging approximately 3-5 nm in diameter. The image also shows that the particles are slightly aggregated when dispersed in the aqueous phase, roughly 300 nm in length. The Energy-Dispersive X-ray Spectroscopy (EDS) graph

indicates a strong presence of titanium and oxygen in the sample. The copper is from the

TEM grid. However, the silicon and calcium are impurities in the sample.

A)

B)
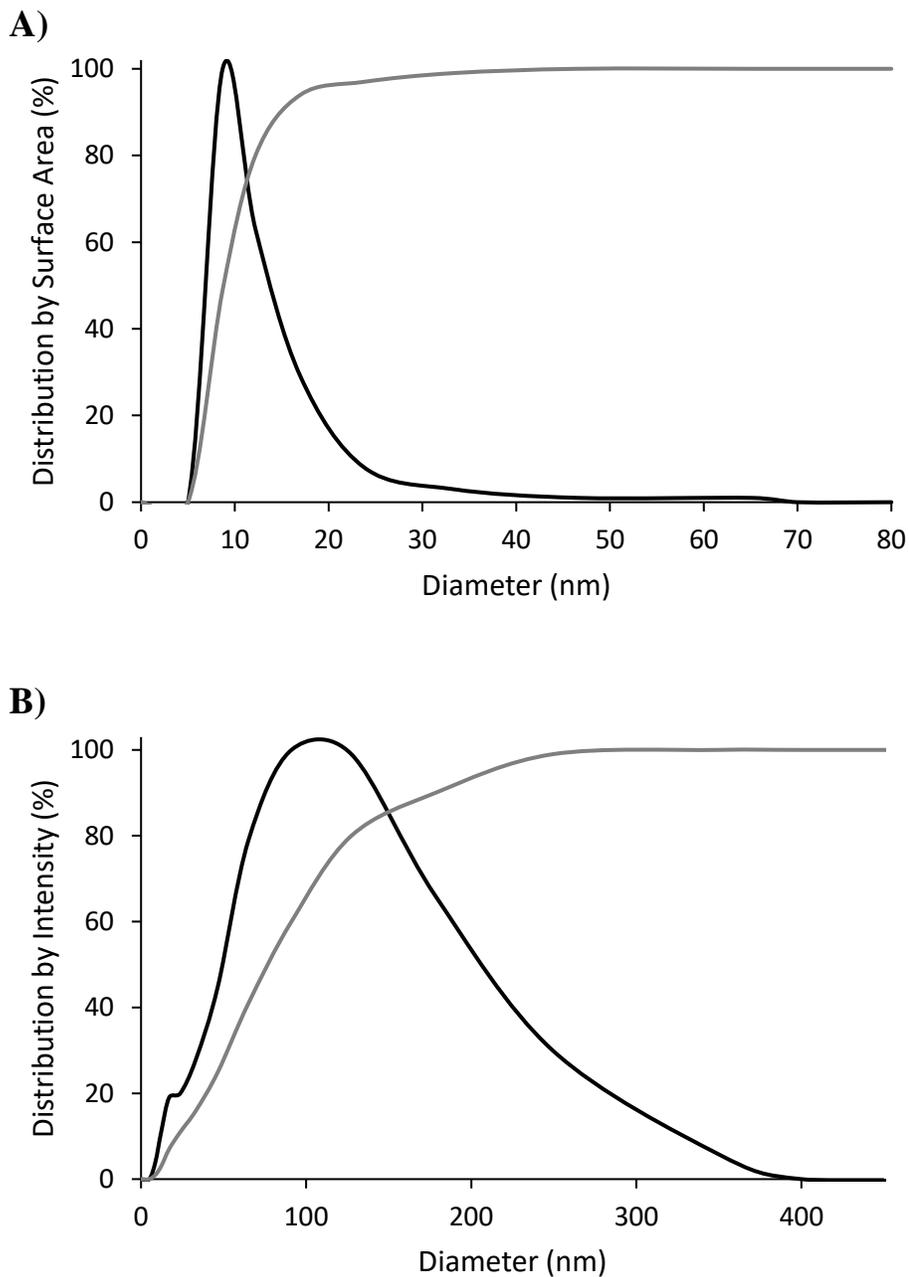
Figure 4-3: DLS results for titania: (A) Distribution by surface area; (B) Distribution by intensity. Black: Distribution; Gray: Cumulative.
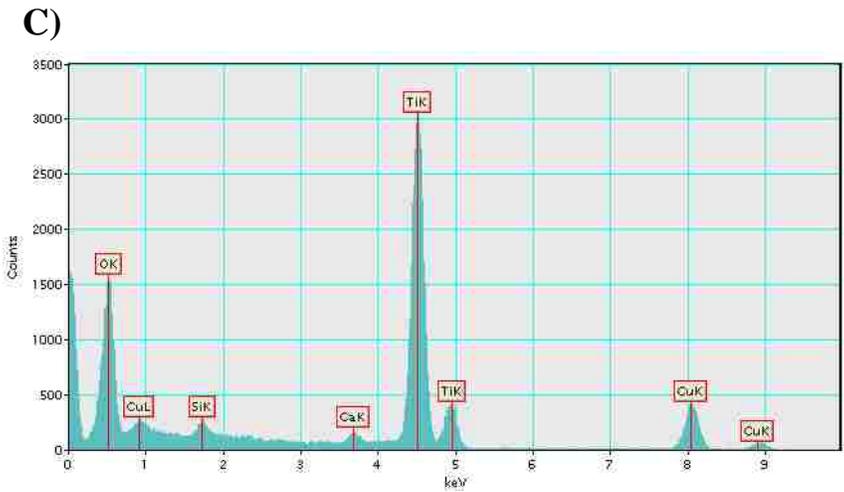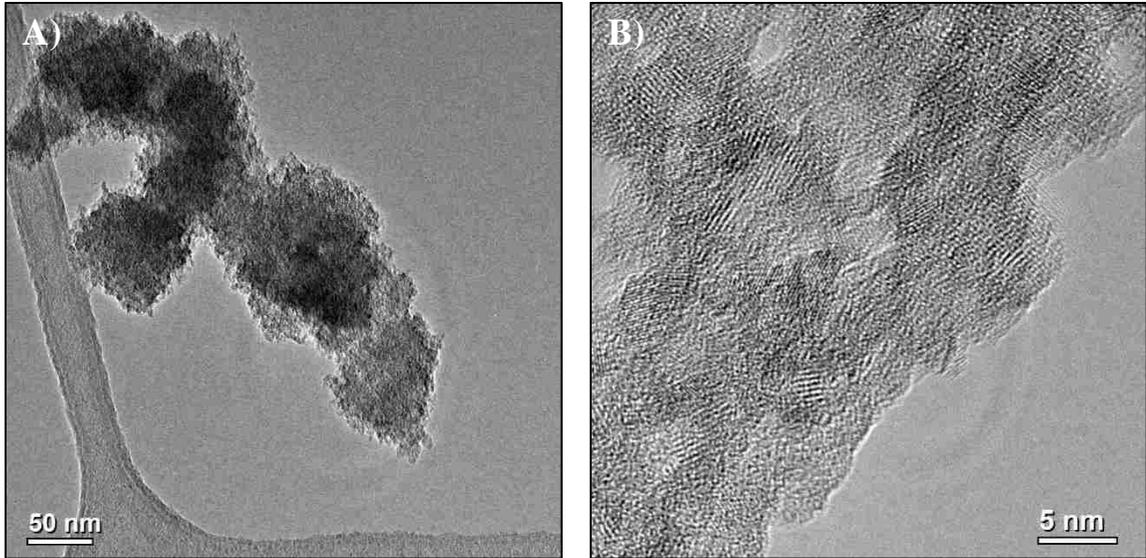
Figure 4-4: TEM images of the crystalline titania nanoparticles. (A) This low magnification image shows an agglomerated particle, roughly 300 nm. (B) This high magnification image shows individual crystallites, approximately 3-5 nm. (C) EDS spectrum of the crystalline titania on a copper TEM grid.

■■■■■ Crystalline Structure

Furthermore, X-ray Diffraction (XRD) was completed on the titania to determine the crystal structure of the particle. There are several crystal structure possibilities for titania, but the most common are anatase, rutile, or a mixture of the two. Peaks at 25°, 38°, 48°, and 55° depict a pure anatase structure (Figure 4-5) (JCPDS card no. 21-1272) [174-177]. The average particle size was estimated to be 10.4 nm using the Debye-Scherrer formula [Equation (1-2)].

XRD and DLS replicate each other well, both suggest a diameter of approximately 10 nm. However, DLS only computes the average hydrodynamic diameter, and the XRD should be an estimation of the average crystallite size. Although 3-5 nm crystallites are present from TEM, they are accumulated in 300-400 nm agglomerates. The agglomerates are sized much greater than λ/4, which means that these particles will produce haze. This is undesirable, therefore surface modification and solvent identification are to be explored next.
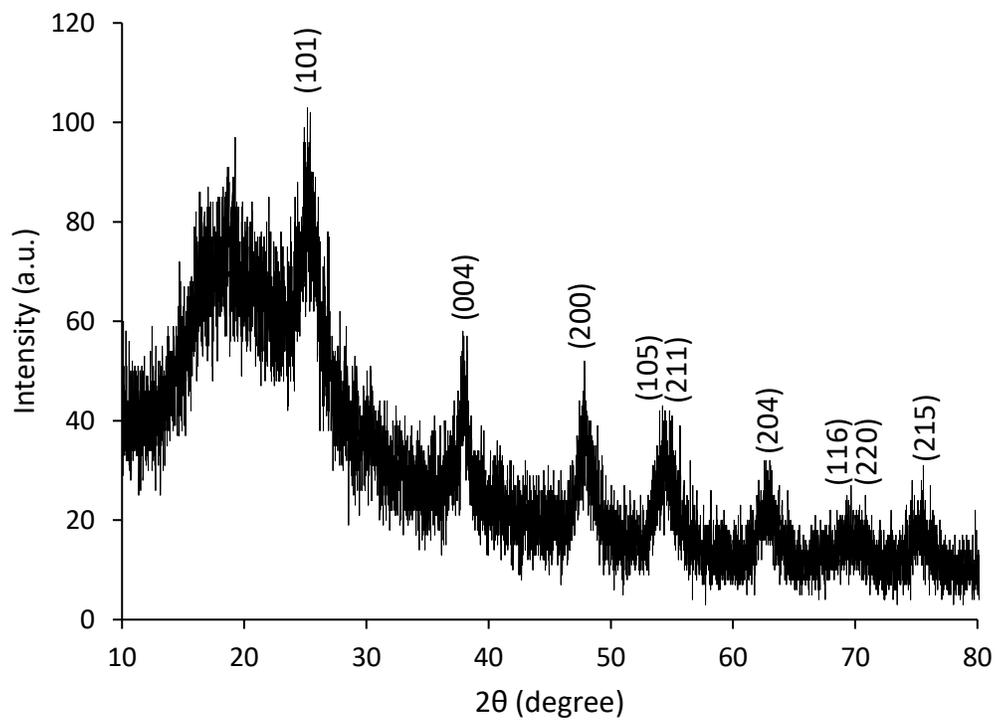
Figure 4-5: XRD of crystalline anatase titania with labeled crystal planes (JCPDS card no. 21-1272).

4.3 Crystalline Titania Nanoparticle Functionalization

4.3.1 Experimental

███████ Materials

The following chemicals, including their sources, purity, and CAS #s, used in the crystalline nanotitania surface functionalization were: (3-acryloxypropyl) trimethoxysilane (SIA 0200.0), Gelest, 96%, 4369-14-6; acetic acid, Sigma, ACS grade, 64-19-7; and ethanol, Decon, 200 proof, 64-17-5.

███████ Methods

Typical nanoparticle stabilizing agents, such as small organic acids, need to be replaced by covalently-bound moieties that can link directly between nanoparticle surfaces and polymer chains. Silanes with vinyl chain units can be used, but surface coverages need to be carefully tailored based on the metal oxide surface chemistries, ensuring that the interphase between particle and polymer is well-controlled.

Surface modification of inorganic nanoparticles, such as metal oxides, with silane coupling agents can help form a robust bond with the organic functional groups of the SR-399 monomer prior to polymerization [178]. (3-acryloxypropyl) trimethoxysilane (SIA0200.0) contains the acrylate organofunctional group connected to a propyl linker chain, similar to that of the SR-399 molecule. The trimethoxy group attached to the silicon atom are hydrolyzable and can bond to the hydroxyl groups present on the surface of the titania through a condensation reaction as shown in Figure 4-6.

A 95% ethanol solution was prepared with the pH adjusted to 5 using acetic acid. SIA0200.0 was added to make a 2% by volume final solution and continuously stirred at 350 rpm for 5 minutes to allow time for hydrolysis. The titania particles were then added and stirred for an additional 2 minutes. The particles were then centrifuged for 2 minutes at 1000 rpm, and cured for 10 minutes at 110 ℃ in an oven.

The acrylate group on the silane was covalently bonded with the SR-399 monomer during chain growth polymerization as shown in Figure 4-7. The free radical was obtained by photoinitiator dissociation due to UV light exposure to initiate polymerization. The 'R' groups are a combination of SR-399 chain units and photoinitiators. The free radical UV photopolymerization of SR-399 is explored in detail in Chapter 6.

During the silanization process, hydrolysis is important to form the hydroxyl groups in place of the methoxy groups, but condensation between neighboring silanol molecules can create siloxanes. As the molecular weight of the siloxanes increase, the nanoparticle dispersion can become unstable and the siloxane coated particles will precipitate out of solution. This would be undesirable. Controlling the rate of hydrolysis in respect to the rate of condensation between silanols is key to preparing a stable dispersion.
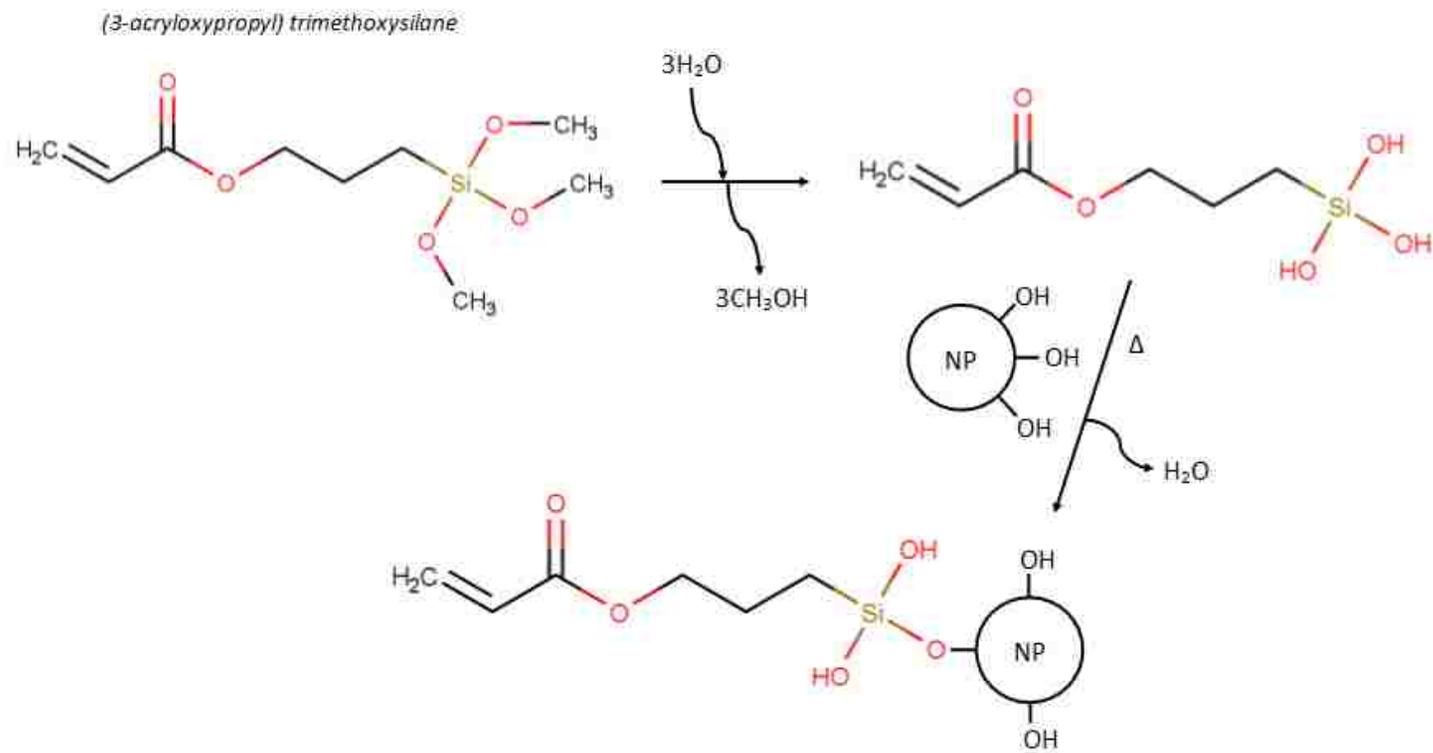
Figure 4-6: Silanization reaction to bond the silane to the surface of the titania nanoparticle.
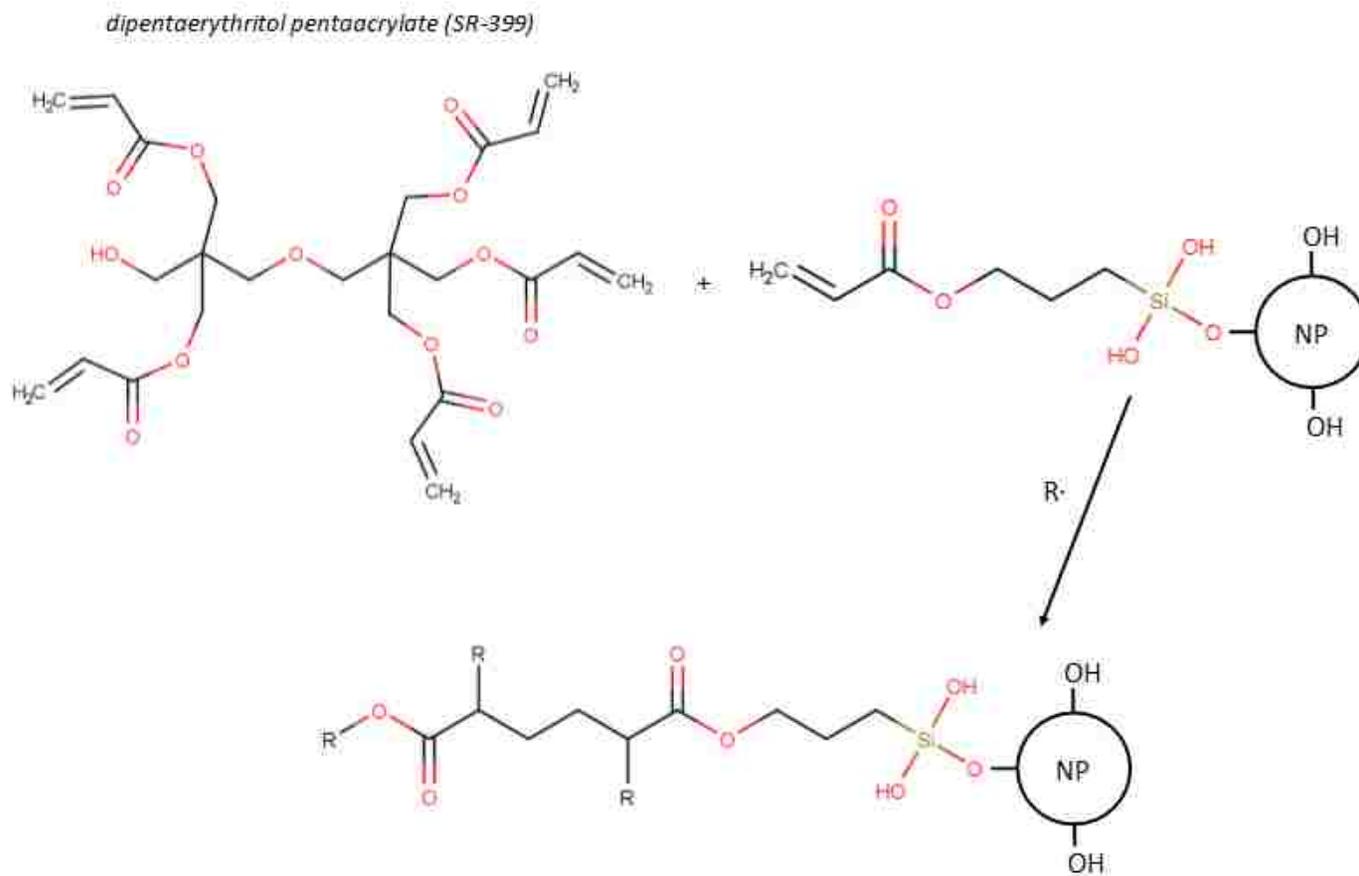
Figure 4-7: Polymerization of SR-399 incorporating the titania nanoparticles.

4.3.2   Results & Discussion

███████   Surface Composition

Fourier Transform Infrared Spectroscopy (FTIR) can be used to measure the Si-O-Si bond present in siloxanes, Si-OCH$_3$ bond, and Si-OH bond. The Si-O-Si bond peaks at 1030 cm^{-1}, Si-OCH$_3$ at 1092 cm^{-1}, and Si-OH at 3500 cm^{-1}. The increase of Si-O-Si bonds represents condensation while the decrease of Si-OCH$_3$ bonds represents hydrolysis. The Si-OH bonds will increase with hydrolysis, but decrease with condensation [179]. Figure 4-8A shows the preliminary results from coating titania with silane at a 1:1 molar ratio of silane to surface hydroxyls.

Thermogravimetric Analysis (TGA) was also completed on the titania and silane-coated titania nanoparticles to determine the weight percent of silane on the surface of the particle. Figure 4-8B shows that the silane coated particles approximately triple the percent weight loss from that of the hydroxyl group. Given that the molecular weight of the silane (234.32 g/mol) is much larger than that of the hydroxyl group (17 g/mol), not all of hydroxyl groups reacted with the silane. A quick calculation [Equation (1-5)] relating the molecular weights of each species to each other and weight loss from the TGA results indicates that 2.39 hydroxyl molecules are present per nm^2 before silanization, and 0.51 silane molecules per nm^2 post-silanization. This means that approximately 20% of the hydroxyl groups reacted with silane assuming each silane molecule is bonded to a single surface hydroxyl molecule. Therefore, if more (or less) silane is required, the rate of hydrolysis needs to be increased by either changing the solution pH, silane concentration, or reaction time.
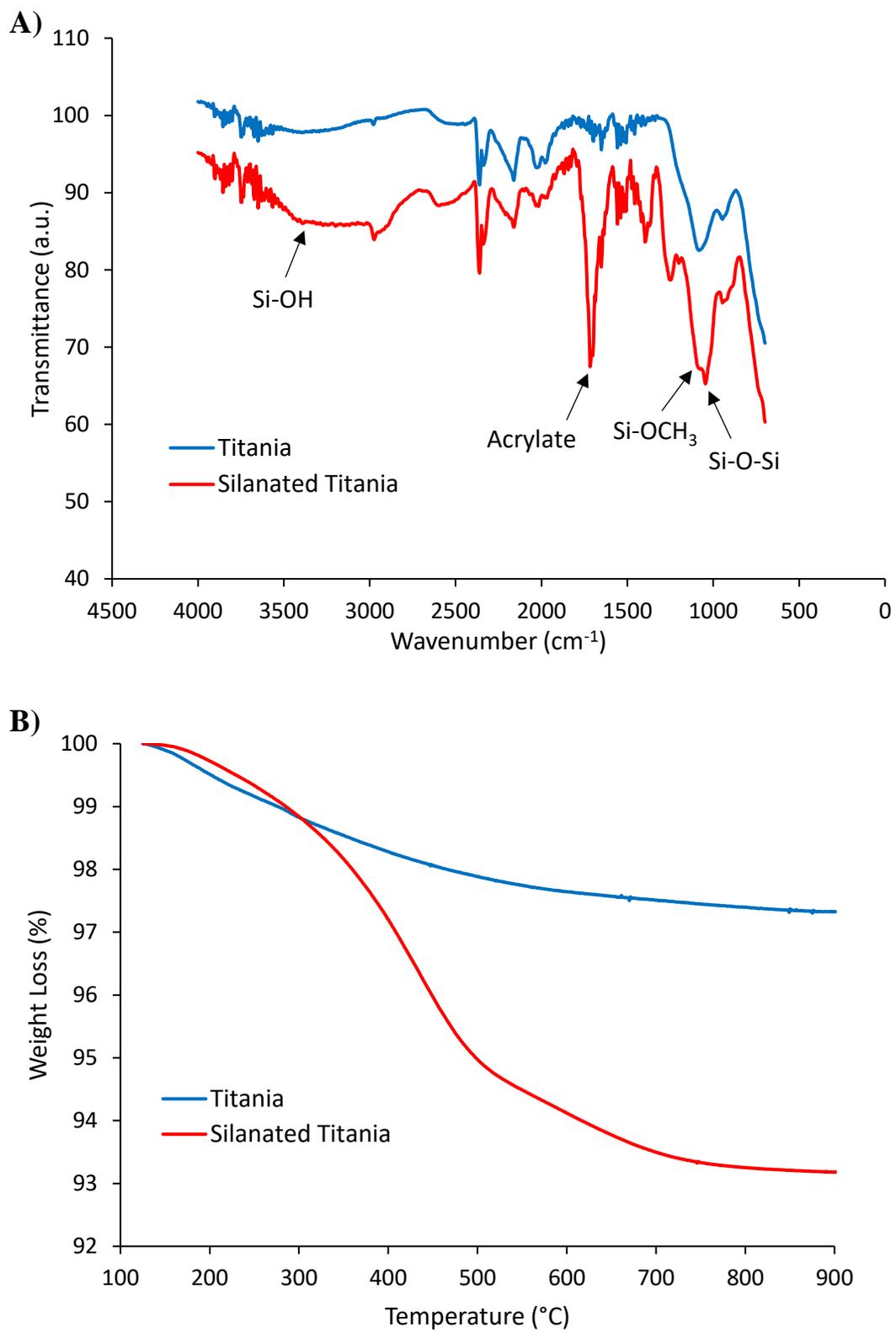
Figure 4-8: (A) FTIR and (B) TGA of titania and silane-coated titania nanoparticles.

4.4   Crystalline Titania Nanocomposite Fabrication

4.4.1   Experimental

██████   Materials

The following chemicals, including their sources, purity, and CAS #s, used in the nanocomposite fabrication were: dipentaerythritol pentaacrylate (SR-399), Sartomer, 100%, 60506-81-2; Irgacure 184, Ciba, 99%, 947-19-3; ethanol, Decon, 200 proof, 64-17-5; isopropyl alcohol, VWR, 99%, 67-63-0; and 1-methoxy-2-propanol, Acros Organics, 98.5%, 107-98-2.

██████   Methods

In order to adjust the refractive index of the microfluidic chip, inorganic nanoparticles are embedded in the monomer to create nanocomposites. Solvents are required to create a stable dispersion of titania in the monomer solution prior to polymerization. The solvents used were water, IPA, ethanol, and 1-methoxy-2-propanol. 2.5% by weight titania nanoparticles were added to an equimolar mixture of the chosen solvent and SR-399. The mixture was stirred at 700 rpm on a hot plate set to 80 ℃. It was then transferred to a rotary evaporator set to 80 ℃ at a gauge pressure of -25 inHg to evaporate the solvent. Once the solvent was fully evaporated, 2% by weight Irgacure 184 was added and the mixture hand-stirred on a hot plate set to 80 ℃. The solution was covered by Al foil and let sit overnight to release the trapped air bubbles. The final mixture was polymerized using a Paul C. Buff, Inc. White Lightning X3200 (Model # WLX3200-120V) flash unit.

4.4.2 Results & Discussion

███████ Phase Diagrams

Water was initially used since it was the dispersing agent used in the titania synthesis, however, water and SR-399 create a two-phase mixture (Figure 4-9), which is undesirable. According to literature, 1-methoxy-2-propanol was used to reduce the solute concentrations to between 5 and 20% [158]. This solvent was used successfully to create a stable dispersion, but the resultant polymer was not transparent. IPA and ethanol were other solvents used, neither of which created an optically clear polymer, but a stable dispersion of titania and SR-399 was achieved in each instance. IPA and ethanol create a homogenous mixture with SR-399 with less than 10% water, as indicated by the ternary phase diagrams (Figure 4-10).
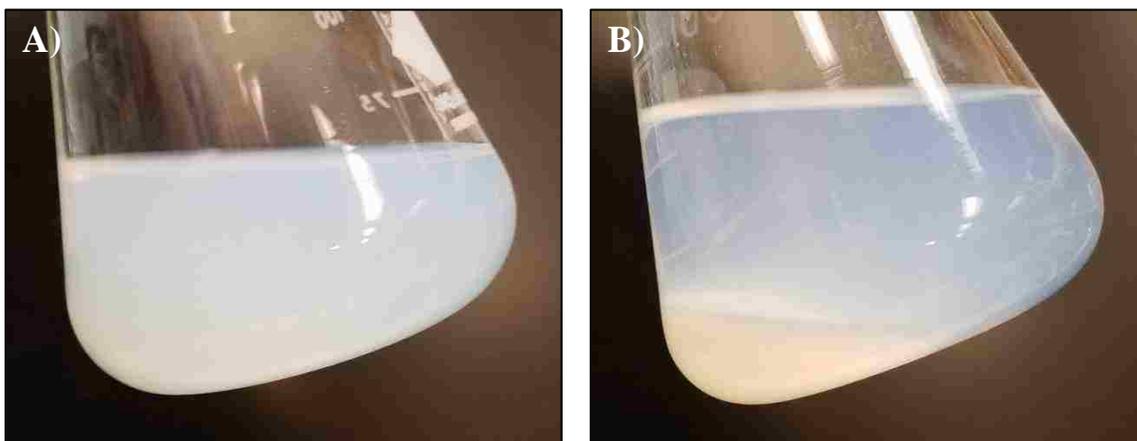
Figure 4-9: Phase equilibria trial. (A) Titania dispersed in water. (B) Two-phase mixture composed of water, titania, and SR-399.

A)

Bubble point at 1.01 bar
Isopropanol = 82.26 C
Water = 100.00 C
sr399 = 619.60 C

Binary Azeotrope
● (Isopropanol,Water) = (68.5%, 31.5%) at 80.32 C

Mole percent (sr399)

Mole percent (Water)

Mole percent (Isopropanol)

B)

Bubble point at 1.01 bar
Ethanol = 78.29 C
Water = 100.00 C
sr399 = 619.60 C

Binary Azeotrope
● (Ethanol,Water) = (89.5%, 10.5%) at 78.05 C

Mole percent (sr399)

Mole percent (Water)

Mole percent (Ethanol)
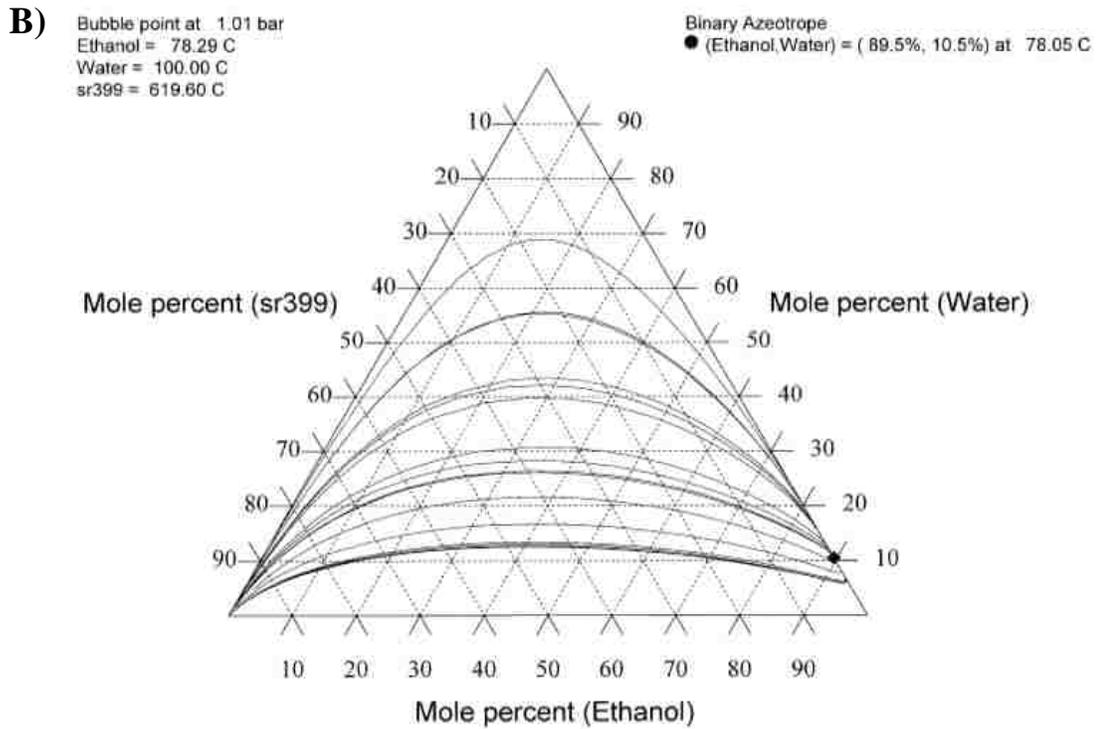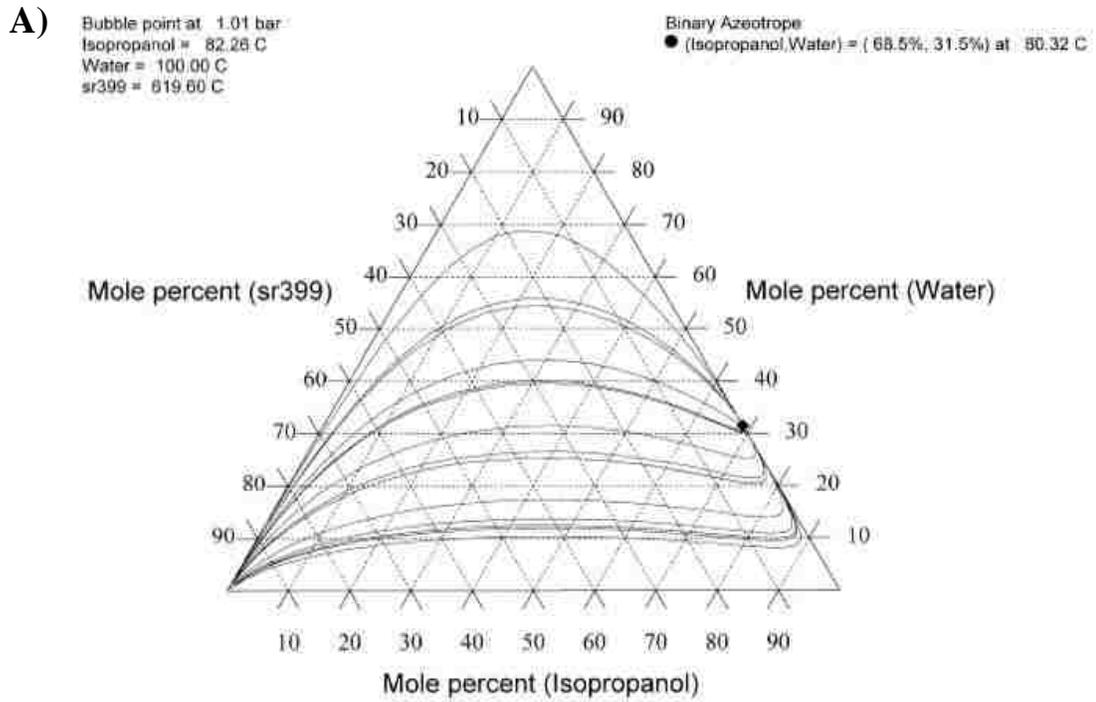
Figure 4-10: Ternary phase diagrams for (A) isopropanol and (B) ethanol.

116

██████ Nanocomposites

The nanocomposites produced were tested in the FTIR to determine if the change in solvent or titania composition was noticeable (Figure 4-11). Four nanocomposite samples were tested and there was no clear indication of a difference among them. One peak stood out above the rest, the acrylate peak which was present in all samples due to the acrylate groups present in SR-399. Each sample, except for the control, contained 2.5 weight percent titania and there was no noticeable difference between those three and the control.
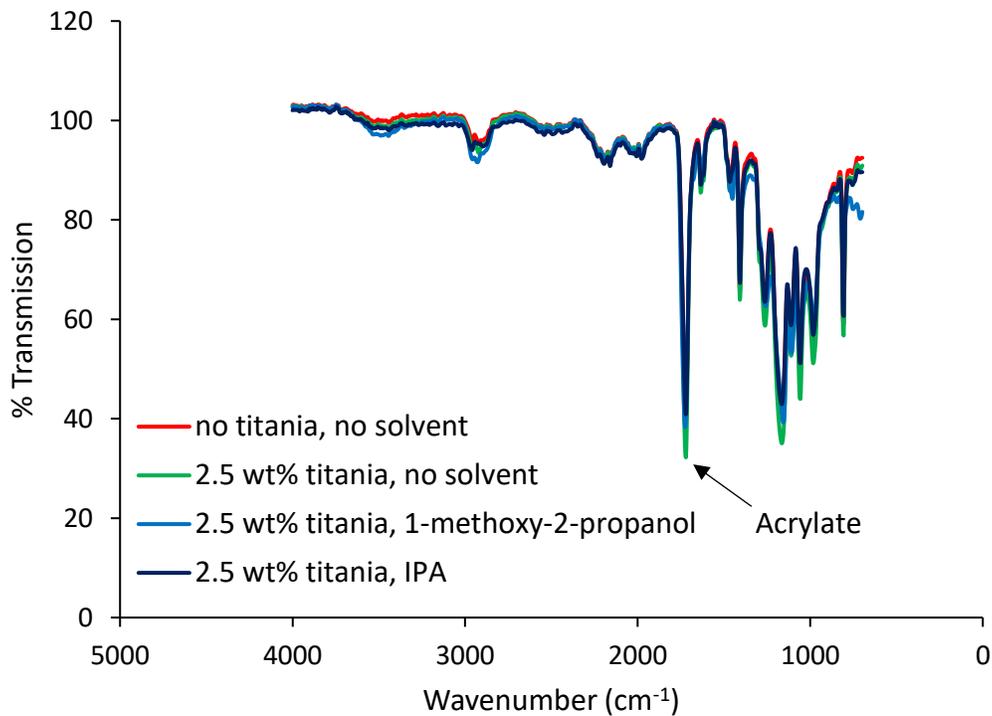
Figure 4-11: FTIR of four SR-399/titania nanocomposites.

In addition, the nanocomposites prepared were not 100% transparent (Figure 4-12). When comparing each of the nanocomposites to the blank SR-399 control, two contained visual agglomerates (the dry TiO_2 and when using IPA as a solvent). Using water as the dispersing agent created a heterogeneous mixture and produces a nanocomposite with high haze. The 1-methoxy-2-propanol and ethanol samples resulted in visually more favorable nanocomposites, but 1-methoxy-2-propanol still contained haze, and the ethanol resulted in a very orange/yellow nanocomposite. Neither of the resulting nanocomposites replicated that of the control, therefore, an entirely new titania synthesis and nanocomposite fabrication method is to be explored.

Figure 4-12: SR-399/titania nanocomposites: (A) SR-399 control; (B) SR-399/TiO_2/H_2O; (C) SR-399/dry TiO_2; (D) SR-399/TiO_2/1-methoxy-2-propanol; (E) SR-399/TiO_2/IPA; (F) SR-399/TiO_2/ethanol.

4.5 Silica-Coated Titania Nanoparticles

4.5.1 Experimental

███████ Materials

The following chemicals, including their sources, purity, and CAS #s, used in the silica-coated titania nanoparticle synthesis were: titanium(IV) isopropoxide (TTIP), Alfa Aesar, >97%, 546-68-9; toluene, Acros Organics, 99.5%, 108-88-3; oleic acid, Sigma, 90%, 112-80-1; and tetraethyl orthosilicate (TEOS), Sigma, >99%, 78-10-4. Lacey carbon, 300 mesh, copper grids (product #01895) from Ted Pella, Inc. were used for electron microscopy.

███████ Methods

A new synthesis method explored was in toluene. Toluene was chosen as the solvent because it is reported as producing titania with narrow size and shape distributions [180, 181], and is soluble in SR-399. Titania is known to be photocatalytic, especially in the UV range. To suppress this photocatalytric nature, a silica protective layer can be applied. Coating titania with silica has been previously explored [182-184].

The following process involves the thermal decomposition of TTIP to form TiO_2 in toluene, similar to Kim et al. [181]: 49.5 mL toluene and 18.9 mL oleic acid were mixed at room temperature. 5.5 mL TTIP was added dropwise and stirred for one hour. Contents were transferred to a Teflon-lined autoclave and heated to 250 °C for 3 hours. The autoclave was then cooled to room temperature and the contents removed.

Several methods of coating titania with silica were attempted, including the use of hydrolysis and acid catalyzed reactions of tetraethyl orthosilicate (TEOS) on the titania surface. All resulted in visible agglomerates. A slow growth of silica on the surface through elevated temperature, anhydrous ligand transfer with oleic acid and polymerization of TEOS was the most successful method. TiO_2 solution, made using the above technique, is diluted with toluene in approximately a 1:4 volumetric ratio. The solution is then stirred and heated to 65 °C. TEOS is added dropwise over 5 hours in a 1:10 volumetric ratio with the diluted TiO_2 solution. The mixture is then held at temperature and stirred for 24 hours.

4.5.2   Results & Discussion

███████   Nanoparticle Characterization

XRD confirmed crystalline titania in the anatase phase. TEM and EDS are shown in Figure 4-13. Grids were prepared by diluting the TiO_2 solution further with toluene, dipping directly into the solution and held for 5 seconds. It is speculated that agglomeration of the particles occurred during the drying process. Individual particles are observed in the range of 3-6 nm. EDS spectra indicates the presence of silicon, not present in the uncoated particles, confirming a silica addition to the titania nanoparticles. The copper peaks are an effect of the copper TEM grids used.
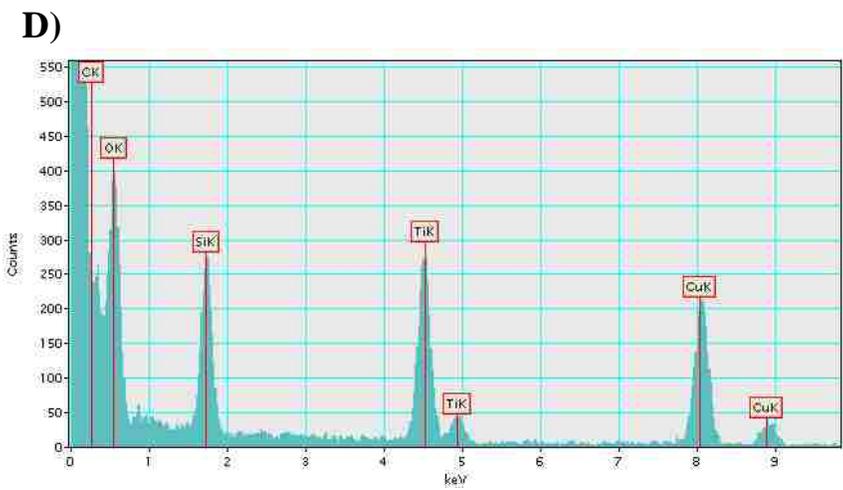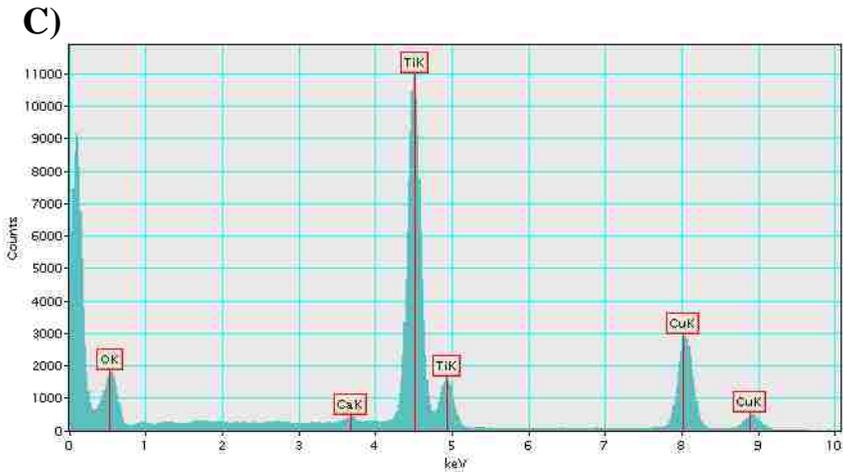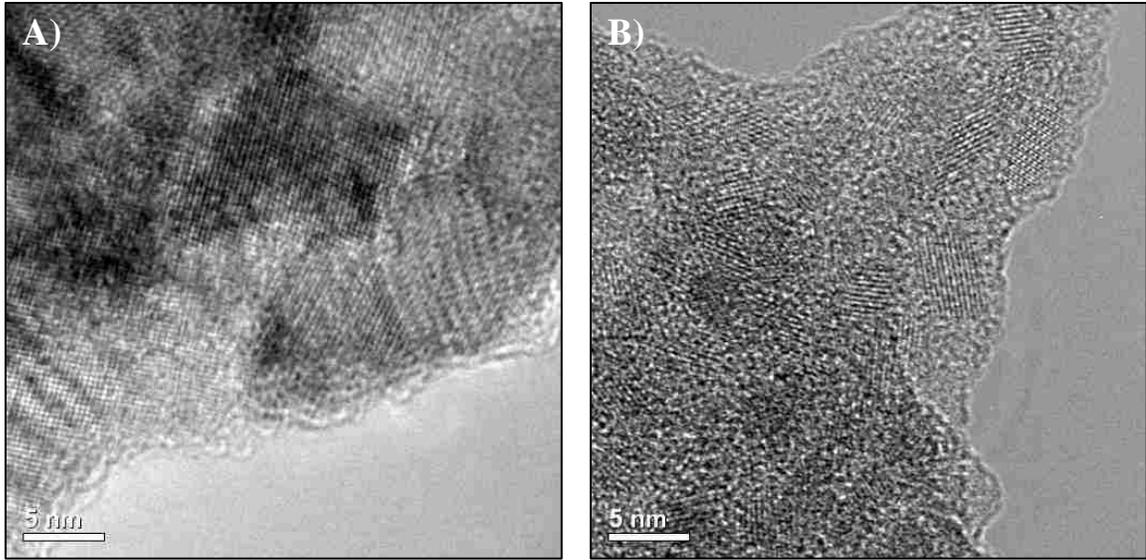
Figure 4-13: TEM images of (A) uncoated and (B) silica-coated TiO_2 nanoparticles. EDS spectra of (C) uncoated and (D) silica-coated TiO_2 nanoparticles.

FTIR was used to identify the bonding structure of the uncoated and silica-coated TiO$_2$ particles. A comparison transmittance spectra is shown in Figure 4-14. The peak at approximately 1060 cm^{-1}, that only appears in the coated spectra, is due to Si-O bond stretching giving further evidence of a silica coating [185].
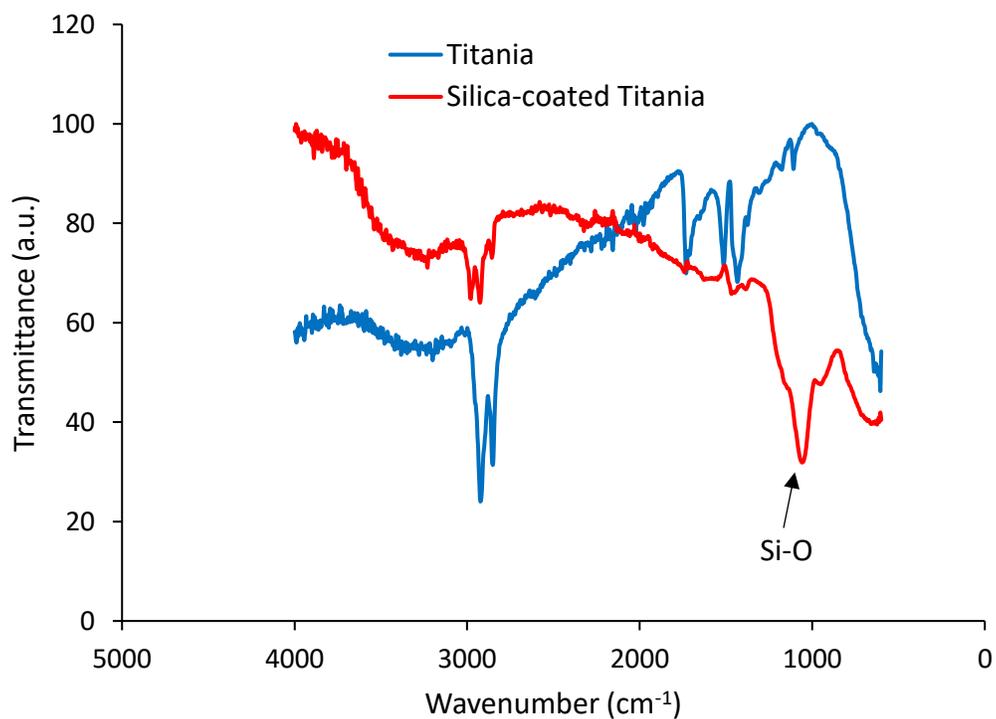
Figure 4-14: FTIR of titania and silica-coated titania nanoparticles.

■■■■■ Coating Growth

The particle size as a function of TEOS weight percent in solution during the coating process was monitored using DLS. Shown in Figure 4-15 is the average hydrodynamic diameter of the particles measured by intensity and surface area as well as the effective diameter. The effective and intensity measurements increased as the weight percent of TEOS increased indicating a coating/shell growth. With a diameter larger than that of a single particle, they are likely small agglomerates dispersed in solution.
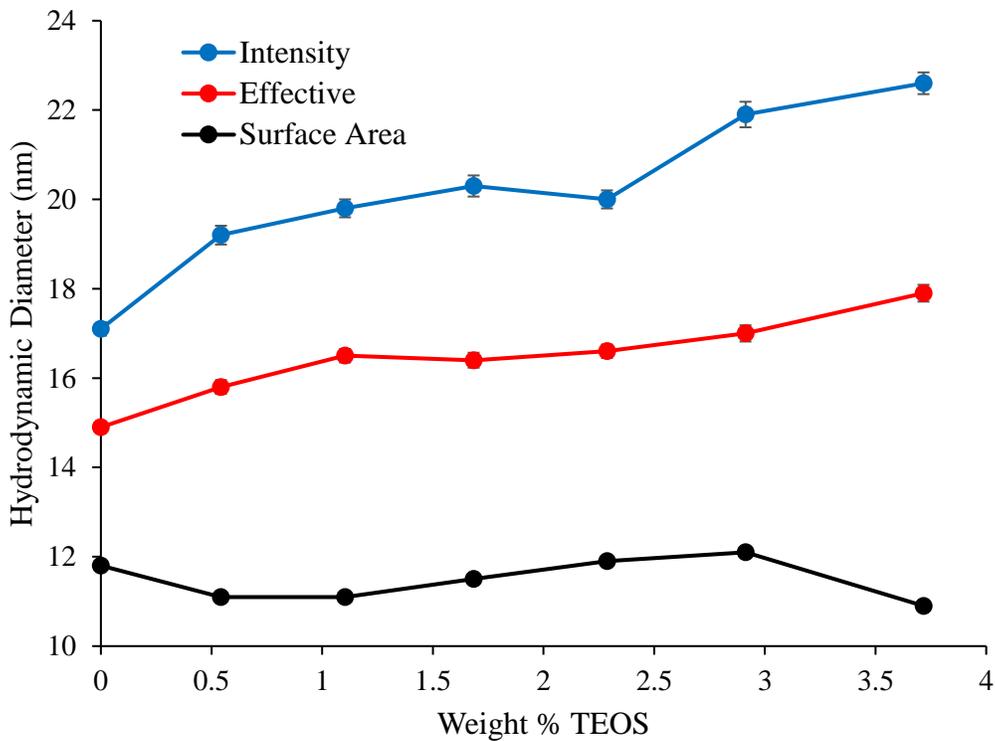
Figure 4-15: Growth of silica-coated TiO$_2$ nanoparticles as a function of weight percent TEOS.

4.6   Amorphous Titania Nanoparticle Synthesis

4.6.1   Experimental

███████   Materials

The following chemicals, including their sources, purity, and CAS #s, used in the amorphous nanotitania synthesis were: titanium(IV) isopropoxide (TTIP), Alfa Aesar, >97%, 546-68-9; ethanol, Decon, 200 proof, 64-17-5; and hydrochloric acid, Sigma, ACS grade (37%), 7647-01-0. Lacey carbon, 300 mesh, copper grids (product #01895) from Ted Pella, Inc. were used for electron microscopy.

███████   Methods

In addition to crystalline titania, amorphous titania was fabricated, characterized, and ultimately embedded in the monomer to create transparent nanocomposites. Amorphous titania was prepared using the sol-gel synthesis method described in Guo et al. [186]. 10 mL of titanium isopropoxide (TTIP) was added dropwise to 33.3 mL absolute ethanol while stirring vigorously. TTIP was added dropwise in 0.5 mL increments (0.5 mL x 20 = 10 mL) at 5 minute intervals. 0.9 mL of concentrated HCl was added in 45 μL increments (45 μl x 20 = 0.9 mL) at 1 minute intervals. Solution remains vigorously stirred for 30 min and sonicated for an additional 30 min. Ethanol and 2.5% concentrated HCl was used as a dispersing agent. This process required slow addition of TTIP in order to create nanoscale titania without agglomeration.

4.6.2   Results & Discussion

███████   Nanoparticle Characterization

   XRD analysis was completed on the dried TiO_2 powder. The material appears to be amorphous as it showed no crystalline peaks (Figure 4-16). TEM and DLS results are shown in Figure 4-17. DLS shows one peak at 2.9 nm in diameter. The primary particle size, analyzed by ImageJ, is 2.3 nm with a standard deviation of 0.35 nm. Compared to TEM results, the hydrodynamic and particle size estimates were very similar, suggesting no evidence of agglomeration, even when dispersed in solution. Some crystallites were present under high magnification; however, the majority of the particles were amorphous.
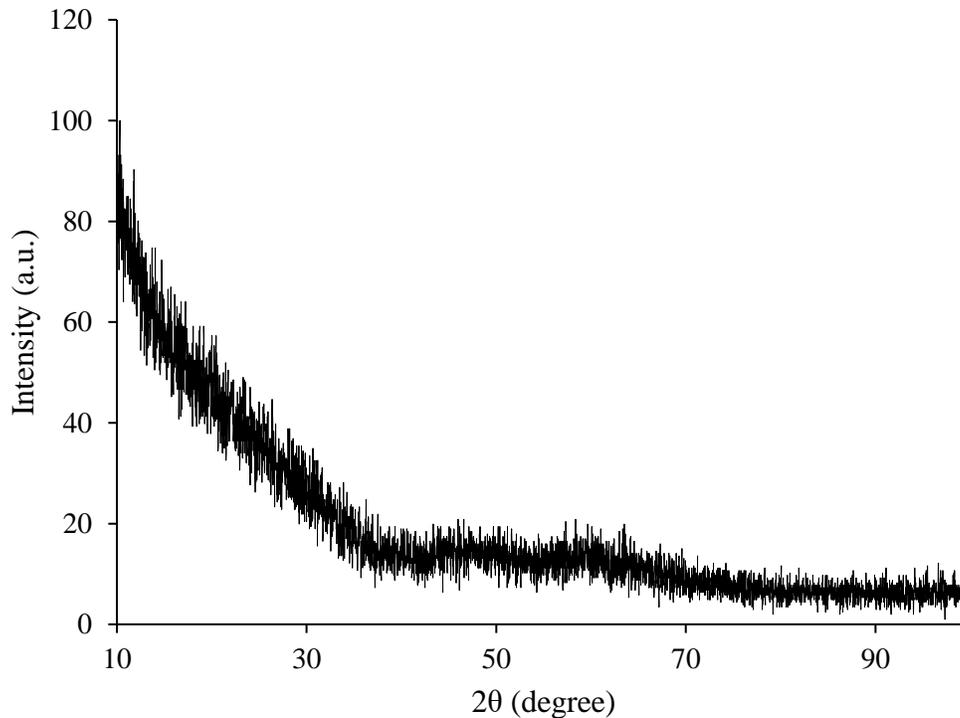
Figure 4-16: XRD of amorphous titania.
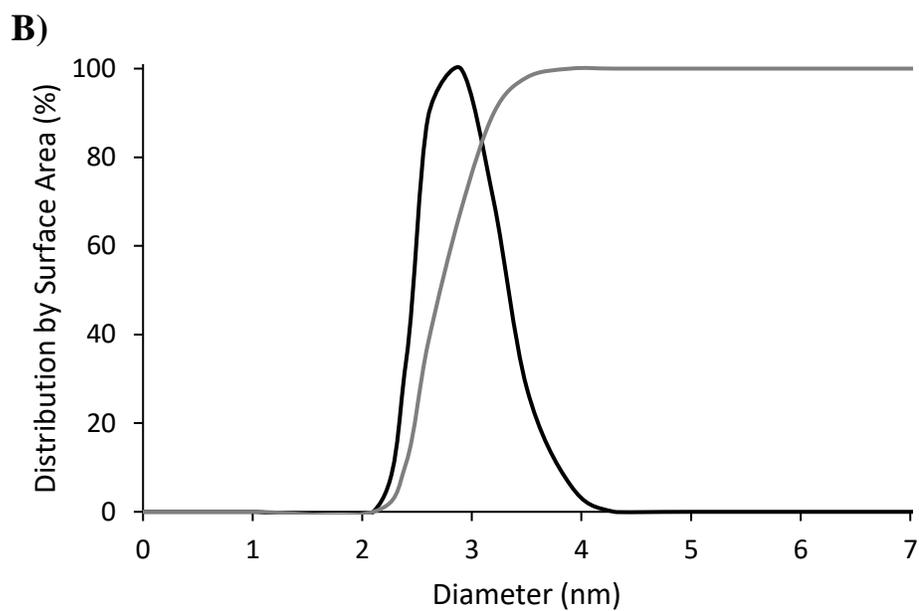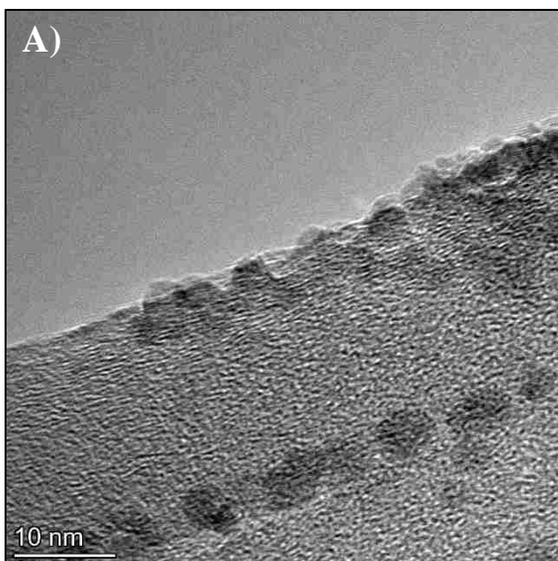
Figure 4-17: TEM and DLS results for amorphous titania: (A) TEM image showing individual TiO_2 particles; (B) DLS distribution by surface area. Black: Distribution; Gray: Cumulative.

TGA results show a 14% weight loss between 100 and 600 °C in Figure 4-18. The particles are uncoated and the FTIR spectrum contains no additional peaks, therefore all weight loss is presumably due to the hydroxyl groups present on the titania surface. The number of hydroxyl groups per nm^2 on the surface of the titania can be calculated based on the weight loss determined from the TGA graph and the average diameter of each particle as determined from TEM using Equation (1-5). According to the expression, approximately 7.49 hydroxyl molecules are present per nm^2. This represents on average 125 hydroxyl molecules per TiO_2 nanoparticle.
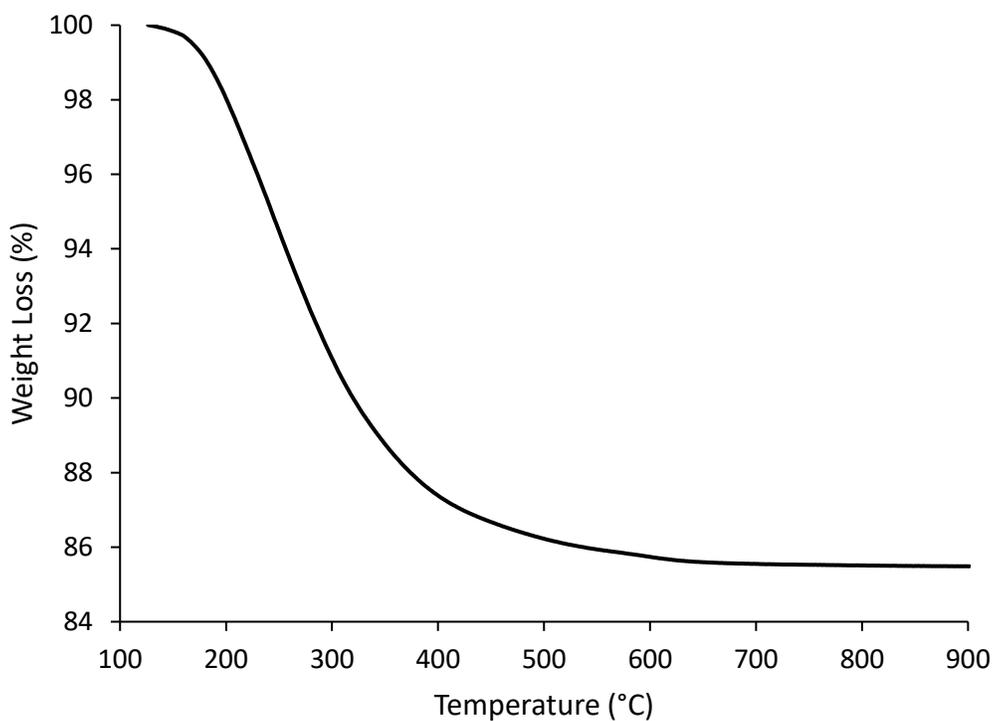
Figure 4-18: TGA of amorphous-titania nanoparticles.

In addition, UV spectroscopy was performed on the amorphous titania nanoparticle dispersion. The amorphous titania absorbs light from a wavelength of 270 to 370 nm, well within the UV spectrum. Four concentrations of TiO_2 are shown in Figure 4-19.
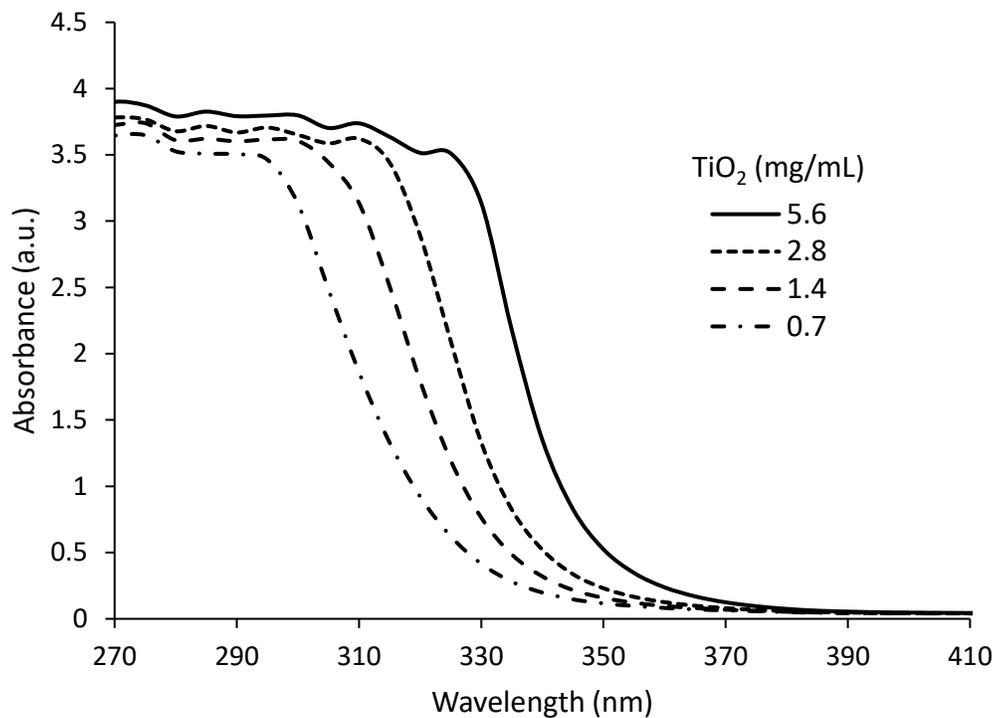
Figure 4-19: The UV light absorbance for amorphous titania nanoparticles.

4.7 Amorphous Titania Nanocomposite Fabrication

### 4.7.1 Experimental

▮▮▮▮▮ Materials

The following chemicals, including their sources, purity, and CAS #s, used in the nanocomposite fabrication were: dipentaerythritol pentaacrylate (SR-399), Sartomer, 100%, 60506-81-2; Irgacure 184, Ciba, 99%, 947-19-3; and ethanol, Decon, 200 proof, 64-17-5.

▮▮▮▮▮ Methods

The amorphous titania nanoparticle dispersion was mixed with SR-399 prior to polymerization using the same experimental procedure as discussed in Section 4.4.1.2. TiO_2 nanocomposites containing 2, 4, 6, and 10 weight percent TiO_2 were prepared and studied. The –OH groups on the surface of the nanoparticles were binding to the monomer unit via a condensation reaction as shown in Figure 4-20. Once thoroughly mixed, and the ethanol evaporated, the monomer/nanoparticle solution was polymerized.
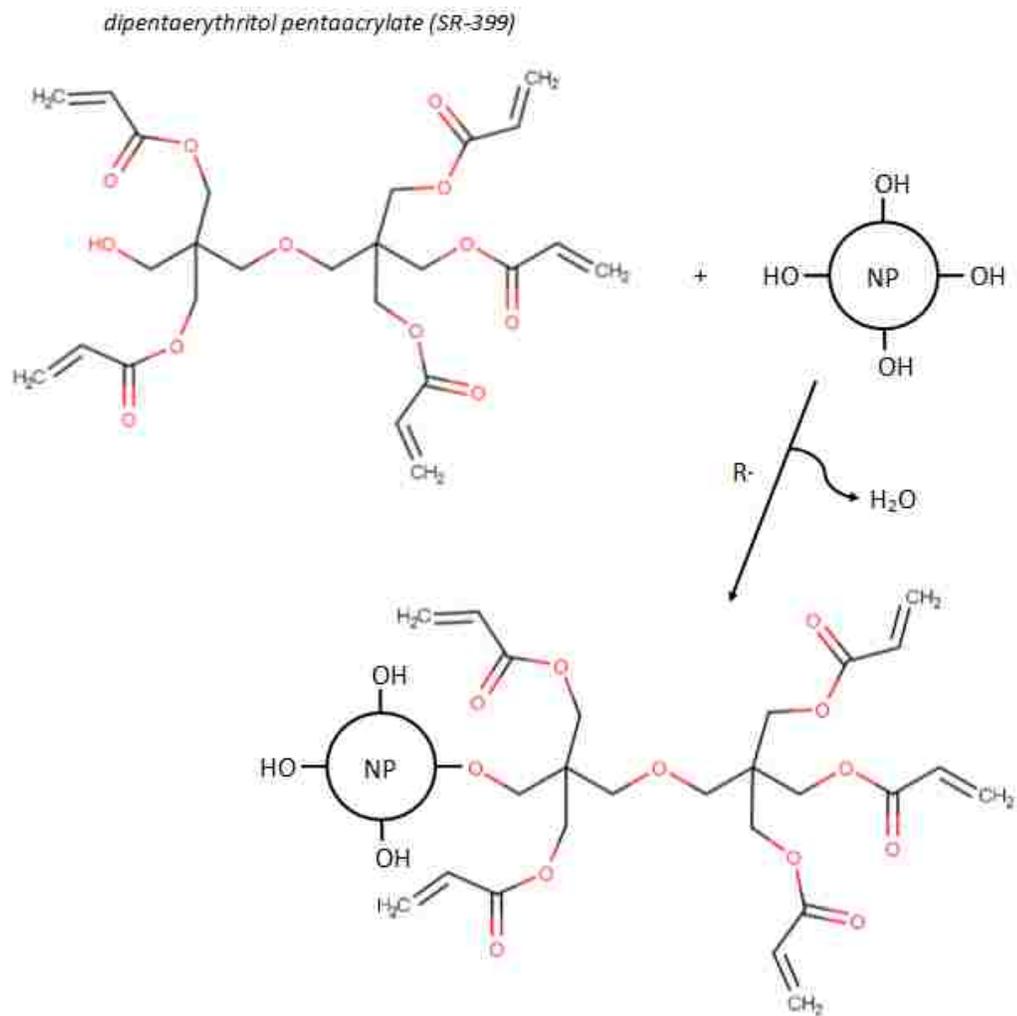
Figure 4-20: Condensation reaction to bond the monomer to the surface of the amorphous titania nanoparticle.

4.7.2 Results & Discussion

██████ Nanocomposites

Upon addition of titania to the monomer, a color change was visually noticeable as shown in Figure 4-21. The monomer itself is colorless; however, as the weight percent of titania increased, the color would transition from clear to yellow to orange. The same would also be true for the resulting polymer. The polymer would still be transparent, but the color would remain yellow-orange. Pigments may be used to alter this color, to either reverse it or to change it to a more pleasing color.

Since titania absorbs a fraction of the UV light emitted from the lamp, the light dose required to create a polymer increased considerably as the titania concentration increased. The light dose was experimentally determined using a photometer at the point when the liquid monomer transitioned into a solid polymer, i.e. the gel point. A linear model best fit the data to approximate the amount of light required to polymerize the titania nanocomposite film with a r-squared value greater than 0.99.
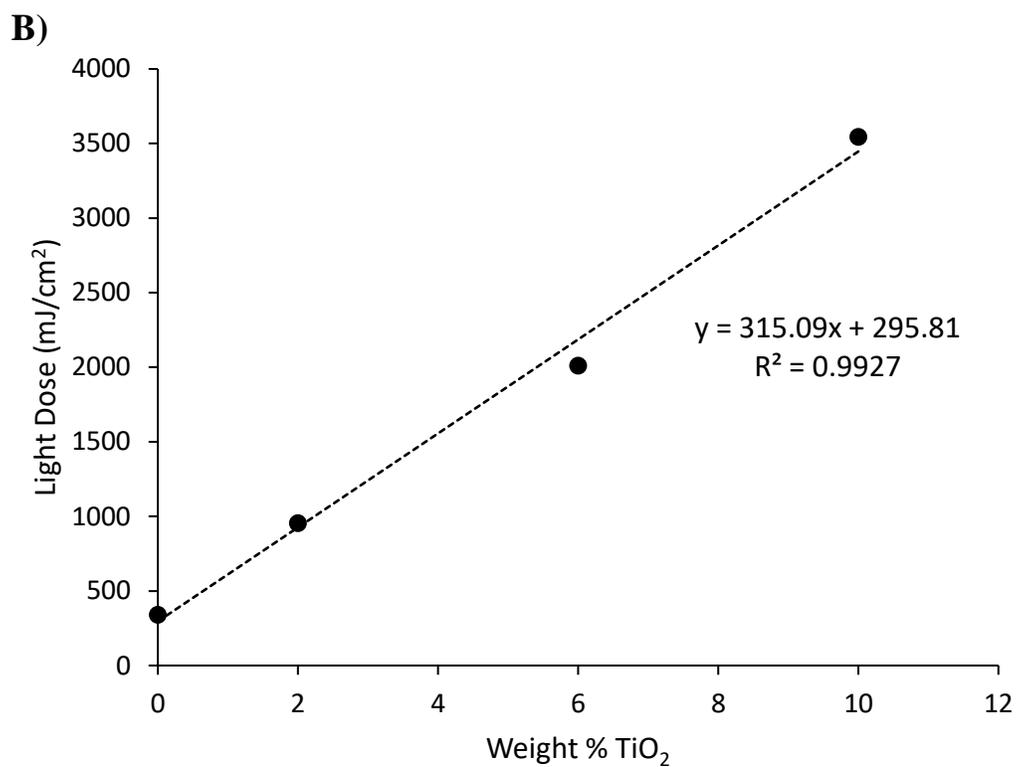
Figure 4-21: (A) The SR-399 monomer mixed with 2, 4, and 6 weight percent amorphous titania nanoparticles, from left to right. (B) The light dose required as a function of weight percent amorphous titania.

■■■■ Refractive Index

Lastly, a liquid refractometer was used to measure the refractive index of the monomer embedded with TiO_2 after evaporation of ethanol. The refractive index is assumed to remain constant during polymerization. The data is compared to the refractive index predicted by the rule of mixtures which is shown in Equation (4-1), where n_c is the refractive index of the composite material, n_m and n_t are the refractive index of the monomer and titania, respectively, and v_m and v_t are the volume fractions of the monomer and titania, respectively.

$$n_c = n_m v_m + n_t v_t \qquad (4\text{-}1)$$

The density and refractive index of SR-399 are 1.192 g/cm^3 and 1.49, respectively. The density and refractive index of amorphous titania are 3.39 g/cm^3 [187] and 2.0 [161], respectively. The density was needed to convert the weight to volume percent. The experimental data follows the rule of mixtures quite well, the data points are within standard error from the predicted value by the rule of mixtures (Figure 4-22).
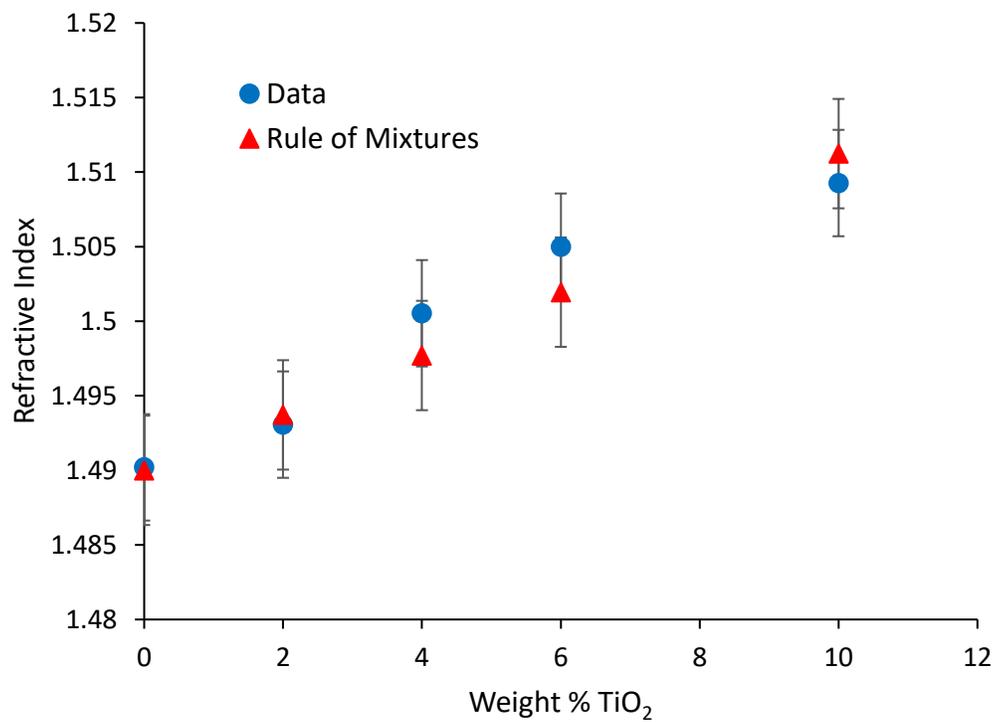
Figure 4-22: Refractive index of the titania nanocomposite measured and predicted by the rule of mixtures.

4.8 Conclusions

This chapter consisted of nanoparticle synthesis, functionalization, and nanocomposite fabrication. Crystalline and amorphous titania nanoparticles were synthesized and embedded in the SR-399 monomer to create nanocomposite films to be used to construct microfluidic chips. Material properties, such as the refractive index, can be altered upon the addition of the titania nanoparticles prior to polymerization. Crystalline TiO_2 functionalized with a surface silane was initially used, however haze was a major issue and visual distortions were present in the resulting nanocomposites. A silicon layer was successfully applied to the surface of the titania nanoparticles, which can be used in future studies to adjust the refractive index and other material properties of the particles themselves. Amorphous titania was later used without any surface modifications to covalently bond the surface hydroxyls to a SR-399 monomer unit. This was completed successfully and a transparent thin film was created. The refractive index of the nanocomposite can be adjusted according to the rule of mixtures; however, a color change from clear to yellow-orange was apparent and the required light dose to polymerize the film increased as the weight percent of titania increased.

5.1   Introduction

The ferrofluid, termed FF-700, used to create channels in the dipentaerythritol pentaacrylate (SR-399) monomer prior to polymerization, as described in Chapter 4, was purchased from Ferrotec. The ferrofluid consists of magnetic nanoparticles dispersed in an aqueous medium. The FF-700 ferrofluid is expensive, therefore the objective was to determine an inexpensive synthesis method to fabricate ferrofluid that can replace the FF-700. Iron oxide nanoparticles were initially synthesized and coated with citric acid, however the coating was minimal and the viscosity of the ferrofluid was too low. Therefore, polyacrylic acid (PAA) was chosen to coat the surface. PAA contains similar functional groups as citric acid. The larger molecules, average molecular weight of 1,800, can sufficiently coat the surface of the iron oxide and theoretically increase the viscosity of the resulting ferrofluid. Ferrofluid was coated by PAA using 1-step and 2-step co-precipitation approaches at different temperatures. PAA has been previously used to coat iron oxide nanoparticles [188-190]. The impact of temperature on particles synthesis, and the stability of the nanoparticles in aqueous media were examined and compared with the commercial ferrofluid (FF-700). The ferrofluid was characterized using the methods as described in Appendix C: Transmission Electron Microscopy (TEM), Dynamic Light Scattering (DLS), Fourier Transform Infrared Spectroscopy (FTIR), Thermogravimetric Analysis (TGA), and X-ray Diffraction (XRD).

5.2 Experimental

5.2.1 Materials

The following chemicals, including their sources, purity, and CAS #s, used in the iron oxide nanoparticle synthesis were: iron(II) chloride tetrahydrate, Alfa Aesar, 98%, 13478-10-9; iron(III) chloride hexahydrate, Alfa Aesar, 97%, 10025-77-1; poly(acrylic acid), Sigma, 9003-01-4; and ammonium hydroxide, Sigma, ACS grade (28% NH_3 in H_2O), 1336-21-6. Lacey carbon, 300 mesh, copper grids (product #01895) from Ted Pella, Inc. were used for electron microscopy. Dialysis tubing from Ward's Science (product #s 470163-404 & 470163-408) with a MWCO of 12-14 kDa was used for dialysis against DI water.

5.2.2 Methods

The iron oxide nanoparticles were obtained by following the method described in Frimpong et al. [191]. Salts of 0.8 g $FeCl_2$-$4H_2O$ and 2.2 g $FeCl_3$-$6H_2O$ (1:2 molar ratio) were dissolved in 40 mL DI water, and followed by adding 5 ml NH_4OH (28% w/w) at the set reaction temperatures with constant stirring in order for the nanoparticles to precipitate as shown by the chemical reaction below:

$$FeCl_2 \cdot 4H_2O + 2[FeCl_3 \cdot 6H_2O] + 8NH_4OH \rightarrow Fe_3O_4 + 20H_2O + 8NH_4Cl$$

An inert gas, nitrogen, was purged with the reaction mixture to prevent oxidation. The coating was carried out in two separate methods, 1-step and 2-step approaches. In the 1-step approach, the nanoparticles were coated by adding PAA, 1,800 MW, in which 25%

w/w of PAA was measured with respect to Fe(II) salt [192]. PAA was immediately added preceding the mixture precipitation with NH_4OH, and stirred for one hour. The final dispersion was then dialyzed against deionized water to remove excess salts. The deionized water was changed every 24 hours for two days. The nanoparticles in the 1-step approach were synthesized at room temperature and 80 ℃. For the 2-step approach, 800 mg of the dried uncoated particles were dispersed in 20 ml DI water by ultrasonication. The mixture was heated to the set temperatures followed by addition of 4 ml PAA and reacting for one hour. In the 2-step approach, the reaction synthesis was done at room temperature, 60 ℃, and 80 ℃. The dispersion was then allowed to cool, and dried. The synthesis conditions of samples 1-RT and 1-80 were synthesized in the 1-step approach, and samples 2-RT/RT, 2-60/60, 2-80/80, 2-80/RT obtained by the 2-step approach are shown in Table 5-1. Samples of uncoated, U-RT and U-80, and citric acid coated, 1-CA, iron oxide nanoparticles were prepared as controls.

Table 5-1: The synthesis conditions of both approaches in which the iron oxide nanoparticles were coated with PAA and citric acid, FF-700, and uncoated.

Nomenclature	Synth Temp (°C)	Coating Temp (°C)	Reaction Type
1-CA	80		
1-RT	RT		1-step
1-80	80		
2-RT-RT	RT	RT	
2-60-60	60	60	
2-80-80	80	80	2-step
2-80-RT	80	RT	
U-RT	RT	-	
U-80	80	-	Uncoated
FF-700	-	-	Commercial

5.3 Results & Discussion

5.3.1 Commercial Ferrofluid Size & Morphology

The FF-700 ferrofluid, purchased from Ferrotec, was initally characterized to determine the surfactant chemical composition and weight percent. The particles were dried onto a lacey carbon copper TEM grid to determine particle size and morphology. ImageJ was used to measure the diameter of each particle in order to obtain a size distribution of the iron oxide particles. Approximately 114 particles were measured and the mean diameter is 15.48 nm with a standard deviation of 3.16 nm, the results fitted to a normal distribution are shown in Figure 5-1. The particles are crystalline as shown by the TEM images (Figure 5-2), and appear to be spherical in shape. EDS confirms the presence of iron and oxygen in the sample.
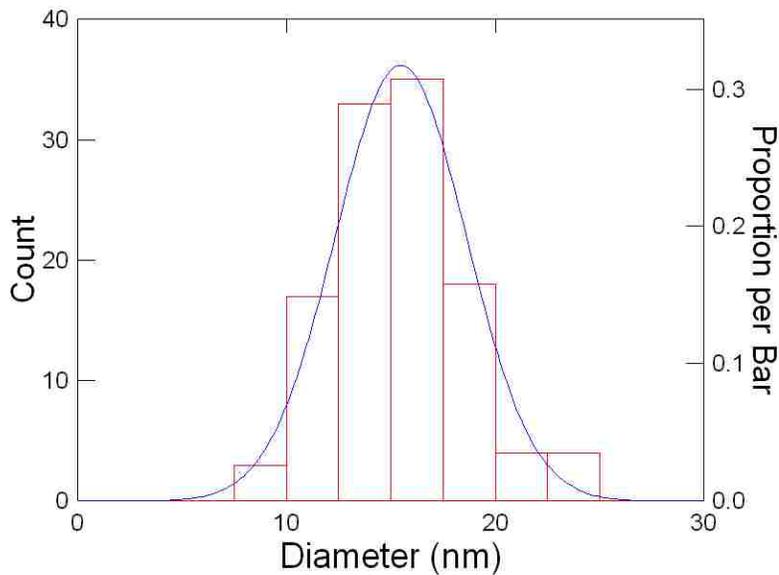
Figure 5-1: Normal distribution of the FF-700 ferrofluid with fitted Gaussian parameters.
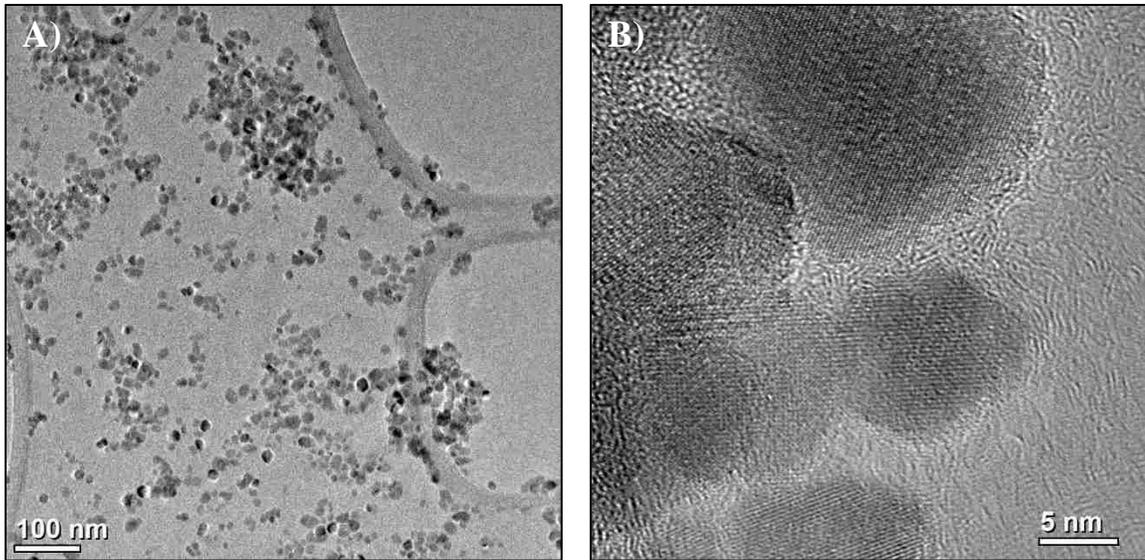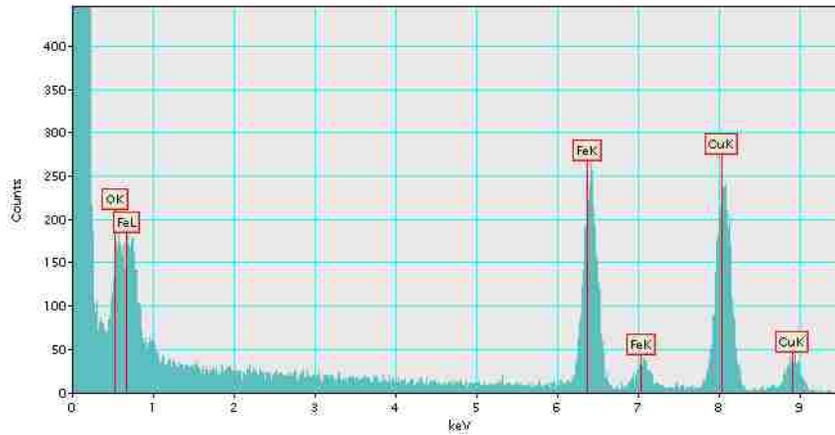
Figure 5-2: TEM images of the FF-700 nanoparticles. (A) This low magnification image shows well dispersed individual particles approximately 15.5 nm in diameter. (B) This high magnification image shows the crystallinity of each particle. (C) EDS spectrum of the FF-700 ferrofluid on a copper TEM grid.

5.3.2 Polyacrylic Acid Coated Magnetite Nanoparticles

███████   Particle Size & Morphology

TEM was completed on 1-RT, 1-80, U-80, and 2-80-80. The idea was to minimalize the samples needed to image by TEM. Visually, the 2-step samples would settle which is undesirable. Therefore, only one of the four samples were chosen for TEM. Also, only one uncoated sample was chosen. The results are shown in Table 5-2.

On average, all samples prepared with PAA were equal in size to the FF-700 particles, except for the 1-RT samples, which were nearly one-third the size of the others. The 1-RT and 2-80-80 samples were largely agglomerated, and the U-80 partially agglomerated, while the 1-80 and the FF-700 were well dispersed and separated from their neighboring particles. This proves that a similar product was obtained that can be well-dispersed in an aqueous environment. The TEM images are shown in Figure 5-3.

Table 5-2: The particle size analysis of PAA-coated iron oxide particles compared to the uncoated and FF-700 particles.

ImageJ/TEM Analysis					
	1-RT	**1-80**	**2-80-80**	**U-80**	**FF-700**
AVG (Est. Diameter) (nm)	4.50	17.25	15.44	13.26	15.48
SD (nm)	0.64	6.70	3.51	3.10	3.16
Min (nm)	3.50	8.89	8.48	7.84	8.49
Max (nm)	6.19	35.42	25.46	19.83	24.00
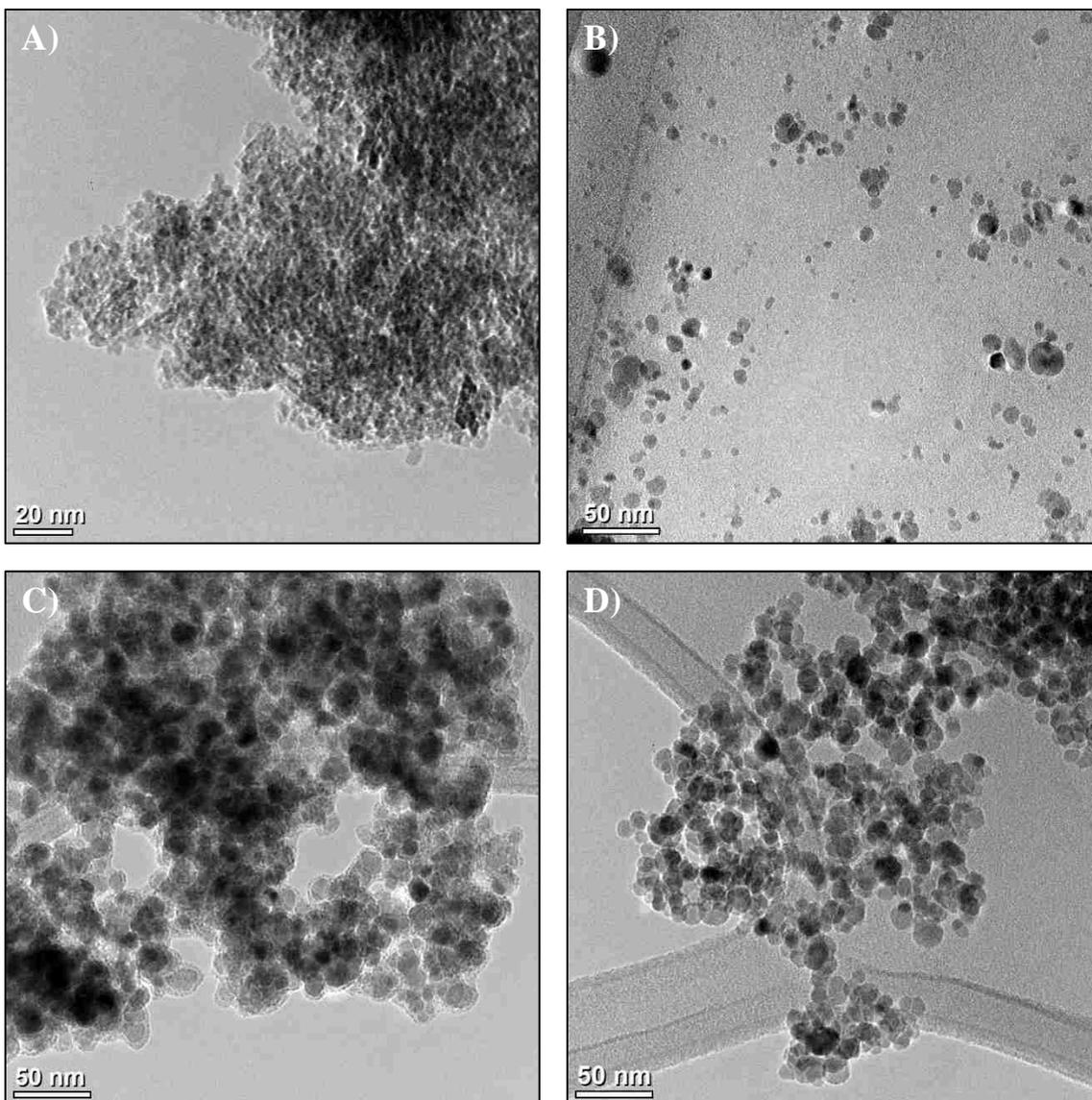
Figure 5-3: TEM images of PAA-coated iron oxide nanoparticles: (A) 1-RT, (B) 1-80, (C) 2-80-80, and (D) U-80.

DLS was completed to compare the hydrodynamic size distributions among all the samples and to the FF-700 (Figure 5-4). The (B) 1-CA ferrofluid was nearly an exact replica of the commercial (A) FF-700; both the FF-700 and 1-CA samples peaked at just below 50 nm. Slightly larger were the (F) 1-80, (C) U-RT, and (D) U-80 samples with an average 1st peak at ~150 nm. This matches the TEM images well, since the 1-80 and the U-80 samples showed no/partial agglomeration. Therefore, the hydrodynamic diameter was also expected to be low. The largest were all four of the (G-J) 2-step samples and (E) 1-RT. These samples showed particles sized in the micron range; settling would also occur in these samples. The 2-step sample (2-80-80) and 1-RT also contained large agglomerates in TEM which translated to large hydrodynamic diameters as shown by DLS.

Diameter (nm)

143
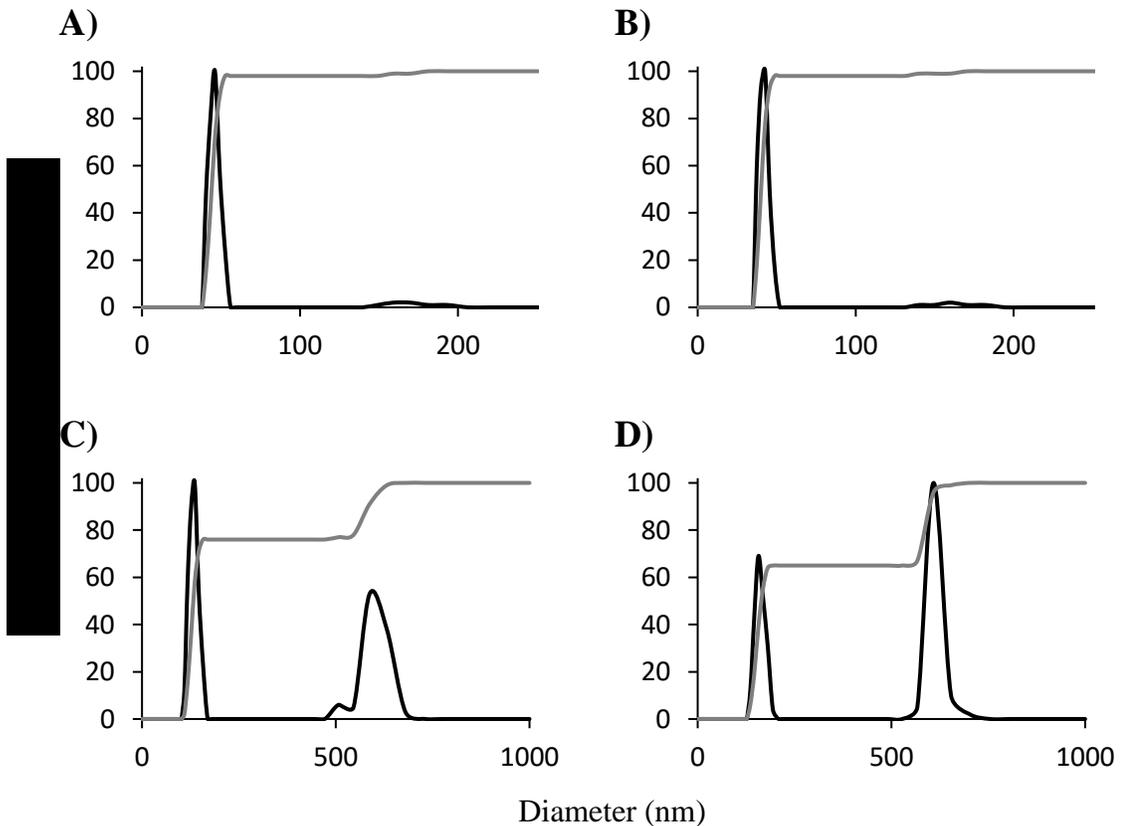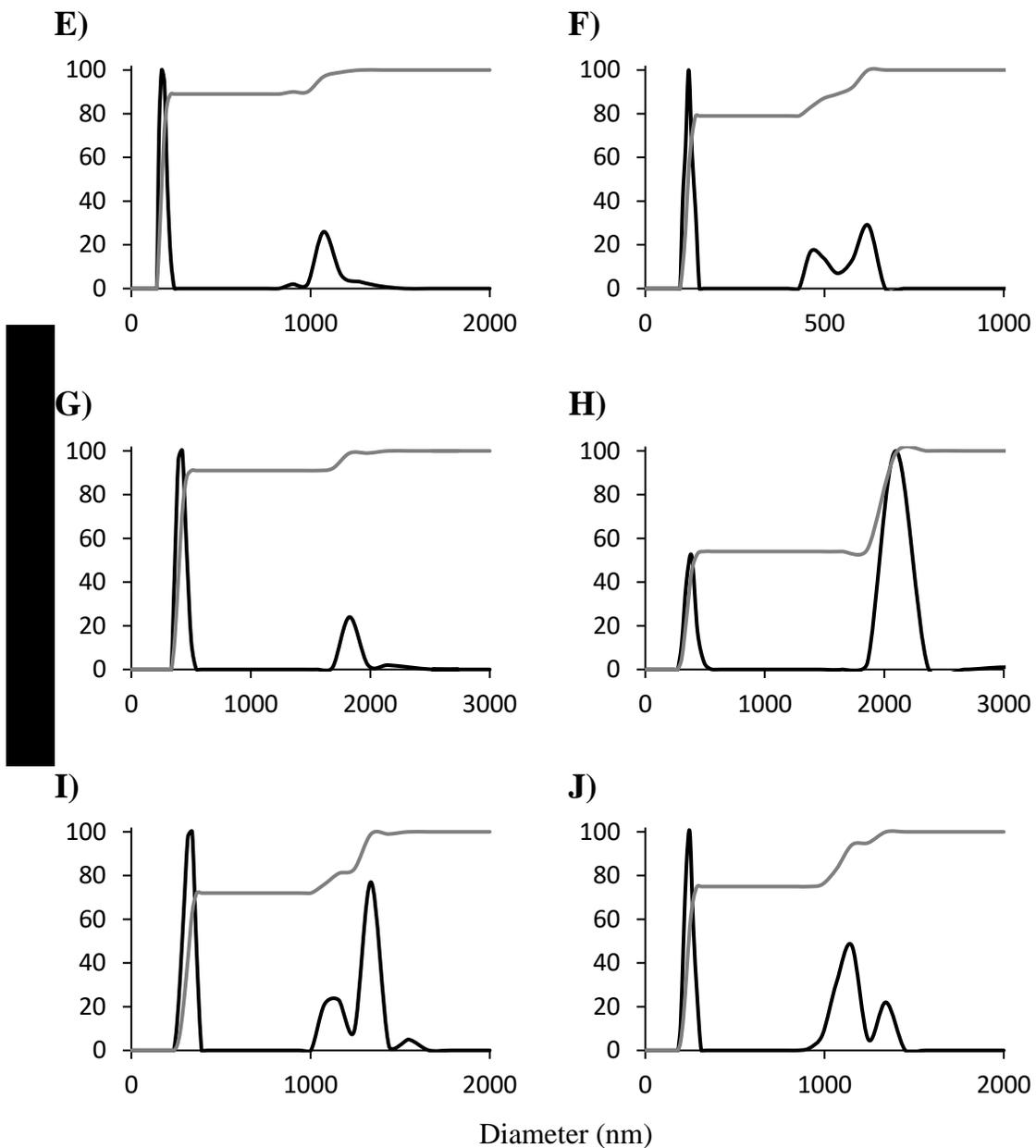
Figure 5-4: DLS results for the ferrofluid samples. Black: Distribution, Gray: Cumulative. (A) FF-700; (B) 1-CA; (C) U-RT; (D) U-80; (E) 1-RT; (F) 1-80; (G) 2-RT-RT; (H) 2-60-60; (I) 2-80-80; and (J) 2-80-RT.

From the FTIR spectra, the peaks shown in Figure 5-5A identify the presence of PAA on the surface of the nanoparticles obtained using both the 1-step and 2-step approaches. The carbonyl stretching is observed between 1300-1800 cm^{-1} (dashed lines) by distinct peaks that correspond to the carboxylic acid functional groups shown in the chemical structure of PAA and citric acid [190, 191]. The peaks of the samples prepared by the 2-step approach are more definitive than those from the 1-step approach, perhaps due to increased coating thicknesses. 1-CA appears to be very similar to the FF-700. However, the peak at approximately 1097 cm^{-1} is only present in the FF-700 which means that an additional surface group is present other than compounds containing the carboxylic acid functional group. The uncoated and 1-step coated samples also appear to be similar, but this can be misleading without also examining the TGA results.

TGA results were analyzed and shown in Figure 5-5B. The percent loss is greatest in the samples that were obtained from the 2-step approach, and also increases with increased coating temperature. However, in the 1-step approach the percent loss of coating was opposite and decreases with increased coating temperature. Therefore, the difference in coatings with temperature could be a reason for the dependence of surface ligand dynamics in nanocrystals growth [191]. Sample 1-80 and 2-80-80 were synthesized at the same temperature, but have drastically different percent coatings, nearly a 15% difference. Thus, using the 2-step approach gives a wide coating coverage in particles. In comparison between the obtained particles coated with PAA and FF-700, it seems that FF-700 was likely synthesized by using the 1-step approach since they have roughly the same percent coating. The uncoated and citric acid coated samples had very little weight loss. Since 1-

CA and FF-700 had similar FTIR spectra, it is likely that FF-700 was coated with citric acid and/or PAA, but additional surface moieties are likely present due to additional FTIR peaks and the larger percent coating on FF-700.

Coating thicknesses for each sample using the diameter determined by TEM were computed by taking into account the weight loss from TGA using Equation (1-5). Assuming volume was additive to compute a theoretical particle density, the coating thickness for 1-RT, 1-80, FF-700, and 2-80-80 was 0.5, 1.5, 1.9, and 2.4 nm, respectively. Although the total weight losses for 1-RT and FF-700 were equivalent, the smaller particle diameter for 1-RT played a significant role in reducing the thickness of the coating per particle. In addition, the average volume of a PAA molecule was calculated and compared to the surface area of each particle. 1-RT was determined to have a monolayer coating, while the other three had multilayer coatings, due to the larger primary particles. The coating thicknesses for 1-80, FF-700, and 2-80-80 are ranked from smallest to largest similar to how they are shown in the graphical TGA results.
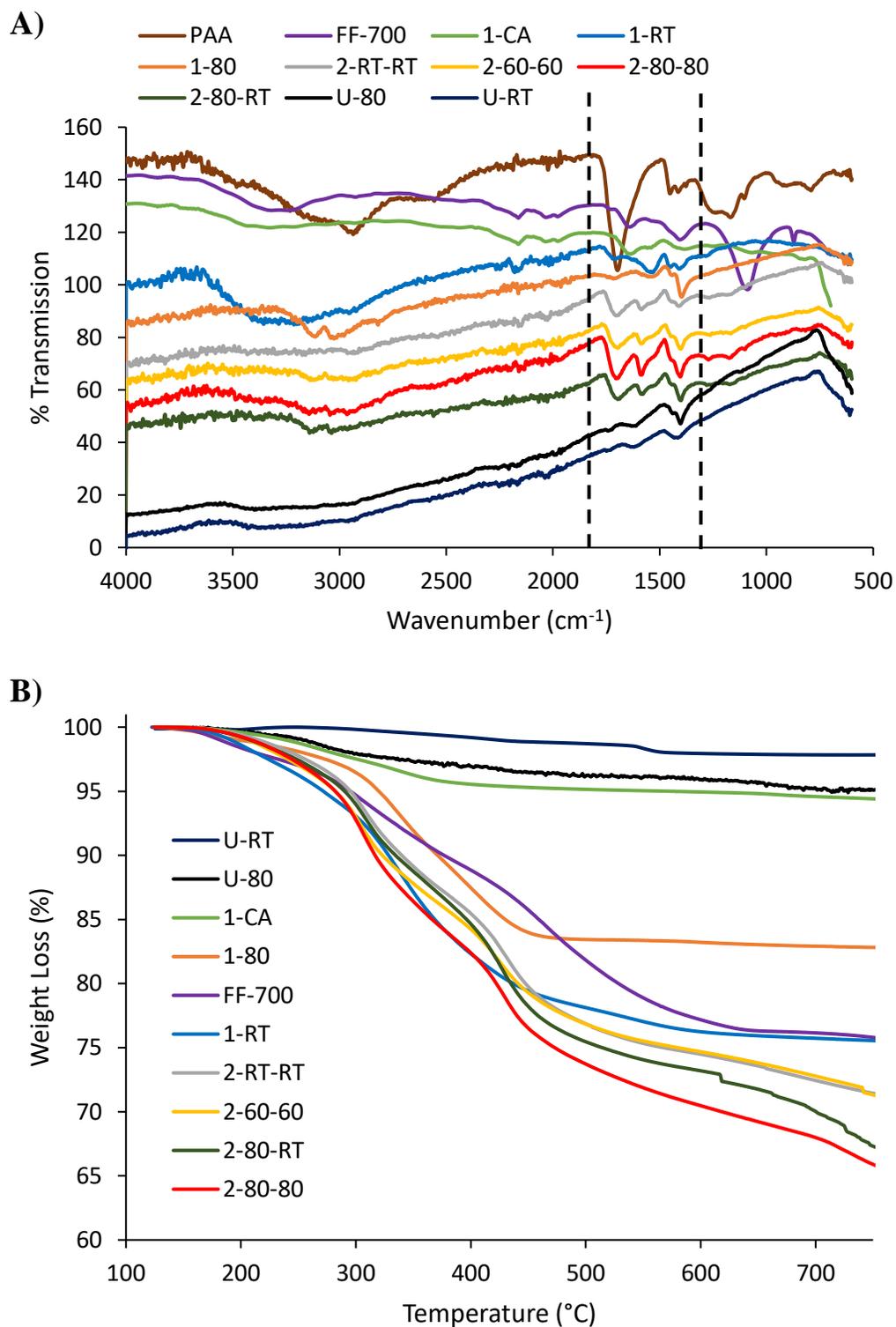
Figure 5-5: (A) FTIR spectra for the ferrofluid samples and pure PAA. The dashed lines are marking the carbonyl stretching range, which is observed between 1300-1800 cm^{-1}. (B) TGA weight loss for the ferrofluid samples.

147

■■■■ Crystalline Structure

The XRD of the iron oxide particles was completed to determine the crystal structure of the particles. All samples' diffraction peaks are consistent with that of magnetite (Fe_3O_4) particles. Peaks at 31°, 36°, 44°, 54°, 58°, and 63° depict magnetite (JCPDS card no. 79-0417) [193]. One sample from each group is shown in Figure 5-6. The average particle size for all 4 samples was estimated to be 11.6 nm using the Debye-Scherrer formula [Equation (1-2)]. This result is slightly smaller than the particle size measurement from TEM images, but still well within the total range of the sample size.
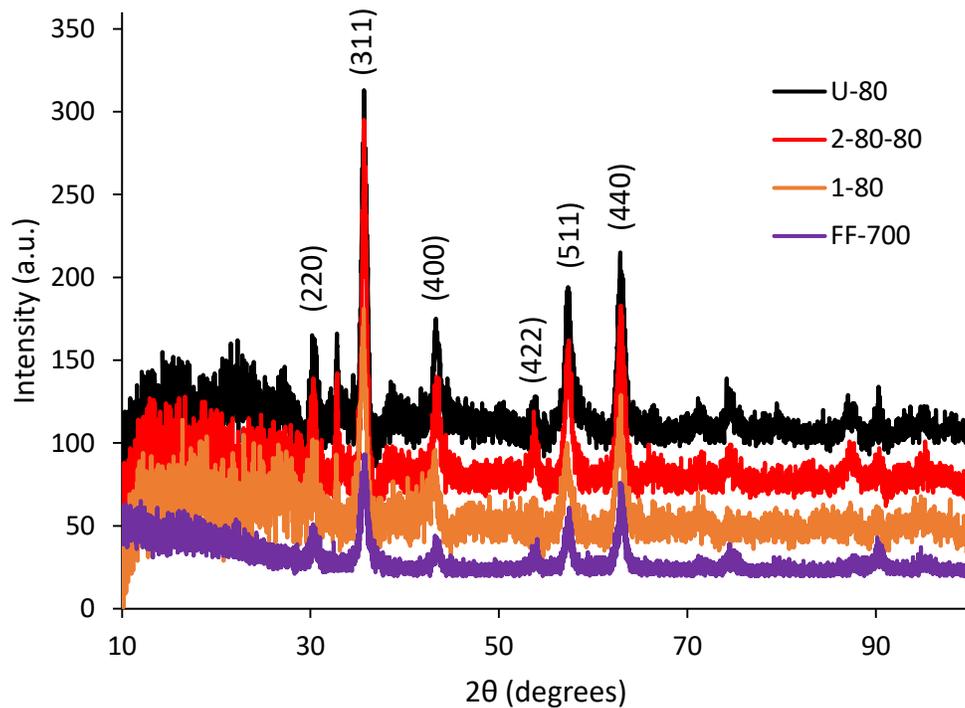
Figure 5-6: XRD of ferrofluid with labeled crystal planes (JCPDS card no. 79-0417).

5.4   Conclusions

PAA-coated iron oxide nanoparticles were synthesized with the intention to replace the commercially available FF-700 ferrofluid to be used in the microfluidic chip manufacturing process (Figure 4-2). The citric acid coated sample (1-CA) did not sufficiently coat the nanoparticle surface. Both 1-step and 2-step co-precipitation approaches were utilized to coat the surface of iron oxide nanoparticles with PAA which are altered by adjusting the synthesis and coating temperatures. This can lead to differences in size and surface properties of the resulting magnetite nanoparticles. The adsorption rates of PAA onto nanoparticle surfaces were noticed to increase with the increased temperature for the 2-step approach. The 2-step approach particles also contained large agglomerates which were confirmed by TEM and DLS. On the other hand, the 1-step approach particles were stable, i.e. have a long shelf life, and do not precipitate. These particles also showed sufficient surface coating from TGA. Therefore, the 1-step approach is suggested to be suitable to generate nanoparticles for replacement of FF-700.

6.1 Introduction

6.1.1 Background

Polymeric thin films have a variety of applications [195]: protective coatings or barriers [196, 197]; optical filters for adjustments of a substrate [198, 199]; biocompatibility of medical devices and drug delivery [200-202]; bioactive interfaces for environmental response [203-206]; membrane fabrication [207]; and microfluidic devices [156]. In each of these applications, targets for the mechanical properties of the coatings and/or films are provided by the manufacturer, but have not been linked with the degree of polymerization required to achieve these. The monomer conversion is directly associated with the energy demand of the photopolymerization process, providing a path to understand the connection between energy applied and resulting mechanical properties.

The degree of polymerization of a multifunctional monomer depends on the photoinitiator, the incident light on the film and its total energy, the resultant polymerization rate, and manufacturing time. A low crosslinking density results in a significantly low modulus, which could be disastrous if the system is expected to hold a load. For the application of microfluidics, strong but not brittle films are generally

preferred, and the manufacturing system must be designed to achieve the required strength. The example product explored in this study is a photopolymerized microfluidics chip that is to be manufactured in large numbers with a flexible manufacturing system. The chip has dimensions similar to those of a microscope slide. The chip manufacturer's vision is to generate chips to order with cycle times under a minute. The monomer pool is supported in a mold, and an ultraviolet (UV) light source is expected to provide a top–down source of energy. A multifunctional acrylate with a photoinitiator is used in order to reach the gel point of the system at low percentage conversions of carbon–carbon double bonds (C=C) while achieving a high modulus for the cured film.

The gel point is based on the fraction of C=C bonds and can determine the mechanical properties of a polymer. Various methods including Fourier transform infrared spectroscopy (FTIR), magnetic resonance imaging (MRI), and confocal Raman microspectroscopy (CRM) have been used to determine the fraction of converted C=C bonds. Geng et al. [208] and Ellis et al. [209] used FTIR to determine the degree of polymerization, or C=C conversion. However, in the sample acrylate system, C=C adsorption bands overlap with other peaks in the spectrum, making FTIR a less than ideal technique to quantify the C=C conversion rate. Wallin et al. [210] used MRI to measure the change of the polymer mobility as it transitions from a liquid (monomer) state to a rubber or solid (polymer) state, as shown by the spin–spin relaxation time. Their model predicted the extent of crosslinking via C=C concentration as a function of depth in the sample. However, MRI was carried out over long-time scales (hours), and UV photopolymerization occurs very rapidly (seconds). Using CRM, Nichols et al. [211] measured C=C bonds as a function of film depth and number of passes through an UV

chamber. In addition, Marton et al. [212] and Oyman et al. [213] measured the C=C consumption as a function of film depth and drying time of an alkyd coating. Mirone et al. [214] also used CRM to measure the C=C concentration and performed tensile tests on various film thicknesses to measure Young's modulus as a function of drying time; further, Mirone et al. correlated the CRM results with the Young's modulus, which is a function of film depth. Raman spectroscopy has been shown to be very effective for depth profiling of thin film coatings [215, 216], and it was determined to be the optimal method for testing. Rodriguez et al. [217] used the Raman spectra of a two-component, solvent-based polymeric coating to study drying kinetics and segregation. Sturdy et al. [218] used Raman spectroscopy to track the changes of the mechanical property of an alkyd film during drying.

Nanoindentation is a localized technique to measure local mechanical properties of a material including Young's modulus and indentation hardness. For example, Comte and Von Stebut [219] used nanoindentation and scanning acoustic microscopy to measure Young's modulus and the Poisson ratio of fused silica and pure aluminum. Geng et al. [208, 220, 221] performed nanoindentation tests on thin film polymers and observed a change in the reduced contact modulus of polymers as a function of indentation load and penetration depth; further, Geng et al. developed an elastic model to estimate interfacial strength between the coating and substrate.

6.1.2   Polymerization Mechanism

Quantitative information regarding the degree of polymerization of thin films generated by free radical photopolymerization is crucial to predicting material properties. SR-399 (dipentaerythritol pentaacrylate) is a viscous, fast cure, low skin irritant monomer that contains five C=C bonds, giving a C=C bond conversion at the gel point of 25% as determined by the generalized Flory-Stockmayer theory. It is a hard, flexible polymer, and also resistant to abrasion. It can be used as a sealant, binder, coating, and as a paint additive. The photoinitiator used is Irgacure 184 (1-hydroxy cyclohexyl phenyl ketone). The polymerization mechanism is summarized in Figure 6-1. In the initiation step, Irgacure 184 dissociates into free radicals upon application of UV light; these radicals initiate the polymerization reaction with the SR-399 monomer. The reaction is terminated by either combination or disproportionation. These mechanisms form an essential aspect of the model to determine C=C conversion, which can then be compared to the experimental results using Raman spectroscopy and nanoindentation.
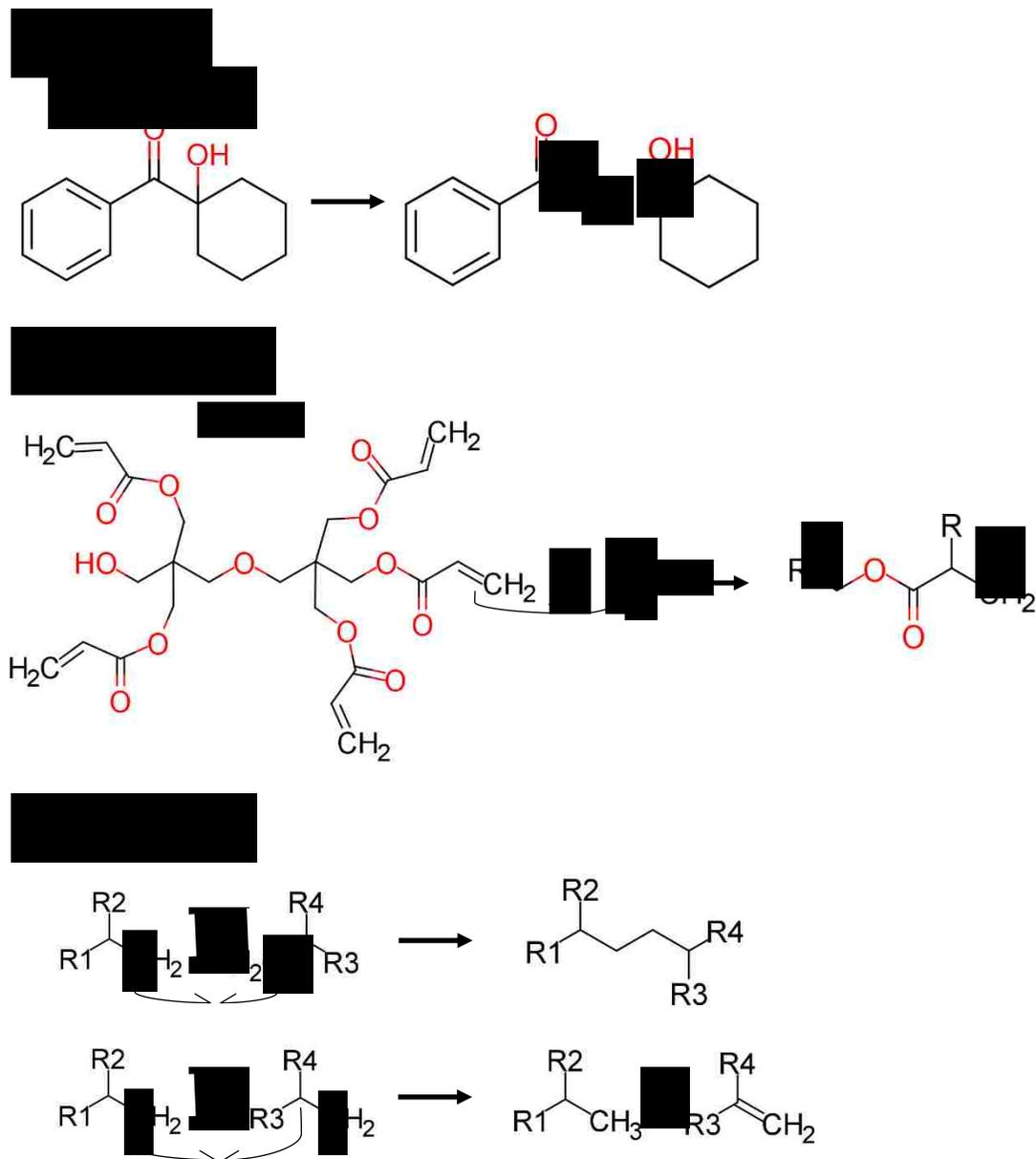
Figure 6-1: Polymerization mechanism of SR-399 with Irgacure 184 photoinitiator.

6.1.3 Project Work Flow

The developed model combines polymerization rate laws with the Beer–Lambert law to predict the conversion gradient along the film depth. A set of equations describing the polymerization of the thin film generates the C=C concentration as a function of time and depth. Polymerization coefficients were tuned to minimize the errors between the model and the Raman data. The model predictions for the C=C levels as a function of depth and light dose were correlated with the mechanical properties using a simple power law. The steps of the modeling procedure are described by the flow chart in Figure 6-2.

Raman microspectroscopy can be applied to measure the C=C consumption, which thus gives a prediction of the degree of crosslinking of the resulting polymer. The C=C composition is expected to change as a function of film depth as the transmission of light dose decreases. Mechanical properties can be measured by nanoindentation as a function of the depth of the film. Figure 6-3 shows schematically a cross section of the polymer. Measurements were taken at points every 50 microns from the top to bottom surface.
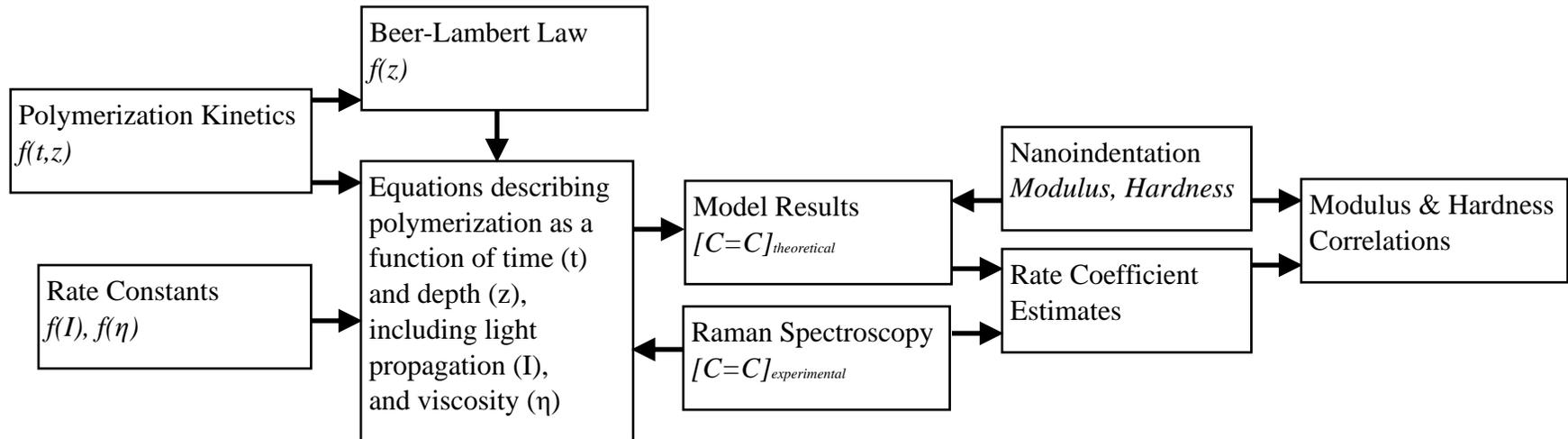
Figure 6-2: Flow chart of the modeling procedure. Structure similar to that of Mirone et al. [214].
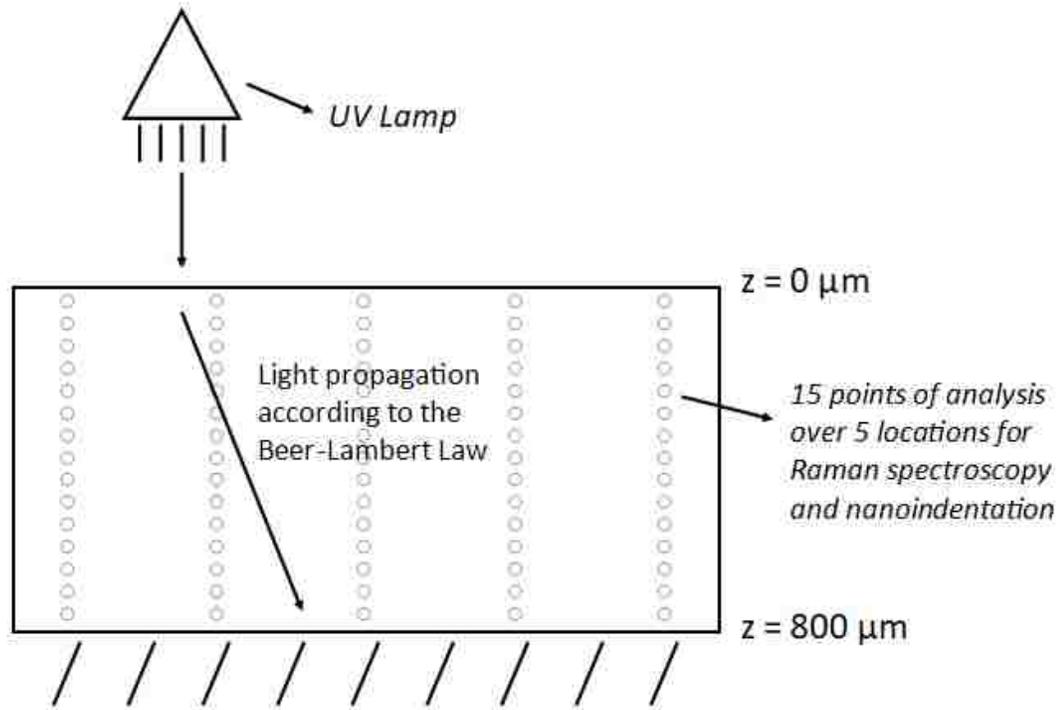
Figure 6-3: Schematic of the polymer film and the locations of each point of measurement.

6.1.4 Polymerization Model

The Beer–Lambert law can be used to predict UV light intensity as a function of the depth in a sample. This law is then combined with the initiator degradation equation to predict the amount of free radicals formed as a function of the depth. Equations (6-1) and (6-2) show the light intensity and adsorption as a function of: I, light intensity; z, the depth in the sample; α, absorption coefficient; ε, molar absorptivity; and c_i, the concentration of each species, i. The molar absorptivity of the monomer and photoinitiator was estimated from the literature to be 86.2 and 940 m^2/mol, respectively [157].

$$\frac{dI}{dz} = -\alpha(z)I \tag{6-1}$$

$$\alpha(z) = \sum_i^n \varepsilon_i c_i(z) \tag{6-2}$$

The rate constant for the decomposition of initiator is dependent on the light intensity. Therefore, the decomposition rate for the initiator is a function of the depth. The typical rate laws for a chain-growth polymerization are solved at each of the analyzed depths in the film [Equations (6-3)-(6-5)]. A key assumption is that the consumption rate of initiator is much faster than its diffusion rate into the film. The rate laws for each species, photoinitiator, monomer, and free radicals are:

$$\frac{d[PI]}{dt} = -fk_I(\lambda)[PI] \tag{6-3}$$

$$\frac{d[M]}{dt} = -k_P[M][R^*] \tag{6-4}$$

$$\frac{d[R^*]}{dt} = 2fk_I(\lambda)[PI] - 2k_T[R^*]^2 \tag{6-5}$$

The rate constants, k_I, k_P, and k_T are associated with the initiation, propagation, and termination steps of the chain-growth polymerization; [PI], [M], and [R*] are the concentrations of photoinitiator, monomer, and free radicals, respectively; f is the initiator efficiency factor [222-226]. Low oxygen inhibition is observed in viscous monomers and is therefore neglected from the rate model [227].

The predictions of the monomer conversion and crosslinking are correlated with local mechanical and optical properties for the purpose of establishing the connection between mechanical properties and chemical structure. This is one of the first studies linking thin film chemistry to physical performance, which is crucial when applying the technology to the part manufacturing. A model predicting the mechanical properties of the degree of polymerization, C=C composition, as a function of film depth and light dose is developed.

6.2 Experimental

6.2.1 Materials

The following chemicals, including their sources, purity, and CAS #s, used were: dipentaerythritol pentaacrylate (SR-399), Sartomer, 100%, 60506-81-2; and Irgacure 184, Ciba, 99%, 947-19-3.

6.2.2 Methods

A mixture of SR-399 and Irgacure 184 (2% by weight) was prepared and photopolymerized by a 50 mW/cm^2 UV lamp held at 7.5, 10, 12.5, and 15 seconds. SR-399 is a pentaacrylate with a cured modulus of 4.04 GPa (per the manufacturer). SR-399 was supplied by Sartomer Americas and Irgacure 184 from Ciba Inc. The Dymax 5000-EC UV curing lamp with a metal halide bulb generates multiple peaks between 260- and 460-nm wavelengths. Each chip volume was filled with monomer so that the final film would be approximately 800 microns thick. After photopolymerization, each of the four samples were cut in cross section, mounted with the cut face up in a two-part epoxy, and polished prior to performing the measurements. Measurements were taken every 50 microns over the cross section at five different locations along the length of the film. Each of the five measurements at the corresponding locations/depths for Raman and nanoindentation was then averaged. The depth of the film was labeled using the z-axis with the top surface, z = 0 μm, and the bottom surface, z = 800 μm (Figure 6-3).

6.2.3 Techniques

The Raman spectra of the thin films were analyzed on a Thermo Fisher Scientific DXR Raman microscope. It was equipped with an Olympus brand microscope and a 10x working distance objective. A 780-nm Raman laser with the power set to 10.0 mW was used for sample analysis. The spot size of the laser beam was 3.1 μm. All Raman spectra were collected in a spectral range of 3400–50 cm^{-1}. Each Raman spectrum was an average of five accumulations consisting of 5 seconds each. OMNIC 8 software (Thermo Fisher Scientific Inc.) was used to acquire the Raman spectra and produce the chemical mapping at each location. The peak height of the C=C bond adsorption at 1637 cm^{-1} was used to monitor the degree of crosslinking [211, 228]. The peak height of an aliphatic ester is present at 1734 cm^{-1} which was used as an internal standard [229].

The nanoindentation tests were performed with a diamond Berkovich indenter (tip radius of 200 nm) using the Nanoindenter G200 (Agilent Technologies) in an argon-filled glovebox. The displacement-controlled mode was used with a strain rate of 0.05 s^{-1} and a maximum depth of 1800 nm. The indenter was held for 10 seconds at the maximum load, and the maximum allowable drift rate was set at 0.5 nm/s. The elastic modulus and hardness were determined using the Oliver–Pharr method [230]. Thermal drift was assessed by holding the indenter in position when 10% of the maximum load was reached on the load removal side.

BioTek Synergy 2 Plate Reader was used to perform UV spectroscopy. The spectra were collected from a wavelength range of 270–410 nm at a step rate of 5 nm. Each spectrum was an average of three total replications at each concentration.

6.3 Results & Discussion

The Raman spectroscopy data are discussed, followed by detailed information on the polymerization model as a function of the film depth. The nanoindentation data were then matched to the Raman results, and the calculated C=C concentrations were correlated with the measured moduli and hardnesses, linking the chemistry with mechanical properties. The light dose at each polymerization time was determined to be 399, 537, 672, and 804 mJ/cm^2 at a time of 7.5, 10, 12.5, and 15 seconds, respectively.

6.3.1 Raman Spectroscopy

Raman spectra were initially taken for the fully cured polymer and the uncured monomer (Figure 6-4). The two peaks of interest are indicated by arrows in the uncured monomer spectrum. The C=C peak (1637 cm^{-1}) is a direct measure of the C=C concentration in the sample. However, peak ratios must be obtained of C=C in relation to another peak unaffected by polymerization. In this case, the aliphatic ester peak (1734 cm^{-1}) was used as an internal standard. Using the aliphatic ester peak as the internal standard does not result in a linear relationship between the change in the standard and the change in the C=C peak. The highest measured cure location for these experiments was at the 50 micron depth for the highest dose of 804 mJ/cm^2 (Figure 6-5). The peak ratio of the uncured monomer is approximately 2.2, while the full cure is at 1.1, indicating that 50% of the C=C double bonds have been reacted for this cure. This corresponds to approximately 2.5 of the 5 C=C present on each monomer reacted during polymerization.
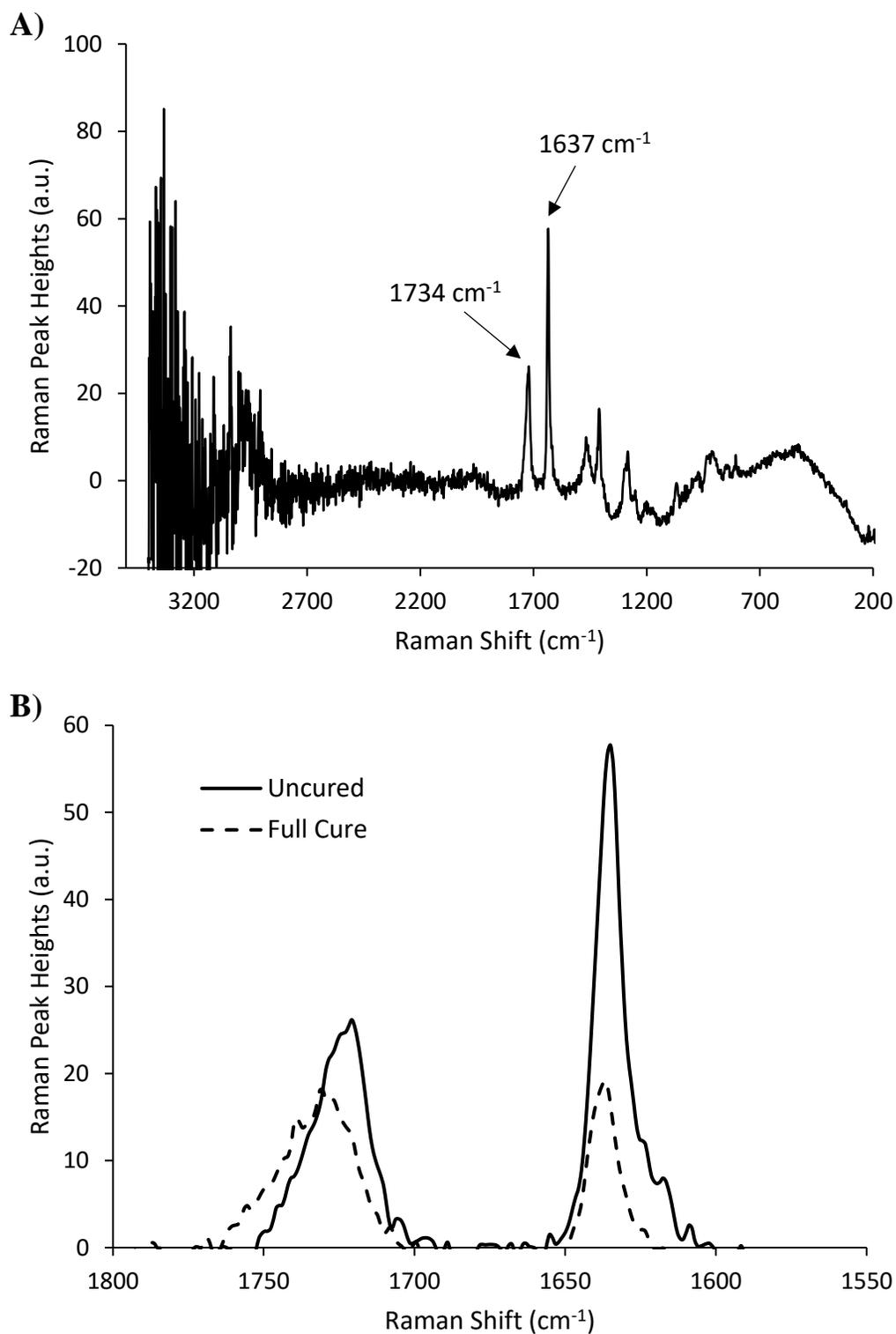
Figure 6-4: (A) The Raman spectrum of the uncured monomer (98% SR-399, 2% Irgacure 184 by weight). (B) Raman shifts show a decrease in the C=C (1637 cm^{-1}) concentration due to the crosslinking observed via polymerization. The aliphatic ester (1734 cm^{-1}) is used as an internal standard.

The ratio of the C=C to ester peaks was determined for all the measurements (Figure 6-5). The Raman spectroscopy measurements show a small increase in the C=C/ester peak ratio as the distance from the top surface increases from zero to the maximum depth of 800 microns. For example, the curve for the light dose of 399 mJ/cm^2 shows an increase in the peak ratio of 0.2. The dashed line indicates the gel point (25% degree of conversion). The bottom surface of the 399 mJ/cm^2 sample is at the gel point, which is slightly tacky by touch. Also, the peak ratio decreases as the light dose increases. The peak ratio for a light dose of 399 mJ/cm^2 at 50 microns is 1.55, while that at 804 mJ/cm^2 is 1.10. This decrease is expected as more light has been absorbed and more C=C bonds have reacted.
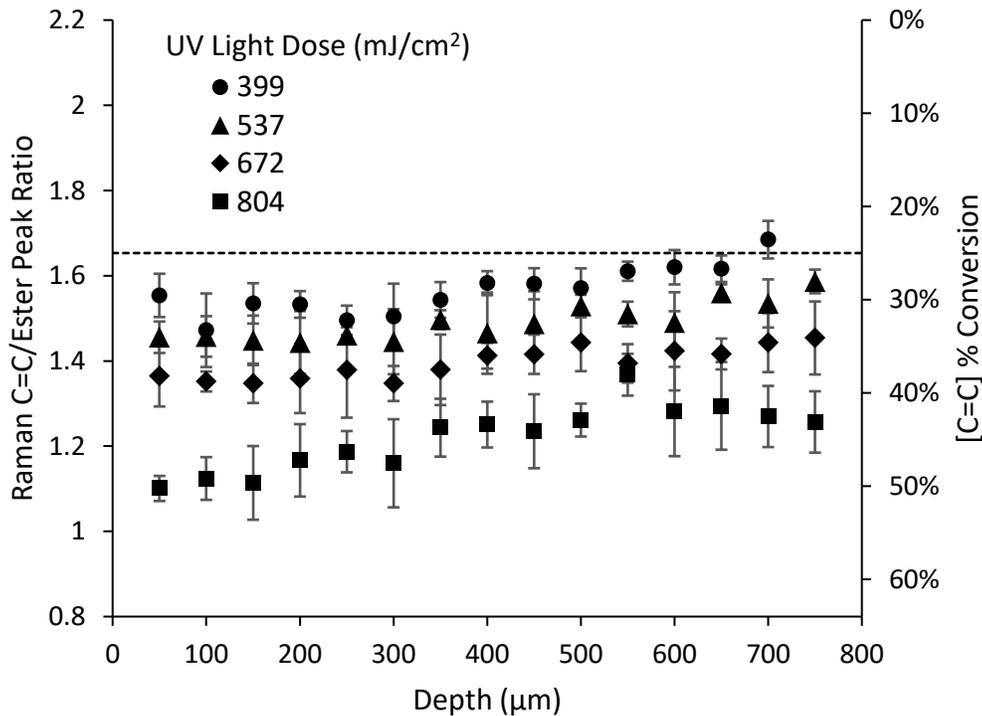
Figure 6-5: Increase in C=C/ester peak ratio as depth increases and UV light dose decreases. The top surface is labeled z = 0 μm, and the bottom surface, z = 800 μm. The dashed line shows the estimated gel point for SR-399 (25% conversion, 8.55 C=C kmol/m^3, or 1.65 peak ratio).

6.3.2 Polymerization Model

■■■■■■   Propagation of UV Light

The UV absorption spectrum of SR-399 and Irgacure 184 are shown in Figure 6-6. Each was dispersed in ethanol, taking into account the ethanol background absorbance. Both show good absorbance well within the UV wavelength of the curing lamp.

Light propagation through the film was modeled by the Beer–Lambert law [Equations (6-1) and (6-2)]. As the photoinitiator is degraded, the absorption decreases, which results in more light propagating through the film. For the polymerization model [Equations (6-3)-(6-5)], the light intensity at a specific depth was computed and used in Equation (6-3) to predict the initiation rate at that depth. The analytical solution for Equations (6-3)-(6-5) was solved for various polymerization times, and the computed conversion was compared with the Raman data in order to fit rate coefficients. The polymerization time is directly linked to the light absorbed in the film; the four polymerization times correspond to four different light dose levels. Light source intensity was kept constant, and the dose is calculated by multiplying its intensity by the time.

Shown in Figure 6-7 is the numerical result for 2% by weight Irgacure 184. The result demonstrates the effect of initiator concentration on the light propagation. At an initial concentration of 2% Irgacure 184, 4.0 mW/cm^2 is absorbed by the sample, equivalent to 8.5% of the total light transmitted from the UV lamp. When Irgacure 184 is completely degraded, the sample is expected to absorb 3.3 mW/cm^2.
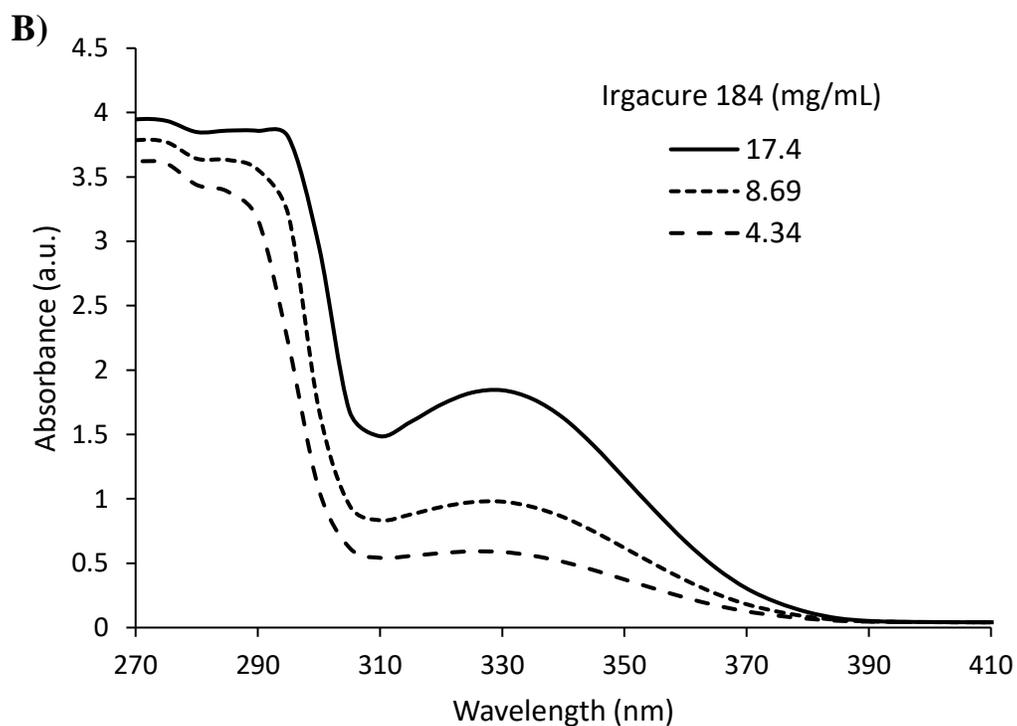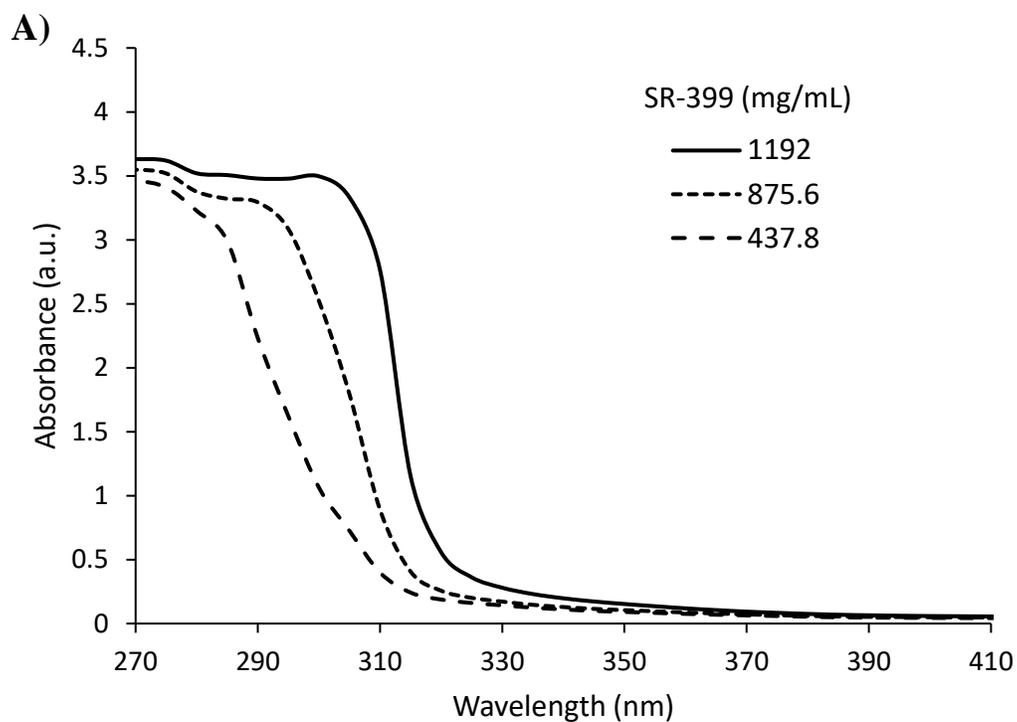
Figure 6-6: (A) The UV absorbance spectra of SR-399 dispersed in ethanol. The weight percent values for [C=C] concentrations of 1192, 875.6, and 437.8 mg/mL are 100%, 80%, and 40%, respectively. (B) The UV absorbance spectra of Irgacure 184 dispersed in ethanol. The weight percent values for [PI] concentrations of 17.4, 8.69, and 4.34 mg/mL are 2%, 1%, and 0.5%, respectively.
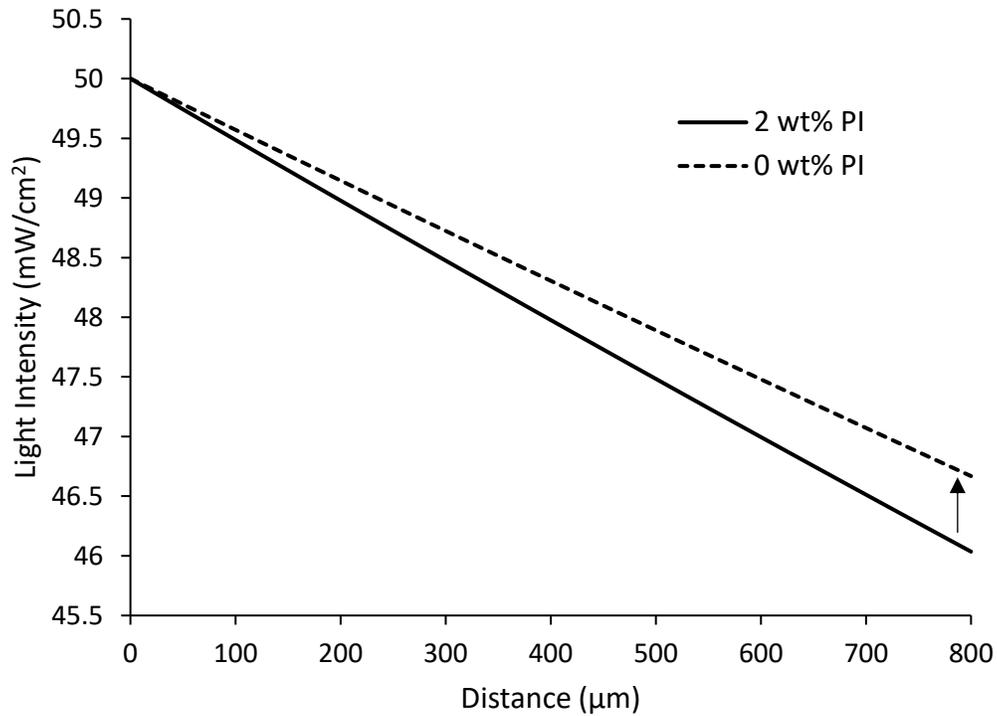
Figure 6-7: Increase in the light propagation though the film depth from its initial point (x_{PI} = 0.02) to the final (x_{PI} = 0) according to the Beer–Lambert law. The top surface is labeled z = 0 μm, and the bottom surface, z = 800 μm.

The polymerization model was used to find appropriate values for the initiation and termination rate coefficients. The photoinitiation rate coefficient is taken to be dependent only on the depth of the sample, as predicted by the Beer–Lambert law. One value is needed: it is applied directly to the polymerization equations at the top surface and is decremented with depth as per the Beer–Lambert law. Its value is estimated from the data for $z = 50$ μm at the longest time/highest light dose level. A set of four depths, 50, 350, 550, and 750 μm, were used for fitting the polymerization model coefficients.

Although the photoinitiator degradation is directly associated with light available at specific depths, the termination and propagation rate constants are expected to be independent of the incident light. The initiator efficiency factor, which accounts for the probability of the recombination of free radicals, decreases above the gel point [222]. The initiator efficiency factor is grouped with the initiator rate constant, giving $k_D = f k_I$, where k_D is a function of intensity.

The photoinitiator concentration was initially at 2 weight percent of the initial monomer concentration, and the propagation rate constant, k_P, was assumed to remain constant. A value of $k_P = 1$ m^3/mol·s was used as it had previously been determined for an acrylate monomer/photoinitiator mixture [224]. The polymerization rate [Equation (6-4)] is directly proportional to k_P while it varies with the initiation and termination rate coefficients to the ½ and -½ powers, respectively. Selecting k_P as a constant value results in a self-consistent set of k_D and k_T coefficients for the polymerization. A 5% change in k_P resulted in an 8.5% change in the C=C concentration, more than double that of k_D or k_T.

As a result, k_P will not vary to the same extent as k_D or k_T. Therefore, since k_P will only vary slightly, if at all, it is assumed to be constant for the purpose of this model in order to determine the full range of k_D and k_T. On the other hand, k_T will largely vary based on the viscosity of the film.

The Trommsdorff effect is a well-known phenomenon in polymerization of linear polymer chains. At very high conversions, the termination rate can drop dramatically as it becomes more difficult for free radical chain ends to diffuse near enough to each other for termination to occur. This is due to the large increases in viscosity of the mixture. It has been reported that the value of k_T and k_P decreases because the viscosity of the polymerizing mixture increases [222]. The polymerization rate gradient through the depth results in a change in viscosity with depth. SR-399, a pentafunctional monomer, should be susceptible to similar effects as it polymerizes past the gel point. The gel point for multifunctional polymers can be estimated using probability arguments [231]. For SR-399, gelation is expected to occur for C=C conversions greater than 25%. Above this conversion, monomer molecules would be tethered into larger chains and relatively immobile. This should greatly decrease their ability to terminate, resulting in a reduction in the termination rate coefficient.

The Raman C=C/ester peak ratios were then converted to C=C concentrations. The initial concentration of C=C is computed at 11.4 kmol/m^3 corresponding to a peak ratio of 2.2. Assuming a linear relationship between the peak ratio and the C=C concentration, the C=C concentration was computed at each point throughout the film (Figure 6-8). After 15 seconds of photoillumination, the top surface of the film was assumed to reach a percent conversion of 50%, since the C=C/ester peak ratio at this point was 1.1.

The method of least squares was used to calculate the initial values of k_D and k_T. However, a single value of k_T did not effectively model the C=C concentrations at different depths. Therefore, one value of k_D was used for all four depths and an average k_T was estimated at each depth by minimizing the difference between predicted C=C levels and those measured by Raman spectroscopy. This approach has the advantage of requiring the model to fit the known overall conversion of C=C bonds. The values from Raman spectroscopy were then used to correlate C=C concentrations with the variation of elastic modulus and hardness with the depth.

Figure 6-8 shows the comparison between numerical results (lines) and the measured C=C concentrations from Raman (points). The model relates well to the Raman results for all light doses except for 804 mJ/cm^2. However, the model also indicates that the photointiator concentration is not fully depleted at this light dose (Figure 6-9). This suggests that the model would eventually match the C=C concentrations measured from Raman, just at a larger light dose. As expected, in both the model and experimental results, the C=C concentration increases as depth increases.
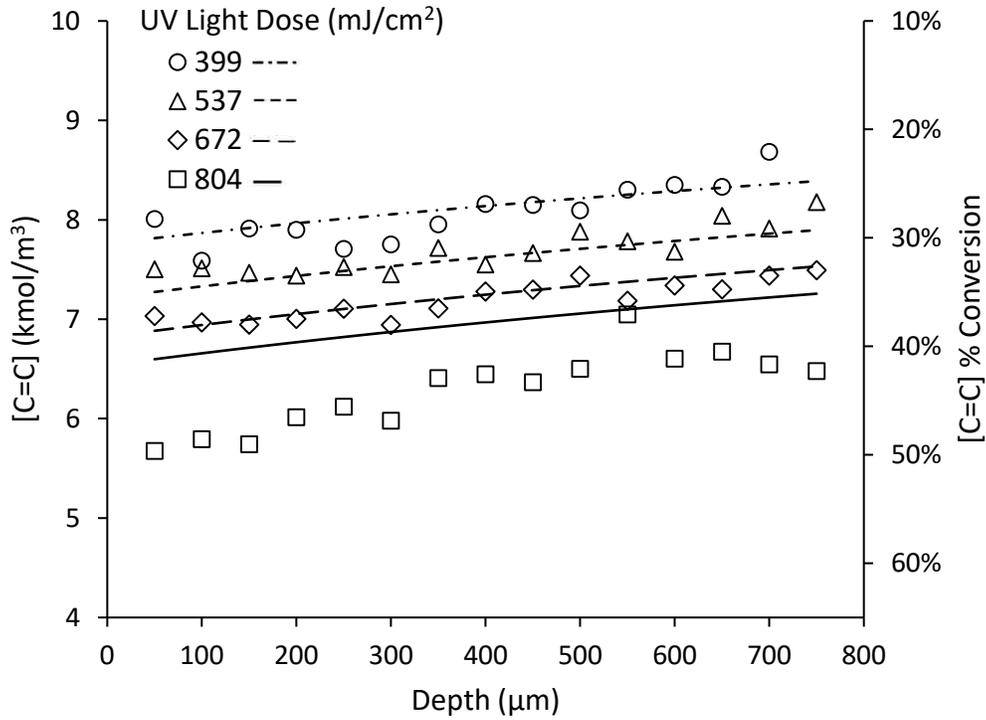
Figure 6-8: Raman C=C concentration results compared to that of the numerical model. The points represent the Raman results and the lines, the model. The top surface is labeled z = 0 μm, and the bottom surface, z = 800 μm.

The concentrations of photoinitiator and monomer (C=C) are shown in Figure 6-9. The photoinitiator concentration rapidly declines, but just marginally as the film depth increases. This indicates a decrease in k_D starting from its initial value of 0.212 s^{-1} (Table 6-1). The decrease in k_D as depth increases (power decreases) has been previously shown to be linear [223]. The C=C concentration looks similar to the decrease in the photoinitiator concentration; however, it levels off at the conversion value of approximately 50%. According to the model, the gel point (25% conversion, indicated by the dashed line) is surpassed by a light dose of approximately 340 mJ/cm^2 at the back surface of the film. This corresponds nicely to the back surface of the sample exposed to a light dose of 399 mJ/cm^2 at the gel point as specified by Raman results. The top surface has a 50% conversion of C=C groups at the highest light dose level, 804 mJ/cm^2 light dose. These data show incomplete polymerization of all C=C groups even at the highest light dose. However, as will be shown by the nanoindentation measurements, the top surface has achieved the expected mechanical properties for a typical, highly crosslinked film.
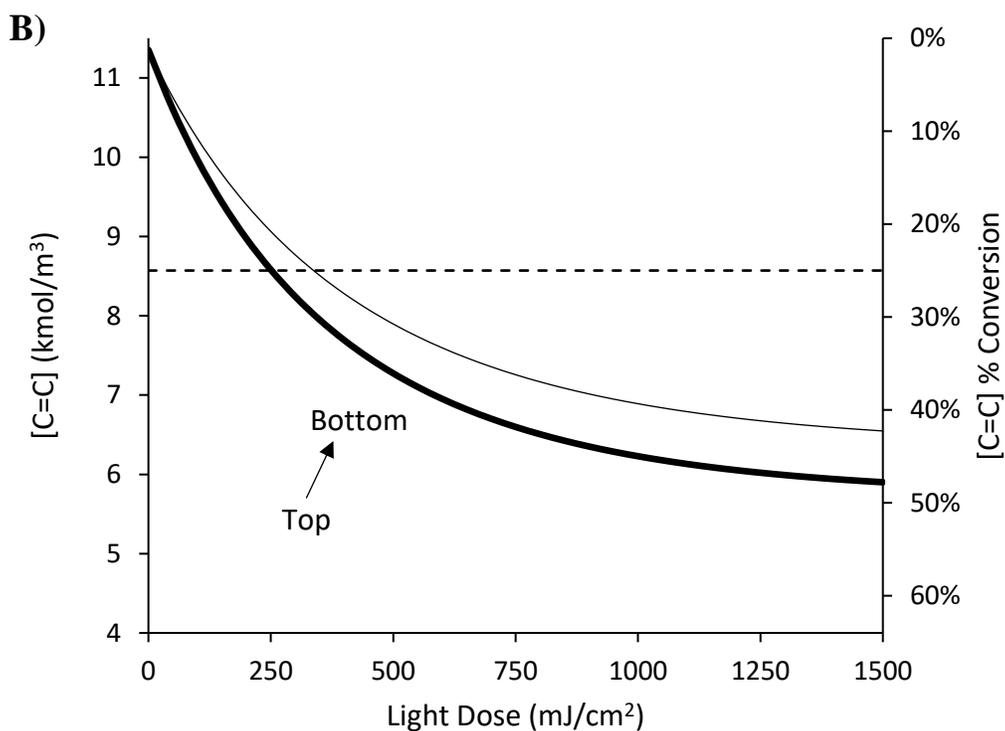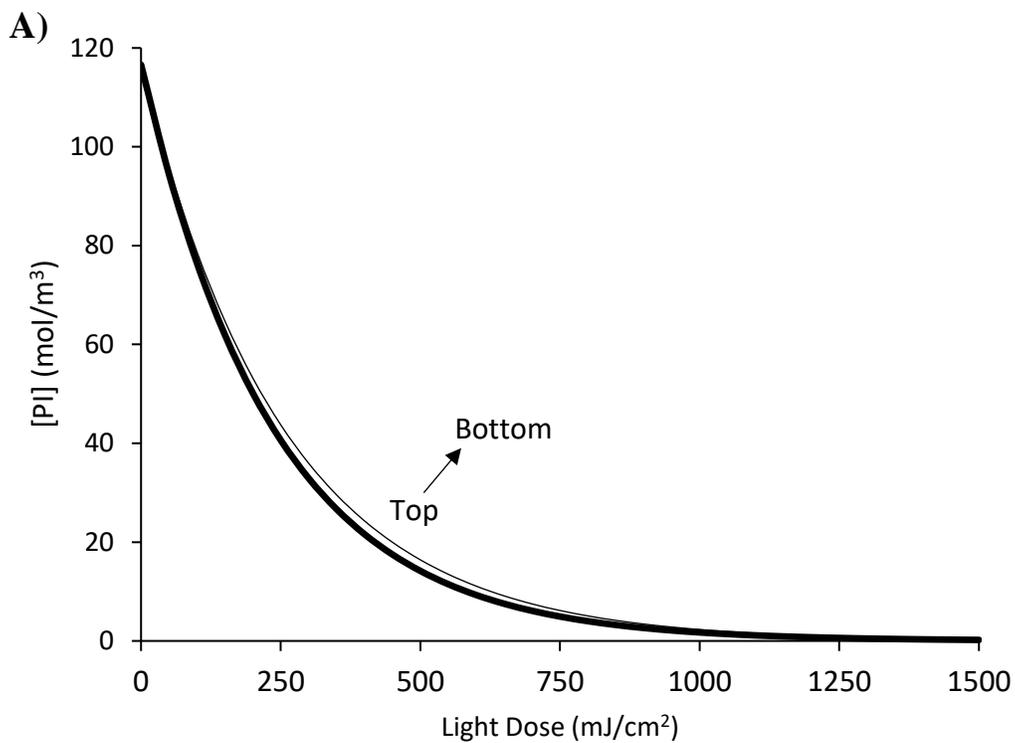
Figure 6-9: Change in the concentration of (A) photoinitiator and (B) monomer (C=C) as a function of light dose. The thick line represents the top surface and the thin line, the bottom. The dashed line indicates the C=C concentration at the estimated gel point (25% conversion).

Table 6-1: Values of rate constants and assumptions made to determine the appropriate quantities.

Rate Constants	Value	Notes
k_D	0.212 s^{-1}	Decreases according to the Beer–Lambert law
k_P	1 m^3/mol·s	Constant [224]
$k_{T,average}$	4.74-7.05 x 10^3 m^3/mol·s	Lower limit value for z = 50 μm; upper limit value for z = 750 μm. Deviations are consistent with the Trommsdorff effect [232]

As depth increases, k_T increases. Again, this is due to the increase in viscosity as polymerization progresses. At the top surface of the film, where power is the greatest, the polymerization proceeds at a greater rate and therefore the viscosity increases more rapidly causing a drop in the termination rate constant compared to the rest of the polymer. k_T increases linearly as power decreases throughout the film depth from 4740 to 7050 m^3/mol·s (Table 6-1).

In addition, the same model was used to estimate the light dose required to polymerize films prepared with titania. The faded line in Figure 6-10 represents a change when TiO$_2$ is added to the monomer prior to polymerization. A shift to the right indicates larger absorption of UV light and increased light dose required to complete photopolymerization. The UV light absorption by titania during polymerization reduces the polymerization rate and, consequently, increases the exposure time. A light dose triple than normal is required to surpass 25% conversion, representing a 50% reduction in the initiation and propagation rate constants.
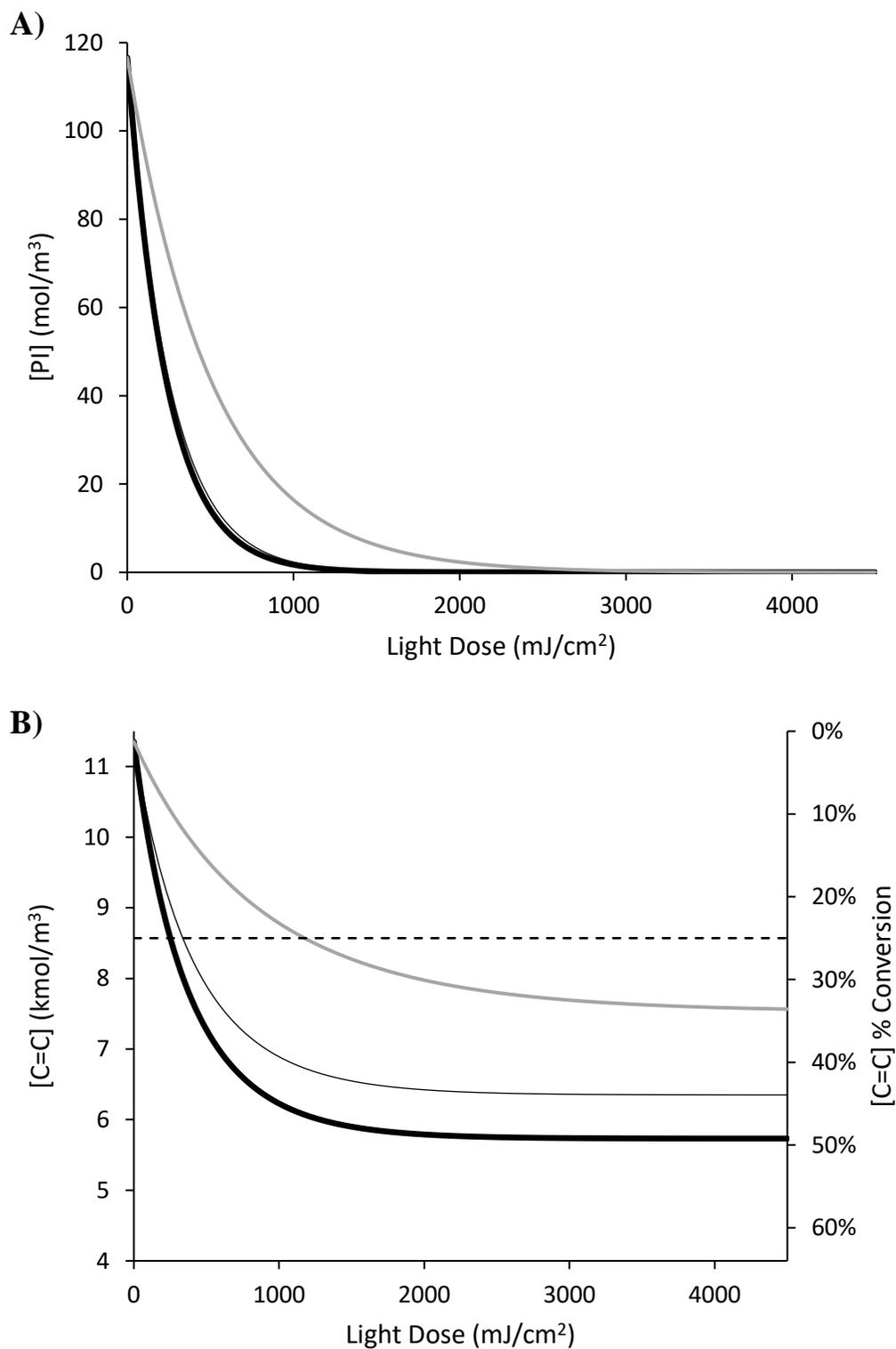
Figure 6-10: Change in the concentration of (A) photoinitiator and (B) monomer (C=C) as a function of light dose. The thick line represents the top surface, the thin line, the bottom, and the gray line, titania nanocomposite. The dashed line indicates the C=C concentration at the estimated gel point (25% conversion).

6.3.3 Nanoindentation

Figure 6-11 shows typical indentation curves, in which the lower plateau is used to monitor the thermal drift of the system. This occurs at 10% of the maximum load and is held between 60 and 100 seconds in order to correct for thermal drift. The upper plateau occurs at maximum load and is held for 10 seconds. Figure 6-12 shows the dependence of the modulus on the holding time. The modulus converges to a constant value for the holding time greater than or equal to 5 seconds.
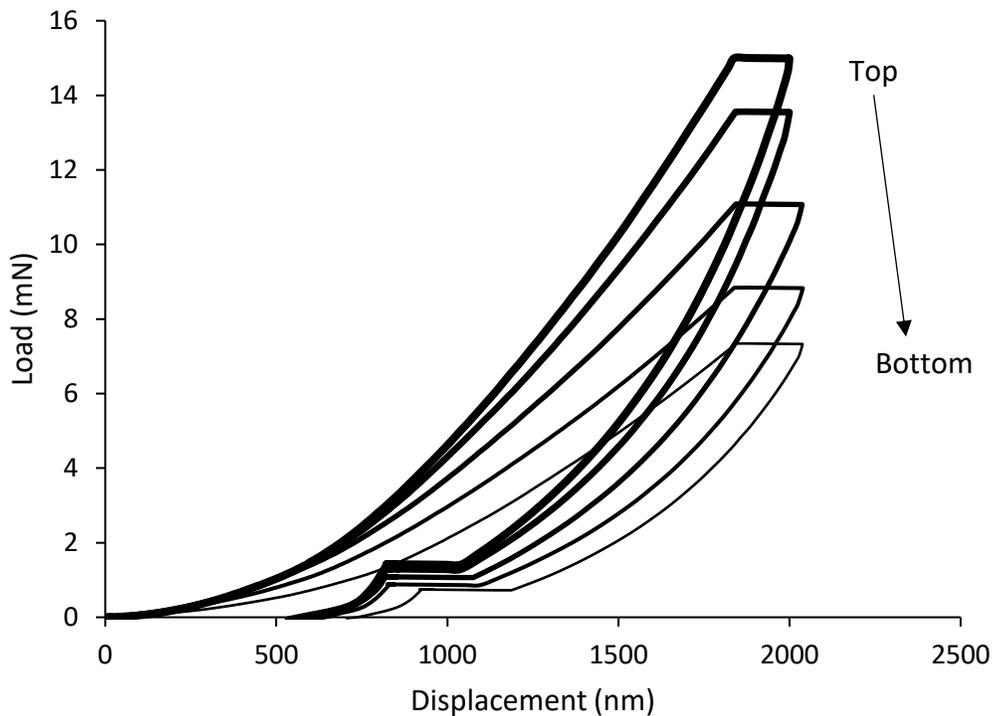
Figure 6-11: Nanoindentation load vs. displacement curves show a change in the mechanical properties due to the various degrees of crosslinking throughout the film depth. The arrow represents an increase in the film depth from the top (thick line) to the bottom (thin line) surface with each line representing measurements 200 μm further into the film depth.
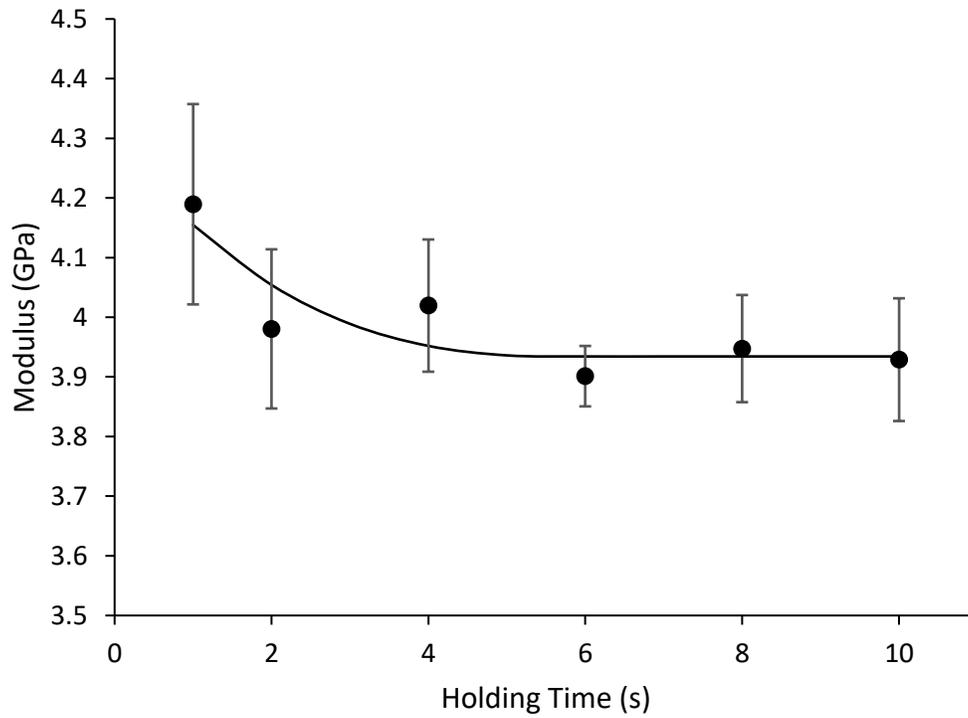
Figure 6-12: The effect of holding time on the modulus of the polymer film.

Both elastic modulus and hardness were measured with nanoindentation well below the glass transition temperature. As expected, due to an increase in crosslinking, the modulus and hardness of the top surface of the film are larger than that of the bottom surface indicating a higher degree of polymerization at the point of the maximum UV light dose (Figure 6-13). The polymerization gradient decreases with the film depth, which is reflected by the decreasing modulus and hardness from the top to the bottom surface. The difference in the modulus between the top and bottom surface is greater than 1 GPa. As light dose increases, both modulus and hardness values increase. The elastic modulus and hardness at any point along the film depth at the end of polymerization (804 mJ/cm^2) are between 1.5 and 2 times of their values after half of the light exposure time (399 mJ/cm^2). The ultimate modulus of SR-399 is reported to be 4.04 GPa [157]. This is equivalent to the modulus recorded at the top surface of the film polymerized with a light dose of 804 mJ/cm^2.
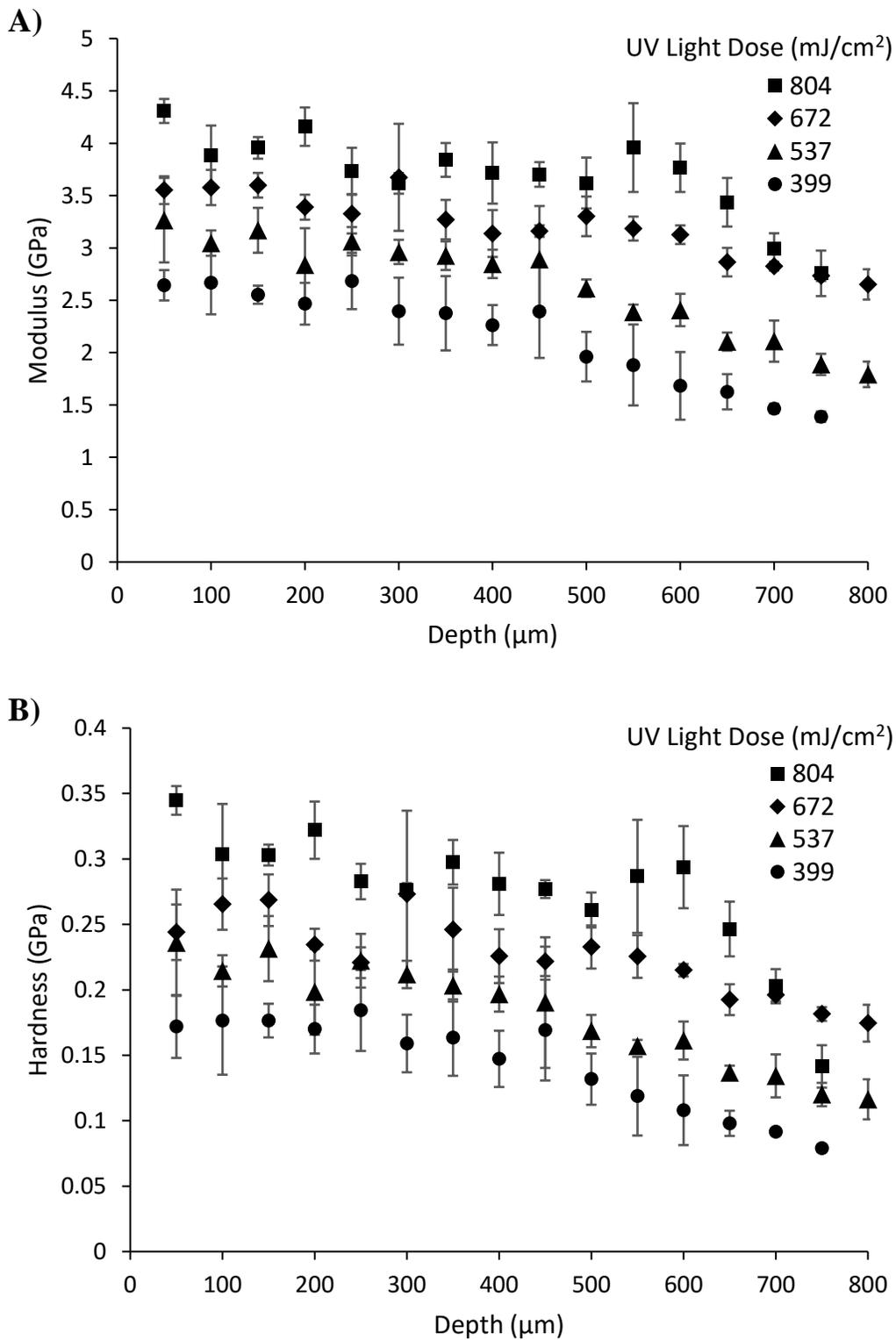
Figure 6-13: Decrease in (A) elastic modulus and (B) hardness as depth increases and UV light dose decreases. The top surface is labeled z = 0 μm, and the bottom surface, z = 800 μm.

The C=C concentrations measured from the Raman data were then correlated with the modulus and hardness values calculated from nanoindentation (Figure 6-14). Linear models can correlate these data with R^2 values of approximately 0.75, but do not link well with the manufacturer's reported modulus of 4.04 GPa for a 'cured' polymer. In fact, moduli of approximately 4 GPa are achieved at monomer conversions of only 50%, suggesting that the maximum film modulus can be achieved for films with only moderate C=C conversions when a pentafunctional monomer is used. A three-constant model based on a power law-type fit is more consistent with these data plus the expected maximum modulus. Equation (6-6) is given by:

$$E = \frac{E_{max}}{1 + \frac{[C = C]^n}{B}}$$
(6-6)

where E is the modulus of the polymer, E_{max} is the polymer modulus at low values of C=C (or high conversion of monomer), B is C=C at ½ the value of E_{max}, and n is a power law exponent. This function [Equation (6-6)] is applied for C=C compositions at the gel point and below; the modulus values approach the expected maximum modulus asymptotically. A similar equation [Equation (6-7)]can be written for correlating hardness with C=C:

$$H = \frac{H_{max}}{1 + \frac{[C = C]^n}{B}}$$
(6-7)

where H is the hardness, H_{max} is the maximum polymer hardness, and B and n have similar interpretations as in Equation (6-6). Equations (6-6) and (6-7) are similar to the Ellis equation used for modeling the effects of shear stress on polymer solution viscosity and are entirely empirical. Table 6-2 shows the parameters and their relative errors for both equations. Figure 6-14 shows the model fits to the data along with the limiting value for the modulus (E_{max}) and an estimated limiting value for the hardness (H_{max}). Even with three parameters rather than two, these models have higher R^2 values than linear fits and both approach asymptotic values at low values of C=C.

As the percent conversion increases over the gel point, the film should be below its glass transition temperature. This has been verified qualitatively by noting that, for the one film location with percent conversion less than the gel point (refer to Figure 6-5), the lower surface of the film was tacky. All other surfaces were solid polymers.

Table 6-2: Parameters for Equations (6-6) and (6-7) fitted by nonlinear regression to the correlation data shown in Figure 6-14.

Equation	R^2 Value	Parameter	Value	Standard Error	Relative Error
(6-6)	0.862	E_{max}	4.04	Assumed value	Not applicable
		B	8.22	0.051	0.62%
		n	10.4	0.76	7.3%
(6-7)	0.800	H_{max}	0.304	0.015	4.9%
		B	8.01	0.089	1.1%
		n	10.5	1.73	16.5%
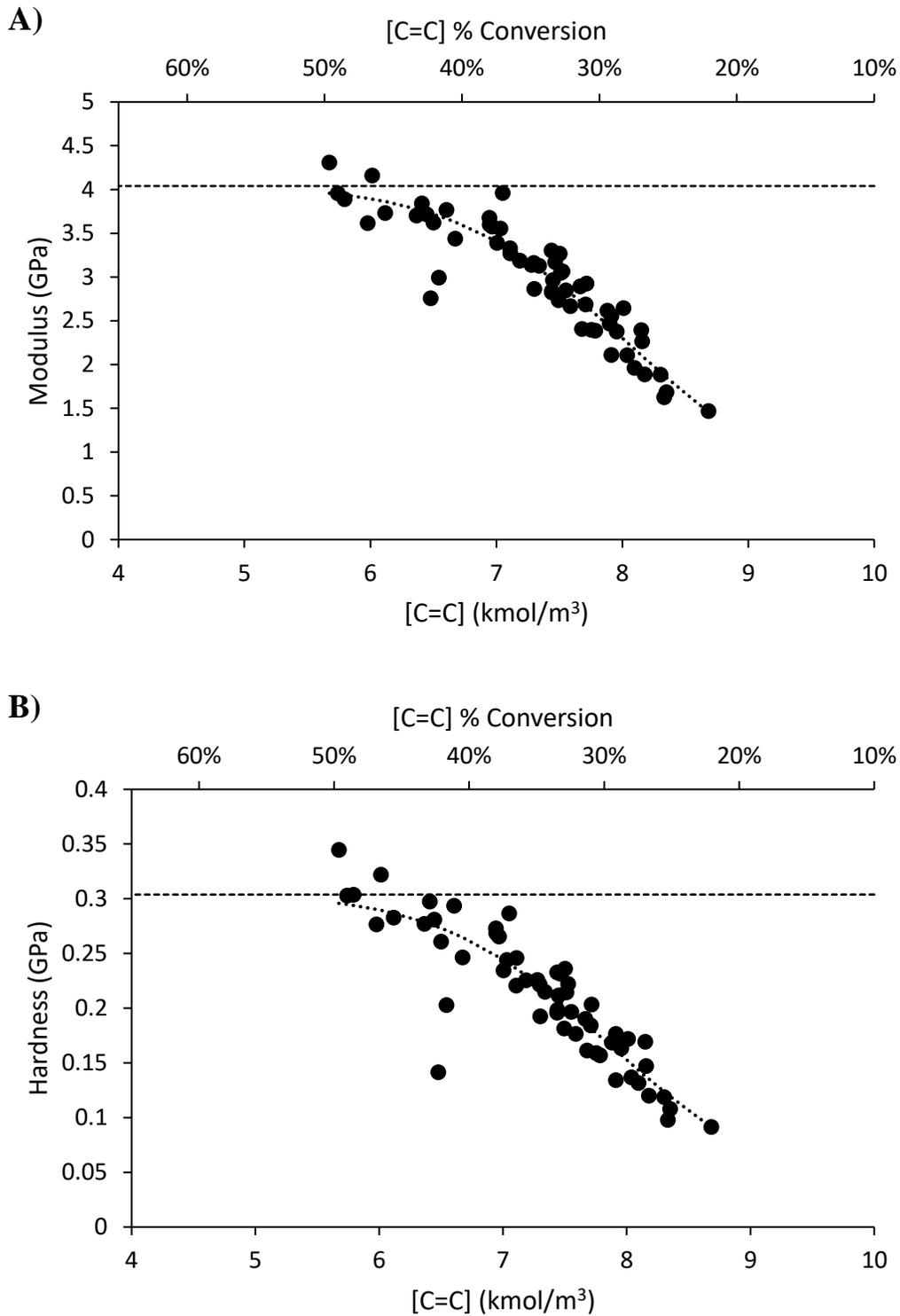
Figure 6-14: Raman C=C concentration approximations compared to the (A) modulus and (B) hardness values. The dotted lines represent the model fit to Equations (6-6) and (6-7), and the dashed lines represent the maximum modulus (4.04 GPa) and hardness (0.304 GPa) values.

While many glassy polymers have moduli of approximately 3 GPa, Figure 6-14 shows significant increases in the film's mechanical properties as the number of unreacted C=C groups decreases. There is a direct link between the moduli gradient and the C=C gradient in the sample. This multifunctional monomer has five functional groups. When 25% of the C=C double bonds are reacted, a gel has been formed, i.e., essentially all monomer units are crosslinked. As C=C groups continue to react, the moduli increase rapidly the asymptotic value of about 4.04 GPa. All locations tested showed C=C conversions between 25% and 50% but no higher. This result is consistent with a large multifunctional monomer crosslinked in place with its various branches having limited mobility to crosslink further. Film locations with 50% conversion show moduli similar to that of the 'fully' reacted value provided by the manufacturer. The empirical models for modulus and hardness as a function of C=C content in the polymer mimic the rapid change in mechanical properties as percent conversion increases and, in the case of the modulus, approach a typical modulus for a well-crosslinked sample. It is, however, not fully crosslinked, as shown by the Raman measurements. Therefore, it is reasonable to consider acrylates with lower functionality for this application; they should crosslink as rapidly above the gel point, and have much less unreacted C=C, which can lead to long-term instability of the film.

6.4   Conclusions

A polymerization model was developed to predict the C=C concentration as a function of the film depth for photopolymerization of a multifunctional monomer in a top-illuminated geometry. Light propagation through the film was predicted using the Beer–Lambert law to estimate the free radical gradient through the film depth. The model converges to ultimately 50% conversion at the top surface of the film. The percent conversion decreases as depth into the film increases. Nanoindentation results confirm this to be accurate. Raman measurements of the C=C/ester peak ratios were converted to C=C concentrations which were used to calculate polymerization coefficients by minimizing the errors between the model and the Raman data.

The calculated C=C concentrations were compared to the measured moduli and hardnesses. A three-constant power law-type model was used in order to predict the modulus and hardness at specific C=C concentrations. The C=C concentrations are directly related to the polymerization time and depth into the film, and therefore, the modulus and hardness can be mathematically predicted at any point within the film.

The model and correlations can be used to optimize the manufacture of microfluidic devices using UV polymerized materials. Microfluidic chip part synthesis requires a strong material, and the results of this research will assist manufacturers in developing a procedure to polymerize and approximate the mechanical properties of the resulting film.

APPENDICES

APPENDIX A: Chapter Highlights

Chapter #	Objective	Contributions	Status
Ch. 1	Complete characterization of nanoceria hydrothermal synthesis with dialysis.	Characterization analysis from TEM, DLS, XRD, TGA, FTIR, Raman, UV-Vis, Zeta-potential, and ^{13}C-NMR.	Manuscript, *in preparation*, 1st author.
Ch. 2	Study nanoceria stability and dissolution in acidic aqueous environments.	Nanoceria stability analyzed at various conditions via DLS after dissolution. Size and shape distributions of primary particles determined via TEM after dissolution.	Published, *Environmental Science: Nano*, last author. [32] Published, *Nanotoxicology*, 2nd author. [33] Manuscript, *in preparation*, 1st author.
Ch. 3	Study nanoceria stability and dissolution in simulated biological fluids (SBFs).	Analysis completed showing surface properties, size and morphology of exposed nanoceria.	Published, *European Journal of Pharmaceutics and Biopharmaceutics*, 2nd author. [34]
Ch. 4	Develop nanotitania synthesis method compatible with photopolymerized nanocomposites.	Stable systems are developed and characterized.	*N/A*
Ch. 5	Modify ferrofluid synthesis to develop a stable system compatible with a photopolymerized chip manufacturing system.	Stable systems can be developed with PAA.	*N/A*

Ch. 6	Study the effects of a crosslinking gradient on material properties of a thin film.	Raman and nanoindentation proves crosslinking/ polymerization gradient along depth of the film.	Published, *Journal of Coatings Technology and Research*, 1st author. [194]
App. D	Physicochemical analyses of nanoparticles employed in health effects research studies.	Nanoparticle characterization completed for a variety of metal oxide nanoparticles.	*N/A*

APPENDIX B: Funding Sources

Chapters 1-3 – NIH Grant #R01GM109195, 2016-19

Chapters 4-6 – Hummingbird Nano, Inc./NSF SBIR #1555996, 2016-18

Appendix D – US EPA Contract #PR-ORD-15-01848/DP-16-D-000038, 2016

APPENDIX C: Instrumentation Methods/Techniques

Scanning Electron Microscopy (SEM)

Powders were mixed in ethanol or water to obtain approximately 0.5 mg/mL dispersions. The sample was sonicated for 10 minutes in a sonication bath. A droplet of the sonicated dispersion was placed on a SEM stub with a carbon-based, adhesive disc. The sample was dried overnight at room temperature. Surface conductivity was improved by sputtering with gold/palladium for 3 minutes. A FEI Quanta 250 was used for imaging and EDS analysis (Oxford detector).

Transmission Electron Microscopy (TEM)

Powders were mixed in ethanol or water to obtain approximately 0.5 mg/mL dispersions. The sample was sonicated for 10 minutes in a sonication bath. The TEM grid was dipped into solution for approximately 5 seconds and dried overnight at room temperature. All samples except for those containing copper were prepared on lacey carbon, 300 mesh, copper grids. Copper samples were prepared on lacey carbon, 300 mesh, nickel grids. The TEMs used were a JEOL 2010F equipped with an Oxford detector for EDS analysis and a Thermo Scientific Talos F200X equipped with a SuperX G2 EDS detector.

Electron Energy Loss Spectroscopy (EELS)

EELS analysis was completed at two locations: the Ohio State University and the University of Kentucky. The FEI Probe Corrected Titan3 80-300 S/TEM was used to determine the valence state of the ceria samples at the Center for Electron Microscopy and Analysis (CEMAS) located at the Ohio State University. The Thermo Scientific Talos F200X was equipped with Gatan's Enfinium ER at the University of Kentucky.

Dynamic Light Scattering (DLS)

Powders were mixed in water to obtain approximately 0.5 mg/mL dispersions. If the dispersion was too hazy for analysis, they were diluted further until they were transparent, then sonicated for 10 minutes. Using the Brookhaven 90Plus Particle Size Analyzer, five analysis runs of 5 minutes each were completed for each sample and the average result of each run was analyzed and recorded. All samples were evaluated using the multimodal setting.

X-ray Diffraction (XRD)

Double -sided sticky tape was attached to a glass microscope slide and dried powder was distributed across the tape. Measurements were made using a Siemens D500 X-ray diffractometer with Cu Kα radiation. The analysis was conducted from 10 to 100 degrees 2θ, 0.01 degree step size, and a speed of 1 degree/min. Sharp, distinct peaks in the XRD spectra indicate a crystalline structure.

Thermogravimetric Analysis (TGA)

TGA (PerkinElmer TGA7) was used to determine the organic percent of the sample. All samples were analyzed under a nitrogen atmosphere to prevent oxidation of organic matter, resulting in pyrolysis of any organic matter on the nanoparticle surfaces. The sample was heated from 20 to 125 °C at 10 °C/min, held at 125 °C for 30 minutes to releases physisorbed water, and then heated to 900 °C at 10 °C/min. The weight loss of the sample is determined to be the percent organic content of that sample.

Fourier Transform Infrared Spectroscopy (FTIR)

A Nicolet 6700 FTIR with a diamond ATR crystal was used to detect organic functional groups on the nanoparticle surfaces. The powder was placed on the crystal and 32 scans were completed.

Brunauer, Emmett, Teller (BET) Surface Area Analysis

The surface area of a particle/powder is determined by the adsorption of nitrogen gas on the surface of the solid. The Micromeritics TriStar BET computes the corresponding monolayer of nitrogen on the surface of the material and reports the specific surface area, m^2/g.

Raman Spectroscopy

The samples were placed on a glass microscope slide. The Raman spectra of the samples were analyzed on a Thermo Fisher Scientific DXR Raman microscope. It was equipped with an Olympus brand microscope and a 10x working distance objective. A 780-nm Raman laser with the power set to 10.0 mW was used for sample analysis. The spot size of the laser beam was 3.1 µm. All Raman spectra were collected in a spectral range of 3400–50 cm^{-1}. Each Raman spectrum was an average of five accumulations consisting of 5 seconds each.

UV-Vis Spectroscopy

BioTek Synergy 2 Plate Reader was used to perform UV spectroscopy. The spectra were collected from a wavelength range of 270 to 410 nm at a step rate of 5 nm. Each spectrum was an average of three total replications at each specified concentration.

Zeta Potential

Anton Paar Litesizer 500 Particle Analyzer was used to determine the zeta potential of nanoparticle dispersions at a concentration of 0.5 mg/mL. 100 runs were completed in sequence with a 30 second equilibration time at 25 °C. The instrument was equipped with a 40 mW laser emitting at a wavelength of 658 nm. Zeta potential was determined multiple times between pH 0.5 and 13. Nitric acid and sodium hydroxide were used to adjust the pH.

^{13}C-NMR

CP/MAS NMR data was collected using a home-built Tecmag Redstone NMR Spectrometer (Houston, TX), Bruker 300 MHz magnet (Billerica, MA), and Chemagnetics (Ft. Collins, CO) NMR probe with 7.5 mm rotors spinning at 4000 Hz. A relaxation delay of 2 seconds was used with 256 acquisition points and 20,480 scans and 1 ms CP contact time. TNMR software (Houston, TX) was used to process the data. 3-methylglutamic acid was used as a reference standard, with the methyl peak referenced to 18.84 ppm.

Nanoindentation

The nanoindentation tests were performed with a diamond Berkovich indenter (tip radius of 200 nm) using the Nanoindenter G200 (Agilent Technologies) in an argon-filled glovebox. The displacement-controlled mode was used with a strain rate of 0.05 s^{-1} and a maximum depth of 1800 nm. The indenter was held for 10 seconds at the maximum load, and the maximum allowable drift rate was set at 0.5 nm/s. Thermal drift was assessed by holding the indenter in position when 10% of the maximum load was reached on the load removal side.

This physicochemical characterization study is part of a large US Environmental Protection Agency (EPA) coordinated study of metal and metal oxide nanomaterials composed of Cu, Ag, CeO_2, and SiO_2 for systemic toxicity in several organs including the lungs, liver, gastrointestinal tract, and eye.

A major purpose of this study was to further investigate the potential hepatotoxicity of CeO_2-containing nanoparticles. Thus, four commercially-available nanoceria particles were studied along with two nanosilica particles with which atomic layer deposition with CeO_2 was attempted. The Cu and Ag containing nanoparticles were selected because of their biocidal properties and their high research interest to the US EPA.

Nanomaterial physicochemical characterization included primary and agglomerated particle size, shape, and morphology by TEM/SEM/DLS, elemental analysis by EDS and EELS, crystal structure by XRD, organic surface analysis by TGA and FTIR, and specific surface area by BET analysis.

The objectives of this study were to: (a) determine and characterize the physicochemical nature of the eleven nanoparticle samples, and (b) link this physicochemical data to a US EPA nanomaterial-toxicity data set useful for structure-

activity and dose-response modelers. The impact of the study is to relate physicochemical properties to nanoparticle biological activity.

Reported properties for all eleven particles used in this study are presented in Table A-1. Four commercially-available nanoceria particles were studied (CeO_2 W4, CeO_2 X5, CeO_2 Y6, and CeO_2 Z7). Two nanosilica particles (SiO_2 K1 and SiO_2 N2) were selected in the attempt to study thin coatings of nano CeO_2 on a commercial SiO_2 base particle [SiO_2 J0)]. A copper nanoparticle sample (Cu 8) was compared with a copper oxide nanoparticle sample (CuO 9), and two silver nanoparticle samples were evaluated (Ag R and Ag S).

Table A-1: Samples - composition, source, and reported properties.

Sample ID	Source	Supplier Description
CeO_2 W4	commercial	~8 nm (XRD) ~15 nm (BET 55 m^2/g), narrow size distribution
CeO_2 X5	commercial	N/A
CeO_2 Y6	commercial	~25 nm (BET)
CeO_2 Z7	commercial	15-30 nm, 30-50 m^2/g (BET)
SiO_2 J0	commercial	~20-30 nm spheroidal
SiO_2 K1	custom	1.5 nm ceria coating, gas phase
SiO_2 N2	custom	2.5 nm ceria coating, gas phase
Cu 8	commercial	< 50 nm (TEM)
CuO 9	custom	~47 ± 24 nm
Ag R	custom	nanorod
Ag S	custom	~50 nm spheroidal, capped with glutathione

Physicochemical Characterization

Elemental composition was done to verify the bulk composition of the nanoparticles and to determine whether there were trace contaminants. Trace contaminants can affect the surface reactions of nanoparticles, their possible solubilities in various environmental milieu, and, in some cases, their crystal structure.

Evaluation of the size and shape of aggregates, agglomerates, and constituent particles can help inform the biological barriers that the material can penetrate. For example, large aggregates on the scale of microns may be excluded from *in vitro* cell populations and may not be able to pass through *in vivo* barriers, such as the GI tract. SEM images can help identify samples that are aggregated and agglomerated, while TEM images can provide information about constituent particle properties, such as the presence of crystallites and artifact particles with different shapes or compositions.

Table A-2 summarizes the morphology observed using electron microscopy. The SEM images demonstrated that most all of the samples were highly aggregated or agglomerated. This information was not included in the manufacturers' reports (Table A-1).

Table A-2: Particle morphology – SEM, TEM, BET, and XRD.

	SEM		TEM		BET	XRD	Shape
	aggregates, μm		constituent particles, nm				
Code	avg	range	avg	range	avg	avg	
CeO$_2$ W4	1.8 ± 0.94	0.64 – 4.7	590 ± 150	220 - 780	15.7	56.9	Spheroidal/Ellipsoidal
CeO$_2$ X5	0.73 ± 0.53	0.18 – 3.4	13 ± 6.1	3.9 - 36	40.3	31.5	Irregular
CeO$_2$ Y6	8.3 ± 5.4	1.7 – 26	22 ± 12	6.8 – 59	20.6	28.7	Trapezoidal/Triangular
CeO$_2$ Z7	4.4 ± 2.6	1.6 - 14	13 ± 3.6	7.3 – 21	14.6	10.3	Aciniform/Hexagonal
SiO$_2$ J0	3.46 ± 1.98	1.18 – 13.9	21.5 ± 3.15	15.4 – 30.7	16.5	-	Aciniform/Spheroidal
SiO$_2$ K1	3.73 ± 1.74	1.19 – 9.54	19.2 ± 3.44	13.0 – 32.1	17.6	-	Aciniform/Spheroidal
SiO$_2$ N2	6.44 ± 5.71	1.66 – 42.7	18.9 ± 2.66	13.3 – 23.8	18.7	-	Aciniform/Spheroidal
Cu 8	1.00 ± 0.90	0.23 - 7.87	25.0 ± 5.21	13.2 - 33.1	64.4	32.2	Irregular
CuO 9	1.25 ± 0.65	0.45 - 4.50	45.9 ± 10.3	26.1 - 66.5	88.0	15.7	Aciniform/Hexagonal
Ag R	2.70 ± 1.94	0.63 - 12.0	40.4 ± 9.12	26.4 - 60.4	-	48.5	Rods; Spheroidal const. particles
Ag S	2.02 ± 1.02	0.71 - 5.98	11.2 ± 9.16	4.16 - 64.4	78.0	34.8	Aciniform/Spheroidal

XRD confirmed the presence of ceria crystallites in all samples. EDS systems on both the SEM and TEM instruments confirmed the presence of cerium and oxygen in all four nanoceria samples. Modest amounts of other elements were detected only in the W4 sample. The SEM EDS system showed the presence of aluminum, while the TEM EDS system showed the presence of aluminum, titanium, and silicon. EDS systems typically respond to elements above the 1 mole% level.

Sample W4 has aggregates averaging 1.8 μm in size and ranging from 0.64 to 4.7 μm. The aggregates have bimodal distributions of constituent particles, with one population about 600 nm in typical size and a second population with a typical size of ~200 nm, denoted by the arrow. The constituent particles are spheroidal, packed at a moderate density within the aggregate, and appear to be fused together. Surface 'films' also appear on both the aggregate and constituent particles. Figure A-1A is an SEM image of sample W4. The

constituent particles are mostly aggregated and appear to have a film associated with their surfaces. One constituent particle appears in the image (lower right hand side) and it also appears to have an associated film.

While Figure A-1A shows a separated spheroidal constituent particle on the lower right hand side, this was not common, suggesting that the sonication used for dispersion did not fracture many aggregates down to their constituent particles. Therefore, samples of W4 used for biological studies would be expected to be mostly aggregates, with a low weight fraction of separated constituent particles. The small and narrow constituent particle range reported by the manufacture (Table A-1) is not observed. TEM images provide additional information about the constituent particles, as shown in Figure A-1B.

Figure A-1B is a TEM image of two constituent particles on a lacey carbon grid, with typical dimensions of ~500 nm and ~700 nm. These both have additional material on their surfaces, which is the 'film' material identified in the SEM image (Figure A-1A). The film material does not appear to have crystalline morphology and occurs on the surface of the constituent particles and as separated material attached to the grid. In a BET experiment, this material might adsorb nitrogen, which could contribute significantly to the sample's BET adsorption, impacting the estimate of an average particle size using the BET method. The film contained Al, Ti, and Si as an amorphous material.

The average particle size estimates for sample W4 vary widely, from ~600 nm (TEM) to 56.9 nm (XRD) to 15.7 nm (BET). However, some 20-30 nm particles could be seen by the TEM, but EDS analysis confirmed that these particles are made up of Ti, not Ce.

Sample W4 appears to be a significant challenge with respect to characterizing sample morphology and size.

Sample X5 (Figures A-1C and A-1D) is also aggregated and appears to have a much higher packing density than sample W4. It has a wide range of aggregate sizes, 0.18 μm to 3.4 μm, with small constituent particles, ~13 nm in diameter. The aggregate size distribution is bimodal, with a few large fused particles and a number of much smaller aggregates that might have been fractured as 'daughter' aggregates during sonication. TEM images of this material does not show any films, with constituent particles ranging from ~3.9 nm to ~36 nm. The average particle size estimates from BET and XRD are still within the size range as determined by TEM, but are larger than the average of 13 nm, 31.5 nm (XRD) and 40.3 nm (BET).

Sample Y6 is aggregated, however, these structures were not reported by the manufacturer. Figure A-1E shows a lacey, open structure of an aggregate with a length of ~25 μm. The average aggregate size is 8 μm. The constituent particles have an average size of 22 nm, consistent with the manufacturer's reported value of ~25 nm (Table A-1).

Figure A-1F shows constituent particles of sample Y6, which have trapezoidal and triangular morphologies. These are aggregated on the ~100 nm scale, suggesting complex morphologies over several scales. The open lacey structure of the assembled particles in Figure A-1F suggests that an average constituent particle size estimate based on BET measurements should correspond well to that estimated from measurements based on TEM images. Table A-2 shows that the asymmetric crystallites range from 7 to 59 nm in dimensions with an average Feret diameter value of 22 ± 12 nm. Feret diameters are based

on the maximum length of the particles [233]. Analysis of the XRD data using the Debye-Scherrer formula [Equation (1-2)] estimates an average crystallite size of 28.7 nm. The BET specific surface area is 40.3 m^2/g, which corresponds to an average equivalent circular diameter of 20.6 nm. Note that, for asymmetrical particles, the equivalent circular diameter is expected to be less than the Feret diameter. These three size estimates seem to be self-consistent based on the observed morphology of sample Y6.

Sample Z7 was expected to have the smallest crystallites of any of the nanoceria based on the manufacturer's report (Table A-1). The SEM (Figure A-1G) shows very large aggregates with interior voids, possible gas bubbles formed by rapid drying of micron-scale particles. However, TEM images, such as Figure A-1H, show fine crystallites with narrow size distributions. These crystallites range from 7.3 to 21 nm (Feret diameter) with an average size of 13 ± 3.6 nm, as determined by tracing around crystallites with clearly defined edges [142]. The BET specific surface area is 57 m^2/g, which corresponds to an average equivalent circular diameter of 14.6 nm. The average diameter based on sample Z7's XRD data is 10.3 nm. As the BET data and the TEM data give similar estimates for the average diameter, it is likely that most of the surface area of individual crystallites is accessible to nitrogen molecules, i.e., the aggregates appear to be 'lightly' fused together. Ultrasonication for dispersion of the sample during TEM mounting did not seem to fracture many of the micron-scale aggregates and few, if any, constituent particles were observed individually. Many of the crystallites show regular light and dark bands, which are characteristic of crystal structures.
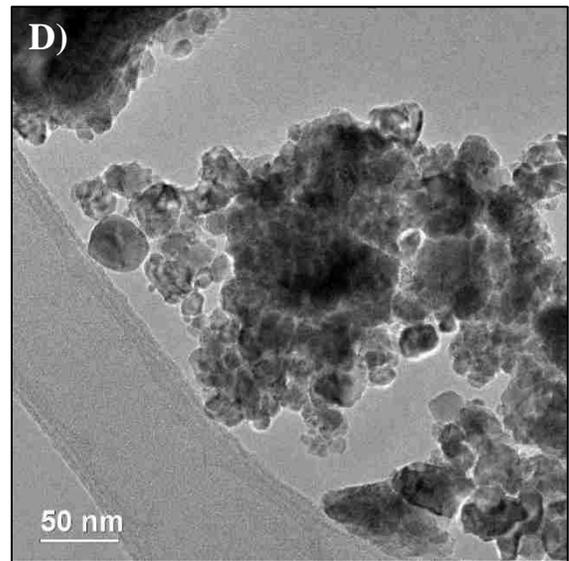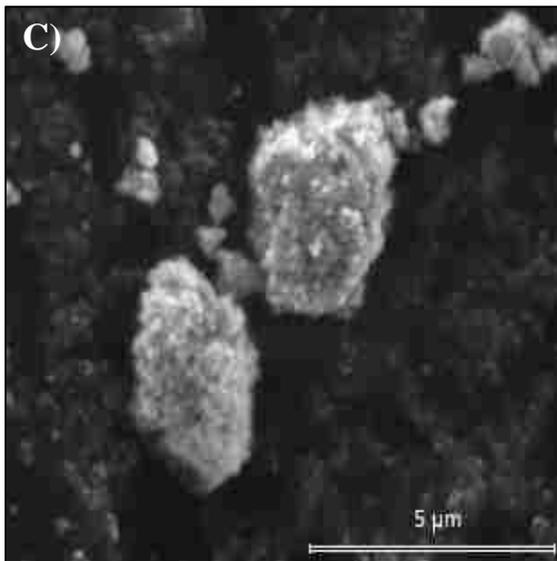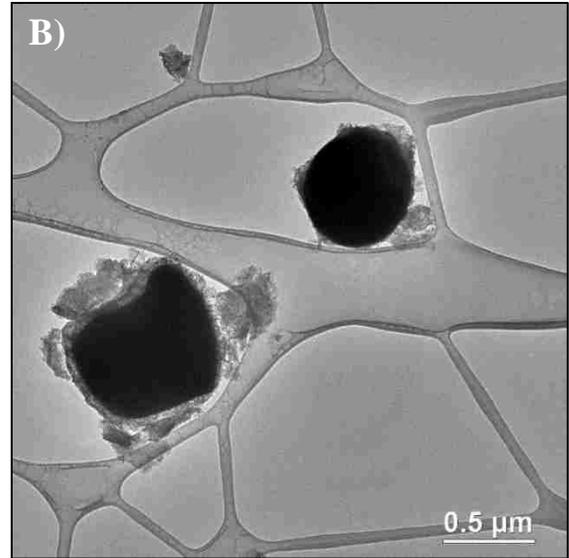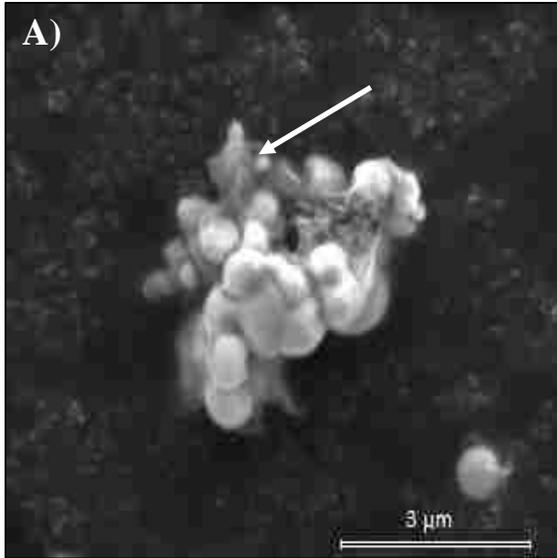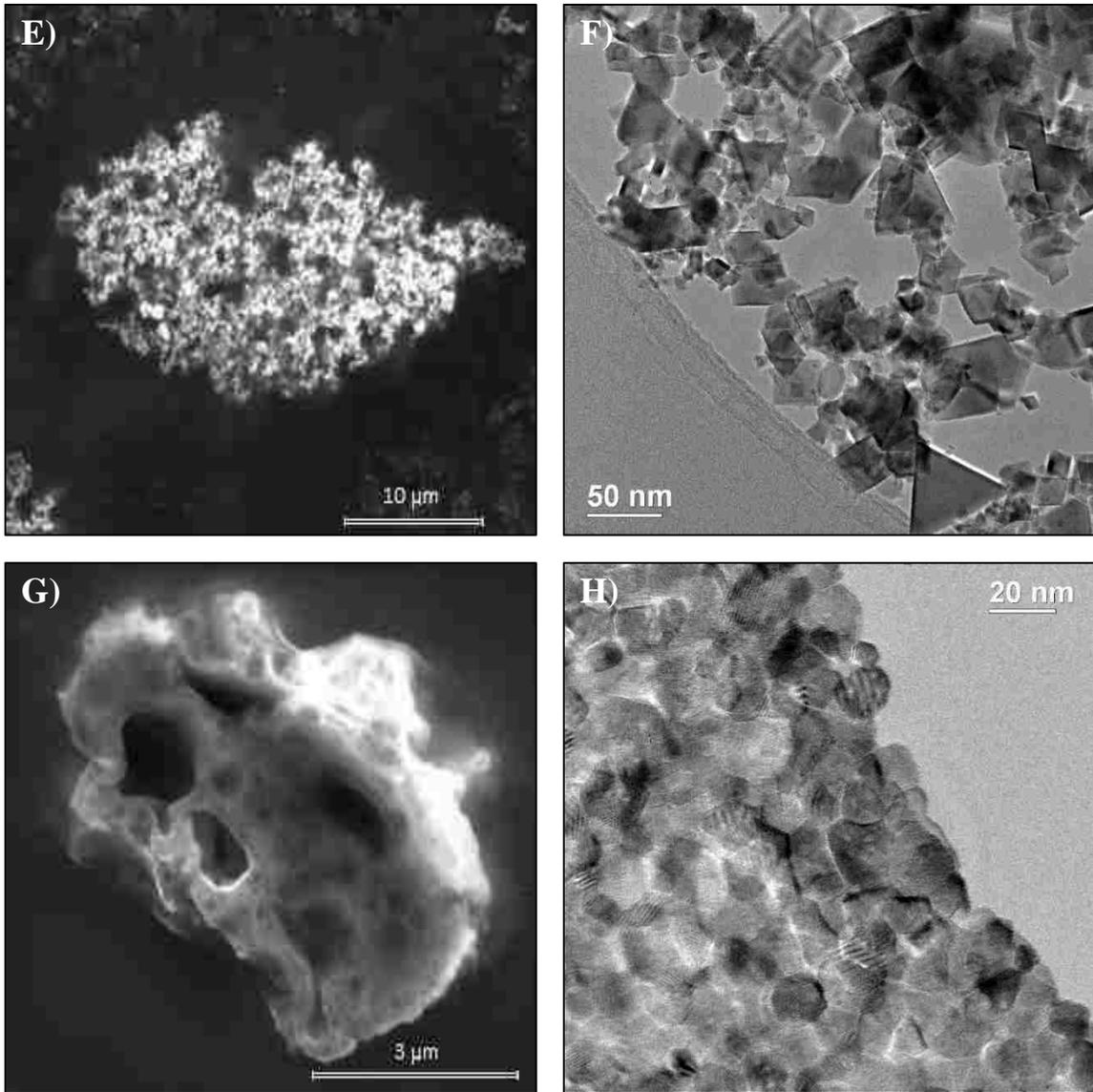
Figure A-1: EM images of ceria samples: (A) W4 – SEM; (B) W4 – TEM; (C) X5 – SEM; (D) X5 – TEM; (E) Y6 – SEM; (F) Y6 – TEM; (G) Z7 – SEM; and (H) Z7 – TEM.

The silica samples (J0, K1, and N2) are all amorphous and therefore no peaks are obtained from XRD. EDS analyses by both SEM and TEM showed only Si and O, but not cerium. Via atomic layer deposition, both the K1 and N2 samples were hoped to have thin shells of ceria on the colloidal silica cores, 1.5 nm and 2.5 nm respectively. Based on the reported colloidal silica size (~25 nm, Table A-1), the coated particles should contain 28.8 vol% and 42.1 vol% ceria, respectively. By either measure, there should have been sufficient ceria present on K1 and N2 to be detected by EDS. Ceria was also found to be missing from K1 and N2 in multiple ICP-OES and ICP-MS experiments.

Table A-2 shows the sizes of aggregate and constituent particles for the silica samples. All three silica samples have large aggregates, but the constituent particles have similar averages and standard deviations. The size estimate from BET correlate very well to those determined by TEM. Figure A-2 shows the aggregates and constituent particles of sample J0, the starting colloidal silica. The K1 and N2 samples are an exact replica of J0 since the ceria coating was unsuccessful. The constituent particles are fused together, making aciniform aggregates.
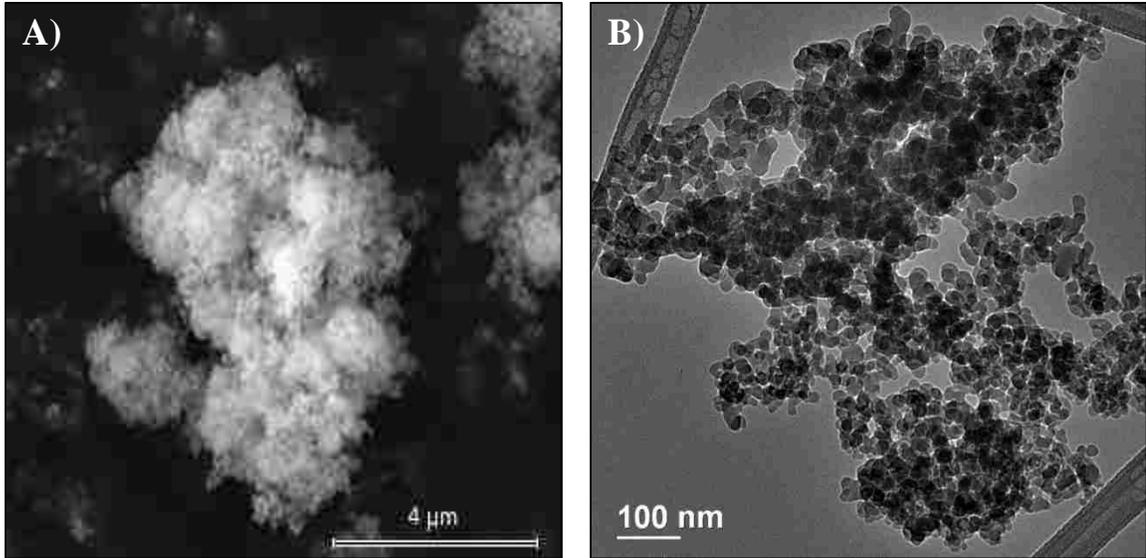
Figure A-2: EM images of silica samples: (A) J0 – SEM and (B) J0 – TEM.

Figure A-3 shows the copper and copper oxide materials. EDS showed the presence of Cu and O. Copper (8) aggregates ranged in size from 230 nm to ~8 microns with tightly packed constituent particles. Its constituent particles averaged 25 nm in size. Copper oxide (9) aggregates ranged from 450 nm to 4.5 microns, with a more open, aciniform structure. Its constituent particles averaged 46 nm in diameter. Table A-2 shows the detailed data, and also compares the constituent particle size estimates from BET and XRD data. The XRD data provide an average particle size based on the crystallites. The XRD estimate is similar to the TEM estimate for the copper sample, but not for the copper oxide sample. The technique used to estimate crystallite size was manual tracing around the constituent particles, which requires a clearly defined crystallite edges [142]. The packing of the copper oxide crystallites (Figure A-3D) makes it easier to find the edges, while the overlapping constituent particle images of the copper crystallites (Figure A-3B) makes the task more challenging. The constituent particle sizes estimated from the BET surface area data exceed both the XRD and TEM estimates. This suggests that the constituent particles of both samples are fused together sufficiently to reduce adsorption of nitrogen to crystallite surfaces.
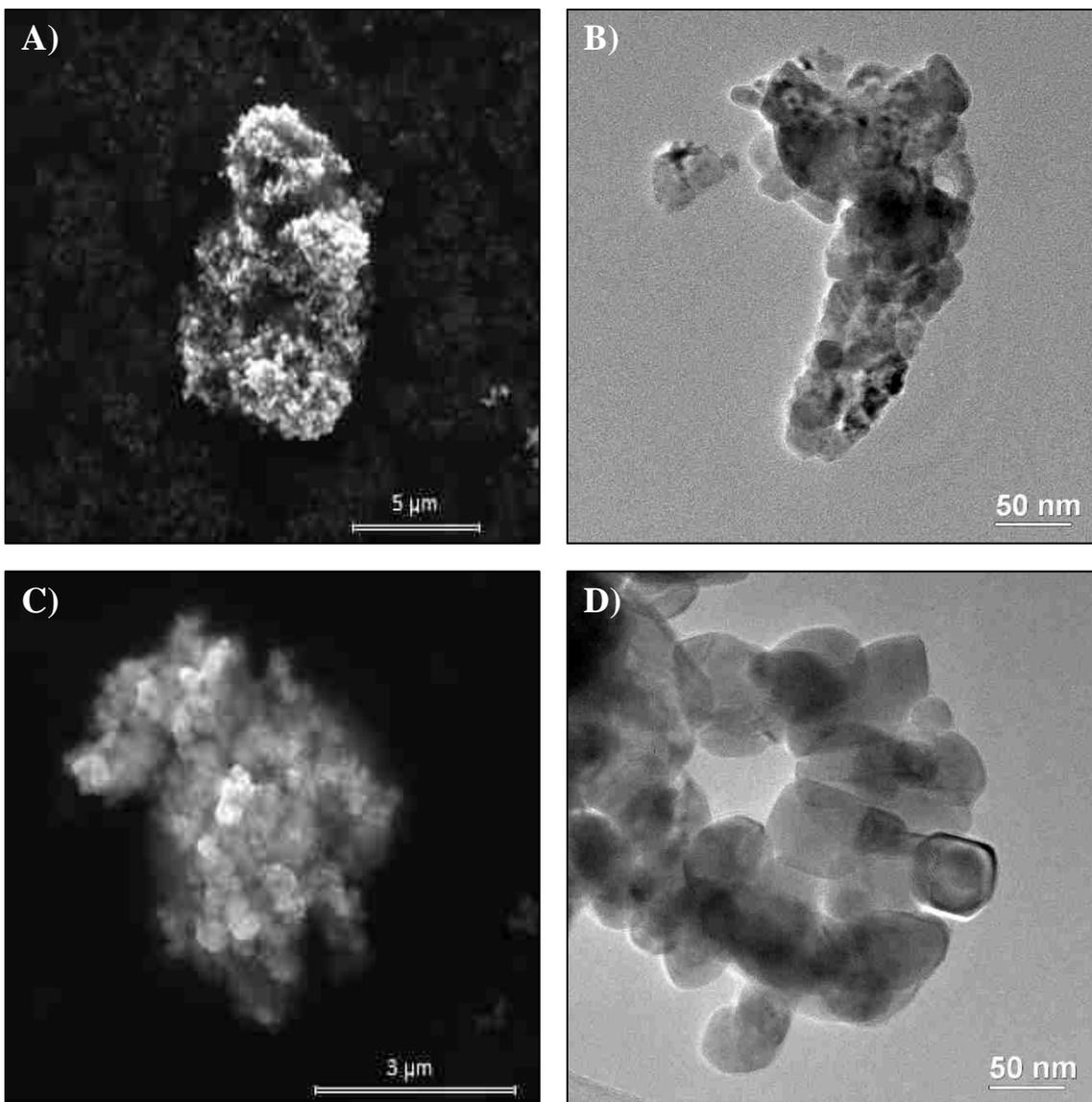
Figure A-3: EM images of copper and copper oxide samples: (A) Cu 8 – SEM; (B) Cu 8 – TEM; (C) CuO 9 – SEM; and (D) CuO 9 – TEM.

Figure A-4 shows silver aggregates and a silver constituent particle for samples R and S. Sample R is mostly composed of silver nanorods, which are aggregated into branched structures, appearing to originate from a specific nucleating site depicted in Figure A-4C. In Figure A-4A, the nanorod diameters are less than 1 micron in diameter. Figure A-4B shows a nanorod constituent particle with a diameter of ~400 nm and a length of ~3 microns (as small as 630 nm and as large as 12 μm). Figure A-4C shows a spherical nanoparticle with a diameter of approximately 48 nm. The silver nanorods changed size and shape after electron-beam illumination, so it is not clear what features are present in the as-received material and what features may have been developed during electron microscopy. Sample S has silver constituent particles assembled into aciniform aggregates (Figures A-4D and A-4E). They have an aggregate size of 2 μm containing 11.2 nm constituent particles on average, some were as large as 64.4 nm. XRD predicts crystallite particles of 34.8 nm, similar to that from TEM. However, the BET size estimate well exceeds that of the TEM and XRD size. SEM EDS showed the presence of Ag, O, and N in sample 'R' and Ag, O, and S in sample 'S'. Sample S was intended to have a glutathione capping/dispersing agent on the surface which can explain the sulfur atoms found by EDS.
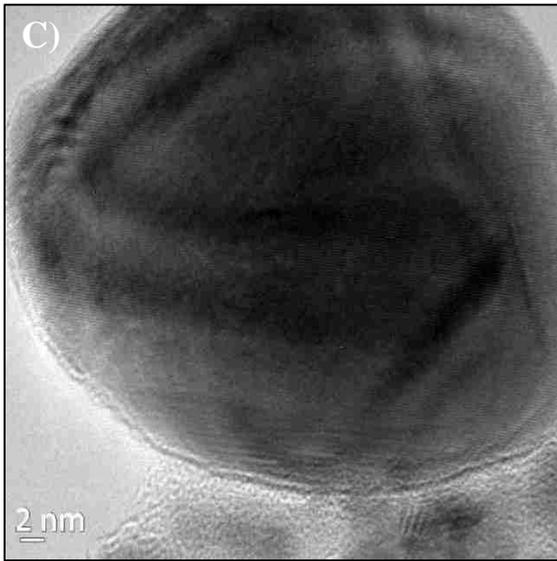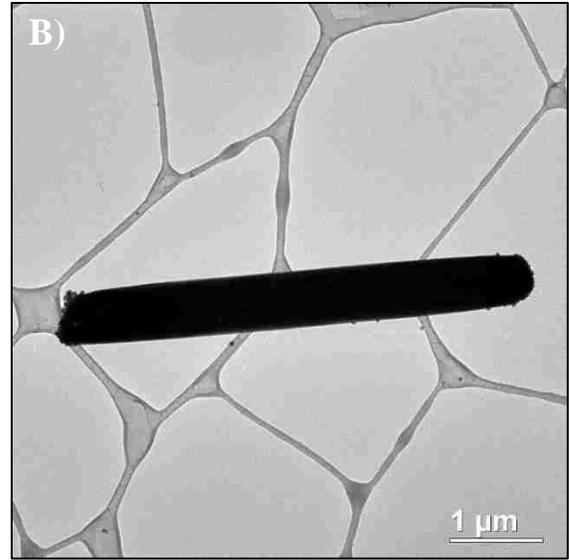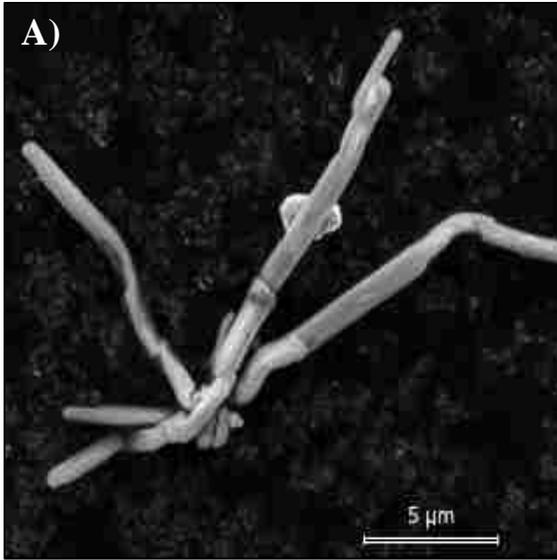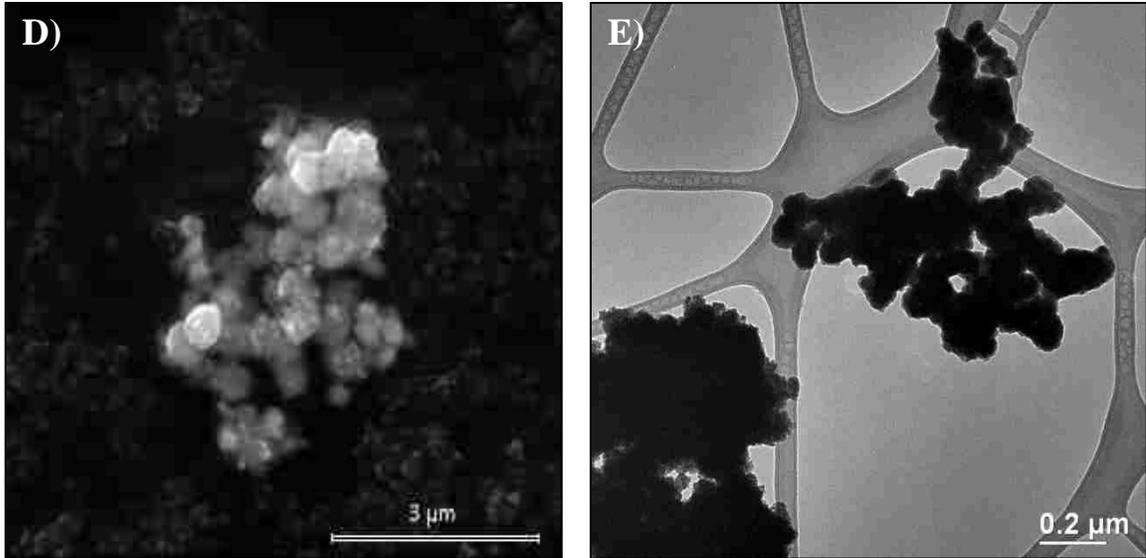
Figure A-4: EM images of silver samples: (A) R – SEM; (B) R – TEM, nanorod; (C) R – TEM, particle; (D) S – SEM; and (E) S – TEM.

XRD results are shown in Table A-3 and Figure A-5. The four ceria samples (W4, X5, Y6, and Z7) exhibit the cubic fluorite crystal structure (JCPDS card no. 34-0394) [98]. The silica samples (J0, K1, and N2) are amorphous. The copper sample (8) is FCC Cu (JCPDS card no. 01-1242) [234], however the crystal structure is altered to exhibit monoclinic CuO post-oxidation via TGA. The CuO sample (9) is monoclinic CuO (JCPDS card no. 80-1916) [235]. Finally, the two silver samples (R and S) are FCC Ag (JCPDS card no. 04-0783) [236].

Table A-3: Crystal structures as determined by XRD of all samples.

Code	Crystal Structure
CeO_2 W4	Cubic Fluorite
CeO_2 X5	Cubic Fluorite
CeO_2 Y6	Cubic Fluorite
CeO_2 Z7	Cubic Fluorite
SiO_2 J0	Amorphous
SiO_2 K1	Amorphous
SiO_2 N2	Amorphous
Cu 8	FCC Cu; Monoclinic CuO (post-TGA)
CuO 9	Monoclinic CuO
Ag R	FCC Ag
Ag S	FCC Ag

A)

B)
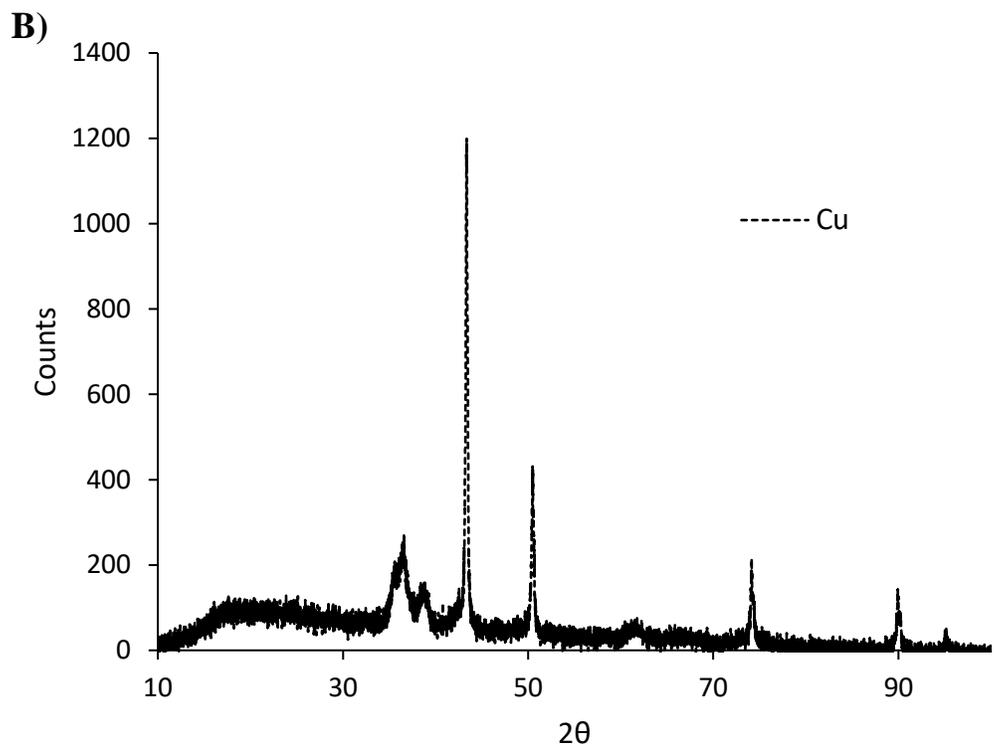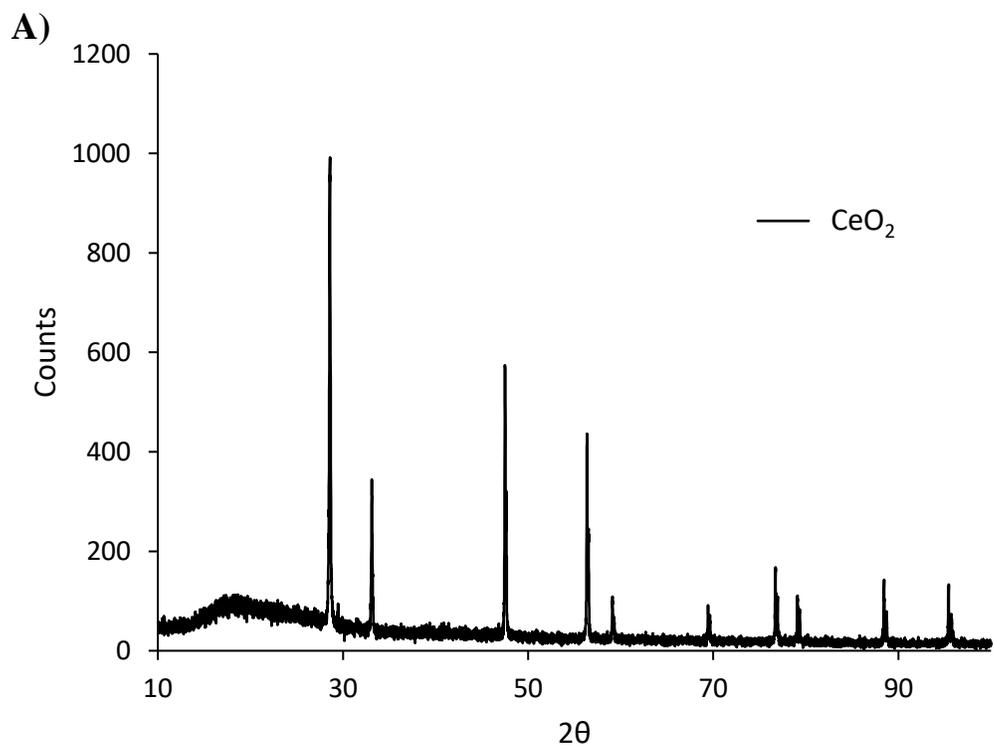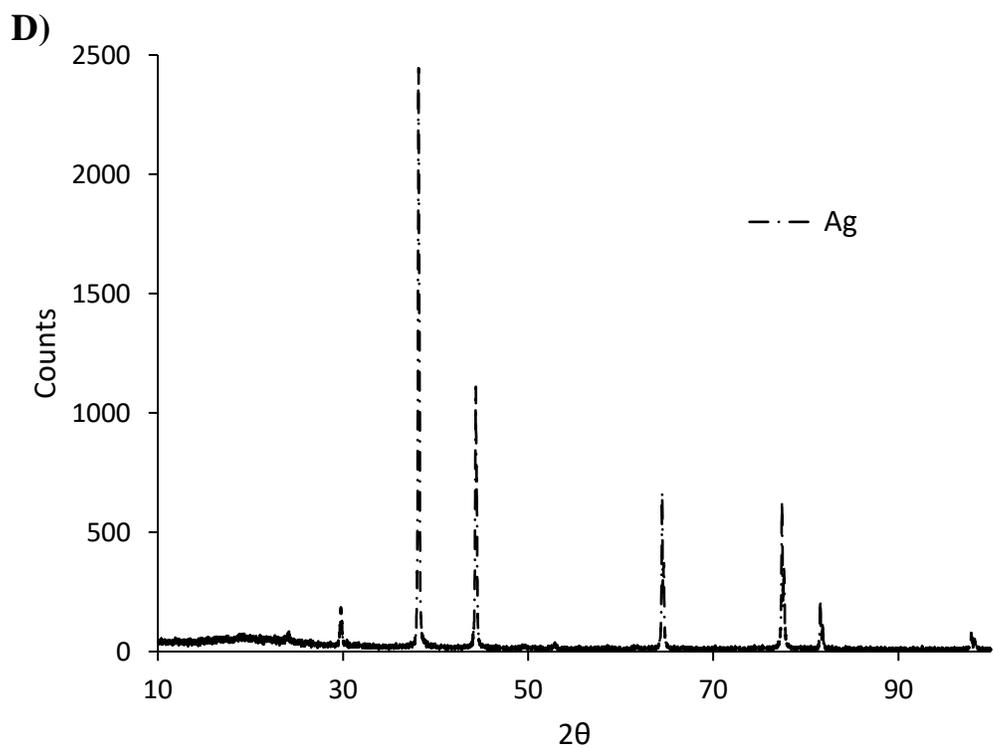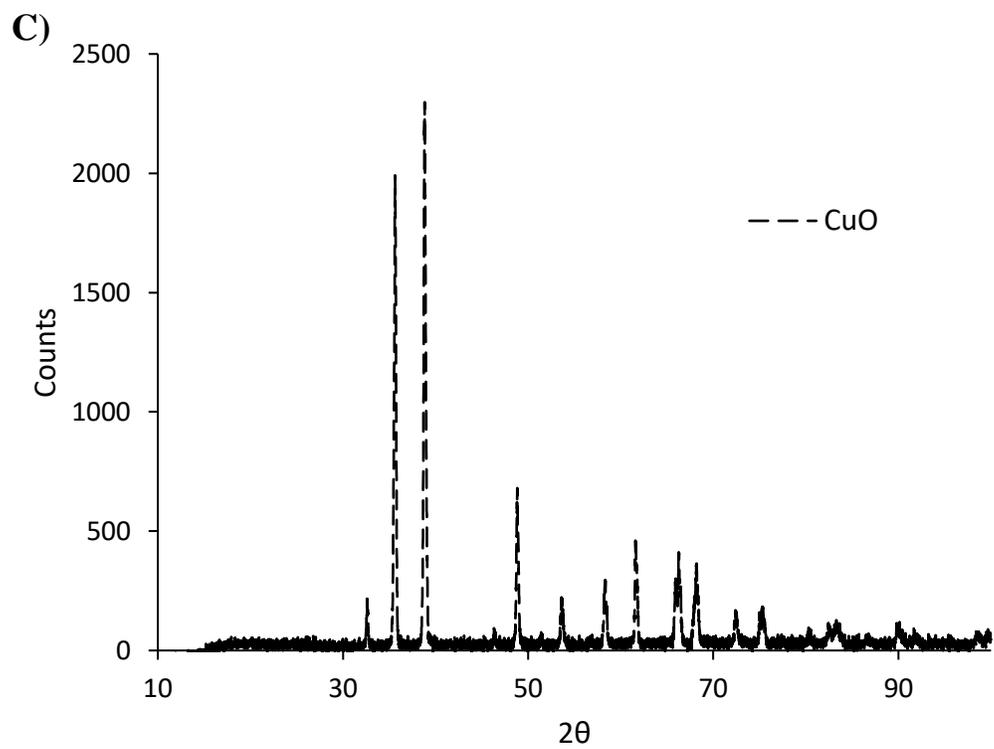
Figure A-5: XRD of (A) CeO$_2$; (B) Cu, (C) CuO; and (D) Ag.

212

The BET surface area measurements are as listed in Table A-4. The average primary particle size can be estimated from this measurement using Equation (A-1). The primary particle diameter, D, in meters is related to the surface area by:

$$D = \frac{0.006}{SA \, \rho} \qquad \text{(A-1)}$$

SA is the surface area obtained by BET (m^2/g) and ρ is the metal oxide density (kg/m^3). This estimate assumes that there is no internal porosity in the sample, either in primary particles or between aggregates, i.e., the nitrogen adsorbs on the external surface of discrete particles. The average diameter of each particle estimated by the BET surface area is relatively similar to those measured by TEM.

Table A-4: BET data and estimates of average constituent particle diameters.

Code	Density, ρ	BET, SA	D, avg
	(kg/m^3)	$(m^2$/g)	(nm)
CeO$_2$ W4	7220	52.8	15.7
CeO$_2$ X5	7220	20.6	40.3
CeO$_2$ Y6	7220	40.3	20.6
CeO$_2$ Z7	7220	57.0	14.6
SiO$_2$ J0	2650	137	16.5
SiO$_2$ K1	2650	129	17.6
SiO$_2$ N2	2650	121	18.7
Cu 8	8960	10.4	64.4
CuO 9	6310	10.8	88.0
Ag R	10490	-	-
Ag S	10490	7.33	78.0

EELS can provide information about the surface oxidation state of cerium, i.e., Ce^{3+} or Ce^{4+}. Figure A-6 shows the M5/M4 peaks of sample Y6. The oxidation state of the elements present in the specimen will affect the ionization edges in the high-loss region of the EELS spectrum. The relative intensities of the M5 and M4 peaks are directly related to Ce^{3+} and Ce^{4+} concentrations, respectively. In Figure A-6A, the M5 peak is less than the M4 peak, which means the nanoceria core has a higher concentration of Ce^{4+} atoms. However, in Figure A-6B, the M5 peak on the edge of the particle is equivalent to the M4 peak, showing that the Ce^{3+} concentration increases towards the outer edge of the particles [96]. All four ceria samples (W4, X5, Y6, and Z7) show Ce^{4+} rich particles on average.
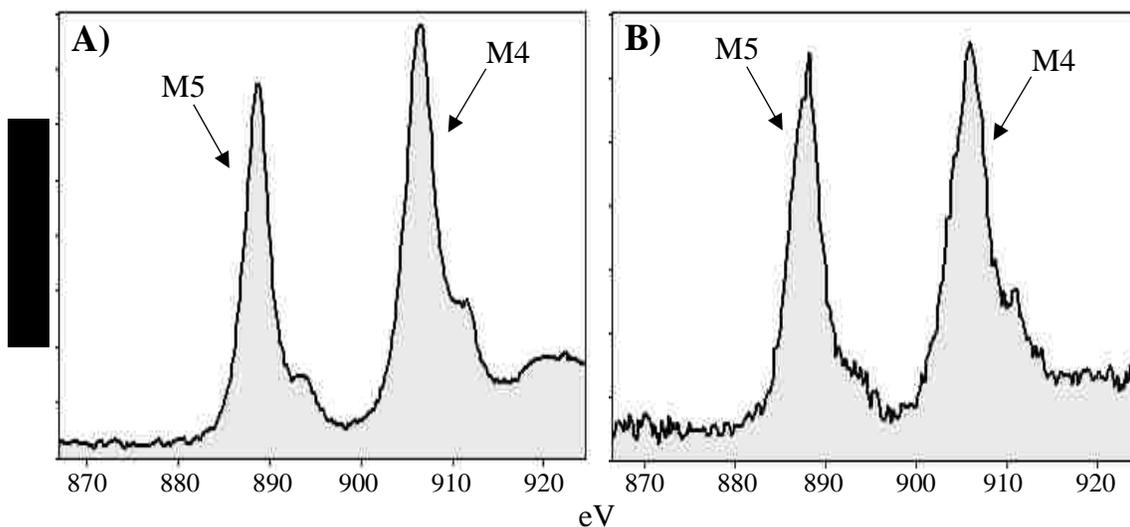
Figure A-6: EELS analysis of nanoceria particles: intensity as a function of eV. (A) Y6 (core) – M5<M4; (B) Y6 (edge) – M5=M4.

Dynamic light scattering data of aqueous dispersions can help demonstrate what the biological system can 'see' for *in vitro* or *in vivo* experiments. Table A-5 shows the presence of multimodal peaks of nanoparticle assembles in aqueous dispersions on a surface area fraction basis using the multimodal analysis tool. DLS can detect particles of several nanometers in size to particles over one micron in size. It is less accurate for sizes greater than several microns.

Sample W4 had no particles less than 250 nm and none were detected ($<$ 1-2%) by DLS. It had one peak near 700 nm and a second of 2.5 microns, consistent with the TEM and SEM data (590 nm and 1.75 μm, respectively). Samples X5, Y6, and Z7 all had constituent particles less than 100 nm (13, 22, and 13 nm, respectively), but no peaks were observed by DLS in this range. Sample X5 had aggregates of 730 nm by SEM, but only two peaks, 110 nm and 380 nm, were observed by DLS. Samples Y6 had large aggregates, 8.3 microns, which were not reported by DLS (above observable range). Sample Z7 had large aggregates of 4.4 microns, which were reported as a smaller peak by DLS. These data suggest that all ceria samples are agglomerated to some degree in aqueous dispersions.

All three silica samples have large scale aggregates of several hundred nanometers. Sample J0 was the base material used in the attempt to coat with ceria. The sizes of samples K1 and N2 are slightly smaller. Aciniform solids tend to fracture near nodule necks during sonication but rarely generate single constituent particles during such processing [237]. According to DLS, 175 nm particles are present in K1 that are not visible in J0 or N2. Also, J0 and N2 have particles in the micron range and K1 does not. However, according to SEM, all three samples have particles in the micron range. This is due to the drying effect on a SEM stub that may reverse the effects of sonication.

Aqueous dispersions of the copper sample (8) showed peaks at 160 and 580 nm. Larger aggregates were not detected as they likely settled from the solution quickly due to copper's high specific gravity. Copper oxide (9) aggregates had peaks at 650 nm and 2.2 microns. No DLS peaks near the average constituent particle sizes were observed for either of these samples. It appears that both samples are highly aggregated in water dispersions.

Aqueous dispersions of the silver sample R showed peaks at 150 and 580 nm. Sample S showed similar results of 210 and 650 nm. As with the copper samples, larger aggregates were not detected as they likely settled from the solution quickly due to silver's high specific gravity. DLS peaks near the average constituent particle sizes were not observed for either sample, however some particles were measured as small as 600-700 nm similar to the upper peaks from DLS.

Table A-5: DLS multimodal peaks of nanoparticle assemblies in aqueous dispersions.

	DLS Peaks		
Code	100-250 nm	250-1000 nm	> 1 μm
CeO_2 W4	-	700	2.5
CeO_2 X5	110	380	-
CeO_2 Y6	100	360	-
CeO_2 Z7	200	-	1.3
SiO_2 J0	-	650	2.7
SiO_2 K1	175	600	-
SiO_2 N2	-	350	1.0
Cu 8	160	580	-
Cu 9	-	650	2.2
Ag R	150	580	-
Ag S	210	650	-

Table A-6: Comparison of TGA data for all samples.

	TGA weight loss, %			
Code	Total	Free H_2O	Organics	Notes
CeO$_2$ W4	-8.1%	-2.2%	-5.9%	
CeO$_2$ X5	-1.0%	-0.4%	-0.6%	
CeO$_2$ Y6	-1.7%	-0.2%	-1.5%	
CeO$_2$ Z7	-2.4%	-1.2%	-1.2%	
SiO$_2$ J0	-6.9%	-2.5%	-4.4%	
SiO$_2$ K1	-6.9%	-2.6%	-4.3%	
SiO$_2$ N2	-7.3%	-2.4%	-4.9%	
Cu 8	11.0%	-0.6%	-0.3%	T < 200°C
			11.9%	T > 200°C
CuO 9	-12.0%	-0.9%	-11.1%	
Ag R	-3.9%	-0.5%	-1.6%	T < 220°C
			-1.8%	T > 220°C
Ag S	-8.6%	-0.5%	-8.1%	

Figure A-7B shows the loss of material from the ceria samples as determined by TGA. Free, chemisorbed surface water is released by holding the sample at 125 °C for 30 minutes (reported in Table A-6). There are two typical causes for weight loss after removal of free water. One is that surface hydroxyls can condense under these conditions and release water. The second is the presence of organic surface coatings, which will pyrolyze as the temperature is increased. Samples X5, Y6, and Z7 show weight losses of ~1 wt% after loss of free water. Sample W4 loses about 6 wt% after the loss free water, suggesting that it has an organic surface coating. The organic weight losses are in the order, X5 < Z7 < Y6 < W4. By the technique of TEM and SEM, W4 had a surface 'film' (Figure A-1A and A-1B). FTIR (Figure A-7A) suggests that W4 and Y6 contain a carboxylic acid group, while X5 and Z7 contain a carbon-carbon double bond (Table A-7). All four samples contain surface hydroxyl groups and -C-H bonds. Only W4 contains a -C-O bond potentially as an ether.

Table A-7: FTIR surface chemistries of ceria samples.

	Group ID								
	-OH	-COOH		-C=C-		-C-H			-C-O-
Code				wave number (cm^{-1})					
CeO$_2$ W4	3303	1623	1397					1186	1067
CeO$_2$ X5	3398			1643	1549	1452			
CeO$_2$ Y6	3445	1623	1415		1536		1329		
CeO$_2$ Z7	3340			1654	1519		1339		
Average	3372	1623	1406	1649	1535	1452	1334	1186	1067
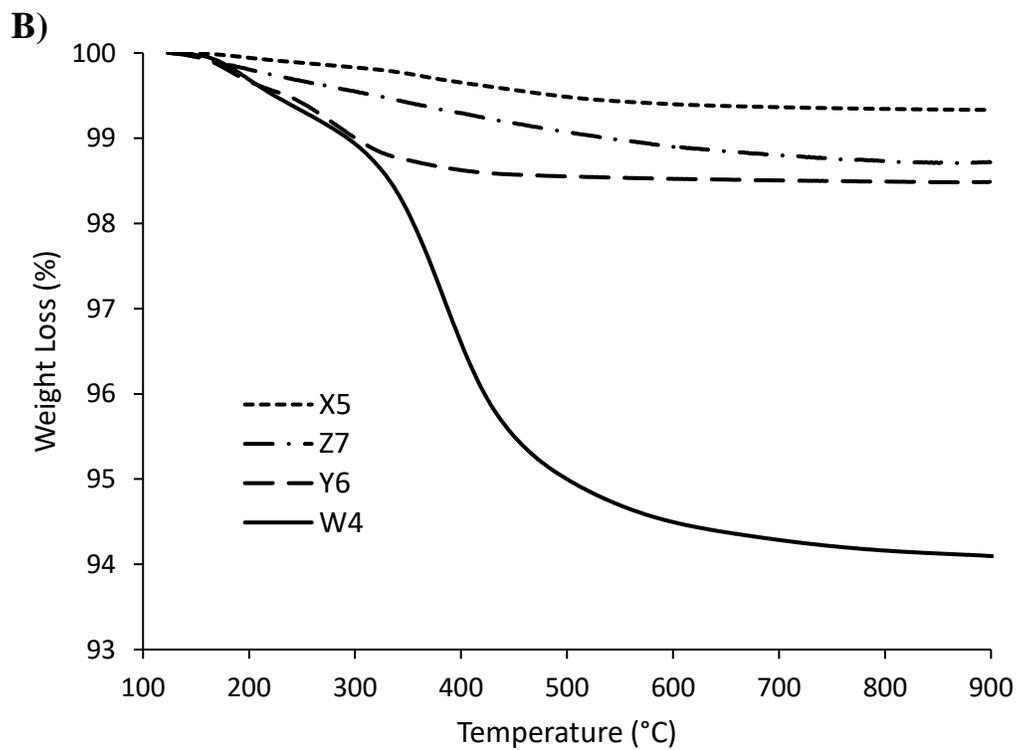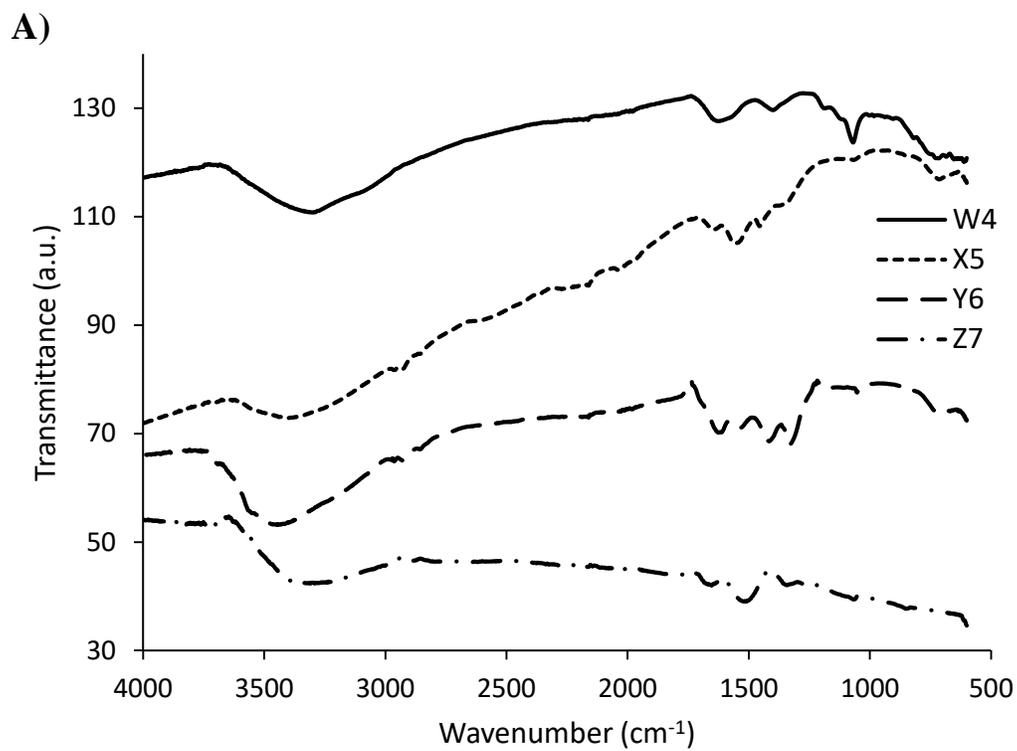
Figure A-7: (A) FTIR and (B) TGA results of ceria samples.

Figure A-8A shows FTIR surface chemistries of the silica samples. As shown in Table A-8, the major peaks were the hydroxyl (3410 cm^{-1}) and the Si-O peaks (1081 and 799 cm^{-1}). There appears to a small organic component on all three samples, as shown by the small -COOH peak (1630 cm^{-1}) and small -C-H peak (957 cm^{-1}). Although these samples were thought to be coated with cerium dioxide, no Ce-O groups were detected by FTIR. The TGA scans of the three samples were similar (Figure A-8B and Table A-6). The total amount of loss averaged $7.0 \pm 0.23\%$. The free water lost by holding samples at 125 °C was $2.5 \pm 0.10\%$ with the remaining loss of $4.5 \pm 0.32\%$ of volatiles, which would be mostly water of condensation. The atomic layer deposition 'coated' samples were devoid of a ceria coating and thus not different from J0 in respect to Ce content.

Table A-8: FTIR surface chemistries of silica samples.

	Group ID				
	-OH	-COOH	-Si-O-	-C-H	-Si-O-
Code	wave number (cm^{-1})				
SiO$_2$ J0	3410	1630	1081	957	799
SiO$_2$ K1	3410	1625	1066	959	797
SiO$_2$ N2	3410	1630	1081	954	797
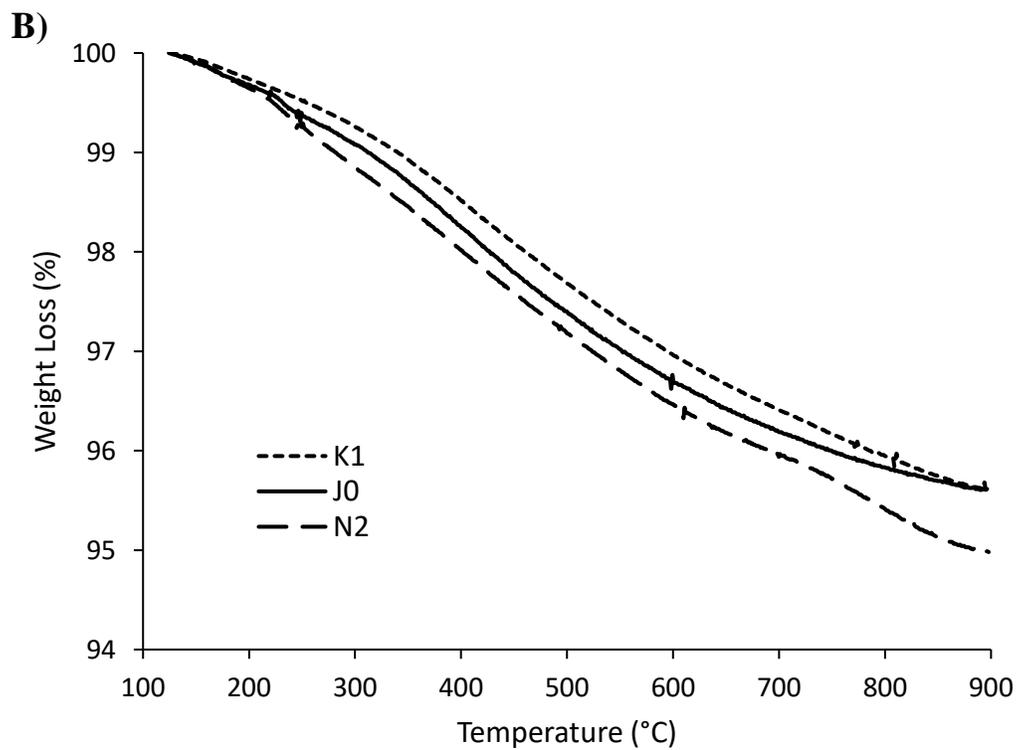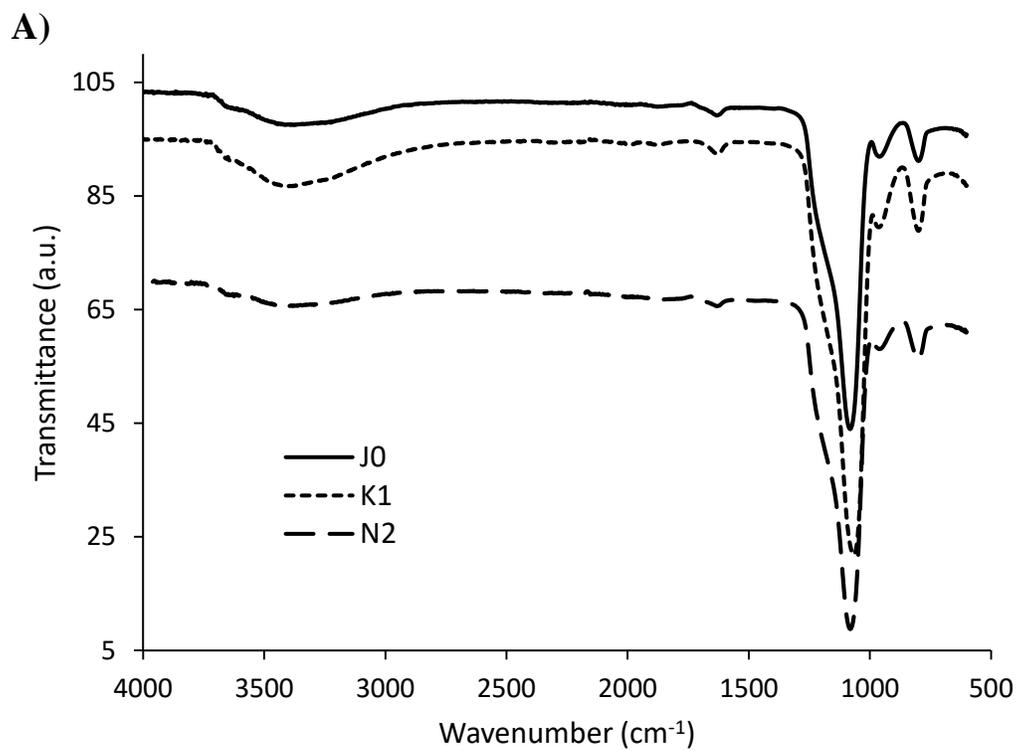
Figure A-8: (A) FTIR and (B) TGA results of silica samples.

No extraneous material was observed on the surface of the copper sample (8) by FTIR (Figure A-9A). The copper oxide sample (9) has hydroxyl groups, which are expected for uncalcined metal oxides, and some organic groups, specifically, -C-H and -C-O (Table A-9). The presence of these groups suggest that the CuO sample has an organic surface coating.

The copper sample (8) actually gained weight in the TGA experiment (Figure A-9B and Table A-6). This was due to the oxidation of the copper to copper oxide, likely by oxygen contaminants in the nitrogen. XRD confirmed that the CuO crystal structure was present in the copper sample post-TGA analysis. FTIR scans showed that the copper oxide sample (9) had a modest organic coating; it lost about 11% of its weight after free water was removed, the majority of which was at temperatures above 700 °C.

Table A-9: FTIR surface chemistries of copper and copper oxide samples.

	Group ID		
	-OH	-C-H	-C-O-
Code	wave number (cm^{-1})		
Cu 8			
CuO 9	3445	1437	1122
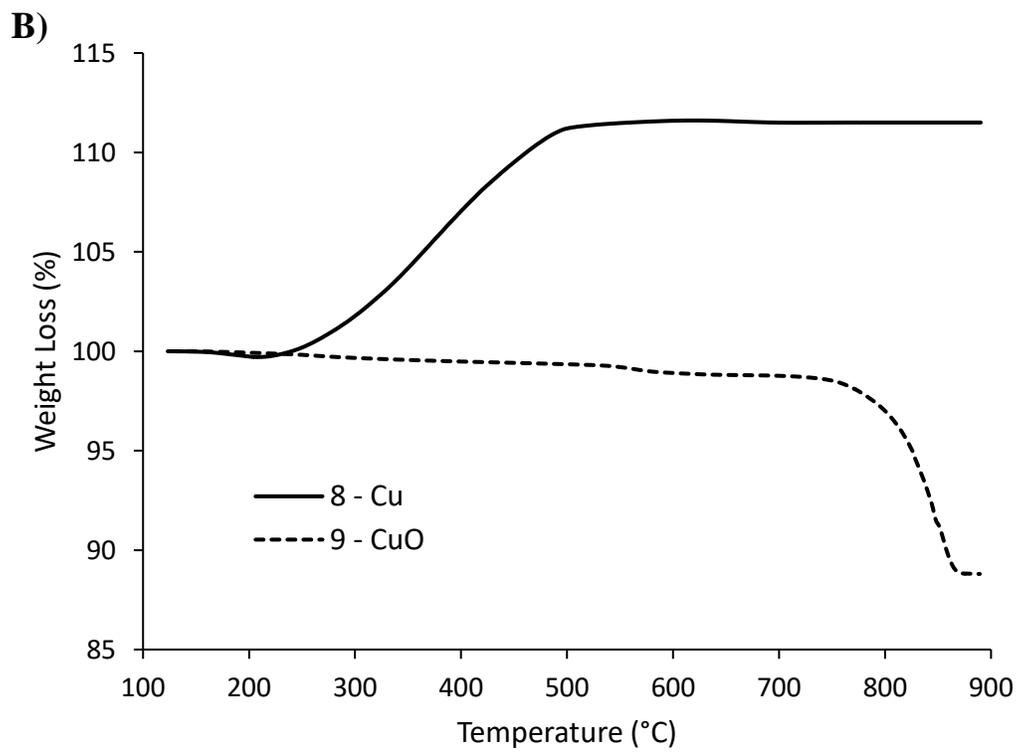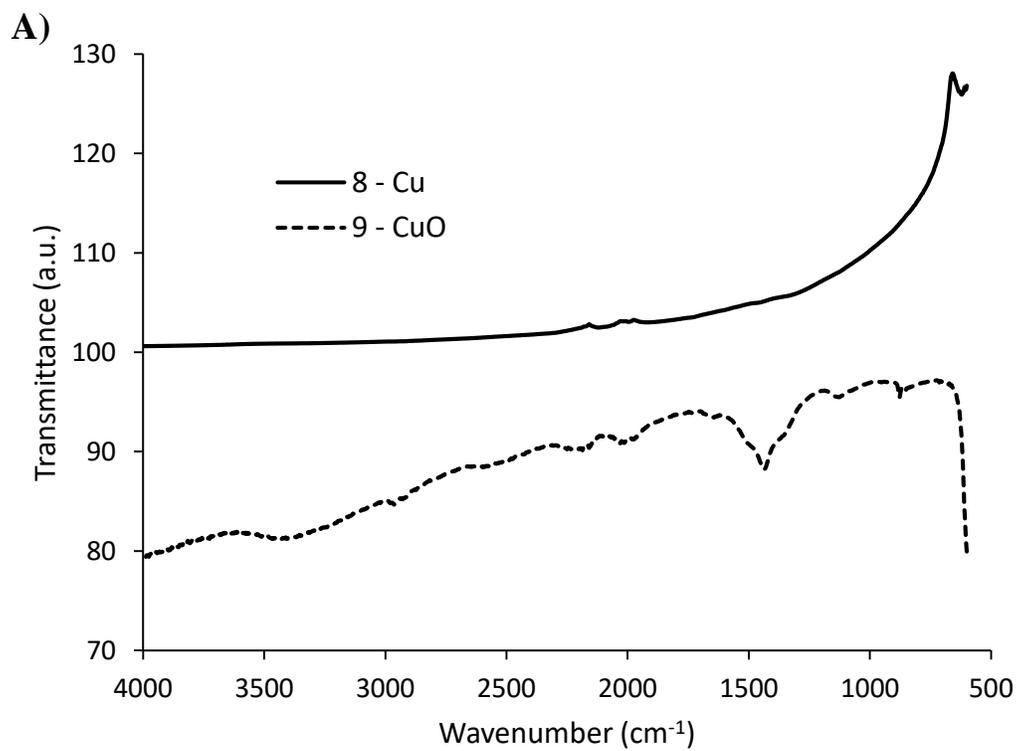
Figure A-9: (A) FTIR and (B) TGA results of copper and copper oxide samples.

The FTIR (Figure A-10A) for the silver sample R showed a hydroxyl, carbon-carbon triple bond, and also small -C-H and -C-O- peaks (Table A-10). Although TGA (Figure A-10B and Table A-6) only reported a loss of 3.4 wt% after free water was removed, two peaks at different temperatures show that there is a small organic surface coating potentially consisting of a carbon-carbon triple bond. The TGA for silver sample S resulted in an 8.1 wt% loss after free water was removed, presumably from the glutathione coating. However, no compositional data was obtained by FTIR.

Table A-10: FTIR surface chemistries of silver samples.

	Group ID			
	-OH	-C≡C-	-C-O-	-C-H
Code	wave number (cm^{-1})			
Ag R	3304	2160	1104	1033
Ag S				
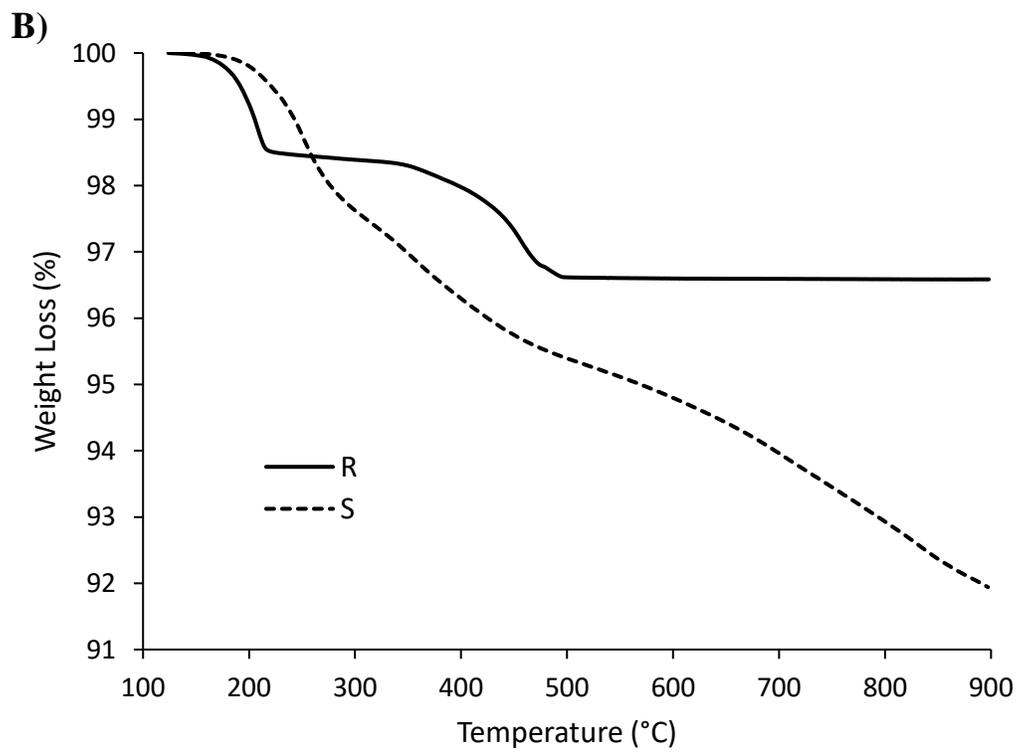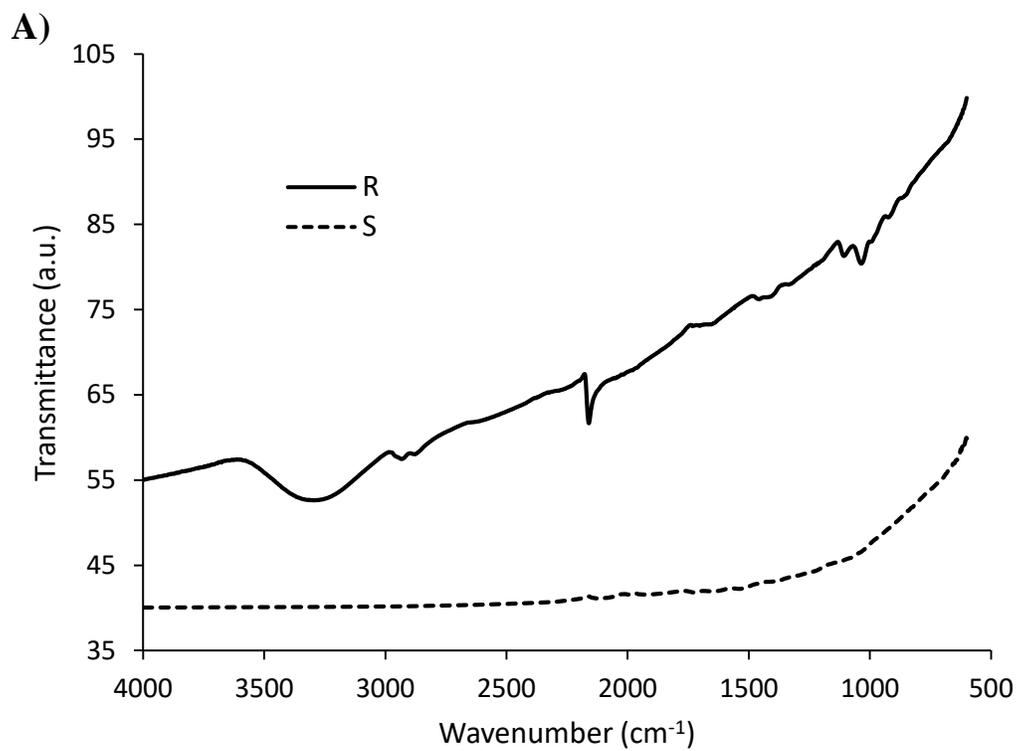
Figure A-10: (A) FTIR and (B) TGA results of silver samples.

REFERENCES

[1]   S. D. Senanayake, D. Stacchiola, and J. A. Rodriguez, "Unique properties of ceria nanoparticles supported on metals: novel inverse ceria/copper catalysts for CO oxidation and the water-gas shift reaction," *Accounts of Chemical Research,* vol. 46, no. 8, pp. 1702-1711, 2013.

[2]   S. Hilaire, X. Wang, T. Luo, R. Gorte, and J. Wagner, "A comparative study of water-gas-shift reaction over ceria supported metallic catalysts," *Applied Catalysis A: General,* vol. 215, no. 1-2, pp. 271-278, 2001.

[3]   M. Yakimova, V. Ivanov, O. Polezhaeva, A. Trushin, A. Lermontov, and Y. D. Tretyakov, "Oxidation of CO on nanocrystalline ceria promoted by transition metal oxides," *Doklady Chemistry,* vol. 427, no. 2, pp. 186-189, 2009.

[4]   S. Tsunekawa, R. Sahara, Y. Kawazoe, and A. Kasuya, "Origin of the blue shift in ultraviolet absorption spectra of nanocrystalline CeO_{2-x} particles," *Materials Transactions, JIM,* vol. 41, no. 8, pp. 1104-1107, 2000.

[5]   M. Yamashita, K. Kameyama, S. Yabe, S. Yoshida, Y. Fujishiro, T. Kawai, and T. Sato, "Synthesis and microstructure of calcia doped ceria as UV filters," *Journal of Materials Science,* vol. 37, no. 4, pp. 683-687, 2002.

[6]   E. Bekyarova, P. Fornasiero, J. Kašpar, and M. Graziani, "CO oxidation on $Pd/CeO_2–ZrO_2$ catalysts," *Catalysis Today,* vol. 45, no. 1-4, pp. 179-183, 1998.

[7]   S. Patil, S. Kuiry, S. Seal, and R. Vanfleet, "Synthesis of nanocrystalline ceria particles for high temperature oxidation resistant coating," *Journal of Nanoparticle Research,* vol. 4, no. 5, pp. 433-438, 2002.

[8]   H. Yahiro, Y. Baba, K. Eguchi, and H. Arai, "High temperature fuel cell with ceria-yttria solid electrolyte," *Journal of the Electrochemical Society,* vol. 135, no. 8, pp. 2077-2080, 1988.

[9]   T. Masui, M. Yamamoto, T. Sakata, H. Mori, and G.-y. Adachi, "Synthesis of BN-coated CeO_2 fine powder as a new UV blocking material," *Journal of Materials Chemistry,* vol. 10, no. 2, pp. 353-357, 2000.

[10] S. Yabe, and T. Sato, "Cerium oxide for sunscreen cosmetics," *Journal of Solid State Chemistry,* vol. 171, no. 1-2, pp. 7-11, 2003.

[11] H. Inaba, and H. Tagawa, "Ceria-based solid electrolytes," *Solid State Ionics,* vol. 83, no. 1-2, pp. 1-16, 1996.

[12] J. G. Dale, S. S. Cox, M. E. Vance, L. C. Marr, and M. F. Hochella Jr, "Transformation of cerium oxide nanoparticles from a diesel fuel additive during combustion in a diesel engine," *Environmental Science & Technology,* vol. 51, no. 4, pp. 1973-1980, 2017.

[13] D. Speed, P. Westerhoff, R. Sierra-Alvarez, R. Draper, P. Pantano, S. Aravamudhan, K. L. Chen, K. Hristovski, P. Herckes, and X. Bi, "Physical, chemical, and in vitro toxicological characterization of nanoparticles in chemical mechanical planarization suspensions used in the semiconductor industry: towards environmental health and safety assessments," *Environmental Science: Nano,* vol. 2, no. 3, pp. 227-244, 2015.

[14] J. B. Hedrick, and S. P. Sinha, "Cerium-based polishing compounds: discovery to manufacture," *Journal of Alloys and Compounds,* vol. 207, pp. 377-382, 1994.

[15] C. Walkey, S. Das, S. Seal, J. Erlichman, K. Heckman, L. Ghibelli, E. Traversa, J. F. McGinnis, and W. T. Self, "Catalytic properties and biomedical applications of cerium oxide nanoparticles," *Environmental Science: Nano,* vol. 2, no. 1, pp. 33-53, 2015.

[16] M. Pešić, A. Podolski-Renić, S. Stojković, B. Matović, D. Zmejkoski, V. Kojić, G. Bogdanović, A. Pavićević, M. Mojović, and A. Savić, "Anti-cancer effects of cerium oxide nanoparticles and its intracellular redox activity," *Chemico-Biological Interactions,* vol. 232, pp. 85-93, 2015.

[17] Y. Gao, K. Chen, J.-l. Ma, and F. Gao, "Cerium oxide nanoparticles in cancer," *OncoTargets and Therapy,* vol. 7, pp. 835, 2014.

[18] H. Li, Z.-Y. Yang, C. Liu, Y.-P. Zeng, Y.-H. Hao, Y. Gu, W.-D. Wang, and R. Li, "PEGylated ceria nanoparticles used for radioprotection on human liver cells under γ-ray irradiation," *Free Radical Biology and Medicine,* vol. 87, pp. 26-35, 2015.

[19] R. A. Madero-Visbal, B. E. Alvarado, J. F. Colon, C. H. Baker, M. S. Wason, B. Isley, S. Seal, C. M. Lee, S. Das, and R. Mañon, "Harnessing nanoparticles to

improve toxicity after head and neck radiation," *Nanomedicine: Nanotechnology, Biology and Medicine,* vol. 8, no. 7, pp. 1223-1231, 2012.

[20] V. C. Minarchick, P. A. Stapleton, E. M. Sabolsky, and T. R. Nurkiewicz, "Cerium dioxide nanoparticle exposure improves microvascular dysfunction and reduces oxidative stress in spontaneously hypertensive rats," *Frontiers in Physiology,* vol. 6, pp. 339, 2015.

[21] J. Niu, A. Azfer, L. M. Rogers, X. Wang, and P. E. Kolattukudy, "Cardioprotective effects of cerium oxide nanoparticles in a transgenic murine model of cardiomyopathy," *Cardiovascular Research,* vol. 73, no. 3, pp. 549-559, 2007.

[22] K. L. Heckman, W. DeCoteau, A. Estevez, K. J. Reed, W. Costanzo, D. Sanford, J. C. Leiter, J. Clauss, K. Knapp, and C. Gomez, "Custom cerium oxide nanoparticles protect against a free radical mediated autoimmune degenerative disease in the brain," *ACS Nano,* vol. 7, no. 12, pp. 10582-10596, 2013.

[23] M. Das, S. Patil, N. Bhargava, J.-F. Kang, L. M. Riedel, S. Seal, and J. J. Hickman, "Auto-catalytic ceria nanoparticles offer neuroprotection to adult rat spinal cord neurons," *Biomaterials,* vol. 28, no. 10, pp. 1918-1925, 2007.

[24] L. L. Wong, and J. F. McGinnis, "Nanoceria as bona fide catalytic antioxidants in medicine: what we know and what we want to know…," *Retinal Degenerative Diseases*, pp. 821-828: Springer, 2014.

[25] L. Fiorani, M. Passacantando, S. Santucci, S. Di Marco, S. Bisti, and R. Maccarone, "Cerium oxide nanoparticles reduce microglial activation and neurodegenerative events in light damaged retina," *PLoS One,* vol. 10, no. 10, pp. e0140387, 2015.

[26] S. Chigurupati, M. R. Mughal, E. Okun, S. Das, A. Kumar, M. McCaffery, S. Seal, and M. P. Mattson, "Effects of cerium oxide nanoparticles on the growth of keratinocytes, fibroblasts and vascular endothelial cells in cutaneous wound healing," *Biomaterials,* vol. 34, no. 9, pp. 2194-2201, 2013.

[27] C. K. Kim, T. Kim, I. Y. Choi, M. Soh, D. Kim, Y. J. Kim, H. Jang, H. S. Yang, J. Y. Kim, and H. K. Park, "Ceria nanoparticles that can protect against ischemic stroke," *Angewandte Chemie International Edition,* vol. 51, no. 44, pp. 11039-11043, 2012.

[28]   R. A. Yokel, T. C. Au, R. MacPhail, S. S. Hardas, D. A. Butterfield, R. Sultana, M. Goodman, M. T. Tseng, M. Dan, and H. Haghnazar, "Distribution, elimination, and biopersistence to 90 days of a systemically introduced 30 nm ceria-engineered nanomaterial in rats," *Toxicological Sciences,* vol. 127, no. 1, pp. 256-268, 2012.

[29]   R. A. Yokel, R. L. Florence, J. M. Unrine, M. T. Tseng, U. M. Graham, P. Wu, E. A. Grulke, R. Sultana, S. S. Hardas, and D. A. Butterfield, "Biodistribution and oxidative stress effects of a systemically-introduced commercial ceria engineered nanomaterial," *Nanotoxicology,* vol. 3, no. 3, pp. 234-248, 2009.

[30]   R. A. Yokel, S. Hussain, S. Garantziotis, P. Demokritou, V. Castranova, and F. R. Cassee, "The yin: an adverse health perspective of nanoceria: uptake, distribution, accumulation, and mechanisms of its toxicity," *Environmental Science: Nano,* vol. 1, no. 5, pp. 406-428, 2014.

[31]   E. Casals, M. F. Gusta, J. Piella, G. Casals, W. Jiménez, and V. Puntes, "Intrinsic and extrinsic properties affecting innate immune responses to nanoparticles: the case of cerium oxide," *Frontiers in Immunology,* vol. 8, pp. 970, 2017.

[32]   E. A. Grulke, M. J. Beck, R. A. Yokel, J. M. Unrine, U. M. Graham, and M. L. Hancock, "Surface-controlled dissolution rates: a case study of nanoceria in carboxylic acid solutions," *Environmental Science: Nano,* vol. 6, no. 5, pp. 1478-1492, 2019.

[33]   R. A. Yokel, M. L. Hancock, E. A. Grulke, J. M. Unrine, A. K. Dozier, and U. M. Graham, "Carboxylic acids accelerate acidic environment-mediated nanoceria dissolution," *Nanotoxicology,* vol. 13, no. 4, pp. 455-475, 2019.

[34]   R. A. Yokel, M. L. Hancock, B. Cherian, A. J. Brooks, M. L. Ensor, H. J. Vekaria, P. G. Sullivan, and E. A. Grulke, "Simulated biological fluid exposure changes nanoceria's surface properties but not its biological response," *European Journal of Pharmaceutics and Biopharmaceutics,* vol. 144, pp. 252-265, 2019.

[35]   U. M. Graham, G. Jacobs, R. A. Yokel, B. H. Davis, A. K. Dozier, M. E. Birch, M. T. Tseng, G. Oberdörster, A. Elder, and L. DeLouise, "From dose to response: in vivo nanoparticle processing and potential toxicity," *Modelling the Toxicity of Nanoparticles*, pp. 71-100: Springer, 2017.

[36]   U. M. Graham, M. T. Tseng, J. B. Jasinski, R. A. Yokel, J. M. Unrine, B. H. Davis, A. K. Dozier, S. S. Hardas, R. Sultana, E. A. Grulke, and D. A. Butterfield, "In vivo processing of ceria nanoparticles inside liver: impact on free-radical scavenging

activity and oxidative stress," *ChemPlusChem,* vol. 79, no. 8, pp. 1083-1088, Aug, 2014.

[37] U. M. Graham, R. A. Yokel, A. K. Dozier, L. Drummy, K. Mahalingam, M. T. Tseng, E. Birch, and J. Fernback, "Analytical high-resolution electron microscopy reveals organ-specific nanoceria bioprocessing," *Toxicologic Pathology,* vol. 46, no. 1, pp. 47-61, 2018.

[38] E. G. Heckert, A. S. Karakoti, S. Seal, and W. T. Self, "The role of cerium redox state in the SOD mimetic activity of nanoceria," *Biomaterials,* vol. 29, no. 18, pp. 2705-2709, 2008.

[39] Y. Lin, C. Xu, J. Ren, and X. Qu, "Using thermally regenerable cerium oxide nanoparticles in biocomputing to perform label-free, resettable, and colorimetric logic operations," *Angewandte Chemie International Edition,* vol. 51, no. 50, pp. 12579-12583, 2012.

[40] K. Reed, A. Cormack, A. Kulkarni, M. Mayton, D. Sayle, F. Klaessig, and B. Stadler, "Exploring the properties and applications of nanoceria: is there still plenty of room at the bottom?," *Environmental Science: Nano,* vol. 1, no. 5, pp. 390-405, 2014.

[41] S. Singh, T. Dosani, A. S. Karakoti, A. Kumar, S. Seal, and W. T. Self, "A phosphate-dependent shift in redox state of cerium oxide nanoparticles and its effects on catalytic properties," *Biomaterials,* vol. 32, no. 28, pp. 6745-6753, 2011.

[42] S. Deshpande, S. Patil, S. V. Kuchibhatla, and S. Seal, "Size dependency variation in lattice parameter and valency states in nanocrystalline cerium oxide," *Applied Physics Letters,* vol. 87, no. 13, pp. 133113, 2005.

[43] T. Masui, H. Hirai, N. Imanaka, G. Adachi, T. Sakata, and H. Mori, "Synthesis of cerium oxide nanoparticles by hydrothermal crystallization with citric acid," *Journal of Materials Science Letters,* vol. 21, no. 6, pp. 489-491, 2002.

[44] Y. Zhang, Y. Lin, C. Jing, and Y. Qin, "Formation and thermal decomposition of cerium-organic precursor for nanocrystalline cerium oxide powder synthesis," *Journal of Dispersion Science and Technology,* vol. 28, no. 7, pp. 1053-1058, 2007.

[45] M. P. Da Silva, L. Soeira, K. Daghastanli, T. Martins, I. Cuccovia, R. Freire, and P. Isolani, "CeO$_2$-catalyzed ozonation of phenol," *Journal of Thermal Analysis and Calorimetry,* vol. 102, no. 3, pp. 907-913, 2010.

[46] Z. L. Wang, and X. Feng, "Polyhedral shapes of CeO$_2$ nanoparticles," *The Journal of Physical Chemistry B,* vol. 107, no. 49, pp. 13563-13566, 2003.

[47] I. A. Mudunkotuwa, and V. H. Grassian, "The devil is in the details (or the surface): impact of surface structure and surface energetics on understanding the behavior of nanomaterials in the environment," *Journal of Environmental Monitoring,* vol. 13, no. 5, pp. 1135-1144, 2011.

[48] H.-I. Chen, and H.-Y. Chang, "Synthesis and characterization of nanocrystalline cerium oxide powders by two-stage non-isothermal precipitation," *Solid State Communications,* vol. 133, no. 9, pp. 593-598, 2005.

[49] Y. Li, J. G. He, and X. W. Huang, "Synthesis and properties of cerium oxide nanoparticles," *Advanced Materials Research,* vol. 299, pp. 118-121, 2011.

[50] N. K. Chandar, and R. Jayavel, "Synthesis and characterization of C$_{14}$TAB passivated cerium oxide nanoparticles prepared by co-precipitation route," *Physica E: Low-Dimensional Systems and Nanostructures,* vol. 58, pp. 48-51, 2014.

[51] A. Verma, N. Karar, A. Bakhshi, H. Chander, S. Shivaprasad, and S. Agnihotry, "Structural, morphological and photoluminescence characteristics of sol-gel derived nano phase CeO$_2$ films deposited using citric acid," *Journal of Nanoparticle Research,* vol. 9, no. 2, pp. 317-322, 2007.

[52] M. Darroudi, M. Sarani, R. K. Oskuee, A. K. Zak, H. A. Hosseini, and L. Gholami, "Green synthesis and evaluation of metabolic activity of starch mediated nanoceria," *Ceramics International,* vol. 40, no. 1, pp. 2041-2045, 2014.

[53] P. Tamizhdurai, S. Sakthinathan, S.-M. Chen, K. Shanthi, S. Sivasanker, and P. Sangeetha, "Environmentally friendly synthesis of CeO$_2$ nanoparticles for the catalytic oxidation of benzyl alcohol to benzaldehyde and selective detection of nitrite," *Scientific Reports,* vol. 7, pp. 46372, 2017.

[54] H. Xu, L. Gao, H. Gu, J. Guo, and D. Yan, "Synthesis of solid, spherical CeO$_2$ particles prepared by the spray hydrolysis reaction method," *Journal of the American Ceramic Society,* vol. 85, no. 1, pp. 139-144, 2002.

[55] X. Feng, D. C. Sayle, Z. L. Wang, M. S. Paras, B. Santora, A. C. Sutorik, T. X. Sayle, Y. Yang, Y. Ding, and X. Wang, "Converting ceria polyhedral nanoparticles into single-crystal nanospheres," *Science,* vol. 312, no. 5779, pp. 1504-1508, 2006.

[56] L. Yin, Y. Wang, G. Pang, Y. Koltypin, and A. Gedanken, "Sonochemical synthesis of cerium oxide nanoparticles—effect of additives and quantum size effect," *Journal of Colloid and Interface Science,* vol. 246, no. 1, pp. 78-84, 2002.

[57] D. Zhang, H. Fu, L. Shi, C. Pan, Q. Li, Y. Chu, and W. Yu, "Synthesis of CeO_2 nanorods via ultrasonication assisted by polyethylene glycol," *Inorganic Chemistry,* vol. 46, no. 7, pp. 2446-2451, 2007.

[58] C. Y. Jimmy, L. Zhang, and J. Lin, "Direct sonochemical preparation of high-surface-area nanoporous ceria and ceria–zirconia solid solutions," *Journal of Colloid and Interface Science,* vol. 260, no. 1, pp. 240-243, 2003.

[59] T. Masui, K. Fujiwara, K.-i. Machida, G.-y. Adachi, T. Sakata, and H. Mori, "Characterization of cerium(IV) oxide ultrafine particles prepared using reversed micelles," *Chemistry of Materials,* vol. 9, no. 10, pp. 2197-2204, 1997.

[60] E. K. Goharshadi, S. Samiee, and P. Nancarrow, "Fabrication of cerium oxide nanoparticles: characterization and optical properties," *Journal of Colloid and Interface Science,* vol. 356, no. 2, pp. 473-480, 2011.

[61] C. Riccardi, R. Lima, M. Dos Santos, P. R. Bueno, J. A. Varela, and E. Longo, "Preparation of CeO_2 by a simple microwave–hydrothermal method," *Solid State Ionics,* vol. 180, no. 2-3, pp. 288-291, 2009.

[62] Y. Tao, F. Gong, H. Wang, H. Wu, and G. Tao, "Microwave-assisted preparation of cerium dioxide nanocubes," *Materials Chemistry and Physics,* vol. 112, no. 3, pp. 973-976, 2008.

[63] M. Dos Santos, R. Lima, C. Riccardi, R. Tranquilin, P. R. Bueno, J. A. Varela, and E. Longo, "Preparation and characterization of ceria nanospheres by microwave-hydrothermal method," *Materials Letters,* vol. 62, no. 30, pp. 4509-4511, 2008.

[64] E. Kumar, P. Selvarajan, and D. Muthuraj, "Synthesis and characterization of CeO_2 nanocrystals by solvothermal route," *Materials Research,* vol. 16, no. 2, pp. 269-276, 2013.

[65]   Z. Yang, Y. Yang, H. Liang, and L. Liu, "Hydrothermal synthesis of monodisperse CeO_2 nanocubes," *Materials Letters,* vol. 21, no. 63, pp. 1774-1777, 2009.

[66]   R. Yu, L. Yan, P. Zheng, J. Chen, and X. Xing, "Controlled synthesis of CeO_2 flower-like and well-aligned nanorod hierarchical architectures by a phosphate-assisted hydrothermal route," *The Journal of Physical Chemistry C,* vol. 112, no. 50, pp. 19896-19900, 2008.

[67]   T. Masui, H. Hirai, R. Hamada, N. Imanaka, G.-y. Adachi, T. Sakata, and H. Mori, "Synthesis and characterization of cerium oxide nanoparticles coated with turbostratic boron nitride," *Journal of Materials Chemistry,* vol. 13, no. 3, pp. 622-627, 2003.

[68]   Z. Yan, J. Wang, R. Zou, L. Liu, Z. Zhang, and X. Wang, "Hydrothermal synthesis of CeO_2 nanoparticles on activated carbon with enhanced desulfurization activity," *Energy & Fuels,* vol. 26, no. 9, pp. 5879-5886, 2012.

[69]   A. A. Baqer, K. A. Matori, N. M. Al-Hada, A. H. Shaari, E. Saion, and J. L. Y. Chyi, "Effect of polyvinylpyrrolidone on cerium oxide nanoparticle characteristics prepared by a facile heat treatment technique," *Results in Physics,* vol. 7, pp. 611-619, 2017.

[70]   H.-X. Mai, L.-D. Sun, Y.-W. Zhang, R. Si, W. Feng, H.-P. Zhang, H.-C. Liu, and C.-H. Yan, "Shape-selective synthesis and oxygen storage behavior of ceria nanopolyhedra, nanorods, and nanocubes," *The Journal of Physical Chemistry B,* vol. 109, no. 51, pp. 24380-24385, 2005.

[71]   H. Gu, and M. D. Soucek, "Preparation and characterization of monodisperse cerium oxide nanoparticles in hydrocarbon solvents," *Chemistry of Materials,* vol. 19, no. 5, pp. 1103-1110, 2007.

[72]   W. J. Stark, "Nanoparticles in biological systems," *Angewandte Chemie International Edition,* vol. 50, no. 6, pp. 1242-1258, 2011.

[73]   M. Dan, P. Wu, E. A. Grulke, U. M. Graham, J. M. Unrine, and R. A. Yokel, "Ceria-engineered nanomaterial distribution in, and clearance from, blood: size matters," *Nanomedicine,* vol. 7, no. 1, pp. 95-110, 2012.

[74]   R. M. Molina, N. V. Konduru, R. J. Jimenez, G. Pyrgiotakis, P. Demokritou, W. Wohlleben, and J. D. Brain, "Bioavailability, distribution and clearance of

tracheally instilled, gavaged or injected cerium dioxide nanoparticles and ionic cerium," *Environmental Science: Nano,* vol. 1, no. 6, pp. 561-573, 2014.

[75]   K. Bjondahl, "Differences in liver weight, mortality in cerium-treated mice and [144]Ce levels in blood, liver, urine and faeces at various intervals after treatment with nafenopin and pregnenolone 16-alpha-carbonitrile (PCN)," *Medical Biology,* vol. 54, no. 6, pp. 454-460, 1976.

[76]   J. G. Graca, F. C. Davison, and J. B. Feavel, "Comparative toxicity of stable rare earth compounds: acute toxicity of intravenous injections of chlorides and chelates in dogs," *Archives of Environmental Health: An International Journal,* vol. 8, no. 4, pp. 555-564, 1964.

[77]   Y. Nakamura, Y. Tsumura, Y. Tonogai, T. Shibata, and Y. Ito, "Differences in behavior among the chlorides of seven rare earth elements administered intravenously to rats," *Toxicological Sciences,* vol. 37, no. 2, pp. 106-116, 1997.

[78]   R. A. Yokel, M. T. Tseng, M. Dan, J. M. Unrine, U. M. Graham, P. Wu, and E. A. Grulke, "Biodistribution and biopersistence of ceria engineered nanomaterials: size dependence," *Nanomedicine: Nanotechnology, Biology and Medicine,* vol. 9, no. 3, pp. 398-407, 2013.

[79]   Y. Cheng, M. Liu, Y. Li, R. Li, C. Bai, and K. Wang, "Formation of domain structure of erythrocyte membrane in Wistar rat fed with $CeCl_3$ per os," *Chinese Science Bulletin,* vol. 45, no. 5, pp. 426-429, 2000.

[80]   C. Chen, P. Zhang, and Z. Chai, "Distribution of some rare earth elements and their binding species with proteins in human liver studied by instrumental neutron activation analysis combined with biochemical techniques," *Analytica Chimica Acta,* vol. 439, no. 1, pp. 19-27, 2001.

[81]   K. Takada, "Effects of low doses of DTPA on the excretion and organ retention of [144]Ce in the rat," *Strahlentherapie,* vol. 153, no. 3, pp. 195-199, 1977.

[82]   K. Takada, and M. Fujita, "Effects of DTPA on the excretion and tissue distribution of [144]Ce administered subcutaneously, intramuscularly and intravenously in rats," *Journal of Radiation Research,* vol. 14, no. 2, pp. 187-197, 1973.

[83] M. Bobtelsky, and B. Graus, "Cerous citrate complexes, their composition, structure and behavior," *Journal of the American Chemical Society,* vol. 77, no. 7, pp. 1990-1993, 1955.

[84] R. Leal, "Composition and stability constant of a complex of cerium and ammonium citrate at alkaline pH," *Journal of Inorganic and Nuclear Chemistry,* vol. 10, no. 1-2, pp. 159-161, 1959.

[85] A. Ohyoshi, E. Ohyoshi, H. Ono, and S. Yamakawa, "A study of citrate complexes of several lanthanides," *Journal of Inorganic and Nuclear Chemistry,* vol. 34, no. 6, pp. 1955-1960, 1972.

[86] R. Baggio, R. Calvo, M. T. Garland, O. Peña, M. Perec, and A. Rizzi, "Gadolinium and neodymium citrates: evidence for weak ferromagnetic exchange between gadolinium(III) cations," *Inorganic Chemistry,* vol. 44, no. 24, pp. 8979-8987, 2005.

[87] B. Müller, W. Kläger, and G. Kubitzki, "Metal chelates of citric acid as corrosion inhibitors for zinc pigment," *Corrosion Science,* vol. 39, no. 8, pp. 1481-1485, 1997.

[88] G. Vanhoyland, J. Pagnaer, J. D'Haen, S. Mullens, and J. Mullens, "Characterization and structural study of lanthanum citrate trihydrate $[La(C_6H_5O_7)(H_2O)_2] \cdot H_2O$," *Journal of Solid State Chemistry,* vol. 178, no. 1, pp. 166-171, 2005.

[89] R.-S. Zhou, J.-F. Song, Q.-F. Yang, X.-Y. Xu, J.-Q. Xu, and T.-G. Wang, "Syntheses, structures and magnetic properties of a series of 2D and 3D lanthanide complexes constructed by citric ligand," *Journal of Molecular Structure,* vol. 877, no. 1-3, pp. 115-122, 2008.

[90] M. Taguchi, S. Takami, T. Naka, and T. Adschiri, "Growth mechanism and surface chemical characteristics of dicarboxylic acid-modified CeO_2 nanocrystals produced in supercritical water: tailor-made water-soluble CeO_2 nanocrystals," *Crystal Growth & Design,* vol. 9, no. 12, pp. 5297-5303, 2009.

[91] R. Baggio, and M. Perec, "Isolation and characterization of a polymeric lanthanum citrate," *Inorganic Chemistry,* vol. 43, no. 22, pp. 6965-6968, 2004.

[92] M. Getsova, D. Todorovsky, V. Enchev, and I. Wawer, "Cerium(III/IV) and Cerium(IV)–Titanium(IV) citric complexes prepared in ethylene glycol medium," *Monatshefte für Chemie/Chemical Monthly,* vol. 138, no. 5, pp. 389-401, 2007.

[93] M.-L. Chen, S. Gao, and Z.-H. Zhou, "Isolations and characterization of highly water-soluble dimeric lanthanide citrate and malate with ethylenediaminetetraacetate," *Dalton Transactions,* vol. 41, no. 4, pp. 1202-1209, 2012.

[94] A. Heller, A. Barkleit, H. Foerstendorf, S. Tsushima, K. Heim, and G. Bernhard, "Curium(III) citrate speciation in biological systems: a europium(III) assisted spectroscopic and quantum chemical study," *Dalton Transactions,* vol. 41, no. 45, pp. 13969-13983, 2012.

[95] M. Auffan, A. Masion, J. Labille, M.-A. Diot, W. Liu, L. Olivi, O. Proux, F. Ziarelli, P. Chaurand, and C. Geantet, "Long-term aging of a CeO_2 based nanocomposite used for wood protection," *Environmental Pollution,* vol. 188, pp. 1-7, 2014.

[96] S. Turner, S. Lazar, B. Freitag, R. Egoavil, J. Verbeeck, S. Put, Y. Strauven, and G. Van Tendeloo, "High resolution mapping of surface reduction in ceria nanoparticles," *Nanoscale,* vol. 3, no. 8, pp. 3385-3390, 2011.

[97] C. Xiong, and S. Friedlander, "Morphological properties of atmospheric aerosol aggregates," *Proceedings of the National Academy of Sciences,* vol. 98, no. 21, pp. 11851-11856, 2001.

[98] J. M. López, A. L. Gilbank, T. García, B. Solsona, S. Agouram, and L. Torrente-Murciano, "The prevalence of surface oxygen vacancies over the mobility of bulk oxygen in nanostructured ceria for the total toluene oxidation," *Applied Catalysis B: Environmental,* vol. 174, pp. 403-412, 2015.

[99] M. Chelliah, J. B. B. Rayappan, and U. M. Krishnan, "Synthesis and characterization of cerium oxide nanoparticles by hydroxide mediated approach," *Journal of Applied Sciences,* vol. 12, pp. 1734-1737, 2012.

[100] C. Veranitisagul, A. Kaewvilai, S. Sangngern, W. Wattanathana, S. Suramitr, N. Koonsaeng, and A. Laobuthee, "Novel recovery of nano-structured ceria (CeO_2) from Ce(III)-benzoxazine dimer complexes via thermal decomposition," *International Journal of Molecular Sciences,* vol. 12, no. 7, pp. 4365-4377, 2011.

[101] M. Sujana, K. Chattopadyay, and S. Anand, "Characterization and optical properties of nano-ceria synthesized by surfactant-mediated precipitation technique in mixed solvent system," *Applied Surface Science,* vol. 254, no. 22, pp. 7405-7409, 2008.

[102] M. van Drunen, R. Finsy, H. Merkus, B. Scarlett, and G. van Rosmalen, "Measurement of cluster formation in aqueous citric acid solutions by photon correlation spectroscopy," *Journal of Crystal Growth,* vol. 134, no. 3-4, pp. 196-202, 1993.

[103] B. Wang, P. Wu, R. A. Yokel, and E. A. Grulke, "Influence of surface charge on lysozyme adsorption to ceria nanoparticles," *Applied Surface Science,* vol. 258, no. 14, pp. 5332-5341, 2012.

[104] J. McBride, K. Hass, B. Poindexter, and W. Weber, "Raman and X-ray studies of $Ce_{1-x}RE_xO_{2-y}$, where RE= La, Pr, Nd, Eu, Gd, and Tb," *Journal of Applied Physics,* vol. 76, no. 4, pp. 2435-2441, 1994.

[105] T. M. Riddick, *Control of Colloid Stability through Zeta Potential*: Livingston Wynnewood, PA, 1968.

[106] V. K. Ivanov, A. Shcherbakov, and A. Usatenko, "Structure-sensitive properties and biomedical applications of nanodispersed cerium dioxide," *Russian Chemical Reviews,* vol. 78, no. 9, pp. 855, 2009.

[107] A. Dhall, and W. Self, "Cerium oxide nanoparticles: a brief review of their synthesis methods and biomedical applications," *Antioxidants,* vol. 7, no. 8, pp. 97, 2018.

[108] D. L. Jones, "Organic acids in the rhizosphere–a critical review," *Plant and Soil,* vol. 205, no. 1, pp. 25-44, 1998.

[109] E. Grulke, K. Reed, M. Beck, X. Huang, A. Cormack, and S. Seal, "Nanoceria: factors affecting its pro-and anti-oxidant properties," *Environmental Science: Nano,* vol. 1, no. 5, pp. 429-444, 2014.

[110] F. Schwabe, R. Schulin, P. Rupper, A. Rotzetter, W. Stark, and B. Nowack, "Dissolution and transformation of cerium oxide nanoparticles in plant growth media," *Journal of Nanoparticle Research,* vol. 16, no. 10, pp. 2668, 2014.

[111] Y. Ma, P. Zhang, Z. Zhang, X. He, Y. Li, J. Zhang, L. Zheng, S. Chu, K. Yang, and Y. Zhao, "Origin of the different phytotoxicity and biotransformation of cerium and lanthanum oxide nanoparticles in cucumber," *Nanotoxicology,* vol. 9, no. 2, pp. 262-270, 2015.

[112] P. Zhang, Y. H. Ma, Z. Y. Zhang, X. He, J. Zhang, Z. Guo, R. Z. Tai, Y. L. Zhao, and Z. F. Chai, "Biotransformation of ceria nanoparticles in cucumber plants," *ACS Nano,* vol. 6, no. 11, pp. 9943-9950, Nov, 2012.

[113] Y. Rui, P. Zhang, Y. Zhang, Y. Ma, X. He, X. Gui, Y. Li, J. Zhang, L. Zheng, and S. Chu, "Transformation of ceria nanoparticles in cucumber plants is influenced by phosphate," *Environmental Pollution,* vol. 198, pp. 8-14, 2015.

[114] J. A. Hernandez-Viezcas, H. Castillo-Michel, J. C. Andrews, M. Cotte, C. Rico, J. R. Peralta-Videa, Y. Ge, J. H. Priester, P. A. Holden, and J. L. Gardea-Torresdey, "In situ synchrotron X-ray fluorescence mapping and speciation of CeO_2 and ZnO nanoparticles in soil cultivated soybean (Glycine max)," *ACS Nano,* vol. 7, no. 2, pp. 1415-1423, 2013.

[115] L. Zhao, J. R. Peralta-Videa, A. Varela-Ramirez, H. Castillo-Michel, C. Li, J. Zhang, R. J. Aguilera, A. A. Keller, and J. L. Gardea-Torresdey, "Effect of surface coating and organic matter on the uptake of CeO_2 NPs by corn plants grown in soil: insight into the uptake mechanism," *Journal of Hazardous Materials,* vol. 225, pp. 131-138, 2012.

[116] Q. Wang, X. Ma, W. Zhang, H. Pei, and Y. Chen, "The impact of cerium oxide nanoparticles on tomato (Solanum lycopersicum L.) and its implications for food safety," *Metallomics,* vol. 4, no. 10, pp. 1105-1112, 2012.

[117] J. Trujillo-Reyes, A. Vilchis-Nestor, S. Majumdar, J. Peralta-Videa, and J. Gardea-Torresdey, "Citric acid modifies surface properties of commercial CeO_2 nanoparticles reducing their toxicity and cerium uptake in radish (Raphanus sativus) seedlings," *Journal of Hazardous Materials,* vol. 263, pp. 677-684, 2013.

[118] W. Zhang, Y. Dan, H. Shi, and X. Ma, "Elucidating the mechanisms for plant uptake and in-planta speciation of cerium in radish (Raphanus sativus L.) treated with cerium oxide nanoparticles," *Journal of Environmental Chemical Engineering,* vol. 5, no. 1, pp. 572-577, 2017.

[119] N. Manier, A. Bado-Nilles, P. Delalain, O. Aguerre-Chariol, and P. Pandard, "Ecotoxicity of non-aged and aged CeO_2 nanomaterials towards freshwater microalgae," *Environmental Pollution,* vol. 180, pp. 63-70, 2013.

[120] B. Collin, M. Auffan, A. C. Johnson, I. Kaur, A. A. Keller, A. Lazareva, J. R. Lead, X. Ma, R. C. Merrifield, and C. Svendsen, "Environmental release, fate and ecotoxicological effects of manufactured ceria nanomaterials," *Environmental Science: Nano,* vol. 1, no. 6, pp. 533-548, 2014.

[121] P. Laux, C. Riebeling, A. M. Booth, J. D. Brain, J. Brunner, C. Cerrillo, O. Creutzenberg, I. Estrela-Lopis, T. Gebel, and G. Johanson, "Biokinetics of nanomaterials: the role of biopersistence," *NanoImpact,* vol. 6, pp. 69-80, 2017.

[122] L. L. Wong, S. M. Hirst, Q. N. Pye, C. M. Reilly, S. Seal, and J. F. McGinnis, "Catalytic nanoceria are preferentially retained in the rat retina and are not cytotoxic after intravitreal injection," *PloS One,* vol. 8, no. 3, pp. e58431, 2013.

[123] S. Patil, A. Sandberg, E. Heckert, W. Self, and S. Seal, "Protein adsorption and cellular uptake of cerium oxide nanoparticles as a function of zeta potential," *Biomaterials,* vol. 28, no. 31, pp. 4600-4607, 2007.

[124] M. T. Tseng, X. Lu, X. Duan, S. S. Hardas, R. Sultana, P. Wu, J. M. Unrine, U. Graham, D. A. Butterfield, and E. A. Grulke, "Alteration of hepatic structure and oxidative stress induced by intravenous nanoceria," *Toxicology and Applied Pharmacology,* vol. 260, no. 2, pp. 173-182, 2012.

[125] F. Muhammad, A. Wang, W. Qi, S. Zhang, and G. Zhu, "Intracellular antioxidants dissolve man-made antioxidant nanoparticles: using redox vulnerability of nanoceria to develop a responsive drug delivery system," *ACS Applied Materials & Interfaces,* vol. 6, no. 21, pp. 19424-19433, 2014.

[126] A. Ahniyaz, and Y. Sakamoto, "Tuning the aspect ratio of ceria nanorods and nanodumbbells by a face-specific growth and dissolution process," *Crystal Growth & Design,* vol. 8, no. 6, pp. 1798-1800, 2008.

[127] J. T. Dahle, K. Livi, and Y. Arai, "Effects of pH and phosphate on CeO_2 nanoparticle dissolution," *Chemosphere,* vol. 119, pp. 1365-1371, 2015.

[128] I. W. Siriwardane, "Adsorption of citric acid on cerium oxide nanoparticles (nanoceria): effects of pH, surface charge and aggregation," *University of Iowa Master of Science Thesis*, 2012.

[129] G. Cornelis, B. Ryan, M. J. McLaughlin, J. K. Kirby, D. Beak, and D. Chittleborough, "Solubility and batch retention of CeO_2 nanoparticles in soils," *Environmental Science & Technology,* vol. 45, no. 7, pp. 2777-2782, 2011.

[130] T. V. Plakhova, A. Y. Romanchuk, S. N. Yakunin, T. Dumas, S. Demir, S. Wang, S. G. Minasian, D. K. Shuh, T. Tyliszczak, and A. A. Shiryaev, "Solubility of nanocrystalline cerium dioxide: experimental data and thermodynamic modeling," *The Journal of Physical Chemistry C,* vol. 120, no. 39, pp. 22615-22626, 2016.

[131] L. Truffault, M.-T. Ta, T. Devers, K. Konstantinov, V. Harel, C. Simmonard, C. Andreazza, I. P. Nevirkovets, A. Pineau, and O. Veron, "Application of nanostructured Ca doped CeO_2 for ultraviolet filtration," *Materials Research Bulletin,* vol. 45, no. 5, pp. 527-535, 2010.

[132] S. Tsunekawa, T. Fukuda, and A. Kasuya, "Blue shift in ultraviolet absorption spectra of monodisperse CeO_{2-x} nanoparticles," *Journal of Applied Physics,* vol. 87, no. 3, pp. 1318-1321, 2000.

[133] N. Zholobak, V. Ivanov, A. Shcherbakov, A. Shaporev, O. Polezhaeva, A. Y. Baranchikov, N. Y. Spivak, and Y. D. Tretyakov, "UV-shielding property, photocatalytic activity and photocytotoxicity of ceria colloid solutions," *Journal of Photochemistry and Photobiology B: Biology,* vol. 102, no. 1, pp. 32-38, 2011.

[134] Y. Zhang, T. A. Blewett, A. L. Val, and G. G. Goss, "UV-induced toxicity of cerium oxide nanoparticles (CeO_2 NPs) and the protective properties of natural organic matter (NOM) from the Rio Negro Amazon River," *Environmental Science: Nano,* vol. 5, no. 2, pp. 476-486, 2018.

[135] V. De Matteis, M. Cascione, V. Brunetti, C. C. Toma, and R. Rinaldi, "Toxicity assessment of anatase and rutile titanium dioxide nanoparticles: the role of degradation in different pH conditions and light exposure," *Toxicology in Vitro,* vol. 37, pp. 201-210, 2016.

[136] M. Li, M. E. Noriega-Trevino, N. Nino-Martinez, C. Marambio-Jones, J. Wang, R. Damoiseaux, F. Ruiz, and E. M. Hoek, "Synergistic bactericidal activity of Ag-TiO_2 nanoparticles in both light and dark conditions," *Environmental Science & Technology,* vol. 45, no. 20, pp. 8989-8995, 2011.

[137] T. G. Waddell, S. K. Geevarghese, B. S. Henderson, R. M. Pagni, and J. S. Newton, "Chemical evolution of the citric acid cycle: Sunlight and ultraviolet photolysis of cycle intermediates," *Origins of Life and Evolution of the Biosphere,* vol. 19, no. 6, pp. 603-607, 1989.

[138] K. A. Christensen, J. T. Myers, and J. A. Swanson, "pH-dependent regulation of lysosomal calcium in macrophages," *Journal of Cell Science,* vol. 115, no. 3, pp. 599-607, 2002.

[139] J. Zhang, M. Yang, C. Li, N. Dorh, F. Xie, F.-T. Luo, A. Tiwari, and H. Liu, "Near-infrared fluorescent probes based on piperazine-functionalized BODIPY dyes for sensitive detection of lysosomal pH," *Journal of Materials Chemistry B,* vol. 3, no. 10, pp. 2173-2184, 2015.

[140] A. J. Allen, V. A. Hackley, P. R. Jemian, J. Ilavsky, J. M. Raitano, and S.-W. Chan, "In situ ultra-small-angle X-ray scattering study of the solution-mediated formation and growth of nanocrystalline ceria," *Journal of Applied Crystallography,* vol. 41, no. 5, pp. 918-929, 2008.

[141] C. L. Forryan, O. V. Klymenko, C. M. Brennan, and R. G. Compton, "Reactions at the solid−liquid interface: surface-controlled dissolution of solid particles. The dissolution of potassium bicarbonate in dimethylformamide," *The Journal of Physical Chemistry B,* vol. 109, no. 7, pp. 2862-2872, 2005.

[142] E. A. Grulke, K. Yamamoto, K. Kumagai, I. Häusler, W. Österle, E. Ortel, V.-D. Hodoroaba, S. C. Brown, C. Chan, and J. Zheng, "Size and shape distributions of primary crystallites in titania aggregates," *Advanced Powder Technology,* vol. 28, no. 7, pp. 1647-1659, 2017.

[143] J. Gagnon, and K. M. Fromm, "Toxicity and protective effects of cerium oxide nanoparticles (nanoceria) depending on their preparation method, particle size, cell type, and exposure route," *European Journal of Inorganic Chemistry,* vol. 2015, no. 27, pp. 4510-4517, 2015.

[144] M. P. Monopoli, D. Walczyk, A. Campbell, G. Elia, I. Lynch, F. Baldelli Bombelli, and K. A. Dawson, "Physical−chemical aspects of protein corona: relevance to in vitro and in vivo biological impacts of nanoparticles," *Journal of the American Chemical Society,* vol. 133, no. 8, pp. 2525-2534, 2011.

[145] É. Pérez-Esteve, M. Ruiz-Rico, C. de la Torre, E. Llorca, F. Sancenón, M. D. Marcos, P. Amorós, C. Guillem, R. Martínez-Máñez, and J. M. Barat, "Stability of

different mesoporous silica particles during an in vitro digestion," *Microporous and Mesoporous Materials,* vol. 230, pp. 196-207, 2016.

[146] P. N. Wiecinski, K. M. Metz, A. N. Mangham, K. H. Jacobson, R. J. Hamers, and J. A. Pedersen, "Gastrointestinal biodurability of engineered nanoparticles: development of an in vitro assay," *Nanotoxicology,* vol. 3, no. 3, pp. 202-214, 2009.

[147] L. Zhong, Y. Yu, H.-z. Lian, X. Hu, H. Fu, and Y.-j. Chen, "Solubility of nano-sized metal oxides evaluated by using in vitro simulated lung and gastrointestinal fluids: implication for health risks," *Journal of Nanoparticle Research,* vol. 19, no. 11, pp. 375, 2017.

[148] M. R. Marques, R. Loebenberg, and M. Almukainzi, "Simulated biological fluids with possible application in dissolution testing," *Dissolution Technologies,* vol. 18, no. 3, pp. 15-28, 2011.

[149] S. Haeberle, and R. Zengerle, "Microfluidic platforms for lab-on-a-chip applications," *Lab on a Chip,* vol. 7, no. 9, pp. 1094-1110, 2007.

[150] X. Weng, H. Jiang, and D. Li, "Microfluidic DNA hybridization assays," *Microfluidics and Nanofluidics,* vol. 11, no. 4, pp. 367, 2011.

[151] V. Srinivasan, V. K. Pamula, and R. B. Fair, "An integrated digital microfluidic lab-on-a-chip for clinical diagnostics on human physiological fluids," *Lab on a Chip,* vol. 4, no. 4, pp. 310-315, 2004.

[152] J. Gardeniers, and A. Van den Berg, "Lab-on-a-chip systems for biomedical and environmental monitoring," *Analytical & Bioanalytical Chemistry,* vol. 378, no. 7, pp. 1700-1703, 2004.

[153] B. S. Cook, J. R. Cooper, and M. M. Tentzeris, "An inkjet-printed microfluidic RFID-enabled platform for wireless lab-on-chip applications," *IEEE Transactions on Microwave Theory and Techniques,* vol. 61, no. 12, pp. 4714-4723, 2013.

[154] R. Osellame, R. M. Vázquez, R. Ramponi, and G. Cerullo, "Integrating optical sensing into lab-on-a-chip systems," *SPIE Newsroom*, 2009.

[155] E. Verpoorte, "Chip vision-optics for microchips," *Lab on a Chip,* vol. 3, no. 3, pp. 42N, 2003.

[156] H. Becker, and L. E. Locascio, "Polymer microfluidic devices," *Talanta,* vol. 56, no. 2, pp. 267-287, 2002.

[157] K. Geng, "Mechanical evaluation of nanocomposite coatings," *University of Kentucky Doctoral Dissertations*, 2006.

[158] T. Druffel, O. Buazza, M. Lattis, S. Farmer, M. Spencer, N. Mandzy, and E. Grulke, "The role of nanoparticles in visible transparent nanocomposites," *NanoScience+ Engineering*, pp. 70300F-70300F-9, 2008.

[159] J.-g. Liu, and M. Ueda, "High refractive index polymers: fundamental research and practical applications," *Journal of Materials Chemistry,* vol. 19, no. 47, pp. 8907-8919, 2009.

[160] A. H. Yuwono, B. Liu, J. Xue, J. Wang, H. I. Elim, W. Ji, Y. Li, and T. J. White, "Controlling the crystallinity and nonlinear optical properties of transparent TiO_2–PMMA nanohybrids," *Journal of Materials Chemistry,* vol. 14, no. 20, pp. 2978-2987, 2004.

[161] Y. Rao, and S. Chen, "Molecular composites comprising TiO_2 and their optical properties," *Macromolecules,* vol. 41, no. 13, pp. 4838-4844, 2008.

[162] P. Anandgaonker, G. Kulkarni, S. Gaikwad, and A. Rajbhoj, "Synthesis of TiO_2 nanoparticles by electrochemical method and their antibacterial application," *Arabian Journal of Chemistry*, 2015.

[163] J. Podporska-Carroll, E. Panaitescu, B. Quilty, L. Wang, L. Menon, and S. C. Pillai, "Antimicrobial properties of highly efficient photocatalytic TiO_2 nanotubes," *Applied Catalysis B: Environmental,* vol. 176, pp. 70-75, 2015.

[164] M. A. Vargas, and J. E. Rodriguez-Paez, "Amorphous TiO_2 nanoparticles: synthesis and antibacterial capacity," *Journal of Non-Crystalline Solids,* vol. 459, pp. 192-205, 2017.

[165] K. Kaur, and C. V. Singh, "Amorphous TiO_2 as a photocatalyst for hydrogen production: a DFT study of structural and electronic properties," *Energy Procedia,* vol. 29, pp. 291-299, 2012.

[166]   S. Boyadzhiev, V. Georgieva, and M. Rassovska, "Characterization of reactive sputtered TiO$_2$ thin films for gas sensor applications," *Journal of Physics: Conference Series,* vol. 253, no. 1, pp. 012040, 2010.

[167]   H. F. Lu, F. Li, G. Liu, Z.-G. Chen, D.-W. Wang, H.-T. Fang, G. Q. Lu, Z. H. Jiang, and H.-M. Cheng, "Amorphous TiO$_2$ nanotube arrays for low-temperature oxygen sensors," *Nanotechnology,* vol. 19, no. 40, pp. 405504, 2008.

[168]   U. Bach, D. Lupo, P. Comte, J. Moser, F. Weissörtel, J. Salbeck, H. Spreitzer, and M. Grätzel, "Solid-state dye-sensitized mesoporous TiO$_2$ solar cells with high photon-to-electron conversion efficiencies," *Nature,* vol. 395, no. 6702, pp. 583, 1998.

[169]   W. Shimizu, S. Nakamura, T. Sato, and Y. Murakami, "Creation of high-refractive-index amorphous titanium oxide thin films from low-fractal-dimension polymeric precursors synthesized by a sol–gel technique with a hydrazine monohydrochloride catalyst," *Langmuir,* vol. 28, no. 33, pp. 12245-12255, 2012.

[170]   N. S. Mandzy, E. A. Grulke, and T. L. Druffle, "Methods of making and using metal oxide nanoparticles," 0202714, United States Patent, 2009.

[171]   D. A. Hanaor, I. Chironi, I. Karatchevtseva, G. Triani, and C. C. Sorrell, "Single and mixed phase TiO$_2$ powders prepared by excess hydrolysis of titanium alkoxide," *Advances in Applied Ceramics,* vol. 111, no. 3, pp. 149-158, 2012.

[172]   S. Mahshid, M. Askari, and M. S. Ghamsari, "Synthesis of TiO$_2$ nanoparticles by hydrolysis and peptization of titanium isopropoxide solution," *Journal of Materials Processing Technology,* vol. 189, no. 1, pp. 296-300, 2007.

[173]   B. E. Yoldas, "Hydrolysis of titanium alkoxide and effects of hydrolytic polycondensation parameters," *Journal of Materials Science,* vol. 21, no. 3, pp. 1087-1092, 1986.

[174]   G. Li, C. P. Richter, R. L. Milot, L. Cai, C. A. Schmuttenmaer, R. H. Crabtree, G. W. Brudvig, and V. S. Batista, "Synergistic effect between anatase and rutile TiO$_2$ nanoparticles in dye-sensitized solar cells," *Dalton Transactions*, no. 45, pp. 10078-10085, 2009.

[175]   T. Theivasanthi, and M. Alagar, "Titanium dioxide (TiO$_2$) nanoparticles XRD analyses: an insight," *arXiv:1307.1091 [physics.chem-ph]*, 2013.

[176] T. Karthik, R. Rathinamoorthy, and R. Murugan, "Enhancement of wrinkle recovery angle of cotton fabric using citric acid cross-linking agent with nano-TiO_2 as a co-catalyst," *Journal of Industrial Textiles,* vol. 42, no. 2, pp. 99-117, 2012.

[177] Y. Masuda, and K. Kato, "Synthesis and phase transformation of TiO_2 nano-crystals in aqueous solutions," *Journal of the Ceramic Society of Japan,* vol. 117, no. 1363, pp. 373-376, 2009.

[178] J. Lin, J. A. Siddiqui, and R. M. Ottenbrite, "Surface modification of inorganic oxide particles with silane coupling agent and organic dyes," *Polymers for Advanced Technologies,* vol. 12, no. 5, pp. 285-292, 2001.

[179] W. Kamphunthong, and K. Sirisinha, "Structure development and viscoelastic properties in silane-crosslinked ethylene–octene copolymer," *Journal of Applied Polymer Science,* vol. 109, no. 4, pp. 2347-2353, 2008.

[180] X. Chen, and S. S. Mao, "Titanium dioxide nanomaterials: synthesis, properties, modifications, and applications," *Chemical Reviews,* vol. 107, no. 7, pp. 2891-2959, 2007.

[181] C.-S. Kim, B. K. Moon, J.-H. Park, S. T. Chung, and S.-M. Son, "Synthesis of nanocrystalline TiO_2 in toluene by a solvothermal route," *Journal of Crystal Growth,* vol. 254, no. 3-4, pp. 405-410, 2003.

[182] A. M. El-Toni, S. Yin, and T. Sato, "Control of silica shell thickness and microporosity of titania–silica core–shell type nanoparticles to depress the photocatalytic activity of titania," *Journal of Colloid and Interface Science,* vol. 300, no. 1, pp. 123-130, 2006.

[183] A. M. El-Toni, S. Yin, and T. Sato, "Dense silica coating of titania nanoparticles by seeded polymerization technique," *Colloids and Surfaces A: Physicochemical and Engineering Aspects,* vol. 274, no. 1-3, pp. 229-233, 2006.

[184] O. K. Park, and Y. S. Kang, "Preparation and characterization of silica-coated TiO_2 nanoparticle," *Colloids and Surfaces A: Physicochemical and Engineering Aspects,* vol. 257, pp. 261-265, 2005.

[185] D. Kannaiyan, S. T. Kochuveedu, Y. H. Jang, Y. J. Jang, J. Y. Lee, J. Lee, J. Lee, J. Kim, and D. H. Kim, "Enhanced photophysical properties of nanopatterned

titania nanodots/nanowires upon hybridization with silica via block copolymer templated sol-gel process," *Polymers,* vol. 2, no. 4, pp. 490-504, 2010.

[186] Q. Guo, R. Ghadiri, T. Weigel, A. Aumann, E. L. Gurevich, C. Esen, O. Medenbach, W. Cheng, B. Chichkov, and A. Ostendorf, "Comparison of in situ and ex situ methods for synthesis of two-photon polymerization polymer nanocomposites," *Polymers,* vol. 6, no. 7, pp. 2037-2050, 2014.

[187] Z. Ismagilov, N. Shikina, N. Mazurkova, L. Tsikoza, F. Tuzikov, V. Ushakov, A. Ishchenko, N. Rudina, D. Korneev, and E. Ryabchikova, "Synthesis of nanoscale TiO_2 and study of the effect of their crystal structure on single cell response," *The Scientific World Journal,* vol. 2012, 2012.

[188] C. Chen, X. Wang, and M. Nagatsu, "Europium adsorption on multiwall carbon nanotube/iron oxide magnetic composite in the presence of polyacrylic acid," *Environmental Science & Technology,* vol. 43, no. 7, pp. 2362-2367, 2009.

[189] J. Fresnais, M. Yan, J. Courtois, T. Bostelmann, A. Bée, and J.-F. Berret, "Poly(acrylic acid)-coated iron oxide nanoparticles: quantitative evaluation of the coating properties and applications for the removal of a pollutant dye," *Journal of Colloid and Interface Science,* vol. 395, pp. 24-30, 2013.

[190] S. Y. Mak, and D. H. Chen, "Binding and sulfonation of poly(acrylic acid) on iron oxide nanoparticles: a novel, magnetic, strong acid cation nano-adsorbent," *Macromolecular Rapid Communications,* vol. 26, no. 19, pp. 1567-1571, 2005.

[191] R. A. Frimpong, J. Dou, M. Pechan, and J. Z. Hilt, "Enhancing remote controlled heating characteristics in hydrophilic magnetite nanoparticles via facile co-precipitation," *Journal of Magnetism and Magnetic Materials,* vol. 322, no. 3, pp. 326-331, 2010.

[192] D. Couto, M. Freitas, V. Vilas-Boas, I. Dias, G. Porto, M. A. Lopez-Quintela, J. Rivas, P. Freitas, F. Carvalho, and E. Fernandes, "Interaction of polyacrylic acid coated and non-coated iron oxide nanoparticles with human neutrophils," *Toxicology Letters,* vol. 225, no. 1, pp. 57-65, 2014.

[193] H. El Ghandoor, H. Zidan, M. M. Khalil, and M. Ismail, "Synthesis and some physical properties of magnetite (Fe_3O_4) nanoparticles," *International Journal of Electrochemical Science,* vol. 7, no. 6, pp. 5734-5745, 2012.

[194] M. Hancock, E. Hawes, F. Yang, and E. Grulke, "Crosslinking gradients of a photopolymerized multifunctional acrylate film control mechanical properties," *Journal of Coatings Technology and Research,* vol. 16, no. 4, pp. 1153-1163, 2019.

[195] M. A. C. Stuart, W. T. Huck, J. Genzer, M. Müller, C. Ober, M. Stamm, G. B. Sukhorukov, I. Szleifer, V. V. Tsukruk, and M. Urban, "Emerging applications of stimuli-responsive polymer materials," *Nature Materials,* vol. 9, no. 2, pp. 101-113, 2010.

[196] R. Armstrong, and D. Wright, "Polymer protective coatings—the distinction between coating porosity and the wetted metal area," *Electrochimica Acta,* vol. 38, no. 14, pp. 1799-1801, 1993.

[197] G. M. Spinks, A. J. Dominis, G. G. Wallace, and D. E. Tallman, "Electroactive conducting polymers for corrosion control," *Journal of Solid State Electrochemistry,* vol. 6, no. 2, pp. 85-100, 2002.

[198] S.-W. Ahn, K.-D. Lee, D.-H. Kim, and S.-S. Lee, "Polymeric wavelength filter based on a Bragg grating using nanoimprint technique," *IEEE Photonics Technology Letters,* vol. 17, no. 10, pp. 2122-2124, 2005.

[199] G. T. Paloczi, Y. Huang, and A. Yariv, "Free-standing all-polymer microring resonator optical filter," *Electronics Letters,* vol. 39, no. 23, pp. 1650, 2003.

[200] C. L. Bayer, and N. A. Peppas, "Advances in recognitive, conductive and responsive delivery systems," *Journal of Controlled Release,* vol. 132, no. 3, pp. 216-221, 2008.

[201] A. S. Hoffman, "The origins and evolution of 'controlled' drug delivery systems," *Journal of Controlled Release,* vol. 132, no. 3, pp. 153-163, 2008.

[202] S. J. Jhaveri, M. R. Hynd, N. Dowell-Mesfin, J. N. Turner, W. Shain, and C. K. Ober, "Release of nerve growth factor from HEMA hydrogel-coated substrates and its effect on the differentiation of neural cells," *Biomacromolecules,* vol. 10, no. 1, pp. 174-183, 2008.

[203] I. Luzinov, S. Minko, and V. V. Tsukruk, "Responsive brush layers: from tailored gradients to reversibly assembled nanoparticles," *Soft Matter,* vol. 4, no. 4, pp. 714-725, 2008.

[204] W. Senaratne, L. Andruzzi, and C. K. Ober, "Self-assembled monolayers and polymer brushes in biotechnology: current applications and future perspectives," *Biomacromolecules,* vol. 6, no. 5, pp. 2427-2448, 2005.

[205] P. M. Mendes, "Stimuli-responsive surfaces for bio-applications," *Chemical Society Reviews,* vol. 37, no. 11, pp. 2512-2529, 2008.

[206] S. Minko, "Responsive polymer brushes," *Journal of Macromolecular Science, Part C: Polymer Reviews,* vol. 46, no. 4, pp. 397-420, 2006.

[207] X. Dong, A. Al-Jumaily, and I. C. Escobar, "Investigation of the use of a bio-derived solvent for non-solvent-induced phase separation (NIPS) fabrication of polysulfone membranes," *Membranes,* vol. 8, no. 2, pp. 23, 2018.

[208] K. Geng, F. Yang, T. Druffel, and E. A. Grulke, "Nanoindentation behavior of ultrathin polymeric films," *Polymer,* vol. 46, no. 25, pp. 11768-11772, 2005.

[209] G. Ellis, M. Claybourn, and S. Richards, "The application of Fourier Transform Raman spectroscopy to the study of paint systems," *Spectrochimica Acta Part A: Molecular Spectroscopy,* vol. 46, no. 2, pp. 227-241, 1990.

[210] M. Wallin, P. Glover, A.-C. Hellgren, J. Keddie, and P. McDonald, "Depth profiles of polymer mobility during the film formation of a latex dispersion undergoing photoinitiated cross-linking," *Macromolecules,* vol. 33, no. 22, pp. 8443-8452, 2000.

[211] M. Nichols, C. Seubert, W. Weber, and J. Gerlock, "A simple Raman technique to measure the degree of cure in UV curable coatings," *Progress in Organic Coatings,* vol. 43, no. 4, pp. 226-232, 2001.

[212] B. Marton, L. G. van der Ven, C. Otto, N. Uzunbajakava, M. A. Hempenius, and G. J. Vancso, "A depth-resolved look at the network development in alkyd coatings by confocal Raman microspectroscopy," *Polymer,* vol. 46, no. 25, pp. 11330-11339, 2005.

[213] Z. Oyman, W. Ming, R. Van Der Linde, J. Ter Borg, A. Schut, and J. Bieleman, "Oxidative drying of alkyd paints catalysed by a dinuclear manganese complex (MnMeTACN)," *Surface Coatings International Part B: Coatings Transactions,* vol. 88, no. B4, pp. 231-316, 2005.

[214]   G. Mirone, B. Marton, and G. J. Vancso, "Elastic modulus profiles in the cross sections of drying alkyd coating films: modelling and experiments," *European Polymer Journal,* vol. 40, no. 3, pp. 549-560, 2004.

[215]   F. Belaroui, Y. Grohens, H. Boyer, and Y. Holl, "Depth profiling of small molecules in dry latex films by confocal Raman spectroscopy," *Polymer,* vol. 41, no. 21, pp. 7641-7645, 2000.

[216]   C. Sammon, S. Hajatdoost, P. Eaton, C. Mura, and J. Yarwood, "Materials analysis using confocal Raman microscopy," *Macromolecular Symposia,* vol. 141, no. 1, pp. 247-262, 1999.

[217]   R. Rodríguez, S. Jiménez-Sandoval, M. Estévez, and S. Vargas, "Drying kinetics and segregation in a two-component anti-adherent coating studied by photoluminescence and Raman spectroscopies," *Journal of Non-Crystalline Solids,* vol. 354, no. 30, pp. 3623-3629, 2008.

[218]   L. F. Sturdy, A. Yee, F. Casadio, and K. R. Shull, "Quantitative characterization of alkyd cure kinetics with the quartz crystal microbalance," *Polymer,* vol. 103, pp. 387-396, 2016.

[219]   C. Comte, and J. Von Stebut, "Microprobe-type measurement of Young's modulus and Poisson coefficient by means of depth sensing indentation and acoustic microscopy," *Surface & Coatings Technology,* vol. 154, no. 1, pp. 42-48, 2002.

[220]   K. Geng, F. Yang, T. Druffel, and E. A. Grulke, "Nanoindentation-induced delamination of submicron polymeric coatings," *Polymer,* vol. 48, no. 3, pp. 841-848, 2007.

[221]   K. Geng, F. Yang, and E. A. Grulke, "Nanoindentation of submicron polymeric coating systems," *Materials Science and Engineering: A,* vol. 479, no. 1, pp. 157-163, 2008.

[222]   T. Carswell, D. Hill, D. Londero, J. O'Donnell, P. Pomery, and C. Winzor, "Kinetic parameters for polymerization of methyl methacrylate at 60 ºC," *Polymer,* vol. 33, no. 1, pp. 137-140, 1992.

[223]   C. Decker, "Kinetic study of light-induced polymerization by real-time UV and IR spectroscopy," *Journal of Polymer Science Part A: Polymer Chemistry,* vol. 30, no. 5, pp. 913-928, 1992.

[224] C. Decker, and A. D. Jenkins, "Kinetic approach of oxygen inhibition in ultraviolet- and laser-induced polymerizations," *Macromolecules,* vol. 18, no. 6, pp. 1241-1244, 1985.

[225] C. Decker, and K. Moussa, "Real-time kinetic study of laser-induced polymerization," *Macromolecules,* vol. 22, no. 12, pp. 4455-4462, 1989.

[226] P. B. Zetterlund, S. Yamauchi, and B. Yamada, "High-temperature propagation and termination kinetics of styrene to high conversion investigated by electron paramagnetic resonance spectroscopy," *Macromolecular Chemistry and Physics,* vol. 205, no. 6, pp. 778-785, 2004.

[227] J.-P. Fouassier, and J. Lalevã, *Photoinitiators for Polymer Synthesis: Scope, Reactivity, and Efficiency*: John Wiley & Sons, 2012.

[228] L. G. B. Albino, J. A. Rodrigues, Y. Kawano, and A. Cassoni, "Knoop microhardness and FT-Raman evaluation of composite resins: influence of opacity and photoactivation source," *Brazilian Oral Research,* vol. 25, no. 3, pp. 267-273, 2011.

[229] J. Rocks, L. Rintoul, F. Vohwinkel, and G. George, "The kinetics and mechanism of cure of an amino-glycidyl epoxy resin by a co-anhydride as studied by FT-Raman spectroscopy," *Polymer,* vol. 45, no. 20, pp. 6799-6811, 2004.

[230] W. C. Oliver, and G. M. Pharr, "An improved technique for determining hardness and elastic modulus using load and displacement sensing indentation experiments," *Journal of Materials Research,* vol. 7, no. 6, pp. 1564-1583, 1992.

[231] C. W. Macosko, and D. R. Miller, "A new derivation of average molecular weights of nonlinear polymers," *Macromolecules,* vol. 9, no. 2, pp. 199-206, 1976.

[232] W. Y. Chiu, G. M. Carratt, and D. S. Soong, "A computer model for the gel effect in free-radical polymerization," *Macromolecules,* vol. 16, no. 3, pp. 348-357, 1983.

[233] S. B. Rice, C. Chan, S. C. Brown, P. Eschbach, L. Han, D. S. Ensor, A. B. Stefaniak, J. Bonevich, A. E. Vladár, and A. R. H. Walker, "Particle size distributions by transmission electron microscopy: an interlaboratory comparison case study," *Metrologia,* vol. 50, no. 6, pp. 663, 2013.

[234] H.-S. Kim, S. R. Dhage, D.-E. Shim, and H. T. Hahn, "Intense pulsed light sintering of copper nanoink for printed electronics," *Applied Physics A: Materials Science & Processing,* vol. 97, no. 4, pp. 791-798, 2009.

[235] S. Wang, H. Xu, L. Qian, X. Jia, J. Wang, Y. Liu, and W. Tang, "CTAB-assisted synthesis and photocatalytic property of CuO hollow microspheres," *Journal of Solid State Chemistry,* vol. 182, no. 5, pp. 1088-1093, 2009.

[236] Y. Sun, and Y. Xia, "Shape-controlled synthesis of gold and silver nanoparticles," *Science,* vol. 298, no. 5601, pp. 2176-2179, 2002.

[237] C. A. Gray, and H. Muranko, "Studies of robustness of industrial aciniform aggregates and agglomerates—carbon black and amorphous silicas: a review amplified by new data," *Journal of Occupational and Environmental Medicine,* vol. 48, no. 12, pp. 1279-1290, 2006.

[238] L. A. Mott, "Towards the rational design and application of polymers for gene therapy: internalization and intracellular fate," *University of Kentucky Doctoral Dissertations*, 2019.

<u>**MATTHEW LOGAN HANCOCK**</u>

EDUCATION:

University of Kentucky. Ph.D. in Chemical Engineering, December 2019

University of Kentucky, Paducah. B.S. in Chemical Engineering, May 2015

West Kentucky Community & Technical College. Associate in Science, May 2013

WORK EXPERIENCE:

University of Kentucky. Graduate Research Assistant; Lexington, KY, 2015-19

NASA Kennedy Space Center, FL. NASA Pathways Intern, 2019

NASA Marshall Space Flight Center, AL. NASA Academy Intern, 2015

Hillbilly Stills. Internship; Barlow, KY, 2014-15.

Paducah-McCracken Joint Sewer Agency. Internship; Paducah, KY, 2013

HONORS & AWARDS:

Wacker Chemie AG Travel Support to present at the 2018 American Coatings Conference in Indianapolis, IN

NASA Marshall Space Flight Center 3rd Place Intern Poster for Engineering - Systems & Communications

University of Kentucky Dean's List

West Kentucky Community & Technical College Mathematics Honors Award

West Kentucky Community & Technical College Certificate for Excellence in Physics

PUBLICATIONS:

M. Hancock, E. Hawes, F. Yang, and E. Grulke, "Crosslinking gradients of a photopolymerized multifunctional acrylate film control mechanical properties," *Journal of Coatings Technology and Research,* vol. 16, no. 4, pp. 1153-1163, 2019.

E. A. Grulke, M. J. Beck, R. A. Yokel, J. M. Unrine, U. M. Graham, and **M. L. Hancock**, "Surface-controlled dissolution rates: a case study of nanoceria in carboxylic acid solutions," *Environmental Science: Nano,* vol. 6, no. 5, pp. 1478-1492, 2019.

R. A. Yokel, **M. L. Hancock**, E. A. Grulke, J. M. Unrine, A. K. Dozier, and U. M. Graham, "Carboxylic acids accelerate acidic environment-mediated nanoceria dissolution," *Nanotoxicology,* vol. 13, no. 4, pp. 455-475, 2019.

R. A. Yokel, **M. L. Hancock**, B. Cherian, A. J. Brooks, M. L. Ensor, H. J. Vekaria, P. G. Sullivan, and E. A. Grulke, "Simulated biological fluid exposure changes nanoceria's surface properties but not its biological response," *European Journal of Pharmaceutics and Biopharmaceutics,* vol. 144, pp. 252-265, 2019.

M. Hancock, R. Yokel, E. Munson, M. Beck, and E. Grulke, "The characterization of citric acid coated cerium oxide nanoparticles prepared via hydrothermal synthesis," *In preparation.*

M. Hancock, R. Yokel, M. Beck, and E. Grulke, "Citric acid coated cerium oxide nanoparticle dissolution and stability in acidic aqueous environments," *In preparation.*

L. Mott, **M. Hancock**, E. Grulke, and D. Pack, "Delivery and intracellular processing of polymer and nanoceria hybrid polyplexes for gene and antioxidant delivery," *In preparation.* (See Chapter 3 of Mott [238])

PRESENTATIONS:

M. Hancock, S. Snyder, and P. Hintze, "Waste water brine purification through electrodialysis ion exchange," *Poster,* 2019 NASA KSC Pathways Intern Poster Expo, Kennedy Space Center, FL.

M. Hancock, E. Hawes, and E. Grulke, "Nanocomposites capable of absorbing ultraviolet radiation by the addition of titania nanoparticles," *Oral,* 2018 AIChE STAR Tech, Houston, TX.

M. Hancock, E. Hawes, F. Yang, and E. Grulke, "Crosslinking gradients of a photopolymerized multifunctional acrylate film control mechanical properties," *Oral,* 2018 AIChE National Conference, Pittsburgh, PA.

M. Hancock, R. Yokel, and E. Grulke, "Ceria nanoparticle dissolution and stability in acidic aqueous environments," *Oral,* 2018 AIChE National Conference, Pittsburgh, PA.

M. Hancock, E. Hawes, F. Yang, and E. Grulke, "Effects of a crosslinking gradient on material properties of a thin film," *Oral,* 2018 American Coatings Conference, Indianapolis, IN.

M. Hancock, E. Hawes, C. Gillette, and E. Grulke, "The fabrication of capillary electrophoresis microfluidic chips with metal oxide nanoparticles to control optical properties," *Poster,* 2017 AIChE National Conference, Minneapolis, MN.

M. Hancock and J. Knox, "Analyzing the structural strength of pelletized carbon dioxide adsorbents," *Poster,* 2015 NASA MSFC Intern Poster Expo, Huntsville, AL.

M. Hancock, M. Haney, and J. Seay, "Using experimental data to model small-scale batch stills for the purpose of scaling-up the column," *Poster,* 2014 AIChE National Student Conference, Atlanta, GA.

M. Hancock and J. Seay, "Using process simulation to estimate the economics of scaling-up experimental results to an industrial scale," *Poster,* 2013 AIChE National Student Conference, San Francisco, CA.